Feasibility and Optimization of Dissimilar Laser Welding Components

Ezzeddin Mohamed Hassan

PhD **2008**

Feasibility and Optimization of Dissimilar Laser Welding Components

By

E. M. Hassan, B. Sc, M. Sc.

This Thesis is submitted to Dublin City University in fulfilment of the requirement for the award of the degree of Doctor of Philosophy (Ph. D.)

Supervisor

Dr. A.G. Olabi

School of Mechanical & Manufacturing Engineering
Dublin City University, Ireland.

March 2008

DECLARATION

I hereby certify that this material, which I now submit for assessment on the programme of study leading to the award of Doctor of Philosophy is entirely my own work and has not been taken from the work of others and to the extent that such work has been cited and acknowledged within the text of my work.

Signed:  **ID No:** **51158272**

Ezzeddin M. Hassan Anawa

Date: **14/07/2008**

ACKNOWLEDGEMENTS

The author would like to express his gratitude and appreciation to his thesis supervisor Dr A.G. Olabi “main supervisor”, lecturer in the School of Mechanical and Manufacturing Engineering in Dublin City University, who has given constant guidance, friendly enthusiasm, constructive criticism, valuable suggestions and encouragement during the completion of this research.

The author wishes to thank Prof. Saleem Hashmi, Head of the School of Mechanical and Manufacturing Engineering, for his support and advice which helped me to achieve this project.

Sincere thanks are due to school technicians for their generous assistance, especially to Mr. Martin Johnson, Mr. Michael May, Mr. Christopher Crouch and Mr. Liam Domican. Thanks are also due to the officers and staff of the school for their help in various stages of the study. The author would also like to thank all his friends and colleagues.

The author is grateful to Garyounis University for having offered the scholarship for pursuing postgraduate study at Dublin City University.

Last but not least, the author wishes to express his gratitude to his mother, father, wife and kids, for their continued encouragement and inspiration throughout his life as well as during this research work**.**

Feasibility and Optimization of Dissimilar Laser Welding Components

Ezzeddin Mohamed Hassan Anawa, Dublin City University

ABSTRACT

Demands placed on dissimilar metals joints have increased from various viewpoints, such as, environmental concerns, energy saving, high performance, cost saving and so on. The aim of this research is to predict and optimize laser welding of some economically important dissimilar materials in industry through applying a Taguchi orthogonal array design as a DOE approach to design the experiments, develop mathematical models and optimize the welding operation. This was achieved by controlling selected welding parameters; laser power, welding speed and focus position, to relate the mechanical properties, weld bead geometry, principal residual stress and unit operating cost to the selected input welding parameters. The dissimilar materials studied in this work are low carbon steel, 316 stainless steel, titanium G2, different types of aluminium alloys such as (6082, 5251H22 and 1050H24) with different thicknesses and different joint designs.

For each dissimilar welded material, mathematical models were developed to predict the required responses. Moreover, the main effects and the interaction effects of the process parameters on the responses were discussed and presented graphically for all dissimilar materials and joint designs. Furthermore, the developed models were optimized by determining the best combinations of input process parameters in order to produce an excellent weld quality.

TABLE OF CONTENTS

DECLARATION I
ACKNOWLEDGEMENTS II
ABSTRACT III
TABLE OF CONTENTS IV
LIST OF FIGURES X
LIST OF TABLES XVI
NOMENCLATURE XIX
1. INTRODUCTION TO OPTIMIZATION OF DISSIMILAR WELDED COMPONENTES 1
1.1 Welding History 1
1.2 Laser Welding 3
1.3 Dissimilar Welding 4
1.4 Objective of the Present Research 5
1.5 Thesis Structure 6
2. LITERATURE REVIEW 8
2.1 Introduction 8
2.2 Types of Lasers 8
2.3 Laser Applications 9
2.4 Laser Cutting and Welding Parameters 11
2.4.1 Laser Cutting 12
2.4.2 Laser Welding Parameters 13
2.4.2.1 Focus position 14
2.4.2.2 Welding speed and laser power 14
2.4.2.3 Shielding gas 15
2.4.2.4 Wavelength 17
2.4.2.5 Welding gap and the alignment of the laser beam 17
2.5 Dissimilar Welding 17
2.5.1 Dissimilar Welding of Joining Ferrous Materials 18
2.5.2 Dissimilar Welding of Joining Nonferrous Materials 21
2.5.3 Dissimilar Welding of Ferrous and Nonferrous Materials 24
2.6 Mechanical Properties 26
2.6.1 Residual Stress 26
2.6.1.1 Controlling residual stress formed during welding 27
2.6.1.2 Residual stress measurement methods 28
2.6.1.3 Hole drill method overview 30
2.6.1.4 Effect of residual stresses on the dissimilar welded materials 32
2.7 Welding Pool 32
2.8 Optimization of Mechanical Properties of Welded Joints 42
2.9 Microstructure 50
2.10 Summary of Literature Review 53
3. DESIGN OF EXPERIMENTS AND OPTIMIZATION 55
3.1 Design of Experiment 55
3.1.1 Planning 56
3.1.2 Screening 57
3.1.3 Optimization 58
3.1.4 Verification 58

3.2 Taguchi Design 58
3.2.1 Overview 58
3.2.2 The Fundamental Terms Used in Taguchi Design 59
3.2.2.1 Orthogonal arrays 59
3.2.2.2 S/N ratios and MSD analysis 62
3.2.2.3 Analysis of variance (ANOVA) 62
3.3 Optimization 64
3.3.1 Determination of Optimal or Near-Optimal Welding Condition(s) 64
3.3.2 Desirability Approach 66
3.3.3 Optimization by Means of Design Expert Software 68
3.4 Experimental Procedure 68
3.4.1 Planning Experiments (Brainstorming) 69
3.4.2 Designing Experiments 69
3.4.3 Running Experiment 70
3.4.4 Analyzing Results 70
3.4.4.1 Developing the mathematical model 71
3.4.4.2 Estimating of the coefficients of the model independent factors 71
3.4.4.3 The Signal-to-noise (S/N) ratio analysis 71
3.4.4.4 ANOVA *Outputs* 71
3.4.4.5 Model reduction 72
3.4.4.6 Development of final model form 73
3.4.5 Running Confirmation Experiments 73
4. MATERIAL AND EXPERIMENTAL WORK 74
4.1 Materials 74
4.1.1 Materials Specifications 74
4.1.2 Description and Use of the Studied Materials 76
4.2 Joint Design and Preparation 78
4.3 Shrouding System Design and Production 81
4.4 Laser Welding 83
4.4.1 Laser Welding Machine 84
4.4.2 Laser Welding Operations 85
4.5 Residual Stress Measurements 85
4.5.1 Incremental Hole-Drilling Method (IHDM) 86
4.5.2 Hole-Drill Method Equipment 91
4.5.2.1 RS-200 milling guide 91
4.5.2.2 Digital strain gauge 92
4.5.2.3 Adhesive 93
4.5.2.4 Cement kit 94
4.5.2.5 Accessory items 94
4.5.3 Hole-Drill Method Procedure 95
4.6 Mechanical Testing 97
4.6.1 Tensile Strength Testing 97
4.6.2 Tensile Shear Strength Testing 98
4.6.3 Impact Strength Testing 99
4.7 Micro-Study and Weld Pool Geometry Determination 100
4.7.1 Sample Preparation 100
4.7.2 Microstructure 101
4.7.3 Weld Pool Geometry 101

4.7.4 Microhardness 103
4.8 Cost Analysis 103
5. RESULTS AND DISCUTION OF DISSIMILAR FEROUS MATERIALS 106
5.1 Joining of Low Carbon Steel AISI 1008 to Stainless Steel AISI 316 (1.5 mm Thickness) 106
5.1.1Orthogonal Array Experiment 109
5.1.2 Development Mathematical Models for Welding Pool Geometry 110
5.1.2.1 The signal-to-noise (S/N) ratio analysis 111
5.1.2.2 Analysis of variance 112
5.1.2.3 Model validation 118
5.1.2.4: Effect of the parameters on responses 121
5.1.3 Development Mathematical Model for Impact Strength 124
5.1.3.1 The signal-to-noise (S/N) ratio analysis 124
5.1.3.2 Analysis of variance 125
5.1.3.3 Validation of the model 127
5.1.3.4 Effect of process parameters on the response 128
5.1.4 Development of a Mathematical Model for Tensile Strength 130
5.1.4.1 The tensile strength signal-to-noise (S/N) ratio analysis 130
5.1.4.2 Analysis of variance 131
5.1.4.3 Model validation 133
5.1.4.4 Effect of the parameters on tensile strength 134
5.1.5 Operating Cost Modeling 137
5.1.6 Models Optimization 138
5.1.6.1 Single -response optimization 138
5.1.6.2 Multiple -response optimization 139
5.2 Joining of Low Carbon Steel AISI1008 to Stainless Steel AISI 316 (2 mm Thickness) 143
5.2.1 Orthogonal Array Experiment 143
5.2.2 Development of Mathematical Models for Residual Stresses 144
5.2.2.1 The S/N ratio analysis 146
5.2.2.2 The ANOVA analysis 149
5.2.2.3 Effect of the parameters on the responses 150
5.2.3 Development Mathematical Models for Welding Pool Geometry 158
5.2.3.1 The S/N ratio analysis 159
5.2.3.2 Analysis of variance 160
5.2.3.3 Model validation 163
5.2.3.4 Effect of the parameters on responses 165
5.2.4 Development of a Mathematical Model for Tensile Strength 168
5.2.4.1 Analysis of the result 168
5.2.4.2 Validation of the model 171
5.2.4.3. Effect of Process Parameters on the Response: 171
5.2.5 Development of the Mathematical Model for Impact Strength 172
5.2.5.1 The S/N ratio analysis 173
5.2.5.2 Analysis of variance 173
5.2.5.3 Model validation 174
5.2.5.4 Effect of process parameters on the responses 175
5.2.6 Operating Cost Modeling 177
5.2.7 Models (multiple –response) Optimization 178

5.2.7.1 Numerical Optimization 178
5.2.7.2 Graphical optimization 179
5.2.8 Micro Harness and Microstructure Studies 183
5.2.8.1 Solidification in the fusion zone 183
5.2.8.2 Microstructure in the HAZ 184
5.2.8.3 Microhardness 186
5.3 Joining of Low Carbon Steel Din: en 10131 to Stainless Steel AISI 316 (3 mm Thickness) 187
5.3.1 Orthogonal Array Experiment 187
5.3.2 Development Mathematical Models for Welding Pool Geometry 188
5.3.2.1 The S/N ratio analysis 189
5.3.2.2 Analysis of variance 190
5.3.2.3 Model validation 192
5.3.2.4 Effect of the parameters on responses 194
5.3.3 Development of a Mathematical Model for Tensile Strength 197
5.3.3.1 Analysis of the result 197
5.3.3.2. Effect of process parameters on the Response: 200
5.3.4 Development Mathematical Model for Impact Strength 201
5.3.4.1 Model validation 205
5.3.4.2 The effect of the parameters on the response 205
5.3.5 Operating Cost Modeling 208
5.3.6 Models (multiple –response) Optimization 209
5.3.6.1 Numerical optimization 209
5.3.6.2 Graphical optimization 213
5.3.7 Microharness and Microstructure Studies 215
5.3.7.1 Microstructure of dissimilar jointed materials 215
5.3.7.2 Microhardness 217
6. RESULTS AND DISCUTION OF DISSIMILAR FEROUS WITH NONFERROUS JOINED MATERIALS 219
6.1 Joining of Aluminium (6082) to Low Carbon Steel Din: en 10131 219
6.1.1 Development of Mathematical Models for Residual Stresses 221
6.1.1.1 The ANOVA analysis 222
6.1.1.2 Model validation 224
6.1.1.3 Effect of the parameters on the responses 225
6.1.2 Development Mathematical Models for Welding Pool Geometry 226
6.1.2.1 Analysis of variance 227
6.1.2.2 Model validation 230
6.1.2.3 Effect of the parameters on responses 232
6.1.3 Development of a Mathematical Model for Tensile Strength 234
6.1.3.1 Analysis of the result 235
6.1.3.2 Validation of the model 236
6.1.3.3 Effect of process parameters on the response: 236
6.1.4 Operating Cost Modeling 238
6.1.5 Microharness and Microstructure Studies 239
6.1.5.1 Microstructure of dissimilar jointed materials 239
6.1.5.2 Microhardness of dissimilar jointed materials 240
6.1.6 Models (multiple –response) Optimization 242
6.1.6.1 Numerical optimization 242

6.1.6.2 Graphical optimisation 243
6.2 Joining of Aluminium (1050 H24) to Low Carbon Steel Din: en 10131 246
6.2.1 Development of Mathematical Models for Residual Stresses 247
6.2.1.1 The ANOVA analysis 249
6.2.1.2 Validation of the model 250
6.2.1.3 Effect of process parameters on the response: 250
6.2.2 Development of a Mathematical Model for Tensile Shear Strength 251
6.2.2.1 Analysis of the result 251
6.2.2.2 Validation of the model 253
6.2.2.3 Effect of process parameters on the response 253
6.2.3 Operating Cost Modeling 254
6.2.4 Microhardness and Microstructure Studies 255
6.2.4.1 Microstructure of dissimilar jointed materials 255
6.2.4.2 Microhardness of dissimilar jointed materials 257
6.2.4.3 Defects of dissimilar jointed materials 258
6.2.5 Models (multiple –response) Optimisation 259
6.2.5.1 Numerical optimisation 259
6.2.5.2 Graphical optimisation 260
6.3 Joining Titanium G2 to Low Carbon Steel Din: en 10131 262
6.4 Chapter Summary 263
7. RESULTS AND DISSUSSION OF DISSIMILAR NONFEROUS WITH NONFERROUS JOINED MATERIALS 265
7.1 Joining of Aluminum (6082) to Titanium G2 265
7.1.1 Development of Mathematical Models for the Welding Pool Geometry 267
7.1.1.1 Analysis of variance 268
7.1.1.2 Model validation 270
7.1.1.3: Effect of the parameters on responses 272
7.1.2 Development of a Mathematical Model for Tensile Strength 273
7.1.2.1 Analysis of the result 274
7.1.2.2 Validation of the model 275
7.1.2.3 Effect of process parameters on the response: 276
7.1.3 Operating Cost Modeling 278
7.1.4 Microharness and Microstructure Studies 279
7.1.4.1 Microstructure of dissimilar jointed materials 279
7.1.4.2 Microhardness of dissimilar jointed materials 280
7.1.5 Models (multiple –response) Optimization 282
7.1.5.1 Numerical optimization 282
7.1.5.2 Graphical optimization 283
7.2 Joining of Aluminum (5251 H22) to Titanium G2 285
7.2.1 Development of Mathematical Models for Residual Stresses 287
7.2.2 Development of a Mathematical Model for Tensile Strength 288
7.2.2.1 Analysis of the result 289
7.2.2.2 Validation of the model 290
7.2.2.3 Effect of process parameters on the response: 291
7.2.3 Operating Cost Modeling 293
7.2.4 Microharness and Microstructure Studies 294
7.2.4.1 Microstructure of dissimilar jointed materials 294
07.2.4.2 Microhardness of dissimilar jointed materials 296

7.2.5 Models (multiple –response) Optimization 297
7.2.5.1 Numerical optimization 297
7.2.5.2 Graphical optimisation 298
7.3 Chapter Summary 299
8. CONCLUSION AND SCOPE FOR FUTURE WORK 301
8.1 General Conclusion 301
8.2 Conclusion for Joining Dissimilar Ferrous Materials 301
8.3 Conclusion for Joining Dissimilar Ferrous to Nonferrous Materials 302
8.4 Conclusion for Joining Dissimilar Nonferrous to Nonferrous Materials 303
8.5 Thesis Contributions 304
8.6 Scope for Future Work 304
REFERENCES 306
APPENDICES 323

LIST OF FIGURES

Fig. 2.1: Relationship between focus position and penetration depth of type 304L and type 316L steels 14
Fig. 2.2 shows the depth ranges of various methods compared with (1) the depth of residual stresses produced by common manufacturing processes and (2) the depth ranges where residual stresses would likely contribute to failure mechanisms. 30
Fig. 3.1: Classification of modeling and optimization techniques in welding problems 65
Fig 4.1: Photography of Spark Analyzer Spectromax. 75
Fig. 4.2: Photograph of the sandblasting machine used for cleaning the materials. .. 80
Fig. 4.3: The fixture used for clamping the plates during welding operation. 80
Fig 4.4 (a): 3D drawing for shrouding system design. 82
Fig 4.4 (b): Photograph of unmovable three parts of shrouding system. 83
Fig 4.4 (c): Photograph of unmovable three parts of shrouding system and gas hoses with specimen. 83
Fig. 4.5: Rofin Dc 015 industrial CO_2 Diffusion-Cooled Slab laser machine. 84
Fig 4.6: Strain gauge rosette arrangement for determining residual stress. 87
Fig. 4.7: Calibrating coefficients of $\bar{a}$ and $\bar{b}$ as a function of hole depth for UM rosettes. 90
Fig. 4.8: RS-200 Milling Guide (a) with microscope (b) with milling bar 92
Fig. 4.9: Photo of the l strain indicator of type P-3500 and the strain indicator and SB-10 switch. 93
Fig. 4.10: Photograph exhibiting the M-Bond 200 adhesive kit. 93
Fig. 4.11: Photograph of the fast-setting cement kit type RS-200-CK Cement kit. .. 94
Fig. 4.12: Photograph of the work station for strain measurements. 95
Fig. 4.13: Strain Gauge Rosette of type CEA-06-062UM- 120 96
Fig. 4.14(a): Photo of the rosette bonded to the surface of the specimen. 96
Fig. 4.14(b): Schematic plot of the rosette bonded to the surface of the specimen. .. 96
Fig. 4.15: Schematic diagram for notched tensile strength (NTS) sample. 97
Fig. 4.16: Schematic diagram illustrating the (a) Center-line welding lap-join, (b) Tensile shear sample. 98
Fig. 4.17: Instron machine and its control unit with computer. 99
Fig 4.18: Photograph showing the different tensile samples (tensile and shear). 99
Fig 4.19: Schematic diagram of impact Sample 100
Fig 4.20: MAT21 universal pendulum impact machine 100
Fig. 4.21: The optical microscope connected to image analyzer software. 102
Fig. 4.22: The MEIJI, EMZ-TR optical microscope. 102
Fig. 4.23: Shows the positions of welding pool geometries on the specimen. 102
Fig. 4.24: Photograph of Microhardness tester. 103
Figs. 5.1 (a, b), Shows the welding seem (a, b face and bottom respectively) of a selected produced dissimilar joints. 107
Fig. 5.2: Shows the effect of the welding parameters on the responses (A, W_1, W_2). 110
Fig. 5.3: Effects plot for S/N ratio of the (A, W_1 and W_2) on the responses with interactions considerations between the responses 112

Fig 5.4 (a, b and c): Interactions between the welding parameters (P, S and F) with respect to the fusion area response. 116
Fig 5.5 (a, b and c): Interactions between the welding parameters (P, S and F) with respect to the welding width at surface 'W_1' response. 117
Fig 5.6 (a, b and c): Interactions between the welding parameters (P, S and F) with respect to the welding width the middle of specimen 'W_2' response. 118
Fig 5.7: Exhibited predicted values of the fusion area vs. actual measured values. 119
Fig 5.8: Exhibited predicted values of the W_1 vs. actual measured values..... 119
Fig 5.9: Exhibited predicted values of the W_2 vs. actual measured values..... 120
Figs. 5.10 (a, b): Contour graphs exhibiting the effect of P, S and F parameters on the response A. 122
Figs. 5.11 (a, b): Contour graphs exhibiting the effect of P, S and F parameters on the response W_1 123
Figs. 5.12 (a, b): Contour graphs exhibiting the effect of P, S and F parameters on the response W_2 124
Fig. 5.13 Effects of the parameters on the impact test and S/N ratio..... 125
Fig 5.14: Exhibited predicted values of the impact strength resistance test vs. actual measured values 127
Fig. 5.15: Contour graphs exhibiting the effect of P, S and F parameters on the impact strength at F = -0.5 mm. 129
Fig.5.16 Perturbation plots exhibiting the effect of welding parameters on the impact strength. 129
Fig 5.17 (a, b): Interactions between the welding parameters (P, S and F) with respect to the tensile strength. 133
Fig. 5.18**:** Predicted values of the tensile strength resistance test vs. actual measured values. 134
Fig.5.19: A 3D graph of the effect of P and S on the tensile strength at F = -0.50.. 135
Fig. 5.20 (a, b): Contours graph exhibiting the effect of welding parameters (P, S, F) on tensile strength. 136
Fig.5.21: Perturbation plots exhibiting the effect of welding parameters on the tensile strength where: A = power, B = Speed and C = Focus.. 136
Fig. 5.22: The desirability for each factor and each response, as well as the combined desirability at the optimal point..... 141
Fig. 5.23 Overlay plot shows the region of optimal welding condition at F =-0.2 mm. 142
Figs. 5.24(a-h): Shows the average effect of welding parameters on residual stresses at HAZ..... 148
Fig. 5.25: 3-D plot for affected parameters against $\sigma_{1.}$ 151
Fig. 5.26: 3-D plot for affected parameters against $\sigma_{2.}$ 151
Fig. 5.27: 3-D plot for affected parameters against σ_3 154
Fig. 5.28: 3-D plot for affected parameters against σ_4 155
Fig. 5.29: 3-D plot for affected parameters against σ_5 155
Fig. 5.30: 3-D plot for affected parameters against σ_6 155
Fig. 5.31: 3-D plot for affected parameters against $\sigma_{7.}$ 156
Fig. 5.32: The effect of the welding parameters on the responses (A, W_1, W_2), and the variation on weld bead geometry, X10. 159
Fig. 5.33: Effects plot for S/N ratio of the responses. 159

Fig. 5.34: The effect of actual welding parameters on the welding pool area 'A' response, against predicted 164
Fig. 5.35: The effect of actual welding parameters on the welding pool width 'W_1' against predicted. 164
Fig. 5.36: The effect of actual welding parameters on the welding pool width at the middle of the spacemen 'W_2' response, against predicted..... 165
Fig. 5.37: The effect of 'P' and 'S' on the 'A' response, at focus value at 'F' = -0.5 165
Fig. 5.38: The effect of 'P' and 'F' on the 'W_1' response, at 'S' = 750mm/min..... 165
Fig. 5.39: The effect of 'P' and 'S' on the 'W_2' response, at focus value 'F' = -0.5 mm 166
Fig. 5.40: 3D graph shows the effect of 'S' and 'F' on 'A' response, at 'P' = 1.24 kW. 168
Fig. 5.41: 3D graph shows the effect of 'P' and 'F' on 'W1' response, at 'S' = 750mm/min. 168
Fig. 5.42: 3D graph shows the effect of 'P' and 'S' 'W_2' response, at 'F' = −0.5 mm. 168
Fig. 5.43: The effect of the laser welding parameters on the tensile strength and S/N ratio. 169
Fig. 5.44: Predicted Vs Actual for notched P tensile strength NTS, MPa. 172
Fig. 5.45: 3D graph shows the effect of and S parameters on the tensile strength of the dissimilar joints at F = -0.92. 172
Fig. 5.46: Effects of the parameters on the impact test and S/N ratio..... 173
Fig. 5.47: Scatter diagram of actual response predicted 176
Fig. 5.48: Contour graph shows against the relationship between P and S at F =-0.5 mm 176
Fig. 5.49: 3D graph shows the effect of P and S on Impact strength atF=-.5mm.... 176
Fig. 5.50: Perturbation plot exhibiting the effect of welding parameters on the impact strength. 176
Fig 5.51: Ramps view of the first optimal criterion shows the desirability for each factor and each response, as well as the combined desirability at the optimal point. 180
Fig 5.52: Exhibiting the feasible solution in the yellow shaded area for the first optimization criteria. 182
Fig 5.53: Exhibiting the feasible solution in the yellow shaded area for second optimization criteria 182
Fig 5.54: Exhibiting the feasible solution in yellow shaded area for third optimization criteria. 183
Fig 5.55(a): AISI1008 base metal 184
Fig 5.55(b): LCS1008 HAZ 184
Fig 5.56(a): SST 316 base metal 184
Fig 5.56(b): SST 316 HAZ 184
Fig 5.57(a): Weld pool, HAZ and BM of AISI1008..... 185
Fig 5.57(b): Weld pool, HAZ and BM of AISI316. 185
Figs. 5.58 (a, b): The redistribution of elements in the fusion zone of a butt weld joining AISI316 to AISI1008..... 185
Fig. 5.59: The microhardness profile of the dissimilar joint for the specimens (1, 5, 7, 15, 22 and 25)..... 187

Fig. 5.60: Shows the effect of the welding parameters on the responses (A, W_1, W_2), and the variation on weld bead geometry, X10..... 189
Fig. 5.61: Effects plot for S/N ratio of the responses..... 190
Fig. 5.62: The effect of actual welding parameters on the welding pool area 'A' response, against predicted 194
Fig. 5.63: The effect of actual welding parameters on the welding pool width at the serves of the specimen 'W_1'response, against predicted 194
Fig. 5.64: The effect of actual welding parameters on the welding pool width at the middle of the spacemen 'W_2' response, against predicted..... 194
Fig. 5.65: 3D graph shows the effect of 'S' and 'F' on 'A' response, at 'P' = 1.23 kW and G = 0.075mm..... 196
Fig. 5.66: 3D graph shows the effect of 'P' and 'S' on 'W1' response, at 'F' = -0.5 mm and G = 0.075 mm 196
Fig. 5.67, 3D graph shows the effect of 'P' and 'S' 'W_2' response, at 'F' = −0.5 mm and G = 0.075 mm..... 197
Fig. 5.68: The effect of the laser welding parameters on the tensile strength and S/N ratio. 198
Fig. 5.69: Predicted Vs Actual for notched tensile strength NTS, MPa 201
Fig. 5.70: 3D graph shows the effect of P and S on the tensile strength of the dissimilar components at F = -0.5mm and G = 0.075 mm..... 201
Fig. 5.71: Exhibited the effect of the laser welding parameters on the impact strength and S/N ratio. 203
Fig. 5.72: The relationship between the actual and predicted values of the response 206
Fig. 5.73: The effect of welding parameters on the Impact Strength..... 206
Fig. 5.74: The interaction between the Laser power and the focusing position..... 207
Fig. 5.75: The interaction between the Laser power and the gap parameter 207
Fig.5.76: Perturbation plots exhibiting the effect of welding parameters on the tensile strength, where: A = power, B = Speed, C = Focus and D = Gap. 208
Fig.5.77: The desirability bar graph of first optimization criteria..... 212
Fig.5.78: The desirability bar graph of second optimization criteria..... 212
Fig.5.79: The desirability bar graph of third optimization criteria. 213
Fig 5.80: The feasibel solution in yallow shaded area for first optimization criteria. 214
Fig 5.81: The feasible solution in yellow shaded area for second optimization criteria. 214
Fig 5.82: The feasibel solution in yallow shaded area for third optimization criteria. 215
Fig 5.83(a): Weld pool, HAZ and BM of Low Carbon Steel Din: en 10131..... 216
Fig 5.83(b): BM, HAZ and weld pool of AISI316 216
Figs. 5.84 (a, b): The redistribution of elements in the fusion zone of a butt weld joining AISI316 to Din: en 10131..... 217
Fig. 5.85 (a): The grain size of BM of Din: en 10131 217
Fig. 5.85 (b): Shows the grain size of HAZ of Din: en 10131 217
Fig. 5.86: The microhardness profile of the dissimilar joint (AISI316 / Din: en 10131) for the specimens (1, 4, 10 and 16)..... 218
Fig. 6.1: The actual vs. predicted values residual stress at level 1(σ_1)..... 224

Fig. 6.2: A 3D graph of the effect of S and F at P = 0.9kW on the response at depth level 1. 226
Fig. 6.3: The effect of the welding parameters on the responses (A_1, W_1, L_1). 227
Fig. 6.4: Interactions between the welding parameters (P, S) with respect to the depth of penetration response. 230
Fig. 6.5: Exhibited predicted values of the W_1 vs. actual measured values 231
Fig. 6.6: Exhibited predicted values L_1 vs. actual measured values 231
Fig. 6.7: Exhibited predicted values of the A_1 vs. actual measured values..... 231
Fig. 6.8: Contour graphs exhibiting the effect of P, S parameters at F = -0.5 on the response W_1..... 232
Fig. 6.9: Contour graphs exhibiting the effect and S parameters on the response L_1 at F = -0.8 mm..... 234
Fig. 6.10: Contour graphs of P exhibiting the effect of F and S parameters on the response A_1 at P = 1.163 kW 234
Fig. 6.11: Predicted Vs Actual for tensile shear strength..... 237
Fig. 6.12: Shows P, F and S parameters and their effect on the tensile strength of the dissimilar components..... 237
Fig 6.13: The interaction between S and F at P = 1.1kW 237
Fig 6.14(a): BM of low carbon steel Din: en 10131 239
Fig 6.14(b): BM of aluminium 6082..... 239
Figs. 6.15 (a, b, c): The redistribution of elements in the fusion zone of an overlap welding joint of aluminium 6082 to LCS Din: en 10131..... 240
Fig. 6.16: The microhardness profile of the dissimilar joint (Al 6082 / Din: en 10131). 242
Fig 6.17: The graphical feasible solution in yellow shaded area for first optimisation criteria at F = 0.00 mm..... 245
Fig 6.18: The graphical feasibel solution in yellow shaded area for second optimisation criteria at F = -1.00 mm 245
Fig 6.19: The feasibel solution in yellow shaded area for third optimisation criteria at F = -1.00 mm..... 245
Fig. 6.20: Predicted Vs Actual for residual stresses 251
Fig. 6.21: Presents contour graph of the effect of S, P at F = 0.0 mm on the response at depth level 1 251
Fig. 6.22: Predicted Vs Actual for tensile shear strength, n/mm 254
Fig. 6.23: 3D graph shows the effect of P and S parameters on the ensile strength of the dissimilar components at F = 0mm 254
Figs. 6.24 (a, b, c and d): The redistribution of elements in the fusion zone of a lap weld joining aluminium 1050 H24 to LCS Din: en 10131. 256
Fig. 6.25: The microhardness profile of the dissimilar joint (Al 1050 H24 / Din: en 10131). 258
Fig 6.26: Defects of dissimilar (steel 10131 /aluminium 1050 H24) joints..... 259
Fig. 6.27: The feasibel solution in yellow shaded area for third optimization criteria at F = 0.6 mm 262
Figs. 7.1 (a, b, c and d): Exhibit the effect of the welding parameters and the variation on the total weld pool dimensions. 268
Fig. 7.2: Interactions between the welding parameters (P, S) with respect to the depth of penetration response at F = -0.5mm. 270
Fig. 7.3: Exhibited predicted values of the W_1 vs. actual measured values 271

Fig. 7.4: Exhibited predicted values of depth of penetration L_1 vs. actual measured values. 271
Fig. 7.5: Contour graphs exhibiting the effect of P, S parameters at F = -0.5 on the response W_1 273
Fig. 7.6: Contour graphs exhibiting the effect of P, S parameters at F = -0.5 on the response L_1 273
Fig. 7.7: Predicted Vs Actual for tensile shear strength. 276
Fig. 7.8: Contour graph shows the effect welding parameters At S = 2700 mm/min 277
Fig. 7.9: Shows the interaction between the laser power and focus at S = 2500 mm/min 277
Fig. 7.10: 3D graph shows the effect of P and F At S = 2700 mm/min 277
Fig. 7.11: Perturbation plots exhibiting the effect of welding parameters on the tensile strength, where: A = power, B = Speed and C = Focus 277
Figs. 7.12 (a-d): The redistribution of elements in the fusion zone of a lap weld joining aluminium 6082 to titanium G2. 280
Fig. 7.13: The Microhardness profile of the dissimilar joint (Al 6082 / titanium G2). 282
Fig. 7.14: The feasible solution in yellow shaded area for optimisation criteria at F = -1 mm 285
Fig. 7.15: Predicted Vs Actual for developed tensile shear strength model. 291
Fig. 7.16: Contour graph shows the effect Welding parameters At S = 2100 mm/min 292
Fig. 7.17: Interaction between the laser power and focus at S = 2100 mm/min 292
Fig. 7.18: 3D graph shows the effect of Power and Speed at F = 0.0 mm. 293
Figs. 7.19 (a, b, c and d): The microstructure of lap weld AL5251 to Ti G2 joint. . 295
Fig. 7.20: The Microhardness profile of the dissimilar joint (Al 5251 / titanium G2). 297
Fig.7.21: The feasible solution in yellow shaded area for optimisation criteria. 299

LIST OF TABLES

Table 3.1: Typical L16 orthogonal array with coded value 60
Table 3.2: Typical L25 orthogonal array with coded values 61
Table 3.3: Sample ANOVA Table for a model..... 63
Table 4.1: Chemical composition of the ferrous materials (wt %) 75
Table 4.2: Chemical composition of the Aluminum grades (wt %) 75
Table 4.3: Chemical composition of the Titanium grade 2 (wt %)..... 76
Table 4.4: Mechanical properties of the materials 76
Table 4.5: Physical properties of the materials 76
Table 4.6 Rofin laser machine technical specifications 85
Table 4.7: Details of the Laser welding operation costs. 105
Table 5.1: Process parameters and design levels used..... 107
Table 5.2: Shows the Taguchi design matrix in actual values of studded welding parameters. 108
Table 5.3: Shows the welding pool geometry, tensile strength, impact strength and cost per meter welding calculations. 109
Table 5.4: Response for signal-to-noise ratio (S/N)..... 112
Table 5.5: ANOVA for response 'A' 113
Table 5.6: ANOVA for response W_1 114
Table 5.7: ANOVA for response W_2 114
Table 5.8: Confirmation experiments of the responses (A, W_1 and W_2) 120
Table 5.9: Response for signal-to-noise ratio (S/N)..... 125
Table 5.10: Shows the ANOVA for the impact strength 126
Table 5.11: Confirmation experiments of the impact strength 127
Table 5.12: Shows the response for S/ N Ratio for tensile strength 131
Table 5.13: Shows the ANOVA for the tensile strength..... 132
Table 5.14: Confirmation experiments of the tensile strength..... 133
Table 5.15: Shows the ANOVA for the welding operating cost..... 137
Table 5.16: Shows the optimization criteria for input/output welding parameters.. 138
Table 5.17: Shows the numerical optimization results based on individual response 138
Table 5.18: Shows the ten optimal solutions using numerical multiple-responses.. 140
Table 5.19: Process parameters and design levels used..... 143
Table 5.20: The Taguchi design matrix in actual values of the studied welding parameters and welding pool geometry, mechanical tests results and cost per meter welding calculations..... 144
Table 5.21: Shows the Depth at which the micro-strains were measured in the specimens. 145
Table 5.22: Shows the experimental assignments with random order and residual stresses. 146
Table 5.23: ANOVA for residual stress at level 1 150
Table 5.24: ANOVA for residual stress at level 2 151
Table 5.25: ANOVA for residual stress at level 3 152
Table 5.26: ANOVA for residual stress at level 4 153
Table 5.27: ANOVA for residual stress at level 5 154
Table 5.28: ANOVA for residual stress at level 6 155
Table 5.29: Shows ANOVA for residual stress at level 7. 156

Table 5.30: Confirmation experiments with absolute error calculation of the developed models 158
Table 5.31: The responses for signal-to-noise ratio (S/N). 160
Table 5.32: ANOVA for 'A' response model 162
Table 5.33: ANOVA for 'W_1' response model 162
Table 5.34: ANOVA for 'W_2' response model 163
Table 5.35: Confirmation experiments and base metal responses 164
Table 5.36: Shows the tensile strength response for S/ N Ratio. 169
Table 5.37: ANOVA for selected factorial model 170
Table 5.38: Confirmation experiments of the responses compared with model results. 171
Table 5.39: ANOVA for selected factorial model 174
Table 5.40: Confirmation experiments of the responses compared with model results. 175
Table 5.41: Shows the ANOVA for the welding operating cost 177
Table 5.42: Three optimization criteria with the optimization results using numerical multiple-response 181
Table 5.43: Process parameters and design levels used 188
Table 5.44: The Taguchi design matrix with the actual values of the studied welding parameters and welding pool geometry, mechanical tests results and cost per meter welding calculations. 188
Table 5.45: The responses for signal-to-noise ratio (S/N). 190
Table 5.46: The ANOVA for 'A' response model 192
Table 5.47: The ANOVA for 'W_1' response model 192
Table 5.48: The ANOVA for 'W_2' response model 192
Table 5.49: The confirmation experiments and base metal responses 193
Table 5.50: Shows the tensile strength response for S/ N Ratio. 198
Table 5.51: Shows the ANOVA for selected factorial model. 199
Table 5.52: Confirmation experiments of the responses compared with model results. 200
Table 5.53: Shows the impact strength response for S/ N Ratio. 202
Table 5.54: Shows the ANOVA for impact strength response model. 204
Table 5.55: Confirmation experiments of the responses compared with model results. 204
Table 5.56: Shows the ANOVA for the welding operating cost 209
Table 5.57: Shows three optimization criteria with the optimization results using numerical multiple-response. 211
Table 6.1: Process parameters and design levels used 220
Table 6.2: Welding input variables, experiment design levels, the welding pool geometry, tensile shear strength and cost per meter welding calculations. 220
Table 6.3: Depths at which the micro-strains were measured in the specimens 221
Table 6.4: The experimental calculated for Al 6082 residual stresses 222
Table 6.5: ANOVA for residual stress at level 1 223
Table 6.6: ANOVA for residual stress at level 2 223
Table 6.7: Confirmation experiments of the residual stress at $\sigma 1$ 225
Table 6.8: ANOVA for response 'W_1' 228
Table 6.9: ANOVA for response 'L_1' 228
Table 6.10: ANOVA for response 'A_1' 229

Table 6.11: Confirmation experiments of the responses (W_1, L_1 and A_1)..... 231
Table 6.12: ANOVA for selected tensile shear model..... 235
Table 6.13: Confirmation experiments of the responses compared with model results. 236
Table 6.14: ANOVA for operating welding cost..... 238
Table 6.15: Microhardness test result of dissimilar ferrous to nonferrous materials241
Table 6.16: Shows three optimization criteria with the optimization results using numerical multiple-response. 244
Table 6.17: Process parameters and design levels used..... 246
Table 6.18: Shows the Taguchi design matrix in actual values of studied welding parameters, tensile shear test and cost per meter welded..... 247
Table 6.19: The experimental calculated for Al 1050 H24 residual stresses..... 248
Table 6.20: ANOVA for residual stress at level 1 249
Table 6.21: ANOVA for selected tensile shear model..... 252
Table 6.22: Confirmation experiments of the responses compared with model results. 253
Table 6.23: ANOVA for operating welding cost..... 255
Table 6.24: Microhardness test result of dissimilar ferrous to nonferrous materials258
Table 6.25: Three optimization criteria with the optimization results using numerical multiple-response 261
Table 6.26: Process parameters and design levels used for titanium / steel 263
Table 7.1: Process parameters and design levels used..... 266
Table 7.2: Welding input variables, experiment design levels, the welding pool geometry, tensile shear strength and cost per meter welding calculations. 266
Table 7.3: ANOVA for response 'W_1'..... 269
Table 7.4: ANOVA for response 'L_1' 269
Table 7.5: Confirmation experiments of the responses (W_1 and L_1) 271
Table 7.6: ANOVA for selected tensile shear model..... 275
Table 7.7: Confirmation experiments of the responses compared with model results. 276
Table 7.8: ANOVA for operating welding cost..... 278
Table 7.9: Microhardness test result of dissimilar ferrous to nonferrous materials. 281
Table 7.10: Shows three optimization criteria with the optimization results using numerical multiple 284
Table 7.11: Process parameters and design levels used..... 286
Table 7.12: Welding input variables, experiment design levels, the residual stresses, tensile shear strength and cost per meter welding calculations..... 287
Table 7.13: Shows the experimental calculated for Al 6082 residual stresses 288
Table 7.14: ANOVA for tensile strength response 290
Table 7.15: Confirmation experiments of the tensile shear strength compared with model results. 292
Table 7.16: ANOVA for operating welding cost..... 294
Table 7.17: Microhardness test result of dissimilar nonferrous to nonferrous materials 296
Table 7.18: The optimisation criteria with the optimisation results using numerical multiple-response 298

NOMENCLATURE

List of symbols

A	Area of the fusion welding zone
ANN	Artificial neuron network
ANOVA	Analysis of variance
$\bar{a}$, $\bar{b}$	Calibration coefficients for 062UM rosette
BM	Base metal
d.f.	Degree of freedom
D	Desirability function
E	Elastic modulus
$\lvert E \rvert$	Absolute error
EBW	Electron beam welding
EC	Electric power cost per kW
F	Focus position
FA	Fusion area
F/A	Ferritic/austenitic
FSW	Friction stirs welding
F_v	Statistical F value
FZ	Fusion zone
G	Gap between the jointed plates
HAZ	Heat affected zone
Hv	Vickers hardness
J	Joule
LCS	Low Carbon steel
LASER	Light Amplification by Stimulated Emission of Radiation
LBW	Laser beam welding
MPa	Mega Pascal
MSD	Mean Squared Deviation
n	Total number of runs (For this work *n* =16 or 25)
Nd: YAG	Yttrium aluminium garnet
NTS	Notched tensile strength
OM	Optical microscopy

P	Laser power
R^2	Measure of the amount of variation around the mean explained by the model
RSM	Response surface methodology
S	Welding speed
SAW	Submerged arc welding
SEM	Scanning electron microscope
S/N	Signal-to-noise
SSt	Stainless steel
SAW	Submerged arc welding
TEM	Transmission electron microscopy
TIG	Tungsten inert gas welding
TMAZ	Thermo-mechanical affected zone
W_1	Welding pool width at the surface
W_2	Welding pool width at the middle depth
WZ	Welding zone
XRD	X-ray diffraction
Z	Hole drilled depth

Greek letters

α	stress direction
ε	micro-strains
ν	Poisson's ratio
σ	principal stress
Ω	resistance

CHAPTER 1

1. INTRODUCTION TO OPTIMIZATION OF DISSIMILAR WELDED COMPONENTES

1.1 Welding History

Welding is a manufacturing process used to join components or parts permanently. It is the most important way to join metals. Welding is widely used to manufacturing or repair all products made of metal. The use of welding is still increasing, primarily because it is the most economic and proficient way to join metals. All metals can be joined by one welding process or another. Some metals are easy to weld, and others are complicated to weld. The physical and mechanical properties, availability, and cost all help decide if a metal will be used in an application in which welding is required. The applications for which welding can be used are wide ranging [1]. The majority of metal welding processes have been invented in recent years, but some, notably the forge welding of iron, diffusion bonding, brazing and soldering, have a very long history. Soldering and the hammer welding of gold appear to have been known during Bronze Age. The welding process in use during the early period is a solid-phase process.

Heat sources of sufficient intensity first became available on an industrial scale at the end of the 19th century, when gas welding, arc welding and resistance welding all made their appearance. By 1916, oxyacetylene welding was a fully developed process capable of producing good-quality fusion welds in thin steel plates, aluminum and deoxidized copper, and differed only in detail from the process as it is known today. Spot and seam welding, which are used for making lap joints in thin sheet, and butt welding, used for chain making and for joining bars and sections, were well established by 1920. This trend has continued. Since the invention of inert-gas shielded welding in 1943, welding processes have developed and multiplied at a most remarkable rate, and as a result the great majority of metals currently used in industry can be welded by one means or another [2].

Welding with consumable electrodes in an atmosphere of CO_2 gas was invented by Lyubavskii and Novoshilov in 1953. The CO_2 welding process

immediately gained favor since it utilized equipment developed for inert gas metal arc welding, but could now be used for economically welding steels. The CO_2 arc is a hot arc and the larger electrode wires require high currents. The process became widely used with the introduction of smaller-diameter electrode wires and refined power supplies. This development was the short-circuit arc variation which was known as Micro-wire, short-arc, and dip transfer welding, all of which appeared late in 1958 and early in 1959. This variation allowed all-position welding on thin materials and soon became the most popular of the gas metal arc welding process variations.

Soon after the introduction of CO_2 welding, a variation utilizing a special electrode wire was developed. The process was called Dual-shield welding, indicating that an external shielding gas was utilized, as well as the gas produced by the flux in the core of the wire, for arc shielding. This process, invented by Bernard, was announced in 1954, but was patented in 1957, when the National Cylinder Gas Company reintroduced it.

In 1959, an inside-outside electrode was produced which did not require external gas shielding. The absence of shielding gas gave the process popularity for non-critical work. This process was named Inner-shield welding. The electro-slag welding process was announced by the Soviets, in Belgium in 1958. It had been used in the Soviet Union since 1951, but was based on work done in the U S by R.K. Hopkins, who was granted patents in 1940. The Arcos Corporation introduced another vertical welding method, called Electro-gas, in 1961. It utilized equipment developed for electro-slag welding, but employed a flux-cored electrode wire and an externally supplied gas shield. It is an open arc process since a slag bath is not involved. A newer development uses self-shielding electrode wires and a variation uses solid wire but with gas shielding. These methods allow the welding of thinner materials than can be welded with the electro-slag process. Robert F. Gage invented plasma arc welding in 1957. This process uses a constricted arc or an arc through an orifice, which creates arc plasma that has a higher temperature than the tungsten arc. It is also used for metal spraying and for cutting.

The electron beam welding process, which uses a focused beam of electrons as a heat source in a vacuum chamber, was developed in France by J.A. Stohr on 1957.

Friction welding, which uses rotational speed and upset pressure to provide friction heat, was developed in the Soviet Union. It is a specialized process and has applications only where a sufficient volume of similar parts are to be welded because of the initial expense of the equipment and tooling. This process is called inertia welding [3].

1.2 Laser Welding

Laser welding is one of the most recent welding techniques available to industry**.** Laser beam welding is a high energy density welding process. The term LASER stands for Light Amplification by Stimulated Emission of Radiation. A laser beam is just a light. The light beam has one wavelength and is in–phase. In-phase means all the particles or waves move together. Laser welding could be considered, as a unique source of thermal energy, precisely controllable in intensity and position for metal joining. For welding, the laser beam must be focused to a small spot size to produce a high-power density. This controlled power density melts the metal and, in the case of deep penetration welds, vaporizes some of it. When solidification occurs, a fusion zone or weld joint (weld pool) results. The laser bead which consists of a beam of photons could be optically amplified by use of mirrors or lenses. The laser beam can be transmitted though the air without serious power reduction or dilapidation [4]. A laser beam is commonly produced by one of three types of laser, which are: Ruby laser, Nd-YAG laser and CO_2 (Carbon Dioxide) laser [5]. Laser welding is not only an unusual technique, but it offers production opportunities that were, prior to this, difficult or impracticable to achieve using welding techniques.

CO_2 laser beam welding with a continuous wave is a high energy density and low heat input process. The result of this is a small heat-affected zone (HAZ), which cools very rapidly with very little distortion, and a high depth-to-width ratio for the fusion zone. The heat flow and the fluid flow in the weld pool can extensively influence the temperature gradients, the cooling rates and the solidification structure. In addition, the fluid flow and the convective heat transfer in the weld pool have been shown to control the penetration and shape of the fusion zone [6].

1.3 Dissimilar Welding

Joining dissimilar materials became inevitable in engineering industries for both technical and economic reasons. The adoption of dissimilar-metal combinations provides possibilities for the flexible design of the product by using each material efficiently, i.e., benefiting from the specific properties of each material in a functional way. Fusion welding is one of the most widely used methods for the joining of metals. Therefore, continuous efforts are made to apply these methods to the joining of dissimilar-metal combinations, despite the many difficulties encountered. These difficulties include problems associated with metallurgical incompatibility, e.g., the formation of brittle phases, the segregation of high- and low-melting phases due to chemical mismatch, and possibly large residual stresses from the physical mismatch.

There are several choices amongst the fusion welding processes, such as, common conventional shielded metal arc, gas tungsten arc, gas metal arc, and submerged arc welding. They also include processes characterized by high energy density, such as plasma arc, electron beam, and laser beam welding. In addition to fusion welding, several other types of joining techniques are also available, and may often be associated with less difficulty for producing dissimilar-metal joints. These are solid-state welding e.g., pressure welding, friction, resistance and diffusion welding, as well as brazing and soldering, adhesive bonding, and mechanical joining. Most of these techniques can eliminate the fusion problems because the base metals remain in the solid state during joining. Therefore, they are better than fusion welding in this aspect.

However, the service conditions may make particular processes unsuitable, e.g., for high-temperature applications, soldering and adhesive bonding cannot be candidates, and for leak-tight joints, mechanical joining is not acceptable. Furthermore, the required joint geometry can make processes, such as friction welding, difficult to apply. Diffusion welding often provides superior technical benefits for joining small dissimilar-metal parts, but the process is rather time consuming. Therefore, solutions relying on high energy density processes, e.g., electron beam welding (EBW) and laser beam welding (LBW), are still of great industrial interest [7].

1.4 Objective of the Present Research

The aim of this work is to predict and optimize laser welding of a selected economically important dissimilar material in industry through applying the design of experiments (DOE) technique, in terms of process input parameters. Developed models could support designers and engineers to achieve outstanding welding properties. Taguchi orthogonal array design as a DOE approach was applied to design the experiments, develop statistical models and optimize the welding operation through controlling selected welding parameters. Taguchi design of the experiment provides a straight evaluation of the influence of the investigated parameters on the laser welding outcomes. Further, Taguchi parameter design can optimize the performance through the settings of design parameters. It can also reduce the fluctuation of system performance to allow the source of variation to be identified [8]. The microstructure and mechanical properties, such as, residual stress, tensile stress, impact strength, and micro hardness will be tested and discussed as responses of dissimilar welding processes.

Three types of dissimilar welding are examined in this study:

1) Dissimilar welding of ferrous materials, such as, low carbon steel with 316 stainless steel at different thicknesses (1.5, 2 and 3 mm)
2) Welding of ferrous with nonferrous dissimilar materials, such as, low carbon steel with titanium G2 and low carbon steel with different types of aluminium alloys, such as, 6082, 5251 H22 and 1050 H24.
3) Welding of nonferrous dissimilar materials, such as, titanium G2 with different aluminium alloys, such as, 6082 and 5251 H22.

The following points summarize the main objectives of this research:

a) Appling Taguchi approach to develop mathematical models for the above mentioned dissimilar materials using Design Expert V7 statistical software to predict and optimize the following process responses:
    - Notched Tensile strength.
    - Shear strength.
    - Impact resistance.

- Fusion welded area and weld pool geometry.
- Heat input by the welding to the work piece.
- The principal residual stress resulting from the welding process.
- Distribution of the principal residual stress through the depth of jointed component.
- Unit operating cost.

(c) Presenting the developed models graphically to illustrate the effect of each welding parameter on the above mentioned responses and also their interactions.

(d) Applying the analysis of variances (ANOVA) to test adequacy of the developed models and examine each term in the developed models using statistical significance tools.

(e) Determining the optimal combinations of input welding factors, using the developed models with numerical optimization and graphical optimization, to achieve the desired criterion for the responses listed above.

f) Study of the microstructure and microhardness of the welded joints and discussion of their effect on the mechanical properties of the dissimilar joints.

Continuous CO_2 laser welding with maximum power equal to 1.5 kW is used for this research. Laser power (P), welding speed (S), focus position (F) and gap between the two jointed plates (G) were considered as input controllable parameters and subjected to the optimization.

1.5 Thesis Structure

The thesis outline is as follows; chapter one provides an introduction to the work with a brief history on the development of welding. Chapter one also includes the thesis objective and thesis structure. Chapter two contains a literature review about laser welding, dissimilar material welding, residual stresses, mechanical properties and microstructure. Chapter three explains how the DOE and Taguchi method were used for optimization of the welding process. Chapter four details the

experimental procedures used in this work, the material compositions and sizes, mechanical properties tests and standard specimens, and the equipment used for testing. Chapter five exhibits the results and discussion of ferrous dissimilar material joined together in this work. Chapter six details the results and discussion of ferrous / nonferrous dissimilar material joined together in this work. Chapter seven exhibits the results and discussion of nonferrous / nonferrous dissimilar material joined together.

Conclusion and further work are presented in chapter eight. Following this the record of references used in this thesis, appendices and publications arising from this work are listed.

CHAPTER 2

2. LITERATURE REVIEW

2.1 Introduction

The aims of this chapter are to exhibit and highlight previous research, similar or related to this work carried out by various researchers and also to develop a basic understanding to laser welding of dissimilar materials.

2.2 Types of Lasers

There are many types of lasers available for research, medical, industrial, and commercial uses. Lasers are often described by the kind of lasing medium they use - solid state, gas, Excimer, dye, or semiconductor. Solid state lasers have lasing material distributed in a solid matrix, e.g., the ruby or neodymium-YAG (yttrium aluminium garnet) lasers. The neodymium-YAG laser emits infrared light at 1.064 micrometers. Gas lasers (helium and helium-neon, HeNe, are the most common gas lasers) have a primary output of a visible red light. CO_2 lasers emit energy in the far-infrared, 10.6 micrometers, and are used for cutting hard materials.

Excimer lasers (the name is derived from the terms excited and dimers) use reactive gases, such as, chlorine and fluorine mixed with inert gases, such as, argon, krypton, or xenon. When electrically stimulated, a pseudomolecule or dimer is produced and when lased, produces light in the ultraviolet range. Dye lasers use complex organic dyes like rhodamine 6G in liquid solutions or suspension as lasing media. They are tunable over a broad range of wavelengths. Semiconductor lasers, sometimes called diode lasers, are not solid-state lasers. These electronic devices are generally very small and use low power. They may be built into larger arrays, e.g., the writing source in some laser printers or compact disk players.

Lasers are also characterized by the duration of laser emission - continuous wave or pulsed laser. A Q-Switched laser is a pulsed laser which contains a shutter-like device that does not allow emission of laser light until opened. Energy is built-up in a Q-Switched laser and released by opening the device to produce a single, intense laser pulse.

Continues Wave (CW) lasers operate with a stable average beam power. In higher power systems, one is able to adjust the power. In low power gas lasers, such as HeNe, the power level is fixed by design and performance usually degrades with long term use.

Single Pulsed (normal mode) lasers generally have pulse durations of a few hundred microseconds to a few milliseconds. This mode of operation is sometimes referred to as long pulse or normal mode.

Single Pulsed Q-switched lasers are the result of an intracavity delay (Q-switch cell) which allows the laser media to store a maximum of potential energy. Then, under optimum gain conditions, emission occurs in single pulses; typically of 10^{-8} second time domain. These pulses will have high peak powers often in the range from 10^{6} to 10^{9} Watts peak.

Repetitively Pulsed or scanning lasers generally involve the operation of pulsed laser performance operating at a fixed (or variable) pulse rate which may range from a few pulses per second to as high as 20,000 pulses per second. The direction of a CW laser can be scanned rapidly using optical scanning systems to produce the equivalent of a repetitively pulsed output at a given location.

Mode Locked lasers operate as a result of the resonant modes of the optical cavity which can affect the characteristics of the output beam. When the phases of different frequency modes are synchronized, i.e., "locked together," the different modes will interfere with one another to generate a beat effect. The result is a laser output which is observed as regularly spaced pulsations. Lasers operating in this mode-locked fashion usually produce a train of regularly spaced pulses, each having a duration of 10^{-15} (femto-) to 10^{-12} (pico-) seconds. A mode-locked laser can deliver much higher peak powers than the same laser operating in the Q-switched mode. These pulses will have enormous peak powers often in the range from 10^{12} Watts peak [9].

2.3 Laser Applications

The applications of lasers in different aspects of life are summarized as following:

Medical Uses of Lasers: The highly collimated beam of a laser can be further focused to a microscopic dot of extremely high energy density. This makes it useful as a cutting and cauterizing instrument. Lasers are used for photocoagulation of the retina to halt retinal hemorrhaging and for the tacking of retinal tears. Higher power lasers are used after cataract surgery if the supportive membrane surrounding the implanted lens becomes milky. Photodisruption of the membrane often can cause it to draw back like a shade, almost instantly restoring vision. A focused laser can act as an extremely sharp scalpel for delicate surgery, cauterizing as it cuts. "Cauterizing" refers to long-standing medical practices of using a hot instrument or a high frequency electrical probe to singe the tissue around an incision, sealing off tiny blood vessels to stop bleeding. The cauterizing action is particularly important for surgical procedures in blood-rich tissue, such as the liver. Lasers have been used to make incisions half a micron wide, compared to about 80 microns for the diameter of a human hair [10].

Surveying and Ranging: Helium-neon and semiconductor lasers have become standard parts of the field surveyor's equipment. A fast laser pulse is sent to a corner reflector at the point to be measured and the time of reflection is measured to get the distance. Some such surveying is long distance, the Apollo 11 and Apollo 14 astronauts put corner reflectors on the surface of the Moon for determination of the Earth-Moon distance. A powerful laser pulse from the MacDonald Observatory in Texas had spread to about a 3 km radius by the time it got to the Moon, but the reflection was strong enough to be detected. We now know the range from the Moon to Texas within about 15 cm, a nine significant digit measurement. A pulsed ruby laser was used for this measurement [11].

Lasers in the Garment Industry: Laser cutters are credited with keeping the U.S. garment industry competitive in the world market. Computer controlled laser garment cutters can be programmed to cut out 400 size 6 and then 700 size 9 garments - and that might involve just a few cuts. The programmed cutter can cut dozens to hundreds of thicknesses of cloth, and can cut out every piece of the garment in a single run. The usefulness of the laser for such cutting operations comes from the fact that the beam is highly collimated and can be further focused to a microscopic dot of extremely high energy density for cutting [11].

Lasers in Communication: Fiber optic cables are a major mode of communication partly because multiple signals can be sent with high quality and low loss by light propagating along the fibers. The light signals can be modulated with the information to be sent by either light emitting diodes or lasers. The lasers have significant advantages because they are more nearly monochromatic and this allows the pulse shape to be maintained better over long distances. If a better pulse shape can be maintained, then the communication can be sent at higher rates without overlap of the pulses. Ohanian [11] quotes a factor of 10 advantages for the laser modulators.

Barcode Scanners: A Laser Barcode Scanner uses a rapidly-moving laser to shine a particular frequency of light at the black and white bars of a barcode. The laser light is reflected off the barcode and read by a photo diode in the barcode scanner. The barcode scanner then interprets the reflection data and decodes it into useful data [12].

Heat Treatment: In laser heat treating, energy is transmitted to the materials surface in order to create a hardened layer by metallurgical transformation. The laser is used as a heat source, and rapidly raises the surface temperature of the material. Heat sinking of the surrounding area provides rapid self-quenching, thus producing a hardened transformation layer. Both CO_2 and Nd: YAG continuous wave lasers currently have the power capabilities to heat treat metals at reasonable rates. The CO_2 laser, however, has poorer surface absorption in most metals, and thus requires the surface to be coated to improve its absorption characteristics. Since the surface absorption of the Nd: YAG laser wavelength is significantly higher, generally less power is required [13].

2.4 Laser Cutting and Welding Parameters

The focused laser beam is one of the highest power density sources available to industry today. It is similar in power density to an electron beam. Together these two processes represent part of the new technology of high energy density processing.

At these high power densities all materials will evaporate if the energy can be absorbed. Thus, when welding in this way a hole is usually formed by evaporation. This "hole" is then traversed through the material with the molten walls sealing up

behind it. The result is what is known as a “keyhole u weld”. This is characterized by its parallel sided fusion zone and a narrow width. Since the weld is rarely wide compared to the penetration it can be seen that the energy is being used where it is needed in melting the interface to be joined and not most of the surrounding area as well. A term to define this concept of efficiency is known as the "joining efficiency". The joining efficiency is not a true efficiency in that it has units of (mm^2 joined /kJ supplied). It is defined as St / PJ, the reciprocal of the specific energy.

Where S = traverse speed, mm/s; t = thickness welded, mm; P = incident power, kW.

The higher the value of the joining efficiency the less energy is spent in unnecessary heating; that is, generating a HAZ or distortion.

The laser welding process has many superior qualities. The main market for the process is usually found in areas requiring the welding of heat sensitive components, such as, heart pace makers, pistons assembled with washers in situ, diaphragms with sealed gas or electronic components. Another application area is in welding magnetic or potentially magnetic material, such as gears for cars. The speed and neatness of the weld is, however, a challenge for the future. Many researchers are currently focusing on the welding of cars, cans, domestic equipment and aircrafts.

2.4.1 Laser Cutting

The CO_2 laser is a proper cutting process for several materials. These include metals, such as, titanium, steel, paper, textiles, wood and plastics. The CO_2 laser can also cut hard and brittle materials, such as, aluminium oxide and silicon carbide. If metals are cut in an oxidizing atmosphere, the cutting speed may be increased. The cutting width, however, is determined by the size of the laser spot. Experiments are reported in which the CO_2 laser was used for welding steel, titanium, plastics, quartz, and glass [14].

Laser cutting is a mostly thermal process in which a focused laser beam is used to melt material in a localized area. A co-axial gas jet is used to eject the molten material from the cut and leave a clean edge. A continuous cut is produced by moving the laser beam or work piece under CNC control. Laser cutting is the largest industrial application of higher power lasers. It is used in industry in a range of

applications from prototyping and smaller batch manufacturing up to continuous production line systems. The process lends itself to automation with offline CAD/CAM systems controlling either 3-axis flat bed systems or 6-axis robots for three dimensional laser cutting.

In recent years, the increase in laser cutting has been dramatic, replacing more conventional mechanical processes due to increased flexibility. The improvements in accuracy, edge squareness and heat input control means that other profiling techniques, such as, plasma cutting and oxy-fuel cutting are being replaced by laser cutting [15].

2.4.2 Laser Welding Parameters

Laser keyhole welding is often referred to as a high energy density or power beam technique. The fact that absorption of a laser beam increases with temperature has enabled the use of the laser beam as a practical heat source for welding.

To form a laser weld, the laser beam is brought to focus on or very near the surface of the work pieces to be joined. In the first instance a large percentage of the incident beam is reflected from the work surface for a minute period; this is because most metals are good reflectors. However, the small amount of laser beam energy, which is initially absorbed by the work, quickly heats the material surface causing production of an energy absorbing ionized metal vapor, which rapidly accelerates the absorption of much of the energy that previously would have been reflected.

At a focused power density in the order of 104 W/mm^2 the rapid removal of metal by vaporization initiates a small keyhole into the work piece [16].

Weld shape and depth are determined by the manner in which the welding energy is applied to the joint. For laser welding, the energy input is controlled by the combination of the following parameters: Focus spot size, keyhole shielding gas, laser power and welding speed. These being correct, the repetition of welding performance then depends on the material preparation, joint fit-up and laser beam to joint alignment. All the above mentioned parameters are the inputs to welding process which are controlling the output quality of the joint and they are covered below.

2.4.2.1 Focus position

The position of focal points has an important influence on welding process and quality. The focal plane should be set where the maximum penetration depths or best process tolerances are produced.

El-Batahgy [17] has studied the relationship between defocusing distance and penetration depth of both 304L and 316L steels. The result is summarized in Fig. 2.1. The results indicated that the most effective range of defocusing distance to get maximum penetration with acceptable weld profile lies between zero and - 1 mm.

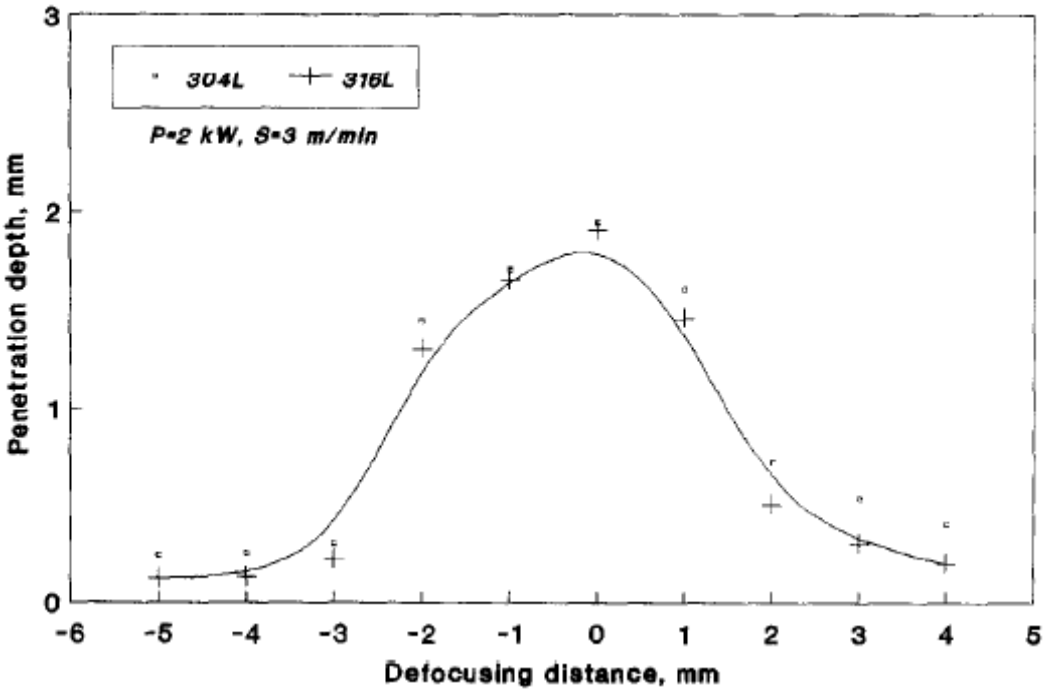

Fig. 2.1: Relationship between focus position and penetration depth of type 304L and type 316L steels [17].

2.4.2.2 Welding speed and laser power

The welding speed has an inversely proportional affect on the penetration and welding shape. The relationship between the welding speed and laser power is almost inversely proportional. The welding speed with the laser power are what determines the weld energy (J/mm of weld length) and hence the weld properties and shape.

Effect of speed on the weld pool and weld bead shape: As the speed increases so will the pool flow pattern and size change. At slow speeds the pool is large and wide and may result in drop out. In this case the ferrostatic head is too large for the

surface tension to keep the pool in place and so it drops out of the weld leaving a hole or depression. This is described in detail by Matsunawa [18]. At higher speeds, the strong flow towards the centre of the weld in the wake of the keyhole has no time to redistribute and is hence frozen as an undercut at the sides of the weld. If the power is high enough and the pool large enough then the same undercut proceeds and edge freezing occurs leaving a slight undercut but the thread of the pool in the centre has a pressure which is a function of the surface tension and the curvature [18].

The effect of heat input as a function of laser power, H = P/S, was clarified by El-Batahgy [17] using type 304L and type 316L steels. All other welding parameters were kept constant. The penetration depth increased sharply with increasing laser power. The results indicated that the development of the weld pool was essentially symmetrical about the axis of the laser beam. Yet, lack of symmetry at the root side was observed particularly at higher welding speed suggesting an unsteady fluid flow in the weld pool. This is due to the presence of two strong and opposing forces, namely, the electromagnetic and the surface tension gradient forces. Laser power has a lesser influence on both weld profile and HAZ width in comparison with its effect on penetration depth. This is in agreement with other researchers work where they pointed out that changing laser power did not result in any significant change in the size or shape of the weld. It is expected that similar results concerning the dependence of penetration depth on laser power could be obtained in the case of type 347 steel due to similarity in both physical and mechanical properties.

2.4.2.3 Shielding gas

In laser welding the shielding gas has two functions:

- To protect the weld keyhole and solidifying molten metal from oxidation and thus avoid porosity and oxide inclusions which give rise to poor weld quality.
- To protect the transmission of the laser beam as it comes to focus on the work and thus ensure good welding penetration by minimizing beam expansion and scattering, which can be caused by vapors and gases around the welding keyhole.

The suitable shielding gas for CO_2 laser welding:

Helium which is recommended for CO_2 laser welding where high quality welds are required and it is specially recommended for welding stainless steel, titanium and zirconium. The only disadvantage to using the helium, it is the high cost. Helium is 2.5 times more expensive than argon and 10 times more than nitrogen.

Argon is an extremely good cover gas for prevention of oxidation. As a keyhole shield for long continuous welds, argon is only recommended where it can fall quickly away from the zone under gravity, or by extraction. The use of argon provides a cost saving compared to helium.

Nitrogen performs nearly as well as helium in terms of preventing an unacceptable plasma formation, but it can cause weld embitterment in certain steels. Nevertheless, for welding automotive sheet steel an acceptable quality could be achieved when using nitrogen as shielded gas.

Carbon dioxide is not recommended as shielded gas for CO_2 laser welding. This is because carbon dioxide very quickly reacts with the focused laser beam, degrades and forms an unacceptable plasma cloud.

A comparative study has been carried out by Ancona et al. [19] on the influence of two different shielding gas delivery systems on the autogenous laser welding process of AA5083. Bead-on-plate tests have been performed by using a 2.5 kW CO_2 laser source and helium as shielding gas, supplied respectively by a coaxial conical nozzle and a two-pipe nozzle. The effects of the variation of the main process parameters, i.e., travel speed, beam focus position, gas flow rate and nozzle standoff distance on the bead profiles (width, penetration depth, melted area), were investigated.

Useful information has been obtained on the role of the welding nozzle geometry on the laser–matter interaction. Several sets of process parameters able to produce acceptable welds were selected. The most important process parameter was the travel speed since it determined the linear energy input released onto the material. The gas flow rate and the nozzle standoff had a small influence on the penetration depth. The two-pipe configuration generally produced joints with a lower width, deeper penetration and larger melted areas, with respect to the coaxial nozzle.

Therefore, it was argued that this gas delivery system allows a more efficient energy transfer producing joints with a higher aspect ratio.

2.4.2.4 Wavelength

Due to the high absorptive within the "keyhole" there is little operational difference when welding with long or short wavelengths. When welding with conduction limited weld then the surface reflectivity becomes paramount and the lower reflectivity with the shorter wavelengths gives a distinct advantage to Excimer lasers or Nd: YAG lasers over the CO_2 laser.

2.4.2.5 Welding gap and the alignment of the laser beam

The welding gap between the two pieces to be jointed and the alignment of the laser beam with the centre of the welding gap are two laser welding parameters which are critical for a butt joint. These parameters are controllable in the actual operation of laser welding, but are interconnected and extremely non-linear; such problems limit the industrial applicability of the laser welding for butt joints.

The neural network technique was applied by Jeng et al. [20] as a tool for predicting the operation parameters of a non-linear model. Back propagation (BP) and learning vector quantization (LVQ) networks were used to predict the laser welding parameters for butt joints. The input parameters of the network include work piece thickness and welding gap, whilst the output parameters include optimal focused position, acceptable welding parameters of laser power and welding speed, and welding quality, including weld width, undercut and distortion for the associated power and speed used. The results of their research show a comprehensive and usable prediction of the laser welding parameters for butt joints using BP and LVQ networks.

2.5 Dissimilar Welding

Demands of dissimilar metals joint have increased from various viewpoints, such as, environmental concern, energy saving, high performance, cost saving and so

on. Joining of dissimilar materials is one of the challenging tasks facing modern manufacturers. The technological difficulty in joining of dissimilar metals is mainly caused by the brittle intermetallic reaction layer formation in the bond region, which results in low joining strength. Many efforts have been made in order to spread the use of fusion welding for dissimilar metals. Laser welding, which is an excellent tool for controlling the heat input and molten pool size, will be useful for controlling the formation of intermetallic reaction layer in dissimilar metals joints. The following is a review of some articles that applied different techniques for producing dissimilar joints.

The application of laser beam welding for the joining of dissimilar metals was overviewed by Sun and Karppi [7]. Sun and Karppi have reviewed the state-of-the-art of electron beam welding "EBW" of dissimilar metals, with special emphasis on showing the potential of the process for achieving high-quality dissimilar-metal joints. Since EBW is a fusion-welding process, metallurgical phenomena associated with fusion still exist and cause difficulties. However, these are often minor compared to those in conventional arc welding. Problems encountered and possible solutions are discussed. The review indicates that although many studies have been performed, there is still a considerable need to further examine existing and new combinations. Future R&D trends are also highlighted.

2.5.1 Dissimilar Welding of Joining Ferrous Materials

The formation of butt joints of AISI304L and AISI12L13 using a laser-welding technique was investigated by Zhang Li and Fontana [21]. The offset and the impingement angle of the laser beam are two key parameters for controlling the melt ratio of the dissimilar materials in order to avoid solidification cracking in the fusion zone and micro-fissuring in the HAZ. Solidification cracking and micro-fissuring result from the harmful elements of Pb, S, P, and Mn contained in AISI12L13. Sound butt joints can be produced on 0.9 mm sheet at a 0.12 mm offset towards the AISI304L with a 15° laser beam impingement angle with respect to the fit-up face of the butt joint. The strength of the laser welds produced was higher than both the yield strength of AISI304L and the rupture strength of AISI12L13 under the test conditions adopted in the study. The greater mechanical properties of the laser welds

demonstrate the beneficial effect of rapid solidification in the fusion zone and of a small HAZ.

Diffusion bonding is an advanced bonding process in which two materials, similar or dissimilar, can be bonded in solid state. This enables a wide range of materials which cannot be bonded with conventional welding methods, from low carbon steels to ceramics and composites. One of the major advantages of this method is to produce new bimetal or dissimilar material couples. The process is diffusion-based and occurs in solid state. Orhan et al. [22] presented a new mathematical model to predict the final bonding time for a sound bonding interface prior to bonding practice. Being different from the previous models, the model assumes a new surface morphology as a sine wave and a new creep mechanism for duplex alloys. The mechanisms operating during diffusion bonding are based on those in pressure sintering studies but here mass transfer by evaporation has been ignored. The driving forces and rate terms for those mechanisms have been altered to reflect the difference of the geometries of the two processes. Also, the effect of grain size has been included in the model in case of joining fine-grained materials. As a result, it was determined that the developed model could be used in order to adequately estimate the final bonding time of the duplex alloys for a sound bond interface and the relationships between its parameters. The predictions from this developed model show very good agreement between practice and theory.

Béjar et al. [23] investigated electro contact-discharge forge welding through similar and dissimilar couples of steel bars of SAE 1020, 1045 or 5160. The couples were electro contact-discharge heated by using an ac arc-welding machine and by contacting and separating intermittently the bars (electrodes). Tension tests were used for evaluating the quality of the welds. The conclusion was that all steel couples could be welded using the electro contact-discharge forge welding, fracture occurring some millimeters away from the welded interface.

The metallurgical characteristics, tensile, hardness, toughness and corrosion resistance of dissimilar welds between X5CrNi18-10 grade austenitic and X20CrMo13 grade martensitic stainless steel have been evaluated by Kachiar and Baylan [24]. Both austenitic and duplex stainless steel electrodes were used to join this combination, using multi-pass manual metal arc welding process. Defect free

welds were made with each welding consumable. The toughness of both the E2209-17 and E308L-16 deposits was acceptable even at low temperature regardless of heat input. Hardness was increased in both welds made with E2209-17 duplex and E308L-16 austenitic electrode along the X20CrMo13/weld metal fusion boundary due to heat annealing and followed by a high cooling rate. The pitting corrosion resistance of the weld metal made with E308L-16 and E2209-17 filler metal was found to be acceptable. The study has detected that both filler metals can be used to join austenitic stainless steel to the martensitic stainless steel.

Continuous drive friction welding for the austenitic/ferritic stainless steel combination has been investigated by Satyanarayana et al. [25]. Parameter optimization, microstructure–mechanical property correlation and fracture behaviour was a major contribution of their study. Sound welds were obtained at certain weld parameter combinations only. The mechanical properties of dissimilar metal welds were comparable to those of ferritic stainless steel welds. They evaluated the joints for resistance to pitting corrosion and revealed that the dissimilar welds exhibit lower resistance to pitting corrosion compared to the ferritic and austenitic stainless steel welds. They concluded that the interface on the austenitic stainless steel side exhibited higher residual stress, possibly due to its higher flow stress and higher coefficient of thermal expansion. The toughness and strength properties of dissimilar metal welds are better than the ferritic stainless steel parent metal. Notch tensile strength, hardness and impact toughness can be expressed in terms of the process parameters by regression equation obtained by statistical analysis.

In a study by M. Sahin [26], experimental joining of high-speed steel and medium-carbon steel was designed and produced to achieve the friction welding of components having equal diameter. In the experiments, high-speed steel (HSS-S 6-5-2) and medium-carbon steel (AISI 1040) were used. Post-weld annealing was applied to the joints at 650 ºC for 4 h. The optimum welding parameters for the joints were achieved using factorial design of experiments and the Fisher ratio. The strengths of the joints were determined by tension, fatigue and notch-impact tests, and results were compared with the tensile strengths of materials. Then, hardness variations and microstructures in the post-weld of the joints were obtained and examined. Finally,

M. Sahin concludes that the continuous drive friction welding method can be suitably adopted for the production of different steels and metals.

An assessment of impact strength of shielded metal arc welded (SMAW) dissimilar weldments between duplex stainless steel (DSS; UNS 31803) and carbon steel (CS; IS 2062) steels was carried out by Srinivasan et al. [27]. The welding of DSS to CS was attempted by SMAW, with E2209 and E309 electrodes. The hardness and impact strength of the weld metal produced with E2209 electrodes were found to be better than that obtained with E309. Although the general corrosion resistance of the weld metal produced with E309 was superior in 1M NaCl solution, they exhibited a higher pitting susceptibility in this test environment. The observations of Srinivasan et al. concluded that the E2209 electrode is the most suitable consumable for joining DSS to CS and the impact strengths of the weld metals are lower than the DSS-BM, and much higher than the CS / CS-HAZ regions of the weldment.

Berretta et al. [28] investigated the technique for welding AISI 304 stainless steel to AISI 420 stainless steel using a pulsed Nd: YAG laser. The main objective of their study was to determine the influence of the laser beam position, with respect to the joint, on weld characteristics. Specimens were welded with the laser beam incident on the joint and displaced 0.1 and 0.2mm on either side of the joint. The joints were inspected in an OM for cracks, pores and to determine the weld geometry. The microstructure of the weld and the HAZ were observed in a SEM. An energy dispersive spectrometer, coupled to the SEM, was used to determine variations in (weight %) the main chemical elements across the fillet weld. Vickers microhardness testing and tensile testing were carried out to determine the mechanical properties of the weld. The results of the various tests and examinations enabled definition of the best position for the incident laser beam with respect to the joint, for joining the two dissimilar stainless steels.

2.5.2 Dissimilar Welding of Joining Nonferrous Materials

Luijendijk [29] studied the welding of dissimilar aluminium alloys of the series 5xxx and 6xxx using GTA-welding for plate thickness of 1.5, 3 and 5 mm. Specific attention was given to the asymmetry of the weld and melting behaviour of the

different weld grooves. Practical solutions were given for realizing optimal weld penetration for materials with a large difference in thermal properties. Due to welding, the strength of the material in the HAZ is reduced. This reduction in strength is smaller for solution hardened and strain hardened alloys, than for precipitation hardened alloys. For the precipitation hardened alloys the reduction in strength due to welding is smaller for the naturally aged condition than for the artificially aged situation. The reduction in strength for the strain hardened alloys is independent of material thickness for the specified range of material thickness.

The joint properties of dissimilar formed aluminium alloys by friction stir welding were investigated by Lee et al. [30]. The dissimilar formed cast A356 Al alloy and wrought 6061 Al alloy jointed and the characteristics were evaluated with various welding speeds, W. Lee et al. observed that the microstructures of the joint showed the mixed structures of two materials. The onion ring pattern, which appeared like lamellar structure, was observed in the stir zone. The microstructure of the stir zone was mainly composed of the material fixed at the retreating side. The mechanical properties of the stir zone showed higher values when 6061 Al alloys were fixed at the retreating side. This result relates to the complex microstructure of the stir zone.

Weldability between an un-reinforced aluminium alloy (Al6082) and an Al6092/SiC/25p composite, using as filler metals both Al–5Mg (ER5356) and Al–5Si (ER4043) un-reinforced alloys, had been studied by P.P. Lean et al. [31]. One of the main requirements considered to obtain metallurgical weldability was to reduce the heat input to limit the possible interfacial reaction among molten aluminium matrix and SiC particles which produces aluminium carbide (Al_4C_3) inside the weld pool and the fusion line. The welding procedure selected was a gas shielded metal arc welding, working in pulsed current mode (MIG-P), to obtain improved control over the metal transfer to the molten pool. Three kind of joint designs were used: “I”, “V” and “X”, working with one and two filler metal runs. Mechanical tests of welded joints showed that tensile strengths, for all these welding conditions, were very similar and close to 223MPa, which is approximately the 65% of the Al6082-T6 one. In all cases, failure was located through the HAZ of the un-reinforced alloy. The

application of a post welding heat treatment made possible to recover the 100% of the parent un-reinforced alloy tensile strength.

Zhang et al. [32] produced heterogeneous dissimilar weld joints in Ti_3Al/TC4 using the electron beam welding (EBW) process. They investigated the microstructure evolution characterizations of the joints by means of OM, SEM, XRD, TEM and the tensile strengths of the joints were tested. The microstructure of the weld metal of every joint was identical. The structures were characterized by martensite, appearing as coarse equiaxed grains. With the increase of heat input, the grain size was significantly raised, yet the composition of the weld metal was independent of heat input. The highest tensile strength of the joints equaled almost 92% of that of Ti_3Al-based alloy. Microstructural analysis of the joint showed that the weld metal was mainly composed of martensitic alpha prime. The microhardness of the joint distribution showed that the hardness increased in the HAZ of both metals and varied in the fusion zone because of the different quantity of martensite in different positions. Martensite concentration rose due to the non-homogeneous distribution of the beta phase stabilizer. Grain size affects the tensile strength of the dissimilar joint critically and this factor is mainly related to the heat input during the welding process. A good joint with high tensile strength, 831MPa, could be obtained by selecting less heat input which penetrates the butted joint to a lesser degree.

A study of the microstructural and mechanical properties of friction stir welded aluminium (1060) with pure copper lap joints was carried out by Abdollah-Zadeh et al. [33]. They carried out a number of friction stir welding “FSW” experiments to obtain the optimum mechanical properties by adjusting the rotational speed and welding speed. Various microstructures with different morphologies and properties were observed in the stir zone. The results indicated that Al_4Cu_9, AlCu and Al_2Cu are the main intermetallic compounds formed in the interfacial region. They have concluded that the lap joints between aluminium and copper could be successfully produced by FSW. An intermetallic compound of Al_4Cu_9, AlCu and Al_2Cu was observed near the Al/Cu interface, where the crack was found to often be initiated and propagated preferentially during tensile testing. Extremely low rotational speed (or high welding speed) resulted in imperfect joints.

2.5.3 Dissimilar Welding of Ferrous and Nonferrous Materials

Zumelzu and Cabezas [34] have investigated the welded joints, DHP copper and AISI 304 stainless steel, in a sea-water environment. The TIG and oxyacetylene welding processes were used. Dissimilar joints were studied regarding hardness, strength and strain distribution. Results show diverse correlations which validate the several techniques used. Correlations of performance and functioning were obtained through the hardness and mechanical strength, current density, current potential, polarization resistance and chemical composition of the weld joints.

Friction welding process in relation to the welding of copper and steel bars was studied and analyzed by Sahin et al. [35]. The welding of Cu and Fe was studied analytically and experimentally. It was found that the temperature variation at the interface in the radial direction plays a key role on the diffusion process and the development of a heat-affected zone, which in turn affects the quality of the weld. The heat-affected zone is wider in the case of a higher thermal diffusivity region than that corresponding to a lower thermal diffusivity region. Diffusion takes place as a result of local melting and physical mixing and it is greater around the region where higher temperatures are obtained. Metals with different thermo physical properties can be joined by friction welding, and a sound weld can be achieved. Some degree of softening may occur during the welding process.

Garmire [36] points out an interesting application of CO_2 lasers to the welding of stainless steel handles on copper cooking pots. A nearly impossible task for conventional welding because of the great difference in thermal conductivities between stainless steel and copper, it is done so quickly by the laser that the thermal conductivities are irrelevant.

Mai and Spowage [37] characterized dissimilar joints in laser welding of Steel–Kovar, Copper–Steel and Copper–Aluminium. They could produce sound welds of three different material combinations by laser welding with a pulsed Nd: YAG laser. They conclude that controlling the melting ratio of metals is an important factor for defect-free welding of dissimilar metals. Due to locally restricted energy input and high power density, laser welding permits a controlled heat distribution and a minimized interaction of the joining materials. Thus, the formation of brittle intermetallic phases could be avoided.

Uzun et al. [38] studied the welding of dissimilar Al 6013-T4 alloy and X5CrNi18-10 stainless steel using the friction stir welding (FSR) technique. They investigated the microstructure, hardness and fatigue properties of the welds produced. OM was used to characterize the microstructures of the weld pool, the HAZ, thermo-mechanical affected zone (TMAZ) and the base materials. The results showed that FSR can be used for joining the dissimilar Al 6013 alloy and the X5CrNi18-10 stainless steel. Seven different zones of the microstructure in the welding were reported as follows: (1) parent stainless steel, (2) HAZ in the stainless steel at advancing side of weld, (3) TMAZ in the stainless steel at advancing side of weld, (4) weld pool, (5) TMAZ in the Al alloy at the retreating side of weld, (6) HAZ in the Al alloy at retreating side of weld and (7) parent Al alloy. A good correlation between the hardness distribution and the welding zones was observed. Fatigue properties of Al 6013-T4 and X5CrNi18-10 stainless steel joints were found to be approximately 30% lower than that of the Al 6013-T6 alloy base metal.

Watanabe et al. [39] tried to butt-weld an aluminium alloy (A5083) plate to a mild steel (SS400) plate by friction stir welding. They investigated the effects of a pin rotation speed, the position for the pin axis to be inserted on the tensile strength and the microstructure of the joint. The behaviour of the oxide film on the faying surface of the steel during welding was also examined. The main results obtained were as follows: Butt-welding of aluminium alloy plate to a steel plate was easily and successfully achieved by friction stir welding. The maximum tensile strength of the joint was about 86% of that of the aluminium alloy base metal. A small amount of intermetallic compounds was formed at the upper part of the steel/aluminium interface, while no intermetallic compounds were observed in the middle and bottom parts of the interface. The regions where the intermetallic compounds formed seemed to be fracture paths in the joint.

Mathieu et al. [40] found that the joining steel with aluminium involving the fusion of one or both materials is possible by laser beam welding technique. The main problem with thermal joining of steel/aluminium assembly with processes such as TIG or MIG is the formation of fragile intermetallic phases, which are detrimental to the mechanical performances of such joints. Braze welding permits a localized fusion of the materials resulting in a limitation on the growth of fragile phases.

Mathieu et al. investigated the use of a Taguchi approach for an overlap assembly configuration of joining Al (6016) to GXES low carbon steel coated with zinc to find the best operating parameters using a filler wire composed of 85% Zn and 15% Al. Tensile tests carried on these assemblies demonstrated a good performance of the joints. The fracture mechanisms of the joints were analyzed by a detailed characterization of the seams. At the optimal conditions, the mechanical performances of the steel/aluminium assemblies have fracture strengths superior to 200 N/mm. In certain condition, the rupture occurs in the heat-affected zone (HAZ) of the aluminium or in the steel sheet itself. The strength values were compatible with the specifications relative to these assemblies in the automotive industry.

Liu et al. [41] have carried out experiments of autogenous laser full penetration welding of dissimilar cast Ni-based super-alloy K418 and alloy steel 42CrMo plates using a 3 kW continuous wave (CW) Nd:YAG laser. They investigated the effects of laser welding velocity, flow rate of side-blow shielding gas and defocusing distance. The microstructure of the welded seam was characterized using OM, SEM and XRD and energy dispersive spectrometer (EDS). Mechanical properties of the welded seam were evaluated by microhardness and tensile strength testing. Results show that a high quality full penetration laser-welded joint can be obtained by optimizing the welding velocity, flow rate of shielding gas and defocusing distance. The laser-welded seam have non-equilibrium solidified microstructures consisting of γ-FeCr0.29 Ni0.16C0.06 austenite solid solution dendrites as the dominant and very small amount of super-fine dispersed Ni3Al γ' phase and levels particles as well as MC needle-like carbides distributed in the interdendritic regions. Although the microhardness of the laser-welded seam was lower than that of the base metal, the strength of the joint was equal to that of the base metal and the fracture mechanism showed fine ductility.

2.6 Mechanical Properties

2.6.1 Residual Stress

Residual stresses are self-equilibrating stresses that are trapped in a specimen even if the specimen is not under external loads. They are stresses that are inside or

locked into a component or assembly of parts. The internal state of stress is caused by thermal and/or mechanical processing of the parts. Common examples of these are bending, rolling or forging a part. Another example is the thermal stresses induced when welding. The formation of residual stresses is inevitable in any welding operation.

Residual stresses usually result from the inability of the material to return to an unstressed condition after experiencing intense heat input of welding. The differential cooling following a localized application of heat gives rise to shrinkage, which in turn causes distortion. In the case of welding, this distortion may be longitudinal, transverse, angular or combinations of these. When thick section pressure vessel is welded, the vessel itself cannot deform to accommodate the contraction of the weld as it solidifies and cools. Residual stresses after welding can thus result in tension stresses of the order of the yield stress of the material and this can initiate and even drive cracking [42].

Protecting produced components from distortion during welding can lead to the imposition of significant through-section residual stresses which will have the same effect as having a continuously applied mechanical load and must be taken into account when designing welds [43, 44]. The presence of residual stresses and specifically their nature (tensile or compressive) has an influence on the behaviour of welded joints in service. In some situations the residual stresses may improve the performance (for example, compressive stresses can improve resistance to stress corrosion cracking). However, in most cases, residual stresses are tensile in nature and are known to have negative effects, such as increasing susceptibility to fracture and decreasing fatigue life of industrial products [45, 46, 47].

2.6.1.1 Controlling residual stress formed during welding

There have been many reports on reducing residual stress. Residual stress control during the welding process can easily protect welded components without the requirement for any additional procedure after welding. Controlling welding conditions, such as heat input (in this study the heat input controlled by laser power and welding speed) or constraints affects the residual stress distribution [48, 49, 50, 51, 52, 53]. The material properties of the base metal and weld metal have an influence on residual stress [54,55] when a consumable with a low-temperature

martensitic phase transformation is applied to a high-tensile steel structure. Pre-strain [56] and pre-heating [57,58] are effective in reducing residual stress. In addition, controlling constraint conditions [59], cooling near a weld pool [60], or combining vibration with welding [61], have been developed as in-process methods of residual stress reduction.

The procedure of residual stress reduction after welding is also important. Post-weld heat treatment, [62,63] and water jet peening, [64,65] are typical methods for reducing residual stress.

Porowski et al. and Nayama [66,67] investigated the methods of residual stress reduction by plastic deformation from a mechanical force applied after welding. Watanabe et al. [68] developed a method for residual stress reduction that involved cooling the welded component by liquid nitrogen after welding. Residual stress reduction, in-process-control during welding is easier to apply than using post-weld treatment. Mochizuki [69] discovered that the water jet peening is useful for obtaining a compressive residual stress on the surface.

2.6.1.2 Residual stress measurement methods

The comparison of the measurement methods is illustrated in Fig. 2.2 and some of the advantages and disadvantages are discussed:

Neutron Diffraction

- This is the only method that can measure variation with depth nondestructively
- It has limited resolution since it averages residual stress over a volume. For example, in this study the stresses of interest are measured through all the full specimen depth (2 mm) - which is difficult for neutrons to resolve.
- The tested part needs to be subjected to a neutron source, i.e., a reactor or a spallation source.
- Microstructural changes can make measurements difficult. Dissimilar welds are especially tough.
- The neutron method is the most expensive residual stress measuring method.

X-ray Diffraction

- This is non-destructive for measuring surface residual stresses.
- If the measured stresses vary with depth it is necessary to etch away layers, which is very time consuming.
- It will not work on non-crystalline materials (neither will neutrons) and is sensitive to grain size and texturing.

Hole-Drilling

- The strain data at pre-determined depths are precisely acquired.
- An established method standardized by ASTM Procedure E837.
- Customized strain gauges.
- Highly sensitive to position and shape of drilled hole.
- Residual stresses determined are the average over the depth of the drilled hole.
- Incremental technique offers qualitative results only.
- It is semi destructive which allows measurement of the stress gradient in the depth of the material.

Crack Compliance (Slitting)

- All the methods above measure both residual stress components in the surface plane; compliance only measures the component normal to the face of the cut.
- If you are cutting into a tensile residual stress field, it is possible for the crack to propagate. It does not happen often but it has happened.

Ring Core (Trepan) Method

- Principal residual stresses are determined as a function of depth.
- The ring core method is valid for residual stresses up to 100% of yield strength.
- Low sensitivity to placement of strain gauge and eccentricity of the machined ring.
- Low sensitivity near the surface.

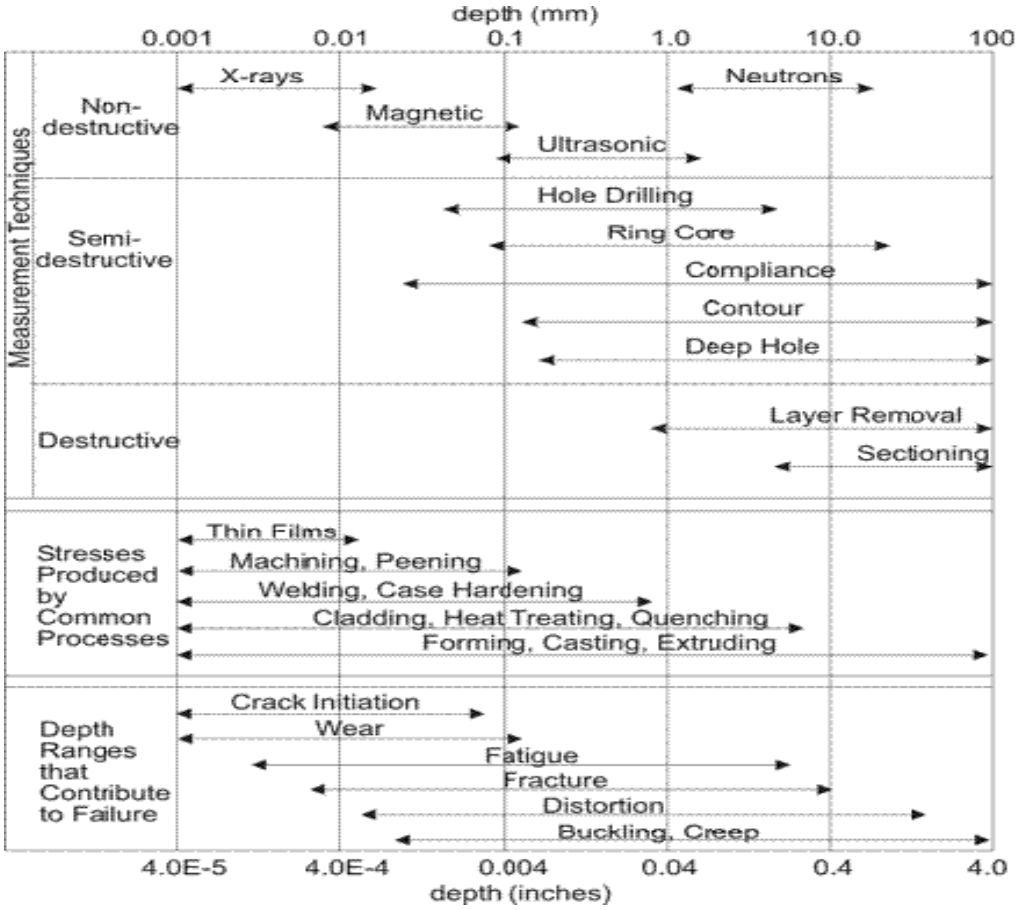

Fig. 2.2 shows the depth ranges of various methods compared with (1) the depth of residual stresses produced by common manufacturing processes and (2) the depth ranges where residual stresses would likely contribute to failure mechanisms [70].

2.6.1.3 Hole drill method overview

This is the only method for measurement of residual stresses that is accepted as an ASTM standard [71]. This is a simple and reliable method and by considering the small size of the damaged area resulting from the test, it is called a semi-destructive method. It is applied for measurement of the residual stresses in welds [72,73] on the clad layer [74], in some heat-treated welded components. Smith et al. developed the deep hole method used for measuring residual stress distribution through the thickness of weld metal [75]. However, this method is considered as a fully destructive method of residual stress measurement. In 1934, Mathar first proposed the availability of through hole analysis for residual stress measurement [76]. It was based on the analytic solution of an elastic problem that a thin plate was subjected to a uniform plane stress field. The detailed procedure of the through-hole method is

summarized in ASTM E837 [71]. A state-of-the-art summary of the hole-drilling method can be referenced in [77]. In 1966, Rendler and Vigness introduced the blind-hole analysis incremental method for thicker plate [78]. According to their experimental results, it has been found that the relationship between residual stress and strain in the blind-hole method was similar to that of the through-hole case. The studies by Bathgate and Kelsey showed similar results for the blind hole-drilling method [79,80]. It should be noted that prior to the hole-drilling measurement, calibration coefficients had to be determined in advance by experimental calibration. The method of calibration coefficients determination and the numerical data of calibration coefficients can be found by the Vishy Measurements Group and are explained in detail in the reference [81]. Power series method [82,83] and integral hole-drilling method [84,85] have thus been developed to improve the conventional hole-drilling method. Based on the hypothesis of these methods, studies have been conducted on the prediction of residual stress by using finite element (FEM) [86]. Integral method offers an advantage in measuring residual stresses, which vary abruptly with depth, such as the interfacial stresses between different layers. The power series method is applied mainly for smoothly varying stresses along depth.

The calibration coefficients determined from other research works are generally valid only for thick plates. The dimensions of the plates have to satisfy the specimen size criterion proposed in [81]. Hampton and Nelson proposed that the calibration coefficients of the blind-hole method for thick plates could be multiplied by a factor for the residual stress measurement of thin plates [87]. However, no study has been conducted on residual stress measurement of relative thin plates using the integral method. The thickness range which can be applied in the residual stress measurement of thin plates has not yet been defined clearly. In 2002, Aoh, and Wei, [88] established a three-dimensional model to determine the calibration coefficients for the integral method. The constraint conditions and loading conditions during hole-drilling can be simulated more realistically with this method. With this new model, coefficients $\overline{a_{i,j}}$ and $\overline{b_{i,j}}$ could be determined within one computation procedure. The calibration coefficients can thus be extended to measure the residual stresses of either thin or thick plates.

2.6.1.4 Effect of residual stresses on the dissimilar welded materials

Welding of dissimilar steels produces different residual stresses in welds as compared with welding of similar steels. The combination of high tensile residual stresses in the region heat affected zone and operating tensile stresses applied can promote brittle fracture; increase the susceptibility of a weld to fatigue damage, stress corrosion cracking during service. Therefore, a good estimation of residual stresses in welds of similar or dissimilar weldments and stress behavior in welds of the weldments under superimposed tensile loads is required to assure the sound design and safety of the structure. However, accurate prediction of welding residual stresses is very difficult because of the complexity of welding process which includes localized heating, temperature-dependent material properties and moving heat source, etc. Consequently, simulation tools based DOE methods are very useful to predict welding residual stresses.

C. Lee and K. Chang have studied the residual stresses in welds of similar and dissimilar steel (structural steels) and they discovered that, in the case of the dissimilar steel weldments, the difference between the longitudinal residual stresses in welds increases with increasing yield stress of the steel welded together with SM400 (SM490 < SM520 < SM570). When tensile loads are applied to edges of the weldments, the same pattern is noted for the longitudinal stresses in welds and the difference is almost the same as that between the longitudinal residual stresses in welds [89].

2.7 Welding Pool

Welding quality is strongly characterized by the weld penetration and the weld pool geometry. Due to that the weld pool geometry plays an important role in determining the mechanical properties of the welded joints. Therefore, the selection of the welding process parameters is essential for obtaining optimal weld pool geometry. The important problem to be solved in welding engineering is to develop a model for determining the optimal process parameters. Generally, the welding conditions can been determined by welding engineers on the basis of information obtained from experience. Knowledge of the heat input intensity and the temperature

gradients in the work piece are extremely important for welding process studies. However, recently, many welding processes have been mechanized and automated, and various models of optimizing the welding parameters have been developed and proposed for control of the welding process. The weld-pool geometry is to be first determined in optimizing the welding process. Usually, the desired welding process parameters are determined based on experience and from handbooks. However, this does not ensure that the selected welding process parameters can produce the optimal or near optimal weld pool geometry for that particular welding machine and environment.

In the last two decades, application of transport phenomena has resulted in improved understanding of fusion welding processes and welded materials. Numerical calculations would provide useful information about the thermal cycles and weld pool geometry in both gas metal arc and laser welding [90]. This is an overview of weld pool geometry optimization research which has been carried out for different welding processes and different methods:

A mathematical model for weld heat sources based on a Gaussian distribution of power density in space was presented by Goldak et al. [91]. In particular a double ellipsoidal geometry was proposed so that the size and shape of the heat source could be easily changed to model both the shallow penetration arc welding processes and the deeper penetration laser and electron beam processes. In addition, it has the versatility and flexibility to handle non-axisymmetric cases, such as strip electrodes or dissimilar metal joining. Previous models assumed circular or spherical symmetry. The model developed by Goldak et al. is a nonlinear transient finite element (FEM) heat flow program for the thermal stress analysis of welds. The agreement between the computed and measured values was shown to be excellent.

Hsu and Rubinsky [92] investigated a two-dimensional, quasi-stationary finite element numerical model to study the fluid flow and the heat transfer phenomena which occur during constant travel speed, keyhole plasma arc welding of metal plates. A Newton-Raphson iteration procedure was developed in their model to accurately identify the solid-liquid interface location during welding. The finite element method was applied for the study of typical keyhole welding process of an AISI 304 stainless plate. The results have shown that the method could be used to

predict the shape of the welding pool as a function of welding parameters and that the widths of both the fusion zone and the heat effected zone decrease as the welding speed increases while the power required for welding increases with an increase in welding speed.

Stares et al. [93] used ultrasonic compression and shear waves to measure the dimensions of molten weld pools during the root-pass TIG welding of mild steel and stainless steel, and also to detect and characterize any defects formed during the process. The results indicate that lack of fusion, inclusions, porosity and undercutting, which are caused by incorrect welding conditions, can all be detected by ultrasonic means. In addition, the size of the weld pool and any changes in penetration due to external disturbances can be accurately measured. Ultrasonic compression and shear waves have been used in order to minimize the future occurrence of defects.

Based on the computation model for quasi-steady heat transfer problems of welding with the boundary element method, Hang and Okada [94] developed a computer program that used for the computation of thermal cycles at heat affected zones with gas shielded metal arc welding “GMAW” on medium thickness plates. The computed results were in good agreement with those from experiments, showing the capabilities and versatilities of the boundary element method to deal with the computerized simulation of welding thermal processes.

Keanini and Rubinsky [95] presented a finite element-based simulation of the plasma arc welding process. The simulation determines the weld pool's three-dimensional capillary surface shape, the approximate solid-liquid phase boundary, and calculates the pool's three-dimensional flow and temperature fields. The simulation was first used to examine the effect of ambient temperature and plate speed on pool shape. Pool flow was then studied.

An analysis of state equation governing the heat flow in circumferential pipe welding was carried out using a semi-analytical finite-element method, and optimal welding parameters obtained using a state-space method by Na and Lee [96]. As the welding parameters to be optimized, the welding velocity, the effective radius of heat source and the heat input were considered. The sequences of welding parameters were optimized and compared with experimental results to verify the accuracy of the

proposed model. The weld-pool geometry measured along the entire weld was found to be almost the same as the calculated results, a uniform weld bead around the pipe circumference being obtained.

In a study by Zhang et al. [97], a polar coordinate model was proposed to characterize the weld pool geometrically. The identification of its parameters involved complicated non-linear optimization which could not be done in real time using conventional algorithms. A neural network ANN was therefore proposed to identify the parameters in real time. By using pulsed laser illumination, clear images of the weld pool were captured. The developed image processing algorithm extracts the boundary of the weld pool in real time. Thus, real-time systems were developed to sense and process the image and identify the polar coordinate model. It was shown that the weld penetration could be accurately determined using the model parameters and a real-time weld penetration monitoring system was also achieved.

Weld pool geometry were computed via numerical solution of a boundary integral equation used as a model for the autogenous full penetration welding of pure materials by Yeh and Brush [98]. Numerical results show that for a given value of the heat input from the arc, the latent heat of fusion provides a substantial correction for the shape of the weld pool compared to solutions that neglect the latent heat. Moreover, the results confirm that the aspect ratio of the weld pool was larger when increasing either the value of the latent heat or the heat input from the arc, and was smaller for higher values of surface convective heat losses. The magnitude of the curvature of the weld pool at the centerline of the trailing edge was increased as the latent heat, the arc velocity or the plate preheat was increased, which may promote weld pool shape transition and/or defect formation.

Wahab and Painter [99] measured the full 3-dimensional weld pool shape for the GMAW process, and to study the use of this information within numerical models. A mechanical ejection device instantaneously emptied the molten metal from a weld pool by rapidly accelerating and decelerating the test plate being welded. A non-contact laser profiling system was used for accurate measurement of the exposed weld pool cavity. Welding speed and welding current were found to have the greatest influence on the length of a weld pool, and increasing heat input level yielded higher values for all critical weld pool dimensions. In conductive heat

transfer finite element models, the welding arc can be represented as a heat flux, but this approach introduces some arbitrariness within the defined heat source. The measured pool cavity has been used as a fixed temperature boundary in 3D quasi-steady state numerical models of the GMAW process. A comparison of predicted and measured T85 cooling times (time taken to cool between 800 and 500°C) had demonstrated the accuracy and viability of this modelling strategy.

Mathematical models of the GMAW process employed by Kim and Bash [100] to predict welding process parameters to obtain the required weld-bead geometry and to study the effects of weld process parameters on the weld-bead dimensions. In their work, an unsteady two-dimensional (2D) axisymmetric model was developed for investigating the heat and fluid flows in weld pools and determining the weld bead geometry, and the velocity and temperature profiles for the GMAW process. The mathematical formulation considers four driving forces for weld pool convection: electromagnetic; buoyancy; surface tension; and drag forces. The formulation also deals with the molten metal droplets. The equation was solved using a general thermo fluid-mechanics computer program. The results showed that the electromagnetic and surface tension forces as well as the molten metal droplets have a major influence in shaping the weld-pool geometry. Good agreement was shown between the predicted and experimentally determined weld-bead dimensions.

Petrov et al. [101] investigated the energy transfer mechanism from an electron beam to a metal target, weld pool and keyhole of formation during electron beam welding. The physical processes in the welding pool and plasma cavity were discussed. The study was shown that the nature of the heat source in a weld pool is non-stationary and the dynamic processes occurring in both the welding pool and the plasma cavity play a dominant role in the formation of the welding seam during electron beam welding of metals. The main reasons for the non-stationary nature of the heat source were associated with the processes of dissipation of the electron beam in evaporated metal as well as with the intense mass transport of liquid metal in the welding pool.

The welding bead microstructures of autogenous TIG welds was studied for a range of welding conditions using an Al–Cu–Mg–Mn alloy by Normae et al. [102]. It was found that a combination of high welding speeds and low power densities

provide the thermal conditions required for the nucleation and growth of equiaxed grains in the weld pool, providing heterogeneous nucleation sites are available. The most likely origin of nucleates is from a combination of dendrite fragments and TiB2 particles that survive in the weld pool. The finest microstructure was observed in the centre of the weld and is attributed to the higher cooling rates which operate along the weld centre line. The measured core concentration of the dendrite side arms was found to rise with increasing welding speed and was attributed to the formation of significant under cooling ahead of the primary dendrite tip, which enriched the liquid surrounding the dendrite side arms.

Tarng et al. [103] have used neural network to construct the relationships between welding process parameters and welding bead geometry in tungsten inert gas TIG welding. They described an intelligent modelling, optimization and classification of weld quality in the TIG welding process. A back-propagation network was used to construct the relationships between the process parameters and the characteristics on the welding bead geometry. An optimization algorithm called simulated annealing was then applied to the network for solving the process parameters with optimal welding bead geometry based on an objective function. The optimal welding bead geometry is defined as the front depth, back height and back width of the weld with a smaller-the-better quality characteristic. Furthermore, the fuzzy c-means algorithm was adopted to test and verify the weld quality using the characteristics on the weld bead geometry. Through the study, highly non-linear, strongly coupled, multivariable TIG welding processes can be further understood, analyzed and controlled.

The results with regard to the geometry prediction of the back-bead in GMAW where a gap exists were discussed by Lee and Um [104]. According to geometry prediction results, these geometry prediction methods showed errors low enough to be applied to real welding. With these results, prediction system of welding process parameters was formulated in order to obtain the desired back-bead geometry. In geometry prediction error by multiple regression analysis, the gap had the largest geometry prediction error, followed by welding speed, arc voltage and welding current. Lee and Um concluded that gap was the most difficult parameter in

comprising prediction system of welding process in order to obtain the desired back-bead geometry in butt-welding.

Reed et al. [105] carried out a systematic study which examined the use of a pulsed Nd: YAG laser to weld sheet materials of V-Cr-Ti alloys. Deep penetration, defect-free, and oxygen contamination free welds were achieved under an optimum combination of laser parameters including focal length of lens, pulse energy, pulse repetition rate, beam travel speed, and an innovative shielding gas arrangement. The key for defect-free welds was found to be the stabilization of the keyhole and providing an escape path for the gas trapped in the molten weld pool.

A visual sensing system was developed by Bae et al. [106] for automatic GMAW of the root pass of steel pipe. The system consisted of a vision sensor that consisted of a charge-coupled device (CCD) camera and lenses, a frame grabber, image processing algorithms, and a computer controller. A specially designed five-axis manipulator was used to position the welding torch and to provide the vision sensor with automatic access to view the welding position. During the root pass welding, an image of the weld pool and its vicinity was captured using the camera without interference of the intensive arc light by viewing at the instance of the welding power of a short-circuit. The captured image was then processed to recognize the weld pool shape. For seam tracking, the manipulator was used to adjust the torch position based upon the pool image to the groove centre. The measured gap size was used to determine the appropriate welding conditions to obtain sound penetration. The welding speed was chosen using fuzzy logic with the knowledge of a skilled welder and measured gap. The automatic welding equipment demonstrated that both welding conditions and torch position could be appropriately controlled to obtain a sound weldment and a good seam tracking capability.

A computational modelling of welding phenomena within a versatile numerical framework was presented by Taylor et al. [107]. The framework embraces models from both the fields of computational fluid dynamics (CFD) and computational solid mechanics (CSM). With regard to the CFD modelling of the weld pool fluid dynamics, heat transfer and phase change, cell-centred finite volume (FV) methods were employed. The FV methods were included within an integrated modelling

framework, which can be readily applied to unstructured meshes. The modelling techniques were validated against a variety of reference solutions.

Kim et al. [108] have applied the factorial design to achieve the optimal bead geometry through the process parameters for GMA welding of AISI1204 steel plates. The optimal bead geometry was based on bead width, bead height and penetration. The factorial design has been adopted to determine the optimal bead geometry. Experimental results have shown that process parameters, such as, welding speed, arc current and welding voltage influence the bead width, bead height and penetration in GMA welding processes. Mathematical models developed from the experimental data could be used to investigate relationships between process parameters and bead geometry and to predict the bead dimensions within 0 – 25% accuracy. Sensitivity analysis has been investigated to represent the effectiveness of the processing parameters on these empirical equations and showed that the change of process parameters affects the bead width and bead height more strongly than penetration. The developed models should be put into perspective with the standard GMA welding power source that was employed to conduct the experimental work. Factorial analysis has the potential for more stringent sensitivity analysis and may be employed for optimal parameter estimation for other mathematical models.

An integral mathematic model of fluid flow and heat transfer of GTAW and weld bead was established by Lu et al. [109]. The established model could avoid the assumption which surface temperature of weld bead is constant and at the same time provide reliable boundary conditions for analyzing of weld bead. Using finite element analysis software ANSYS, behavior of welding arc and weld bead was systematically analyzed including welding arc temperature field, current density distribution, fluid flow in weld pool and effects of a few forces on weld bead shape. Arc temperature distribution plays an important role in determining current density distribution of arc and weld bead. Surface tension is the definitive force for weld pool shape. Welding arc character and weld bead shape were fairly agreeable with experiments. The conceived results provided that the integral mathematic model built was reliable and effective.

Numerical heat transfer models of GMA fillet welding do not always predict correct temperature fields and fusion zone geometry. The inaccuracy results, to a

large extent, from the difficulty in correctly specifying several input parameters, such as arc efficiency, from scientific principles. In order to solve this problem, a heat transfer model was combined with an optimization algorithm by Kumar and DebRoy [90] in order to determine several uncertain welding parameters from a limited volume of experimental data. The resulting smart model guarantees optimized prediction of weld pool penetration, throat and leg-length within the framework of phenomenological laws. A boundary fitted coordinate system was used to account for the complex fusion zone shape. The weld bead surface profile was calculated by minimizing the total surface energy. Apart from the direct transport of heat from the welding arc, heat transfer from the metal droplets was modeled considering a volumetric heat source. An appropriate objective function that represented the difference between the calculated and experimental values of the penetration, throat and leg-length was minimized. The calculated shape and size of the fusion zone, finger penetration characteristics of the GMA welds and the solidified free surface profile were in fair agreement with the experimental results for various welding conditions.

A unified mathematic model was developed by Lu et al. [110], to detect the interaction between welding arc and weld pool of the TIG welding arc and pool. The moving interface was solved by updating the calculation region of arc and weld pool continually. Fluid flow and heat transfer of TIG welding arc and weld pool were analyzed based on the developed model. The weld pool shape calculated by dynamic coupling welding arc and pool was more close to the experiment than that of non coupling calculation.

Wang et al. [111] carried out a simulation of the pressure distribution around the keyhole during the deep penetration laser welding. The simulation physically relates to the process of a focused laser beam irradiating on the surface of a moving work piece. A calculation of the velocity vectors and absolute pressure near the front wall and dynamic pressure in the laser weld bead shows that the pressure gradients was directly related to the velocity magnitude of the pool fluid flow, and the dynamic pressure gradient against the welding direction at the rear of weld bead is a retarding force. The velocity of fluid flow near the real wall of the keyhole was smaller, and

the formation of the shoulder in the weld bead was contributed to by the movement of the keyhole relative to the work piece.

Tani et al. [112] developed an analytical system for the prediction of the actual energy transmitted to the work piece by modelling the plasma plume physical state related to the process parameters. In this way, by determining the laser beam energy lost in the plasma plume and the conduction energy transmitted to the work piece, an evaluation of the laser material interaction could be carried out. The developed model allows evaluating the geometry of the molten pool by means of the computation of the interface between the solid and the re-melted material. The effect of the plasma plume presence, by comparison with a modelisation without plasma implemented in similar way by the authors, was to reduce the molten pool and in particular the penetration depth and allowed simulation results to be closer to the experimental data.

Fusion zone area and shape were evaluated by V Gunaraj and N Murugan [113] as a function of the selected submerged arc welding (SAW) parameters. Response surface methodology (RSM) was used as statistical design of experiment (DOE) technique for optimizing the selected welding parameters in terms of minimizing the fusion zone. Mathematical models were developed to describe the influence of the selected parameters on the fusion zone area and shape, to predict its value within the limits of the variables being studied. The result indicates that the developed models can predict the responses satisfactorily. The study highlights the use of RSM for planning, conduction, execution and development of mathematical models. The achieved result was also useful for selecting optimum process parameters to produce the desired quality and process optimization.

A range of the process parameters for TIG welding of stainless steel with the optimal weld bead geometry have been discussed by Juang and Tarng [114]. The optimal weld bead geometry has four the-smaller-the-better quality characteristics, i.e. the front height, front width, back height and back width of the weld bead. The modified Taguchi method was adopted to solve the optimal weld bead geometry with four the-smaller-the-better quality characteristics. Experimental results have shown that the front height, front width, back height and back width of the weld bead in the TIG welding of stainless steel are greatly improved by using this approach.

2.8 Optimization of Mechanical Properties of Welded Joints

Welding processes can have various effects on the base metal. For example, high heat input may affect the mechanical properties of the base metal adversely. Cracking occurs when a material is unable to resist the stresses that are applied to it. The level of applied stress varies with the welding process. The joining may change the mechanical properties of the base metal; consequently, this factor must be considered in conjunction with usefulness after joining. The weld or HAZ may be different from the base metal especially in dissimilar welding applications in terms of hardness, strength, impact resistance, creep strength, and wear resistance. The mechanical properties of welded joint are the major factors deciding the welding quality. Knowledge of how welding parameters affect the mechanical properties of welds is important. Consequently, the aim of the welding process designer is to optimize the mechanical properties in order to produce excellent welded joints. For a accomplishing this purpose different methods and approaches have been developed and applied. This is a review of some applied methods for optimizing the mechanical properties of welded joints.

Scotti and Rosa [115], have explored the optimization of automatic flux cored arc welding parameters for crack-free hard-facing. A series of tests were carried out for verifying the influence of current, travel speed, torch angle, oscillation amplitude, dwell time and frequency, contact-tip work distance and pre-heating on crack information. Experimental statistics were used for planning and analyzing the experiments. The results show that pre-heating and oscillation amplitude were the most significant factors: the greater the pre-heating temperature and the narrower the oscillation amplitude, the less the amount of cracking. The relationship between crack occurrence and increase in hardness was explored also. No association was found with the microstructure, despite the influence of some parameters and dilution on the microstructure. It is concluded that it is possible to eliminate cracking in hard-facing with no hardness decrease.

Dai [116] studied the use of high-intensity ultrasonic wave on aluminium alloy 7075-T6 to observe the effect of emission waves on the weldability during GTA welding. Through the HAZ and the weld pool, the ultrasonic-wave emissions with different paths were examined and directly correlated to the heating time, dwell time,

cooling rate, as well as peak temperature of the thermal cycle, and to the grain growth, weld penetration, and hardness of the weldment. Also he has presented a methodology based on the characteristic curves of the relative amplitude ratios of the reflected longitudinal wave and vertical shear wave for improving the weldability of aluminium alloy 7075-T6.

Weng et al. [117] have chosen the GTAW to yield TiNi alloy overlay on AISI 1048 medium carbon steel substrates, and they have explored the solid/liquid mixture erosion behaviour. Weng et al. had concluded that the GTAW TiNi overlay maintains the B2 phase structure as source rod material, and the hardness of overlay was increased to threefold of source material by the trace oxide formation. The GTAW TiNi overlay can thus reduce the erosion rate of AISI 1048 substrate significantly over a wide range of impact angle solid/liquid erosion because its higher work-hardening effect and the high hardness of the as-welded structure.

Laser beam weldability of steel/hard metal joints was examined with high power CO_2 laser and Nd: YAG laser by Costa et al. [118]. Two different hard metals compositions (K10 and K40) were examined. Power, speed and vertical focal point position were investigated in order to decrease the problem of porosity and crack formation in the hard metal. The laser parameters power (P), speed (s), vertical focal point position (f.p.p.) and horizontal f.p.p. were investigated. Weld bead size, microstructure, bending tests and hardness were evaluated. These results show that laser welding is an alternative joining technique for hard metals. It proved its effectiveness for the production of cutting tools, joining with success hard metals and steel. The process has the overall advantage of producing small beads and HAZ and minimizing residual stresses. Continuous Nd: YAG laser was found to present the best results. This technique has a good potential for application in the welding of cutting tool tips, with the advantage of higher life time than brazing and less shape problems than mechanical clamping.

An experimental set up was designed and statistically analyzed in order to achieve the friction welding of plastically deformed steel bars by Shahin and Akata [119]. The parts, having same and different diameters deformed plastically, were welded with different process parameters. The strengths of the joints were determined by tension tests. Hardness variations and microstructures in the welding

zone were obtained and the effects of welding parameters on the welding zone were investigated and the following results were obtained. The tensile strength of the joints decreases according to the width amount increases. Hardness in the horizontal direction of the joints increases at the central zone. Hardness variation in the vertical distance of the joints is almost equaled from the side to the centre of parts. Increased hardness, due to rapid cooling, especially, on the horizontal distance to the centre in the welding zone of the joints caused the strength to decrease because of affecting notch. The strength of the joints was weak due to martensite structure that is a hard and brittle phase. Therefore, welded parts will not be stronger. It should be noted that the optimum parameters of the joints should be ordinarily selected in the experiments. The weld strength of the joints is not affected prior to plastic deformation due to two reasons. First, plastic deformation in friction welding process is larger than the degree of prior plastic deformation. Secondly, the effect of prior plastic deformation is removed in the welding zone due to high temperature in the welding zone. As a result, plastically deformed steels can easily be applied by the friction welding method.

Sterjovski et al. [120] have study the longitudinal and circumferential welds in transportable pressure vessels, which were produced by submerged-arc welding using a single V-shaped preparation and multiple weld runs. They have evaluated the weld procedure and cross-weld performance of weldments in 11 and 12 mm on quenched and tempered steel plate before and after post weld heat treatment (PWHT). After PWHT, tensile tests indicate a reduction in the ultimate tensile strength of all samples and a decrease in yield strength for the 12 mm sample only. The hardness results were consistent with the tensile test results because they revealed significant softening in the HAZ and weld pool as a result of PWHT. Additionally, residual stress measurements before and after PWHT showed that PWHT is effective in reducing surface residual stresses to levels low in the elastic range. It is concluded that although PWHT exerts the beneficial effect of reducing residual stresses, the ductility of the weld region is satisfactory without PWHT, and PWHT decreases the cross-weld tensile strength.

A microstructure of the 3D parts, built by rapid prototyping (RP) based on deposition by GTA welding was examined by Jandric et al. [121]. Material used for

building 3D parts was AISI 1018. A new experimental setup was developed which consists of a six-axis robot, a CNC machine, a wire-feeding mechanism, a torch, and a welding power supply. Two sets of experiments were carried out. In the first experiment, since the final microstructure of the steel depends upon its composition and the thermo-mechanical history, the temperature at the locations with different heat-transfer conditions were monitored by thermocouples. The relationships between the geometry of the deposited beads and the welding parameters were developed. The microstructure analysis of fusion and the heat-affected zone was performed. Different heat-transfer conditions cause different cooling rates and, consequently, different microstructures. Thus, all the deposited beads exhibit equiaxed dendrites at the top layer, but different grain sizes within the bead with different conditions. The best microstructure was achieved with samples that have the most uniform heat-transfer conditions at 360º angle. Samples from the second experiment were examined on Vickers micro-hardness tests. The results from all samples showed that layers possess a maximum microhardness at the top deposited layer, while there was a slight decreasing trend towards the middle and the bottom layers. Both experiments proved that 3D parts built in this manner have a uniform microstructure, and there is no porosity or cracks. The obtained results show that RP based on GTA welding can be successfully used for building 3D parts. In order to further improve the quality of deposited layers, it is necessary to adjust the heat input according to the volume of the heat sink, so that the same maximum temperature was achieved across the layers.

Caiazzo et al. [122] have an experimental study carried out on Ti6Al4V using CO_2 laser welding about both the weld bead geometry and mechanical properties. Two different shielding gases (He and Ar) were used and the results obtained illustrated the different behaviors of the welded material both qualitatively (i.e. greater internal defectiveness for Ar) and quantitatively (i.e. greater melting depth for He than for Ar when the welding parameters are equal). Comparison of the geometry weld bead measurement trends highlighted that there is no great difference in these results compared to those obtained using other materials. The micro-hardness values found on the weld bead cross-section underlined a considerable increase, i.e. from 28 to 48%, beginning at the base metal up to the weld pool. These proportional values

were approximately twice those of the micro-hardness increase from the base metal up to HAZ. As regards the parameters and thicknesses used, a low welding speed influence on the mean micro-hardness of the joint was noted, caused by the low thermal conductivity of the alloy. Finally, tensile tests were carried out on two specimen types, i.e. bead on plate (BoP) and butt welds, in order to verify the effectiveness of the choice of welding parameters regardless of the preparation of the edge specimens before welding. As regards the BoP specimens, the diagram of stress–strain shows a similar trend to that of the base metal, while for butt joints, the failure almost always occurred at the beginning of the plastic field, achieving 75% of the mean ultimate strength for the base metal.. The results obtained for the different thicknesses almost emphasized failure that began at the bead foot and spread towards the same bead, HAZ or base metal. This phenomenon is caused by the greater contamination of the joint (in agreement with the higher levels of micro-hardness found) in the bead foot. This necessitates the protection of the joint in the lower side by He. As regards the butt joints, the lower values of UTS can be attributed to an excessive air gap and a non-perfect alignment between the edges to be joined.

Preston et al. [123] have developed a finite element model to predict the evolution of residual stress and distortion which takes into account the history-dependence of the yield stress–temperature response of heat-treatable aluminium alloys during welding. The model was applied to TIG welding of 2024-T3 aluminium alloy, and the residual strain predictions validated using high resolution X-ray synchrotron diffraction. The goal was to capture the influence of the permanent evolution of the microstructure during the thermal cycle with an uncomplicated numerical procedure, while retaining a sound physical basis. Hardness and resistivity measurements after isothermal hold-and-quench experiments were used to identify salient temperatures for zero, partial and full dissolution of the initial hardening precipitates, and the extent of softening – both immediately after welding, and after natural ageing. Based on this data, a numerical procedure for weld modelling was proposed for tracking the different yield responses during heating and cooling based on the peak temperature reached locally. The model also enabled predictions to be made of the hardness profile immediately after welding, which is difficult to measure experimentally. Comparison with the post-

weld naturally aged hardness provided insight into the competition between dissolution and coarsening in the HAZ. The origin of the microstructural softening is secondary as far as residual stress is concerned, but is critical in determining the final strength of the weld.

Canyurt [124], has explain the use of the stochastic search process that is the basis of Genetic Algorithms (GA), in developing the strength value of the welded parts. Non-linear estimation models were developed using Gas. Developed models were validated with experimental data. The Genetic Algorithm Welding Strength Estimation Model (GAWSEM) was developed to estimate the mechanical properties of the welded joint for the brass materials. The effects of five welding design parameters on the strength value using the GAWSEM have been examined. The results indicated that the changes of the gap between the joint parts and the torch angle have a significant effect on the welded joint strength value and the optimum quantity of the shielding gas and the pulse frequencies exist in the tensile strength of welded joints.

Z. Sterjovski et al. [125] have study the effectiveness of three back-propagation ANNs models that predict (i) the impact toughness of quenched and tempered pressure vessel steel exposed to multiple PWHT cycles, (ii) the hardness of the simulated HAZ in pipeline and tap fitting steels after in-service welding and (iii) the hot ductility and hot strength of various microalloyed steels over the temperature range for strand or slab straightening in the continuous casting process. Predicted and actual experimental values for each model were well matched and emphasize the success of applying ANNs in predicting mechanical properties. The capability of ANNs in predicting multiple outputs (hot ductility and hot strength) is also demonstrated. Although the study shows that ANNs can be employed for optimizing steel and process design parameters, some difficulty can arise when inter-relationships exist between input variables. An understanding of the inter-relationships between input variables is essential for interpreting the sensitivity data and optimizing design parameters. ANNs could be used to minimize the need for expensive experimental investigation and/or inspection of steels used in various applications, hence resulting in large economic benefits for organizations.

Amirizad et al. [126] have applied friction stir welding for aluminum matrix composite A356+15%SiCp. Fragmentation of SiC particles and silicon needles existing in eutectic phase as well as their homogenous distribution as a result of stirring with high plastic strains, improve mechanical properties. Modulus of elasticity, yield strength, tensile strength and elongation to failure of the stir zone show an increase in the order of 57%, 26%, 34% and 154% with respect to the base composite, respectively. Finally, considering the results of this research and problems of fusion welding methods for joining metal matrix composites, FSW is proposed as a very suitable alternative for metal matrix composites.

The semi-analytical simulation of the FSW process has been investigated by Heurtier et al. [127], which highlights the thermo-mechanical history of the various material elements of the weld. This original modelling provides the trajectory of each material element of the weld, the strain, strain rates and estimations of the temperatures and micro-hardness in the various weld zones. The micro-hardness profile was calculated with the thermal history and derived from the model and calibration with heat treated samples. A study of the evolution of the micro-hardness profile points to the welding parameters which reduce the inhomogeneties of the fusion area properties; thus, increasing the tool velocity smoothes out the hardness profile close to the fusion area. This improvement was caused by a decrease of the average temperature of the fusion area. Another advantage of the model was the prediction of the oxide distribution after welding to indicate the presence of a weakened zone in the weld.

Yoon et al. [128] have investigated the optimization of friction welding with more reliability and wider application. They have also developed a method to perform in-process real-time weld quality (such as strength and ductility) evaluation using acoustic emission for dissimilar friction welding of nuclear reactor components from JLF-1 and SUS304. Yoon et al. confirmed experimentally that real-time quality evaluation of a weld was possible by the acoustic emission (AE) technique. The main friction welding parameters were selected to ensure good quality welds on the basis of visual examination, tensile tests, and Vickers hardness surveys of the bond of area and heat affected zone (HAZ). The results was experimentally confirmed by considering at 100% weld joint efficiency, weld strength and toughness, that the

optimum friction welding conditions are n = 2000 rpm, P_1 =80MPa, P_2 = 180MPa, t1 = 1–3 s, and t2 = 5 s. It was confirmed by hardness distribution that the fracture of tensile occurred at the hardness valley in JLF-1 steel aside the HAZ.

Sierra et al. [129] have investigate the laser welding of a low carbon steel to a (6016 and 6056) aluminium alloy using key-hole joining mode in a steel-on-aluminium overlap configuration. The welded assemblies were investigated by a material approach involving a microstructural study and chemical analysis, and also by a mechanical approach using a tensile shear test and a specifically dedicated tearing-off test to characterize the Al–steel interface. Embrittlement of the joining zone was observed, mainly located on the weld–aluminium interfaces composed of Fe_2Al_5 and/or $FeAl_3$ phases with thicknesses between 5 μm and 20 μm. Limiting penetration to below 500 μm allowed to restrict steel to aluminium dilution in order to confine the hardness of the welds. With such penetration depths, up to 250 N/mm in linear strength could be achieved, with failures located in the weld–aluminium interfaces. Increasing penetration depth led to a change in the assembly weak points (in the weld and on the steel–weld interfaces) and induced a severe decrease in strength.

The weldability of AA7075 using a hybrid laser/ GMA welding process was inspected by Hu and Richardson [130]. After welding process optimization, the influence of filler wire composition, natural ageing, artificial ageing and a short duration solution heat treatment was considered to improve weld microstructural and mechanical properties. Results show that after a short solution heat treatment, a large fraction of the dendrite boundaries in the weld pool dissolved in the primary phase. Tensile tests and micro-hardness tests show that the weld has a comparable strength to the T6 base alloy when welding with an AA2319 consumable. Fracture surfaces observed under a SEM indicate a large number of fine ductile type voids and larger sized dimples. The improved ductility of the weld together with the strength comparable to the base alloy makes the weld more formable than none solution heat-treated welds.

Tarng et al. [131] have studied the use of grey-based Taguchi methods for the optimization of the submerged arc welding (SAW) process parameters in hard-facing with considerations of multiple weld qualities. In their approach, the grey relational

analysis is adopted to solve the SAW process with multiple weld qualities. A grey relational grade obtained from the grey relational analysis was used as the performance characteristic in the Taguchi method. Then, optimal process parameters were determined by using the parameter design proposed by the Taguchi method. Experimental results have shown that optimal SAW process parameters in hard-facing can be determined effectively so as to improve multiple weld qualities through this new approach.

2.9 Microstructure

Welding process is resulting in three distinct regions in the weldment. These are the fusion area (FA), also known as the weld metal, the heat-affected zone (HAZ), and the unaffected base metal (BM). The FA experiences melting and solidification, and its microstructural characteristics are directly affecting the welding quality. The microstructure growth in the FA depends on the solidification behaviour of the weld pool. The principles of solidification control the size and shape of the grains, segregation, and the distribution of inclusions and porosity. Solidification is also critical to the hot-cracking behaviour of alloys. FA can be considered as mini-casting region. Therefore, parameters important in determining microstructures in casting, such as growth rate, temperature gradient, under cooling, and alloy composition determine the development of microstructures in welds as well. But unlike in casting, during welding, where the molten pool is moved through the material, the growth rate and temperature gradient vary considerably across the weld pool. In welds, weld pool solidification often occurs without a nucleation barrier. Therefore, no significant under-cooling of the liquid is required for nucleation of the solid. Solidification occurs instinctively by epitaxial growth (the growth of one layer of crystals on another such that they have the same structure) on the partially melted grains during autogenous welding. Generally, weld solidification models assume epitaxial growth and for most of the cases the assumption seems to be appropriate. The heat, fluid-flow models and modelling techniques now available can help describe the phase evolution during weld solidification.

Li and Fontana [21] have adopted a laser-welding technique for the fabrication of the hydraulic valves, in which the butt welds joining the AISI304L to the AISI12L13 were performed in such a way as to control solidification cracking and micro-fissuring. Metallurgical analyses revealed that both solidification cracking in the fusion zone and micro-fissuring in the heat-affected zone result from S, Pb and P contained in the AISI12L13. The relationships between the redistribution of elements in the fusion zone, the welding parameters, and the microstructures were investigated. A 0.12 mm off-set of the laser beam towards the AISI304L and an impingement angle of 15° with respect to the fit-up face of the butt joints can produce sound welds on the hydraulic valves made of 0.9 mm thick AISI304L and AISI12L13. Tests of the mechanical properties of the hydraulic valves revealed good-strength welds, high repeatability, and reliability of the welding parameters adopted. The results provided a contribution to overcoming problems of dissimilar fusion joints, where one of two materials was unweldable, by the application of the laser welding technique.

Zhang et al. [132], have explored a new modelling approach for aluminium weldments. In the approach, the microstructure data calculated from welding analysis are directly transferred to the deformation and damage analysis. With an interpolation equation between the properties of the base metal and the fully reverted HAZ, the exact dimension and gradient of mechanical properties of the whole HAZ are automatically predicted. The overall effect of the microstructure evolution during welding, and the resulting deformation and damage capacity of the welded joint can then be analyzed. This approach has been applied in two case studies, one cross weld tensile specimen, which was used for the parameter study, and one real T-joint from which test data were available. With a linear interpolation for the flow stress and ductile damage parameter, the finite element results based on this approach were in good agreement with the test data.

Evolution of the microstructure in AISI 1005 steel weldments was studied during GTA welding experimentally and theoretically by Zhang et al. [133]. The experimental work involved real-time mapping of phases in the HAZ using a synchrotron-based spatially resolved X-ray diffraction (SRXRD) technique and post weld microstructural characterization of the fusion zone (FZ). A three-dimensional

heat transfer and fluid flow model was used to calculate the temperature and velocity fields, thermal cycles, and the geometry of the FZ and the HAZ. The experimental SRXRD phase map and the computed thermal cycles were used to determine the kinetic parameters in the Johnson–Mehl–Avrami (JMA) equation for the ferrite to austenite transformation during heating in the HAZ. Apart from providing a quantitative expression for the kinetics of this transformation, the results are consistent with a decreasing nucleation rate of austenite from a ferrite matrix with time. In the FZ, the volume fractions of micro-constituents were calculated using an existing phase transformation model and the computed thermal cycles. Good agreement was found between the calculated and experimental volume fractions of allotriomorphic and widmanstatten ferrites in the FZ. The results indicate significant promise for understanding microstructure evolution during GTA welding of AISI 1005 steel by a combination of real time phase mapping and modelling.

A one-dimensional numerical diffusion model has been developed by Zhang et al. [134] to simulate the kinetics of the austenite (γ) to ferrite (δ) transformation in 2205 duplex stainless steel during welding. In the model, it was assumed that the transformation is driven by the diffusion of nitrogen under Para-equilibrium conditions. Transformation kinetics from both uniform and non-uniform starting microstructures was investigated. The uniform starting structure was accounted for by using a pair of γ and δ grains of constant sizes, whereas non-uniform structures were simulated by considering four γ and δ grains of varying sizes. Interactions between neighboring grains, particularly hard and soft impingements, are taken into account by properly adjusting the boundary conditions. It is found that the transformation may take 30% more time for the non-uniform starting microstructure, where the ratio of thickest to thinnest grains is about 2, than for the uniform structure under typical weld heating conditions. Time–temperature-transformation and continuous-heating-transformation diagrams were constructed using the numerical diffusion model, providing a graphical means for predicting the kinetics of the $\gamma \rightarrow \delta$ transformation. The computed results were confirmed by experiments using an in-situ X-ray diffraction technique, thus validating the model.

Karimzadeh et al. [135] have studied the effect of epitaxial growth on microstructure of Ti–6Al–4V alloy weldment using an artificial neural network

(ANN). The microplasma arc welding (MPAW) procedure was performed at different currents, welding speeds and flow rates of shielding and plasma gas. Microstructural characterizations were studied by optical and scanning electron microscopy (SEM). An artificial neural network was developed to predict grain size of FZ at different currents and welding speeds. The results showed that a coarse primary β phase develops in the fusion zone as a result of epitaxial nucleation on coarsened β grains near the heat affected zone (NHAZ) which grow competitively into the molten weld pool. Based on ANN analyses, a map of current and welding speed for α → β transformation in the HAZ can be constructed. For a lower energy input, grain growth of β phase in the HAZ could be restricted by α phase. The presence of small quantities of this phase at high peak temperatures in the weld cycle is sufficient to prevent the grain growth of β phase in HAZ and FZ.

A combined modelling approach based on the Kampmann and Wagner method was applied by Kamp et al. [136,137] to predict the behaviour of high strength 7xxx aluminium alloys. Thermal modelling, microstructure modelling and strength modelling were performed in succession to give some insight into the complex precipitation mechanism occurring during FSW. A quantitative assessment of a recent numerical model to predict the evolution of the precipitate distribution was performed for a high strength 7449 aluminium alloy subjected to a FSW process. An optimized model calibration procedure was also presented for the 7449 alloy. The robustness of this calibration was then tested by applying the model to a different 7xxx series alloy. The predicted microstructures are found to be in good quantitative agreement with the characterized experimental microstructures. The model has also been used to investigate the effect of different FSW parameters on the predicted precipitate evolution. Predicted precipitate distributions were used to estimate the strength of the material. These predictions generally agreed well with measured hardness values.

2.10 Summary of Literature Review

According to the literature review, dissimilar metals welding using LBW have been a subject of interest in recent years. Due to special features of LBW, e.g., high energy density and accurately controllable beam size and location, in many cases it

has proven to be an efficient way of joining dissimilar metals. Numerous successful results have been achieved, and some of them have already been exploited in production. LBW continues to be the subject of investigations and further development and improvements in the joining of dissimilar metals remains one of the aims. Even many studies have been performed; there is still a considerable need to further examine existing and new combinations. Therefore, studies of the availability and optimization of different dissimilar ferrous and non ferrous metals are highlighted in this research. Whereas conventional techniques (experimental techniques that include statistical design of experiment, such as Taguchi method) were attempt to provide an optimal solution. For this purpose a comprehensive knowledge about the application of DOE inspired by the Taguchi method and statistical analysis are provided in next chapter. Chapter three also explains how the DOE and Taguchi method were used for optimization of the welding process.

CHAPTER 3

3. DESIGN OF EXPERIMENTS AND OPTIMIZATION

3.1 Design of Experiment

DOE is a systematic approach for investigation of a system or process. A series of structured tests are designed in which planned changes are made to the input variables of a process or system. The effects of these changes on a pre-defined output are then assessed. DOE is important as a formal way of maximizing information gained while minimizing resources required. It has more to offer than 'one change at a time' experimental methods, because it allows a judgment on the significance to the output of input variables acting alone, as well input variables acting in combination with one another.

'One change at a time' testing always carries the risk that the experimenter may find one input variable to have a significant effect on the response (output) while failing to discover that changing another variable may alter the effect of the first (i.e. some kind of dependency or interaction). This is because the temptation is to stop the test when this first significant effect has been found. In order to reveal an interaction or dependency, 'one change at a time' testing relies on the experimenter carrying the tests in the appropriate direction. However, DOE plans for all possible dependencies in the first place, and then prescribes exactly what data are needed to assess them i.e. whether input variables change the response on their own, when combined, or not at all. In terms of resource the exact length and size of the experiment are set by the design (i.e. before testing begins) [138]. DOE can be used to find answers in situations such as "what is the main contributing factor to a problem?", "how well does the system/process perform in the presence of noise?", "what is the best configuration of factor values to minimize variation in a response?" etc. In general, these questions are given labels as particular types of studies. In the examples given above, these are problem solving, parameter design and robustness studies. In each case, DOE is used to find the answer; the only thing that makes them different is factors used in the experiment [139].

The order of tasks to using this tool starts with identifying the input variables and the response (output) that is to be measured. For each input variable, a number of levels are defined that represent the range for which the effect of that variable is desired to be known. An experimental plan is produced which tells the experimenter where to set each test parameter for each run of the test. The response is then measured for each run. The method of analysis is to look for differences between response (output) readings for different groups of the input changes. These differences are then attributed to the input variables acting alone (called a single effect) or in combination with another input variable (called an interaction).

DOE is team oriented and a variety of backgrounds (e.g. design, manufacturing, statistics etc.) should be involved when identifying factors and levels and developing the matrix as this is the most skilled part. Moreover, as this tool is used to answer specific questions, the team should have a clear understanding of the difference between control and noise factors.

It is very important to get the most information from each experiment performed. Well-designed experiments can produce significantly more information and often require fewer runs than haphazard or unplanned experiments. In addition, a well-designed experiment will ensure that the evaluation of the effects that had been identified as important. For example, if there is an interaction between two input variables, both variables should be included in the design rather than doing a 'one factor at a time' experiment. An interaction occurs when the effect of one input variable is influenced by the level of another input variable. Designed experiments are often carried out in four phases: planning, screening (also called process characterization), optimization, and verification.

3.1.1 Planning

Careful planning helps to avoid problems that can occur during the execution of the experimental plan. For example, personnel, equipment availability, funding, and the mechanical aspects of the system may affect the ability to complete the experiment. The preparation required before beginning experimentation depends on the nature of the problem. The following are some of the steps that may be necessary.

Problem Definition: Developing a good problem statement helps make sure that the correct variables are studied. At this step, the questions that need to be answered are identified.

Objective Definition: A well-defined objective will ensure that the experiment answers the right questions and yields practical, usable information. At this step, the goals of the experiment will be defined.

Develop an experimental plan that will provide meaningful information: At this step it is necessary to make sure that the relevant background information has been reviewed, such as theoretical principles, and knowledge gained through observation or previous experimentation. For example, you may need to identify which factors or process conditions affect process performance and contribute to process variability. Or, if the process is already established and the influential factors have been identified, it may be necessary to determine the optimal process conditions.

Making sure the process and measurement systems are in control: Ideally, both the process and the measurements should be in statistical control as measured by a functioning statistical process control (SPC) system. Even if it does not have the process completely in control, it must be able to reproduce process settings. Also, it is necessary to determine the variability in the measurement system.

3.1.2 Screening

In many process development and manufacturing applications, potentially influential variables are numerous. Screening reduces the number of variables by identifying the key variables that affect product quality. This reduction allows process improvement efforts to be focused on the really important variables, or the "vital few." Screening may also suggest the "best" or optimal settings for these factors, and indicate whether or not curvature exists in the responses. Then, it can use optimization methods to determine the best settings and define the nature of the curvature.

Two-level full and fractional factorial designs are used extensively in industry.

Plackett-Burman designs have low resolution, but their usefulness in some screening experimentation and robustness testing is widely recognized.

General full factorial designs (designs with more than two-levels) may also be useful for small screening experiments.

3.1.3 Optimization

Next step after identified the "vital few" by screening, the "best" or optimal values for these experimental factors needed to be determine. Optimal factor values depend on the process objective. For example, maximize the welding speed and minimize the laser power. The optimization methods available in "Design Expert 7" [140] software used in this research, include general full factorial designs (designs with more than two-levels), response surface designs, mixture designs, and Taguchi designs.

3.1.4 Verification

Verification involves performing a follow-up experiment at the predicted "best" processing conditions to confirm the optimization results. For example, in this study for each developed model three confirmation experiments were performed at the optimal settings and a confidence interval was then obtained for the mean response.

3.2 Taguchi Design

3.2.1 Overview

Dr. Genichi Taguchi is regarded as the foremost proponent of robust parameter design, which is an engineering method for product or process design that focuses on minimizing variation and/or sensitivity to noise. When used properly, Taguchi designs provide a powerful and efficient method for designing products that operate consistently and optimally over a variety of conditions. In robust parameter design, the primary goal is to find factor settings that minimize response variation, while adjusting (or keeping) the process on target. When the factors affecting variation have been determined, it could be used to find settings for controllable factors that

will either reduce the variation, make the product insensitive to changes in uncontrollable (noise) factors, or both. A process designed with this goal will produce more consistent output [141]. A product designed with this goal will deliver more consistent performance regardless of the environment in which it is used. Engineering knowledge should guide the selection of factors and responses [142].

3.2.2 The Fundamental Terms Used in Taguchi Design

3.2.2.1 Orthogonal arrays

The Taguchi method utilizes orthogonal arrays from design of experiments theory to study a large number of variables with a small number of experiments. Using orthogonal arrays significantly reduces the number of experimental configurations to be studied. Furthermore, the conclusions drawn from small scale experiments are valid over the entire experimental region spanned by the control factors and their settings [143]

Orthogonal arrays are not unique to Taguchi. They were discovered considerably earlier [144]. However, Taguchi has simplified their use by providing tabulated sets of standard orthogonal arrays and corresponding linear graphs to fit specific projects [145].

Examples of standard orthogonal arrays:

L-4, L-8, L-12, L-16, L-32 and L-64	all at 2 levels
L-9, L-18 and L-27	at 3 & 2 levels
L-16 and L-32	modified at 4 levels
L-25	at 5 levels

Standard notations for orthogonal arrays:

L-16 (3 5), 16 = Number of experiments
3 = Number of levels
5 = Number of factors

To select an appropriate orthogonal array for the experiments, the total degrees of freedom need to be computed. The degrees of freedom are defined as the number of comparisons between process parameters that need to be made to determine which level is better and specifically how much better it is. For example, a two-level process parameter counts for one degree of freedom. The degrees of freedom

associated with interaction between two process parameters are given by the product of the degrees of freedom for the two process parameters. In the present study, the interaction between the laser welding parameters is considered.

Once the degrees of freedom are known, the next step is selecting an appropriate orthogonal array to fit the specific task. The degrees of freedom for the orthogonal array should be greater than or at least equal to those for the process parameters [146]. The tabulations of the typical orthogonal arrays used in this research with coded values are shown in Tables 3.1 and 3.2.

Table 3.1: Typical L16 orthogonal array with coded value

Std	Run	Factor 1	Factor 2	Factor 3	Factor 4	Factor 5	Response 1
1	1	1	1	1	1	1	
6	2	2	2	1	4	3	
8	3	2	4	3	2	1	
2	4	1	2	2	2	2	
5	5	2	1	2	3	4	
4	6	1	4	4	4	4	
10	7	3	2	4	3	1	
15	8	4	3	2	4	1	
16	9	4	4	1	3	2	
14	10	4	2	3	1	4	
13	11	4	1	4	2	3	
7	12	2	3	4	1	2	
12	13	3	4	2	1	3	
11	14	3	3	1	2	4	
3	15	1	3	3	3	3	
9	16	3	1	3	4	2	

Table 3.2: Typical L25 orthogonal array with coded values

Std	Run	Factor 1	Factor 2	Factor 3	Factor 4	Factor 5	Factor 6	Response 1
14	1	3	4	1	3	5	2	
11	2	3	1	3	5	2	4	
8	3	2	3	4	5	1	2	
25	4	5	5	4	3	2	1	
23	5	5	3	2	1	5	4	
3	6	1	3	3	3	3	3	
4	7	1	4	4	4	4	4	
24	8	5	4	3	2	1	5	
18	9	4	3	1	4	2	5	
2	10	1	2	2	2	2	2	
16	11	4	1	4	2	5	3	
10	12	2	5	1	2	3	4	
1	13	1	1	1	1	1	1	
22	14	5	2	1	5	4	3	
15	15	3	5	2	4	1	3	
7	16	2	2	3	4	5	1	
5	17	1	5	5	5	5	5	
6	18	2	1	2	3	4	5	
12	19	3	2	4	1	3	5	
19	20	4	4	2	5	3	1	
17	21	4	2	5	3	1	4	
21	22	5	1	5	4	3	2	
13	23	3	3	5	2	4	1	
9	24	2	4	5	1	2	3	
20	25	4	5	3	1	4	2	

3.2.2.2 S/N ratios and MSD analysis

Taguchi recommends the use of signal to noise ratio (S/N) as opposed to simple process optimizing process parameters. The rationale is that while there is a need to maximize the mean (signal) in the sense of its proximity to nominal value, it is also desirable to minimize the process variations (noise). The use of S/N accomplishes both objectives simultaneously [147].

In order to evaluate the influence of each selected factor on the responses: The S/N for each control factor should be calculated. The signals have indicated that the effect on the average responses and the noises were measured by the influence on the deviations from the average responses, which would indicate the sensitiveness of the experiment output to the noise factors.

The appropriate S/N ratio must be chosen using previous knowledge, expertise, and understanding of the process. When the target is fixed and there is a trivial or absent signal factor (static design), it is possible to choose the S/N ratio depending on the goal of the design. S/N ratio selection is based on Mean Squared Deviation (MSD) for analysis of repeated results. MSD expression combines variation around the given target and is consistent with Taguchi's quality objective [148]. The relationships among observed results, MSD and S/N ratios are as follows (3.1 to 3.4) [149]:

$$\text{MSD} = \frac{\left(\left(Y_1 - \overline{Y}\right)^2 + \left(Y_2 - \overline{Y}\right)^2 + ...\left(Y_n - \overline{Y}\right)^2\right)}{n} \quad \text{…For nominal is better} \quad \textbf{... (3.1)}$$

$$\text{MSD} = \frac{\left(Y_1^2 + Y_2^2 + ... + Y_n^2\right)}{n} \quad \text{… For smaller is better} \quad \textbf{... (3.2)}$$

$$\text{MSD} = \frac{\left(\frac{1}{Y_1^2} + \frac{1}{Y_2^2} + ... \frac{1}{Y_n^2}\right)}{n} \quad \text{... For bigger is better} \quad \textbf{... (3.3)}$$

$$\text{S/N} = -\ 10\text{Log (MSD)} \quad \text{… For all characteristic} \quad \textbf{... (3.4)}$$

3.2.2.3 Analysis of variance (ANOVA)

Analysis of variance (ANalysis Of VAriance) is a general method for studying sampled-data relationships [150,151]. The method enables the difference between two or more sample means to be analyzed, achieved by subdividing the total sum of

squares. One way ANOVA is the simplest case. The purpose is to test for significant differences between class means, and this is done by analyzing the variances. Analysis of variance (ANOVA) is similar to regression in that it is used to investigate and model the relationship between a response variable and one or more independent variables. In effect, analysis of variance extends the two-sample t-test for testing the equality of two population means to a more general null hypothesis of comparing the equality of more than two means, versus those that are not all equal [152]. Table 3.3 is a sample of the ANOVA Table used for analysis of the models developed in this work. Sum of squares and mean square errors are calculated using Eq. 3.5 to 3.8 [153,154].

Table 3.3: Sample ANOVA Table for a model

Source	**SS**	***df***	**MS**	**F_v – Value**	**Prob.> F_v**
Model	SSM	p	Each SS Divided by Its *df*	Each MS Divided by MSE	From Table or automatically from the software
P	SS1	1			
S	SS2	1			
F	SS3	1			
PS	SS12	1			
PF	SS13	1			
SF	SS23	1			
P^2	SS11	1			
S^2	SS22	1			
F^2	SS33	1			
Residual (Error)	SSE	$n - p - 1$		-	-
Cor. Total	SSt	$n - 1$	-	-	-

Where; p: Number of coefficients in the model,

df: Degree of freedom, SS: Sum of squares, MS: Mean squares,

n: total number of runs (For this work n =16 or 25)

Cor. Total: Sum of squares total corrected for the mean.

$$SSM = \sum_{i=1}^{n} (\hat{Y}_i - \overline{Y})^2 \quad \text{… (3.5)}$$

$$SSr = \sum_{i=1}^{n} (Y_i - \hat{Y}_i)^2 \quad \text{… (3.6)}$$

$$SSt = \sum_{i=1}^{n} (Y_i - \overline{Y})^2 \quad \text{… (3.7)}$$

$$MSE = \frac{SS_E}{df} \quad \text{… (3.8)}$$

3.3 Optimization

The optimization will allow the industrial user to achieve the optimum welding composition and process parameter to achieve the desired weld pool shape and mechanical properties. All independent variables are measurable and can be repeated with negligible error. The objective function can be represented by:

$$\text{Objective} = f(x_1, x_2, \ldots, x_n) \quad \text{... (3.9)}$$

Where: n is the number of independent variables.

3.3.1 Determination of Optimal or Near-Optimal Welding Condition(s)

With time, complexity in welding process dynamics has increased and as a consequence, problems related to determination of optimal or near-optimal welding condition(s) are faced with discrete and continuous parameter spaces with multi-model, differentiable as well as non-differentiable objective function or response(s). Search for optimal or acceptable near-optimal solution(s) by a suitable optimization technique based on input–output and in-process parameter relationship or objective function formulated from model(s) with or without constraint(s), is a critical and difficult task for researchers and practitioners [155, 156 ,157]. A large number of techniques have been developed by researchers to solve these types of parameter optimization problems, and may be classified as conventional and nonconventional optimization techniques. Fig. 1 provides a general classification of parameters relationships modelling and optimization techniques in welding.

Whereas conventional techniques attempt to provide a local optimal solution, non-conventional techniques based on extrinsic model or objective function development, are only an approximation, and attempt to provide near-optimal welding condition(s). Conventional techniques may be broadly classified into two categories. In the first category, experimental techniques that include statistical design of experiment, such as Taguchi method, and response surface design methodology (RSM) are referred to. In the second category, iterative mathematical search techniques, such as linear programming (LP), non-linear programming (NLP), and dynamic programming (DP) algorithms are included.

Non-conventional meta-heuristic search-based techniques, which are sufficiently general and extensively used by researchers in recent times are based on genetic algorithm (GA), tabu search (TS), and simulated annealing (SA).

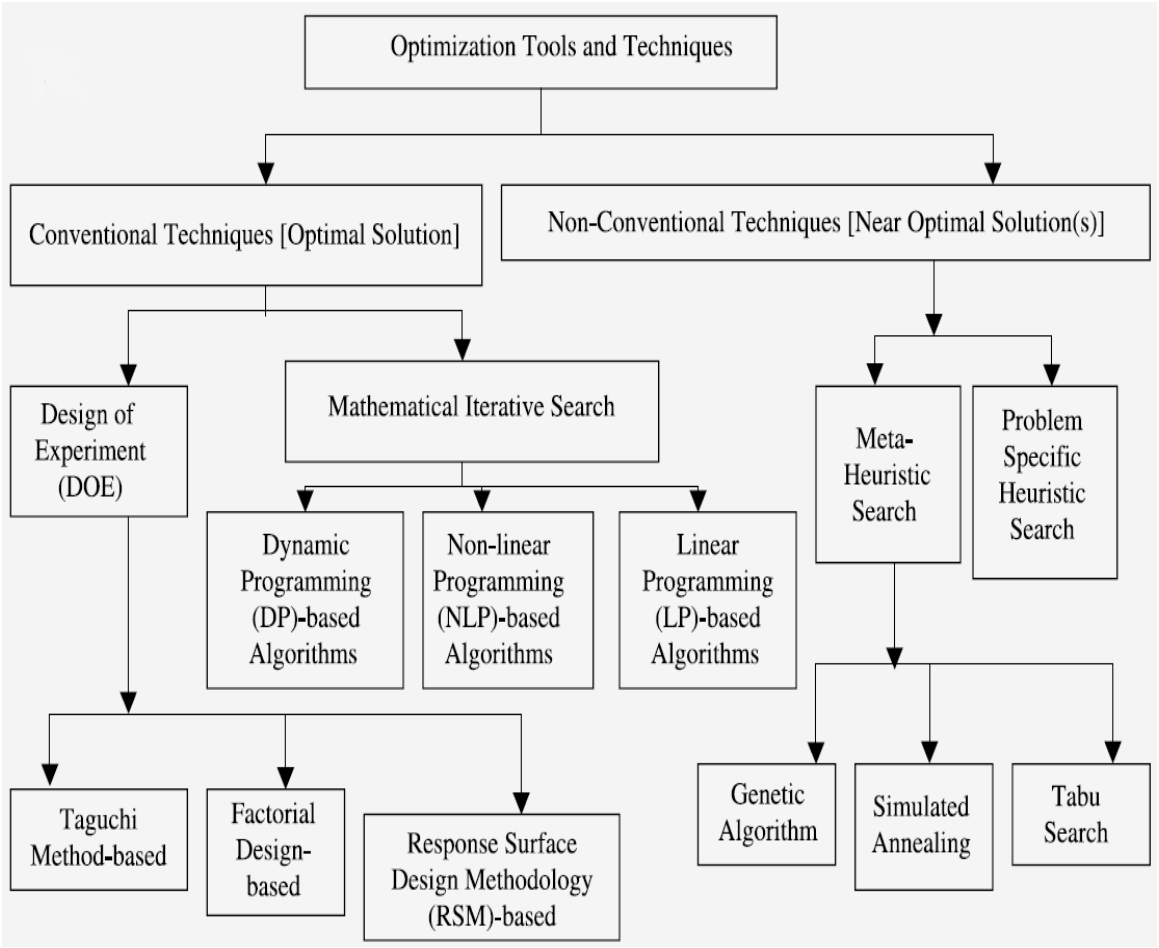

Fig. 3.1: Classification of modeling and optimization techniques in welding problems [158].

3.3.2 Desirability Approach

The desirability function approach is one of the most widely used methods in industry for the optimization of multiple response processes. It is based on the idea that the "quality" of a product or process that has multiple quality characteristics, with one of them outside of some "desired" limits, is completely unacceptable. The method finds operating conditions ***x*** that provide the "most desirable" response values. The goal of optimization is to find a good set of conditions that will meet all the goals, not to get to a desirability value of 1.0.

For each response **Yi(x)**, a desirability function **di(Yi)** assigns numbers between 0 and 1 to the possible values of **Yi**, with **di(Yi) = 0** representing a completely undesirable value of **Yi** and **di(Yi) = 1** representing a completely desirable or ideal response value [159]. The individual desirabilities are then combined using the geometric mean, which gives the overall desirability D:

$$D = (d_1 \times d_2 \times \ldots \times d_n)^{\frac{1}{n}} = \left(\prod_{i=1}^{n} d_i \right)^{\frac{1}{n}} \quad \textbf{... (3.10)}$$

Where: n is the number of responses in the measure. If any of the responses or factors falls outside their desirability range, the overall function becomes zero.

Depending on whether a particular response ***Yi*** is to be maximized, minimized, or assigned a target value, different desirability functions ***di*(*Yi*)** can be used. A useful class of desirability functions was proposed by Derringer and Suich [160]. Let ***Li, Ui*** and ***Ti*** be the lower, upper, and target values, respectively, that are desired for response ***Yi***, with $Li \leq Ti \leq Ui$. In this work the individual desirability (using Eqs. 3.11-3.14) [161] for each response **(di)** was calculated. The shape of the desirability for each goal can be changed by the "weight" field. Weights are used to give added emphasis to the upper/lower bounds, or to emphasize the target value. With a weight of 1 the **di** will vary from 0 to 1 in a linear fashion. Weights greater than 1 (maximum weight is 10), give more emphasis to the goal. Weights less than 1 (minimum weight is 0.1), give less emphasis to the goal.

In the desirability objective function **D(X),** each response can be assigned an importance relative to the other responses. Importance (**ri)** varies from the least

important (+) a value of 1, to the most important (+++++) a value of 5. If varying degrees of importance are assigned to the different responses, the objective function is shown below Eq. 3.11:

$$D = \left(d_1^{r_1} \times d_1^{r_2} \times \ldots \times d_1^{r_n}\right)^{\frac{1}{\Sigma r_i}} = \left(\prod_{i=1}^{n} d_i^{r_i}\right)^{\frac{1}{\Sigma r_i}} \quad \text{...(3.11)}$$

Where: n is the number of responses in the measure. If all the importance values are the same, the simultaneous objective function reduces to the normal form for desirability [140].

If a response is of the "target is best" kind, then its individual desirability function is:

$$d_i(\hat{Y}_i) = \begin{cases} 0 & \text{if } \hat{Y}_i(x) < L_i \\ \left(\frac{\hat{Y}_i(x) - L_i}{T_i - L_i}\right)^s & \text{if } L_i \le \hat{Y}_i(x) \le T_i \\ \left(\frac{\hat{Y}_i(x) - U_i}{T_i - U_i}\right)^t & \text{if } T_i \le \hat{Y}_i(x) \le U_i \\ 0 & \text{if } \hat{Y}_i(x) > U_i \end{cases} \quad \text{... (3.12)}$$

Where: The exponents (s) and (t) determine how important it is to hit the target value. For **s = t = 1**, the desirability function increases linearly towards **Ti;**

for **s < 1, t < 1**, the function is convex, and

for **s > 1, t > 1,** the function is concave.

If a response is to be maximized, the individual desirability is defined as:

$$d_i(\hat{Y}_i) = \begin{cases} 0 & \text{if } \hat{Y}_i(x) < L_i \\ \left(\frac{\hat{Y}_i(x) - L_i}{T_i - L_i}\right)^s & \text{if } L_i \le \hat{Y}_i(x) \le T_i \\ 1.0 & \text{if } \hat{Y}_i(x) > T_i \end{cases} \quad \text{...(3.13)}$$

Where: **T*i*** in this case interpreted as a large enough value for the response.

If a response is to be minimized, the individual desirability is defined as:

$$d_i(\hat{Y}_i) = \begin{cases} 1.0 & \text{if } \hat{Y}_i(e) < T_i \\ \left(\frac{\hat{Y}_i(e) - U_i}{T_i - U_i}\right)^s & \text{if } T_i \le \hat{Y}_i(e) \le U_i \\ 0 & \text{if } \hat{Y}_i(e) > U_i \end{cases} \quad \text{...(3.14)}$$

Where: **T*i*** denoting a small enough value for the response.

3.3.3 Optimization by Means of Design Expert Software

The optimization module in Design-Expert searches for a combination of factor levels that simultaneously satisfy the requirements placed on each of the responses and factors. Optimizations of responses were performed in this work numerically by choosing the desired goals for each factor. The desired goal for each factor and response can be selected from the menu in the used software. The possible goals are: maximize, minimize, target, within range, none (for responses only) and set to an exact value (factors only). A minimum and a maximum level were provided for each parameter. A weight can be assigned to each goal to adjust the shape of its particular desirability function. The "importance" of each goal can be changed in relation to the other goals. The default is for all goals to be equally important at a setting of 3 pluses (+++). A goal with most important, could be changed up to 5 pluses (+++++) [140].

3.4 Experimental Procedure

The Taguchi method is used to improve the quality of welded components. Improved quality results when a higher level of performance is consistently obtained. The highest possible performance is obtained by determining the optimum combination of design factors. The consistency of performance is obtained by

making the process insensitive to the influence of the uncontrollable factor. In Taguchi's approach, optimum design is determined by using design of experiment principles, and consistency of performance is achieved by carrying out the trial conditions under the influence of the noise factors.

The following steps are performed in order to develop and optimize a mathematical model in case of dissimilar laser welding.

3.4.1 Planning Experiments (Brainstorming)

This is a first step in any application. The session should include individuals with first hand knowledge of the project. The literature review covers this step.

- Determine the vital process factors in this study; the laser welding variables were determined from the literature review.

- Identify all influencing factors and those to be included in the study. The selected welding parameters for this study are: welding power, welding speed, focus point position and gap between the plates to be jointed in some butt welding experiments.

- Determine the factor levels. Before determining the factor levels the operating range has been determined through a pilot experiment which is carried out by changing one factor at time. Visual inspections were carried out and the criteria selected for accepting the applicable range were; the absence of welding defects, a continuous, smooth and uniform welding line and in some experiments a full depth penetration were decided. Once the operating range was determined, Design-Expert 7 software was used to divide the operating range into levels according to the selected design. Three and five levels were chosen depending on a select orthogonal array.

3.4.2 Designing Experiments

Using the factors and levels determined in the previous step, the experiments now can be designed and the method carrying them out established. To design the experiment, implement the following:

- Select the appropriate orthogonal array.

In the present study, the interaction between the welding parameters is considered. Therefore, degrees of freedom owing to the three and four sets of five-level and four-levels welding process parameters were evaluated. The degrees of freedom for the orthogonal array should be greater than or at least equal to those for the process parameters. In this study, L25 and L16 orthogonal arrays with three columns and 25 and 16 rows respectively were used. Those arrays have sufficient degrees of freedom to handle five-level and four-level process parameters. Twenty-five level experiments were required to study the welding parameters using L25 orthogonal array. Sixteen four-level experiments were required to study the welding parameters using L16 orthogonal array. "Design Expert 7" software was used for designing the matrices for each experiment in random order.

3.4.3 Running Experiment

All the experiments of laser welding were carried out (during joining process only) in random order of the developed matrices by the software to avoid any systematic error during the experiments. After the joining process the responses, mentioned earlier in this work, were tested and measured in sequential order following the standard procedures when available for each response. An average of at least three (in most cases) recorded measurements is calculated and considered for more analysis.

3.4.4 Analyzing Results

Before analysis, the raw experimental data might have to be combined into an overall evaluation criterion. This is particularly true when there are multiple criteria of evaluation.

Analysis is performed to determine the following:

- The optimum design.
- Influence of individual factors.
- Performance at the optimum condition.
- Relative influence of individual factors.

The steps in this analyzing stage are followed in this sequence:

3.4.4.1 Developing the mathematical model

Design expert software develops and exhibits the possible modules which can fit input data and suggest the model that best fits the experiment data.

3.4.4.2 Estimating of the coefficients of the model independent factors

Regression analysis is carried out by software to estimate the coefficients for all factors in each experiment.

3.4.4.3 The Signal-to-noise (S/N) ratio analysis

A signal to noise ratio in the ANOVA Table is presented as an Adequate Precision. Equations 3.15 and 3.16 are applied to the model to compares the range of the predicted values at the design points to the average prediction error. Ratios greater than 4 indicate adequate model discrimination.

$$\text{Adequate Precision} \rangle \left[\frac{\max(\hat{Y}) - \min(\hat{Y})}{\sqrt{\bar{V}(\hat{Y})}} \right] \rangle 4 \qquad \textbf{... (3.15)}$$

$$\bar{V}(\hat{Y}) = \frac{1}{n} \sum_{i=1}^{n} V(\bar{Y}) \frac{P\sigma^2}{n} \qquad \textbf{... (3.16)}$$

P = number of model parameters, σ^2 = residual MS from ANOVA table, n = number of experiments.

3.4.4.4 ANOVA *Outputs*

The analyses of variances (ANOVA) were applied to test adequacy of the developed models. Each term in developed models was examined by the following statistical significance tools using Eq. 3.15 - 3.20 [140]:

F_v value: Test for comparing model variance with residual (error) variance. When the variances are close to each other, the ratio will be close to one and it is less likely that any of the factors have a significant effect on the response. Model F_v-Value and associated probability value (Prob. > F_v) to confirm model significance. F_v value is calculated by term mean square divided by residual mean square.

Prob. > F_v: Probability of seeing the observed F_v value if the null hypothesis is true (there is no factor effect). If the Prob. > F_v of the model and/or of each term in the model does not exceed the level of significance (for chosen $\alpha = 0.05$ in this work) then the model can be considered adequate within the confidence interval (1 - α).

Precision of a parameter estimate is based on the number of independent samples of information which can be determined by degree of freedom (df).

Degree of Freedom (df): the degree of freedom equals to the number of experiments minus the number of additional parameters estimated for that calculation.

The same tables show also the other adequacy measures R^2, adjusted R^2 and adequacy precision R^2 for each response. In this study, all adequacy measures were close to 1, which indicates adequate models.

The Adequate Precision compares the range of the predicted value at the design points to the average predicted error. The adequate precision ratio above 4 indicates adequate model discrimination. In this study, the values of adequate precision are significantly greater than 4.

$$R^2 = 1 - \frac{SS_r}{SS_M + SS_r} \quad \textbf{…(3.17)}$$

$$Adj.\ R^2 = \left(\frac{n-1}{n-p}\right)\left(1 - R^2\right) \quad \textbf{…(3.18)}$$

$$Predicted\ R^2 = 1 - \left(\frac{PRESS}{SS_r + SS_M}\right) \quad \textbf{…(3.19)}$$

$$PRESS = \sum_{i=1}^{n}\left(Y_i - \hat{Y}_{i,-i}\right)^2 \quad \textbf{…(3.20)}$$

3.4.4.5 Model reduction

Model reduction consists of eliminating those terms that are not desired or which are statistically insignificant. In this case it was done automatically by the software used. For each response regression the starting model can be edited by specifying fewer candidate terms than the full model would contain. In the three

automatic regression variations, those terms which are forced into the model regardless of their entry/exit α values could be controlled. There are three basic types of automatic model regression:

Step-Wise: A term is added, eliminated or exchanged at each step. Step-wise regression is a combination of forward and backward regressions.

Backward elimination: A term is eliminated at each step. The backward method may be the most robust choice since all model terms will be given a chance of inclusion in the model. Conversely, the forward selection procedure starts with a minimal core model, thus some terms never get included.

Forward selection: A term is added at each step.

3.4.4.6 Development of final model form

The program automatically defaults to the "Suggested" polynomial model which best fits the criteria discussed in the Fit Summary section. The responses could be predicted at any midpoints using the adequate model. Also, essential plots, such as Contour, 3D surface, and perturbation plots of the desirability function at each optimum can be used to explore the function in the factor space. Also, any individual response may be graphed to show the optimum point.

3.4.5 Running Confirmation Experiments

The final step is to predict and verify the improvement of the response using the optimal level of the welding process parameters. In addition, to verify the satisfactoriness of the developed models, at least three confirmation experiments were carried out using new test conditions at optimal parameters conditions, obtained using the Design Expert software.

CHAPTER 4

4. MATERIAL AND EXPERIMENTAL WORK

4.1 Materials

4.1.1 Materials Specifications

The materials selected to be jointed by CO_2 laser welding and subjected to this study can be classified as following:

Ferrous Materials:

- Stainless steel 316

Thicknesses of used plates are 1, 2, and 3 mm. Length and width of the plates 160 x 80 mm.

- Low carbon steel AISI 1008 Cold drawing

Thicknesses of used plates are 1.5 and 2 mm. Length and width of the plates 160 x 80 mm.

- Low carbon steel Din: en 131 Cold drawing

Thicknesses of used plates are 2 and 3 mm. Length and width of the plates 160 x 80 mm.

Nonferrous Materials:

- Aluminum 1050 H 24 with dimension of 160 x 80 x 2 mm.
- Aluminum 5251 H22 with dimension of 160 x 80 x 1.5 mm.
- Aluminum 6082 T6 with dimension of 160 x 80 x 2 mm.
- Titanium grade 2 with dimension of 160 x 80 x 1 mm.

Chemical composition of the materials selected in this study were analyzed by Spark Analyzer Spectromax shown in Fig. 4.1, each reading was an average of five readings except titanium, the chemical composition was received from the manufacturer. Software DIA 2000SE combined with spark analyses was used for data analyzing and management. The received results were comparable to the standard for each grade. The chemical compositions of ferrous materials are

presented in Table 4.1. The chemical compositions of nonferrous materials are presented in Table 4.2 and Table 4.3.

Table 4.1: Chemical composition of the ferrous materials (wt %)

Material	C	Si	Mn	P	S	Cr	Ni	Nd	Mo	Fe
AISI 1008	0.093	0.027	0.21	0.001	0.005	0.043	0.065	0.024	0.006	Bal.
Din: en 10131	0.023	0.017	0.16	0.001	0.002	0.043	0.076	0.004	0.017	Bal.
SST316	0.048	0.219	1.04	0.013	0.033	18.028	10.157	0.098	1.83	Bal.

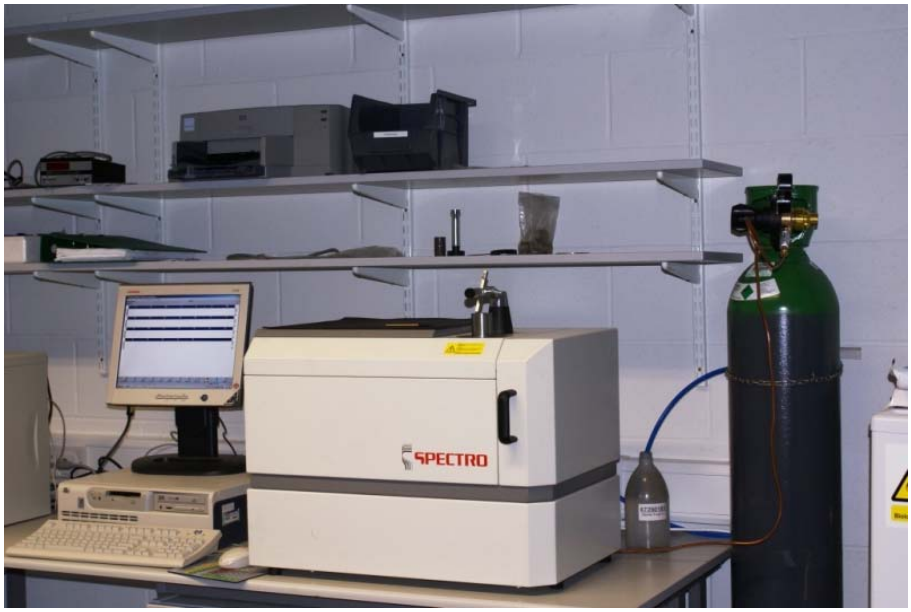

Fig 4.1: Photography of Spark Analyzer Spectromax.

Table 4.2: Chemical composition of the Aluminum grades (wt %)

Material	Si	Fe	Cu	Mn	Mg	Cr	Zn	Ni	Ti	Al
Al 1050	0.085	0.445	0.005	0.011	0.003	0.01	0.032	0.023	0.031	Bal.
Al 5251	0.407	0.509	0.154	0.154	2.152	0.154	0.15	0.002	0.147	Bal.
Al 6082	1.05	0.5	0.106	0.934	1.05	0.262	0.223	0.008	0.114	Bal.

Table 4.3: Chemical composition of the Titanium grade 2 (wt %)

Material	C	Fe	H	N	O	Ti
Ti G2	0.1	0.3	0.015	0.03	0.25	99.2

The standard mechanical properties and physical properties for the materials are presented in Table 4.4 and 4.5 respectively.

Table 4.4: Mechanical properties of the materials

Grade	**Tensile Strength, [MPa]**	**Yield Strength [MPa]**	**Elongation %**	**Hardness Brinell [HB], max**	**Elastic Modulus [GPa]**
AISI 1008	340	290	20	95	190
Din10131	390	280	37	111	203
SST316	485	170	40	217	193
Al 1050 H24	105	75	5	33	71
Al 5251 H22	190	120	6	56	70
Al 6082	210	140	11	94	70
Ti G2	344	275	20	14.5	105

Table 4.5: Physical properties of the materials

Grad	**Thermal Conductivity W/m. °C**	**Melting Point °C**	**Thermal Expansion µm/m/°C**	**Density Kg/m3**
AISI 1008	59.5	1565	13.8	7870
Din: en 10131	46.73	1530	11.94	7800
SST316	16.3	1385	17.82	8000
Al 1050 H24	222	650	24	2710
Al 5251 H22	134	650	25	2690
Al 6082	180	555	24	2700
Ti G2	16.4	1665	9.36	4510

4.1.2 Description and Use of the Studied Materials

Low carbon steel AISI/SAE 1008 is suitable for general engineering applications in industry, typical uses are in the power generation, chemical,

petrochemical, nuclear industries. This material is very ductile and extremely difficult to machine in terms of chip breaking [162].

Low carbon steel Din: en 131 cooled rolled, is one of the most popularly used materials for different engineering applications in industry, typical uses are in automobile body panels, tin plate, simple structural components, power plants and wire products.

Stainless steel 316 , typical uses include exhaust manifolds, furnace parts, heat exchangers, jet engine parts, pharmaceutical and photographic equipment, valve and pump trim, chemical equipment, digesters, tanks, evaporators, pulp, paper and textile processing equipment, parts exposed to marine atmospheres and tubing. Type 316L is used extensively for weldments where its immunity to carbide precipitation due to welding assures optimum corrosion resistance.

Aluminium, EN AW-1050 H24 is used in most industry sectors (electro technical, chemical, food processing, aircraft, engineering, building, automotive etc.) for construction joints and members, low tension mechanical applications, applications requiring material of high formability, good weldability, high corrosion resistance, excellent heat and electrical conductivity and flexibility. It is suitable for most welding techniques but is not recommended for use in cutting tool applications due to insufficient strength.

Typical products: electro-technical products, chemical device exchangers', automotive coolers, reflectors and mirrors, packaging products, covers, containers, crockery, window frames and doors, building facades, roofing material, automotive accessories etc.

Aluminium, EN AW-5251 H22 is a medium strength material with very good chemical and corrosion resistance and very good burnishing qualities. Weldable is suitable in an argon protective atmosphere. Cold working elevates solidity and yield limit, but reduces ductility. Forming does not affect corrosion resistance and weldability. It is used for medium stressed constructions, corrosion and sea water resistance and technological ductility applications. It is used extensively in the food, chemical, architecture, interior design, automotive and construction industries. Typical product applications include: pipes, liquid containers, safety barriers,

shelving systems, energy transfers, watch casings, decking for navel and river vessels, wallpaper and packaging products. Aluminium wire is used for rivet production.

Aluminium, EN AW-6082 is a construction material with good ductility, polishing ability and corrosion resistance, good electrolytic oxidation and is suitable for welding. It has good plasticity qualities in an annealed state suitable when hardened. Formability is very good in the temperature range 450 to 500 °C. It has very good corrosion resistance, and is not inclined to suffer stress corrosion cracking. Cutting tool workability in an annealed state is not suitable but is acceptable in a hardened temper. It is used for medium strength components with long operation schedules in temperatures from 50°C up to 70°C, applications requiring specific technological properties, corrosion resistance, aesthetic features, when in contact with food, high specification aviation and automotive components. Typical product applications include: airplane cabins, helicopter cockpits, floor coverings, door frames, safety barriers, escalators, furniture, rivet stems, cranes and columns.

Titanium grade 2, the combination of high strength-to-weight ratio, excellent mechanical properties, and corrosion resistance makes titanium the best material choice for many critical applications. Titanium grade 2 is used for demanding applications, such as, static and rotating gas turbine engine components. Some of the most critical and highly-stressed civilian and military airframe parts are made of titanium. The use of titanium has expanded in recent years to include applications in nuclear power plants, food processing plants, oil refinery heat exchangers, marine components and medical prostheses.

The high cost of titanium alloy components may limit their use, lower-cost alloys, such as, aluminium and stainless steels, are often chosen instead.

4.2 Joint Design and Preparation

A weld joint transfers the stresses between the jointed components and throughout the welded assembly. The type of service and force applied of the weldment influences the selection of a joint design.

Butt joints are joints between two abutting members lying approximately in the same plane. Butt joints are preferable in uses where fusion-welded joints in sheet metal are required. The sample preparation was carried out by cleaning the specimen using (grade 400) emery paper, especially on the edges that are to be assembled together, to remove any contaminations that may affect the joint quality. The plate's edges were well prepared to ensure full contact between the plates along the welding line during the butt-welding. This design of joint was applied in this study as the first method for joining the 1.5 mm and 2 mm dissimilar low carbon steel AISI 1008 and stainless steel 316 components and to join 3mm dissimilar low carbon steel Din: en 10131 and stainless steel 316 components.

Lap joints designs were made with two overlaps members. They were applied for joining the nonferrous dissimilar and ferrous with nonferrous materials selected in this study. The materials were cleaned by sand blasting using the sandblasting machine exhibited in Fig. 4.2. After sand blasting, a compressed air jet was directed at the specimen to remove any sand dust resulting from the previous operation. Then acetone was used to degrease the interfaces of the specimens to remove grease and any other contaminates.

In this study two types of design weld joints have been applied, firstly, the butt joint design was applied for joining ferrous to ferrous dissimilar components, and secondly, the overlap joint design was applied for joining the ferrous / nonferrous dissimilar materials and nonferrous / nonferrous dissimilar materials.

Fig. 4.2: Photograph of the sandblasting machine used for cleaning the materials.

A fixture was used to clamp the plates during the welding operation in both joint designs (butt and lap joint) to avoid any thermal deformation caused by heat input to the materials during the welding process. The fixture was also used during residual stress measurements. The fixture is exhibited in Fig. 4.3.

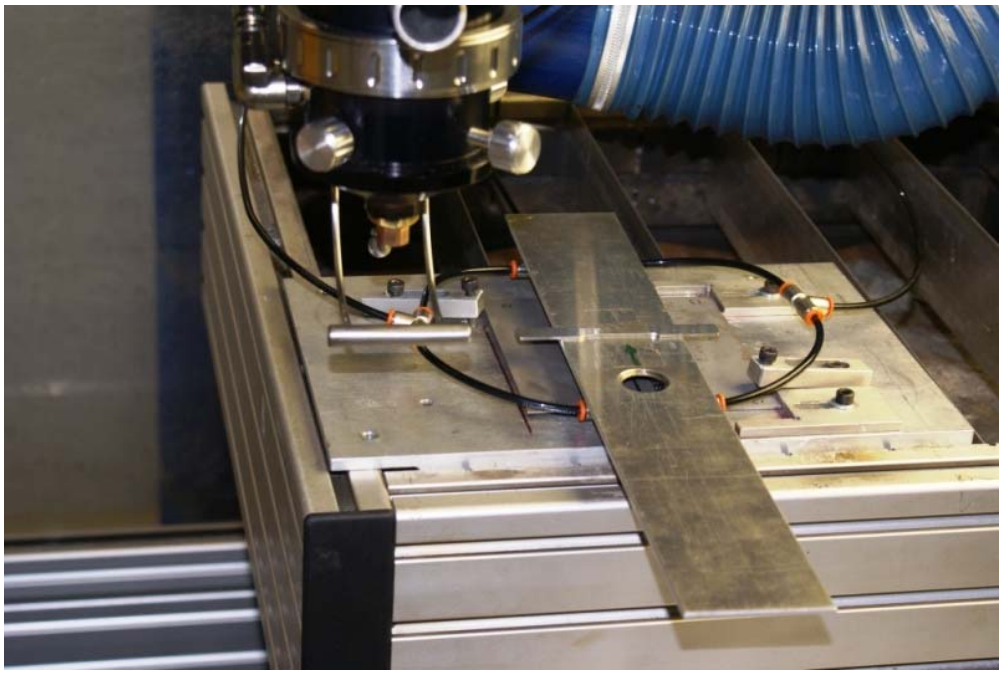
Fig. 4.3: The fixture used for clamping the plates during welding operation.

4.3 Shrouding System Design and Production

The shroud system was designed to provide total coverage of the melt and the reactive hot region of the weld especially for nonferrous materials to avoid formation of carbides or oxides composites which are mostly brittle composites that have a harmful effect on welding quality. It was designed to protect the work piece without affecting flow rates which may cause waves on the weld pool. The shading gas can be blown against the specimen in four ways divided in two types as following:

Movable shading gas

The movable shading gas is blown from the laser head nozzle and moves with the laser beam during the welding process to provide the only primary shielding of the molten weld puddle as presented in Figs 4.4 (a, b and c). Argon gas with a flow rate of 5 l/min was used. It was controlled by the laser machine control system and it was directed perpendicular to the specimen.

Unmovable shading gas

The unmovable shading gas was secondary shielding which is designed to protect the solidified weld metal and associated heat-affected zones until the temperature reaches below the reactive point. The unmovable shading gas was designed and produced to suit the laser machine tolerances. The work piece fixture was modified to supply shading gas through three parts as following:

Part one: A tube of 180mm in length and 6mm diameter with drilled holes of 1mm in diameter in three rows, blowing out gas up towards the specimen. This tube was connected below the work piece fixture.

Part two: Two rectangular arms used for fixing the specimen during welding with dimensions of (160 x 10 x 10) mm were utilized to blow out gas through two rows of holes of 1mm diameter. The distance between hole to hole centers is 5mm. The first row holes is 3mm above the specimen service and the holes were drilled with inclination angle of 30° to make the blown gas hit the specimen and avoid causing waves on the molten weld puddle. The second row holes are 6mm above the specimen service. Two rows of holes of 6mm in diameter in the opposite side of the

gas-out tube, holes distance 150mm from each other are connected to two hoses and were implemented to supply the shaded gas.

Part three is a cover for the shrouding system to maintain the gas in the system reducing gas consumption. It consists of an aluminium plate, of dimension (40 x 350) mm, which is placed on top of the fixture arms with a hole of 15 mm diameter to let the laser head downwards through it to the specimen and moving with laser head movement.

In this work, Google Sketchup 6 was used to design the shrouding system as exhibited in Fig. 4.4 (a), the detailed sketch design is presented in Appendix A. The shrouding system was produced in the Mechanical Engineering School workshop and it is exhibited in Fig. 4.4 (b, c). Argon gas was used in unmovable shading gas with flow rate of 5 l/min, which was manually controlled. The gas is started a minute before laser weld is starting and remains continuous until the specimen temperature drops below reaction point of the active welded material.

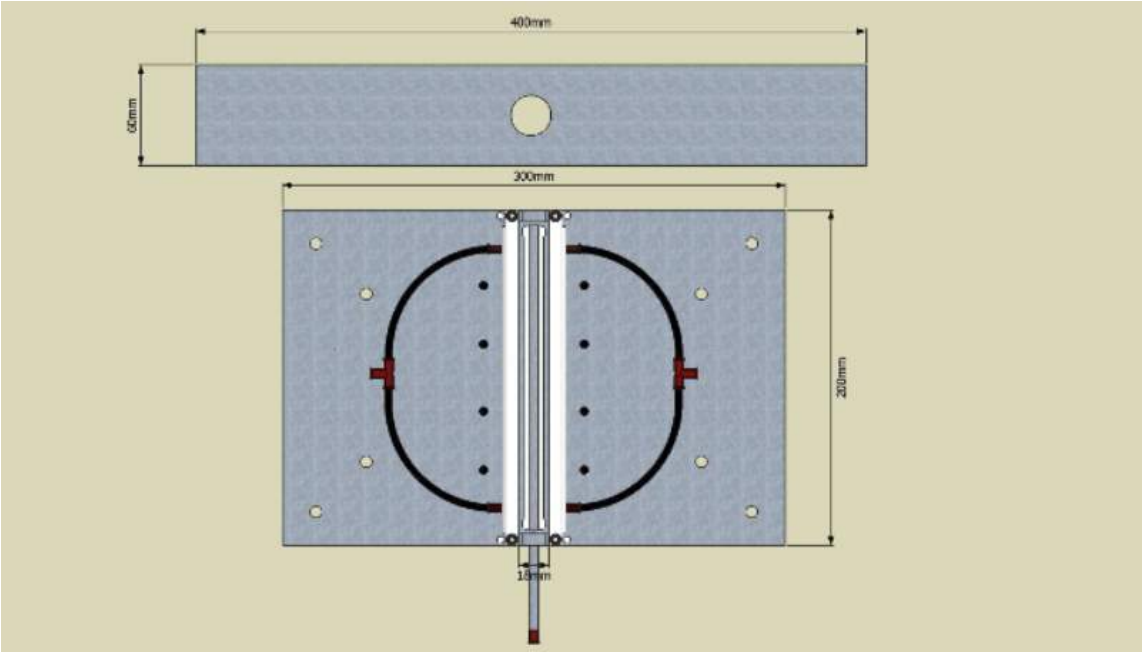

Fig 4.4 (a): 3D drawing for shrouding system design.

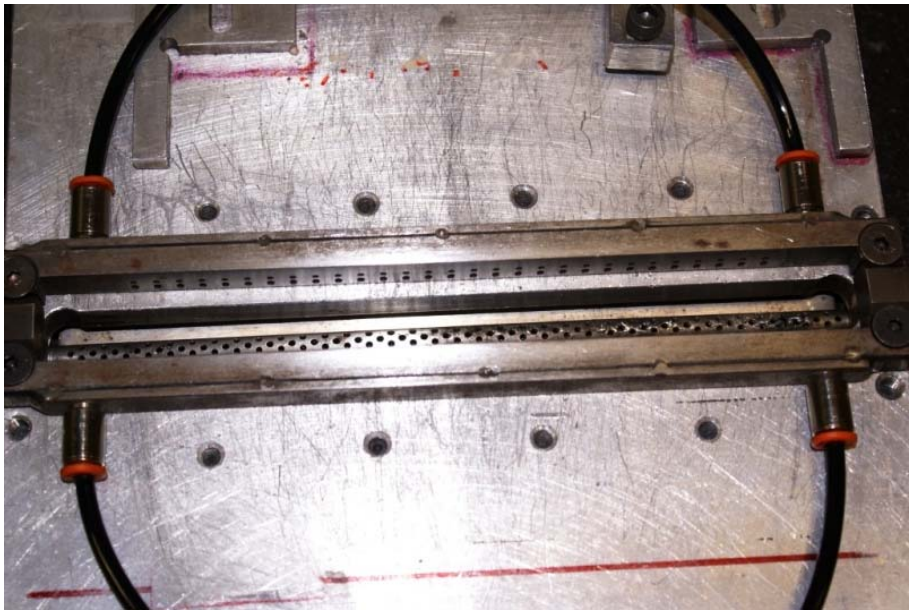

Fig 4.4 (b): Photograph of unmovable three parts of shrouding system.

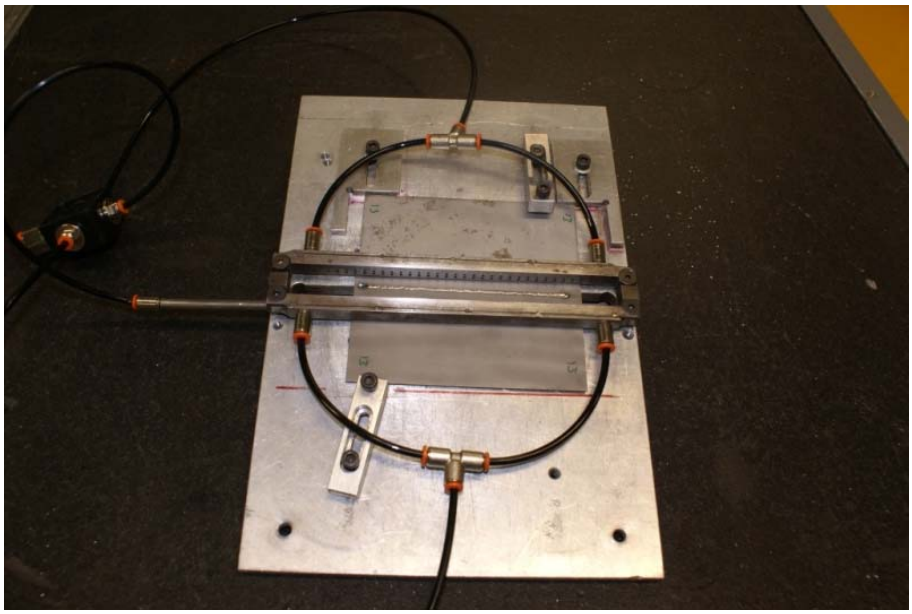

Fig 4.4 (c): Photograph of unmovable three parts of shrouding system and gas hoses with specimen.

4.4 Laser Welding

After the material preparation and shrouding system produced laser welding were carried out by a laser welding machine specified below.

4.4.1 Laser Welding Machine

Rofin Dc 015 industrial CO_2 Diffusion-Cooled Slab laser with a maximum output power of 1.5 kW and 10.6 µm wavelength, shown in Fig. 4.5, was used. The Rofin laser machine technical specifications are exhibited in Table 4.6. The whole laser machine system (Rofin laser, two dimension moving table, control software, laser cooling system, air compressor and accessories) were provided by Mechtronic Industry. The speed control has a control range from 1 mm/min up to 5000 mm/min incriminating by 1 mm. The beam delivery system is operating on 127 and 190 mm focal length 'FL' high pressure lenses. The machine beam system has a high pressure nozzle assembly with four thumbscrew adjusters to keep the assist gas around the beam and replaceable copper nozzle allows a stand-off distance between laser head and work piece of 1mm at 50 % height. The lens assembly allows ± 10 mm lens focal position, relative to up to the tip via manually operated micrometer movement. Premix laser gas is used for operating the laser machine. The gas consists of a 94 % mixture of (Carbon Dioxide, Helium, Nitrogen and Xenon) and 6 % of Carbon Monoxide. The laser bottle contains 1500 standard liters [163,164].

Fig. 4.5: Rofin Dc 015 industrial CO_2 Diffusion-Cooled Slab laser machine.

Table 4.6 Rofin laser machine technical specifications [165]

Technical data	ROFIN DC 015
Excitation	HF
Output power	1500 W
Power range	150-1500 W
Beam quality factor	K > 0,9
Pulse frequency	0 or 2 up to5000 Hz; cw

4.4.2 Laser Welding Operations

Pilot experiments of laser welding were carried out in Engineering School workshop to determine the practical operating range of each individual selected laser welding parameters in order to produce acceptable quality welding of different dissimilar materials. Assessment welding trials were carried out by fixing the welding parameters and changing one at a time for each dissimilar joint material. Visual inspections for the joints were applied to decide the parameter operating range. The visual inspections are applied to detect the following welding defects: Surface flaws - cracks, porosity, unfilled craters, slag inclusions, poorly formed beads, misalignments and/or there is not full penetration in some cases.

Once the parameters ranges for all selected welding parameters were determined, the designing of experiments using the Taguchi approach, described in the previous chapter, using L16 and L25, was carried out using Design Expert 7 software. A random sequence was used to carry out the experiment runs to avoid any systematic error. Argon gas was used as a primary and secondary shielding gas during and after the welding operations. The jointed plates were rigidly clamped during welding to keep away from any thermal deformation caused by heat input that my effect the studied responses. Welding was performed without any preheating or post heating treatments.

4.5 Residual Stress Measurements

Residual stresses are usually defined as stress that remains in mechanical parts not subjected to any outside loading. Those stresses develop as a result of the

welding process. Residual stresses are dependent upon the order in which pieces are joined as well as other process parameters. Referring to the literature review in chapter two, there are many non-destructive and destructive methods for measuring the residual stresses.

The x-ray method is a non-destructive method for measuring the residual stresses which is very accurate method for stress determination and has a high resolution. One of the disadvantages of this method is that only specimen surfaces can be measured. It is therefore impossible to determine a three-dimensional stress field using non-destructive means. The destructive method cannot be used for this study because the same specimen should be subjected to another mechanical properties testing. Therefore, the incremental hole-drill method, which was classified as a semi-destructive method, is the most suitable method to be implemented in this research. This method is based on the stress-relaxing technique, in which the stress is a measure of stress-relaxing when a metal part is removed by drilling a hole in the specimen. Measuring the deformation caused by relaxation in the drilled hole and analyzing the successive state of equilibrium, the values of the residual stress existing in specimen before drilling the hole could be calculated [81].

4.5.1 Incremental Hole-Drilling Method (IHDM)

The relieved strains are measured by mounting three resistance strain gauges in the form of a rosette around the site of the hole before drilling. Such a rosette is shown schematically below in Fig 4.6; where three radially oriented strain gauges are located with their centers at the radius R from the centre of the hole.

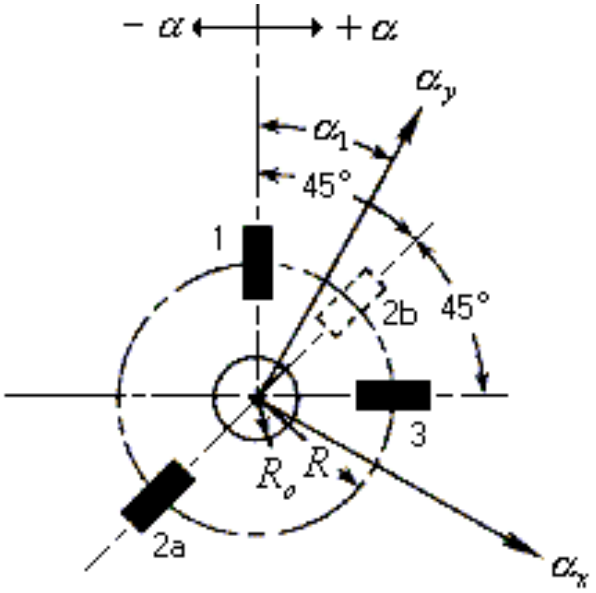

Fig 4.6: Strain gauge rosette arrangement for determining residual stress [81].

Although the angles between gauges can be arbitrary (but must be known), a 45-degree angular increment leads to the simplest analytical expressions, and thus has become the standard for commercial residual stress rosettes. As indicated in Fig 4.6, α_1 is the acute angle from the nearer principal axis to gauge no. 1, while $\alpha_2 = \alpha_1 + 45^{\circ}$ and $\alpha_3 = \alpha_1 + 90^{\circ}$, with positive angles measured in the direction of gauge numbering. When space for the gauge is limited, as in measuring residual stresses HAZ of the weld location 2b is permits positioning the hole closest to the area of welding line.

Strain equations can be written three times, once for each gauge in the rosette:

$$\varepsilon_1 = A(\sigma_x + \sigma_y) + B(\sigma_x - \sigma_y)\cos 2\alpha \quad \textbf{... (4.1)}$$

$$\varepsilon_2 = A(\sigma_x + \sigma_y) + B(\sigma_x - \sigma_y)\cos 2(\alpha + 45^{\circ}) \quad \textbf{... (4.2)}$$

$$\varepsilon_3 = A(\sigma_x + \sigma_y) + B(\sigma_x - \sigma_y)\cos 2(\alpha + 90^{\circ}) \quad \textbf{... (4.3)}$$

When the above Eqs. (4.1, 4.2 and 4.3) are solved simultaneously for the principal stresses and their direction; the results can be expressed as:

$$\sigma_{Max} = \frac{\varepsilon_3 + \varepsilon_1}{4\overline{A}} + \frac{\sqrt{(\varepsilon_3 - \varepsilon_1)^2 + (\varepsilon_3 + \varepsilon_1 - 2\varepsilon_2)^2}}{4\overline{B}} \quad \text{...(4.4)}$$

$$\sigma_{Min} = \frac{\varepsilon_3 + \varepsilon_1}{4\overline{A}} - \frac{\sqrt{(\varepsilon_3 - \varepsilon_1)^2 + (\varepsilon_3 + \varepsilon_1 - 2\varepsilon_2)^2}}{4\overline{B}} \quad \text{... (4.5)}$$

Where: α is the angle from the nearer principal axis to gauge no. 1 (in the direction of gauge numbering, if positive; or opposite, if negative). Reversing the sense of α to more conveniently define the angle from gauge no. 1 to the nearer axis, while retaining the foregoing sign convention,

$$\alpha = \frac{1}{2}\tan^{-1}\left(\frac{\varepsilon_3 + \varepsilon_1 - 2\varepsilon_2}{\varepsilon_3 - \varepsilon_1}\right) \quad \text{... (4.6)}$$

$$\overline{A} = -\frac{1+\nu}{2E} \times \overline{a} \quad \text{... (4.7)}$$

$$\overline{B} = -\frac{1}{2E} \times \overline{b} \quad \text{... (4.8)}$$

Where: E = modules of elasticity of the metal

ν = Poisson's ratio.

In residual stress analysis application for blind-hole drilling, the coefficients $\overline{A}$ and $\overline{B}$ (or $\overline{a}$ and $\overline{b}$) must be determined to calculate the stresses from the relieved strains.

For any given initial state of residual stress, and a fixed hole diameter, the relieved strains generally increase (at a decreasing rate) as the hole depth is increased. Therefore, in order to maximize the strain signals, the hole is normally drilled to a depth corresponding to at least Zi / D = 0.4 (Zi / D = 0.4 for the maximum hole depth [166]).

Where:

Z = the hole drilled depth.

i = the depth level, in this study i = 0.127, 0.254, 0.762, 0.508, 1.016, 1.27 and 1.524mm.

D = the rosette diameter = 5.13 mm.

D_0 = the hole (cutter) diameter in this study D_0 = 1.6 mm.

The data reduction coefficients of $\bar{a}$ and $\bar{b}$ as a function of depth illustrated in Fig. 4.7 [81] was used to determine the coefficients $\bar{a}$ and $\bar{b}$, then equations (4.7 and 4.8) could be solved for calibration coefficients values of $\bar{A}$ and $\bar{B}$. Maximum and minimum stresses and their directions than could be calculate using equations (4.4, 4.5 and 4.6 respectively).

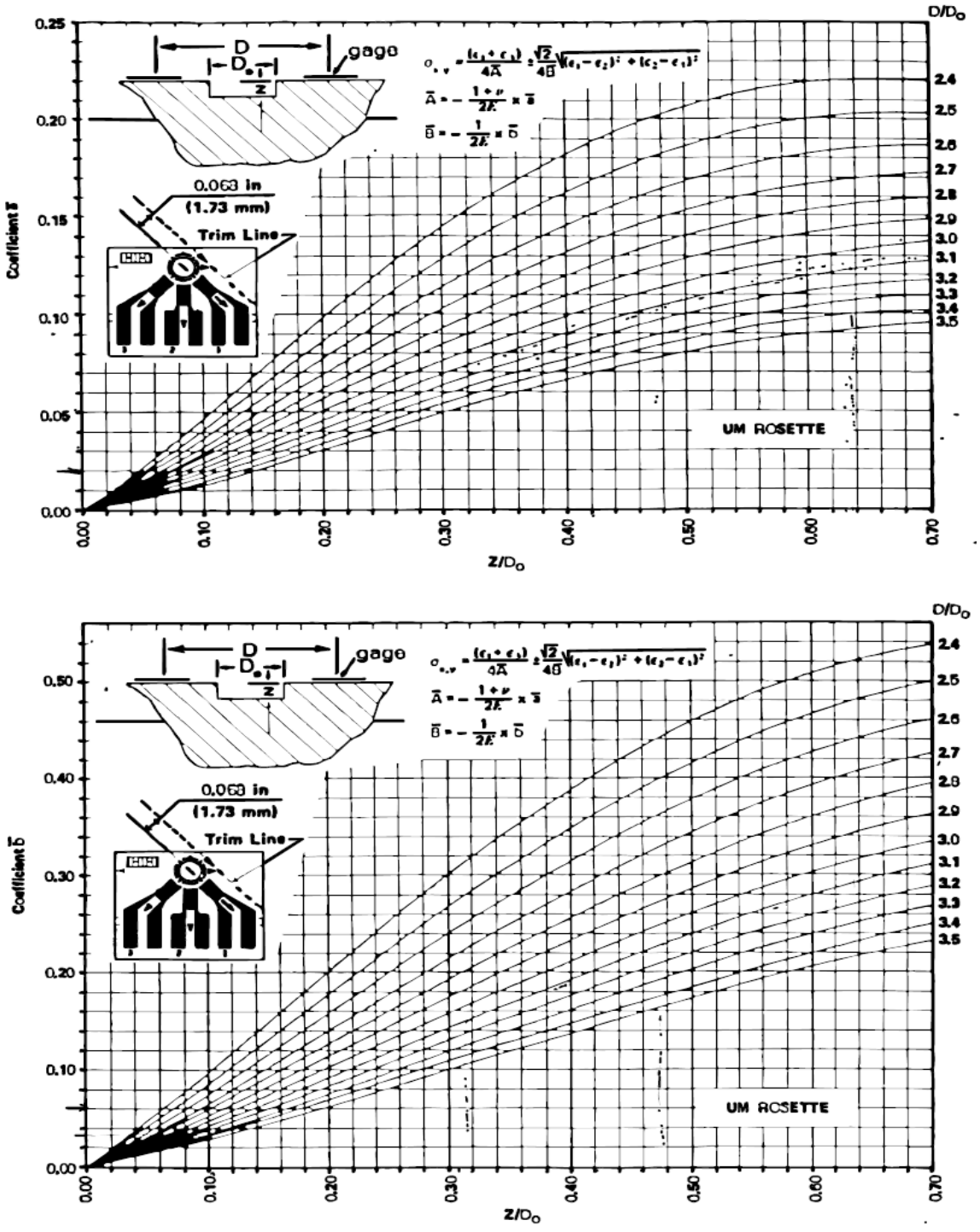

Fig. 4.7: Calibrating coefficients of $\bar{a}$ and $\bar{b}$ as a function of hole depth for UM rosettes [166].

4.5.2 Hole-Drill Method Equipment

4.5.2.1 RS-200 milling guide

The RS-200 Milling Guide is a precision fixture for accurate positioning and drilling of a hole through the centre of a special strain gauge rosette. When installed on the work-piece, the guide is supported by three leveling screws footed with swivel mounting pads to facilitate attachment to uneven surfaces. Alignment of the milling guide relative to the strain gauge rosette is accomplished by inserting a special-purpose microscope into the guide's centering channel, and then positioning the guide precisely over the centre of the rosette by means of four X-Y adjusting screws. The microscope assembly, consisting of a polished steel housing with eyepiece, reticule, and objective lens, permits alignment to within 0.0015 in (0.038 mm) of the gauge centre. The microscope is also used to measure the diameter of the hole after it is drilled. An illuminator attaches to the base of the guide to aid in the optical alignment procedure.

After alignment, the microscope is removed from the guide, and the milling bar or high-speed air turbine is inserted in its place. The milling bar is used for slow-speed drilling of the hole. The standard milling cutters was: 0.062 in (1.6 mm) diameter. The milling bar is equipped with a universal joint for flexible connection to a drill motor. The RS-200 Milling Guide with microscope and with milling bar photos are exhibited in Fig. 4.8 (a, b) respectively.

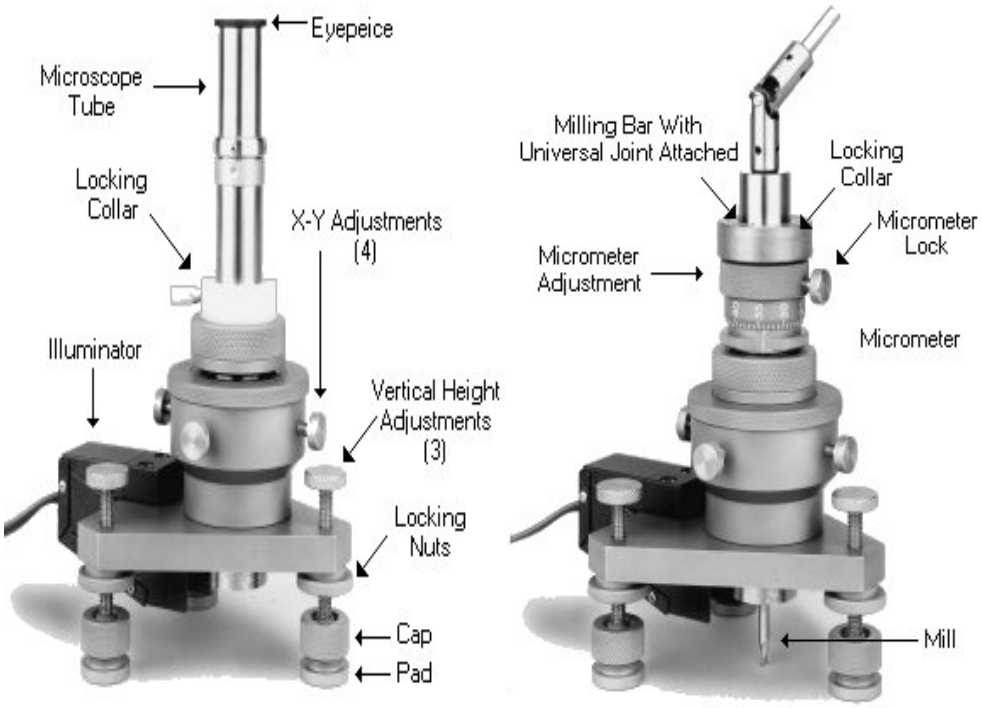

(a) (b)

Fig. 4.8: RS-200 Milling Guide (a) with microscope (b) with milling bar

4.5.2.2 Digital strain gauge

Digital strain indicator of type P-3500 was used for strain measuring in this work. It is a portable, battery-operated instrument capable of simultaneously accepting four inputs from quarter-, half-, and full-bridge strain-gauge circuits, including strain-gauge-based transducers. A highly stable measurement circuit, regulated bridge excitation supply, and precisely settable gauge factor enable measurements of ± 0.1% accuracy and 1 με resolution. Bridge completion resistors of 120, 350 and 1000 Ω are built in for quarter-bridge operation with measurement capacity up to 199990 με in both sides. A SB-10 switch and balance unit was connected to the digital strain indicator which is designed to provide ten channels of output information on one strain indicator. For this work only three channels were used. Before starting to measure the strain each channel has to be balanced to zero to simplify data interpretation and reduction. The digital strain indicator and SB-10 switch and balance unit are exhibited in Fig. 4.9.

Fig. 4.9: Photo of the l strain indicator of type P-3500 and the strain indicator and SB-10 switch.

4.5.2.3 Adhesive

M-Bond 200, a recommended special adhesive for bonding strain gauges, was used for bonding the strain gauges to the work piece. It requires one minute of thumb pressure followed by two minutes before tape removal. In total it takes five minutes to reach to the required bond strength. Fig 4.10 exhibited the used adhesive kit.

Fig. 4.10: Photograph exhibiting the M-Bond 200 adhesive kit.

4.5.2.4 Cement kit

A fast-setting cement kit type RS-200-CK Cement, exhibited in Fig. 4.11, was used. Two-component resinous-type dental cement especially suited for firmly attaching the milling guide to the specimen. Standard packaging is approximately two ounces. The cement was produced using a mixture of two spoons of cement powder with 10 drops of the grip cement liquid.

Fig. 4.11: Photograph of the fast-setting cement kit type RS-200-CK Cement kit.

4.5.2.5 Accessory items

Accessory items were used for cleaning and surface preparation of the welded specimen and soldering was used to solder the wire connecting between the strain gage and digital strain indicator. Cutters were used for high-speed air turbine. Cutters are inverted-cone, carbide-tipped: ATC-200-062, 0.062 in (1.6 mm) diameter. The whole work station used for the strain measurements is exhibited in Fig. 4.12.

Fig. 4.12: Photograph of the work station for strain measurements.

4.5.3 Hole-Drill Method Procedure

1. A special three-element Micro-Measurements strain gauge rosette of type CEA-06-062UM- 120, exhibited in Fig 4. 13, was selected for this work because it was necessary to measure stresses as close as possible to the weld pool area in the HAZ. It was bonded to the welded specimen using M-Bond 200 at points where residual stresses were to be determined on the HAZ, where the critical (serious) residual stresses are present in the joined component. The rosette was bonded to the predetermined side of the dissimilar joint in which the residual stresses would be greater.

2. Each rosette grid element is connected (by soldering the wires to rosette) to a strain measuring instrument, as it is exhibited in Fig 4.14 (a).

3. The gauge circuits were balanced to “zero” readings before hole-drilling was started.

4. The RS-200 Milling Guide was positioned over the centre of the gauge using the microscope guide and securely attached to the dissimilar jointed plate.

5. The RS-200 was optically aligned so that its drilling axis is precisely positioned over the target at the centre of the strain gauge rosette and fixed using RS-200-CK cement.

6. A blind hole was drilled through the centre of the rosette into the HAZ of dissimilar jointed plate gradually up to final level of depth of 1.524 mm at 2-3 mm from the centre welded line in the middle of the specimen, as presented in Fig. 4.14 (a, b).

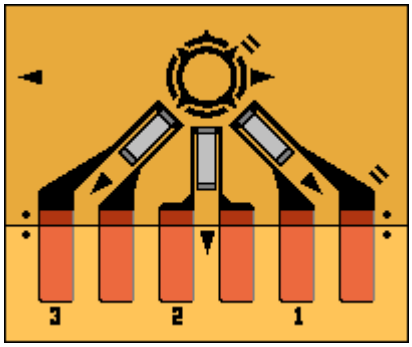

Fig. 4.13: Strain Gauge Rosette of type CEA-06-062UM- 120

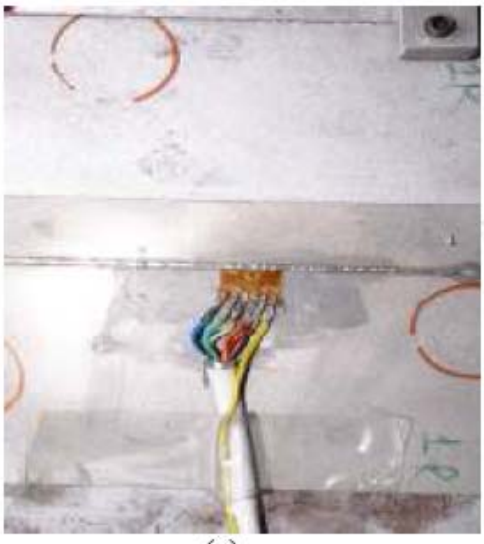

(a)

Fig. 4.14(a): Photo of the rosette bonded to the surface of the specimen.

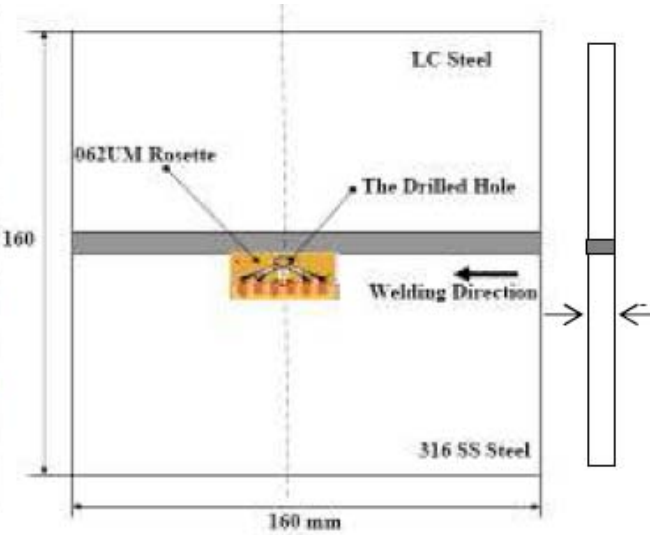

(b)

Fig.4.14 (b): Schematic plot of the rosette bonded to the surface of the specimen.

7. Strain gauge instrumentation was used to obtain strain readings at each predetermined level of the specimen. The hole was drilled in increments, being careful not to generate heat that would induce residual stresses. The high-speed air

turbine was used for drilling, and it also cooled the plates at the same time. Strains were record after the strain indicator had stabilized at each level.

8. Stresses were calculated using strain data and stress equations. The measurements were repeated for all experiments runs (25 or 16).

4.6 Mechanical Testing

4.6.1 Tensile Strength Testing

After measuring the residual stresses in the welded specimen, the next step is to cut the specimens to prepare for tensile testing. Tensile strength was tested for ferrous materials butt-jointed. Notched tensile strength (NTS) samples [167] exhibited in Fig. 4.15 were produced from the jointed samples by laser cutting in the same laser machine used for welding. Five or more NTS samples were cut from each dissimilar welded specimen.

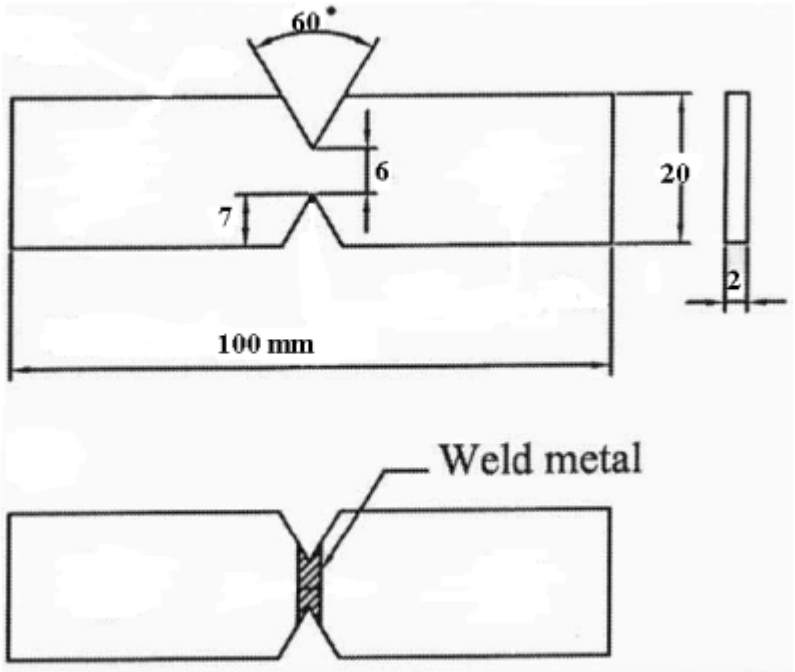

Fig. 4.15: Schematic diagram for notched tensile strength (NTS) sample [168].

4.6.2 Tensile Shear Strength Testing

For nonferrous dissimilar materials that were lap-jointed five or more tensile shear samples were prepared from each specimen using laser cutting for testing. Fig. 4.16 (a, b) exhibited the centre-line welding lap joint and the shape, with dimension, of the tensile shear sample. In all weld plates, the roll direction was kept perpendicular to the welding direction. In all tensile samples the weld pool was at the centre of the sample gauge length. The joint strength was evaluated by tensile testing at room temperature, using the Instron Universal Electromechanical Testing Machine Model 4202, exhibited in Fig. 4.17. Two crosshead speeds were used of 5 mm min^{-1} for butt-joints and 1 mm min^{-1} for lap-joints to avoid the strain hardening effect. Averages of at least three samples were calculated for all dissimilar joints. Tested samples used in this study are exhibited in Fig 4.18.

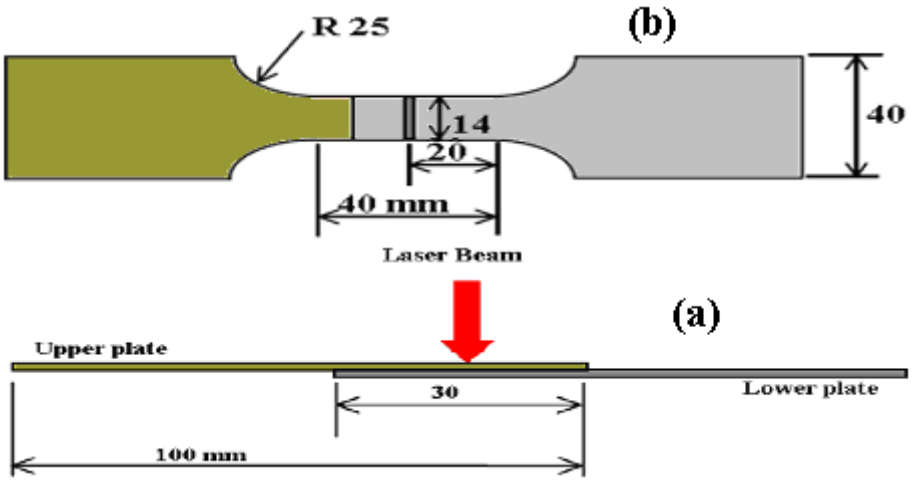

Fig. 4.16: Schematic diagram illustrating the (a) Center-line welding lap-join, (b) Tensile shear sample[169].

Fig. 4.17: Instron machine and its control unit with computer.

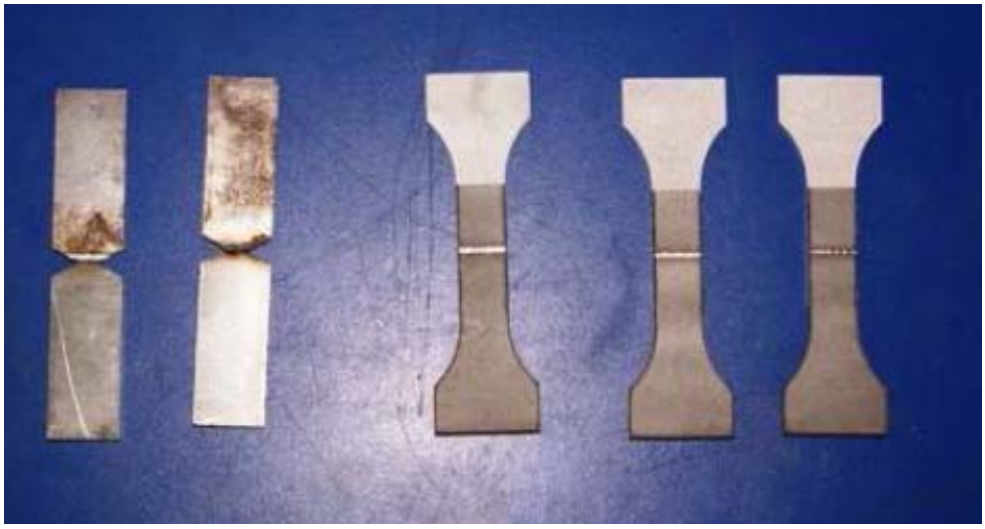
Fig 4.18: Photograph showing the different tensile samples (tensile and shear).

4.6.3 Impact Strength Testing

Impact strength is an energy required to fracture a specimen subjected to shock loading, as in an impact test. Alternate terms are impact energy, impact value, impact resistance and energy absorption. It is an indication of the toughness of the material.

Samples for impact strength were cut and prepared from the dissimilar jointed plates by means of laser cutting and following ASTM E23-02a [168]. The impact strength samples dimensions were 55 x 10 x (different thicknesses 2 or 3) mm and

the V groove was perpendicular to the middle welding line as exhibited in Fig. 4.19. The impact strength samples were tested at room temperature using a MAT21 universal pendulum impact tester, exhibited in Fig. 4.20. The average of at least three results of impact was calculated for each sample and the obtained results were considered as responses for this study. The experimentally measured responses were tabled for further analysis. In this work, the impact strength was measured for the base materials also; to compare the results obtained from the dissimilar welded joints which in most cases indicated that the impact strength ranges of the dissimilar joints fall in the range between the base metals impact strengths.

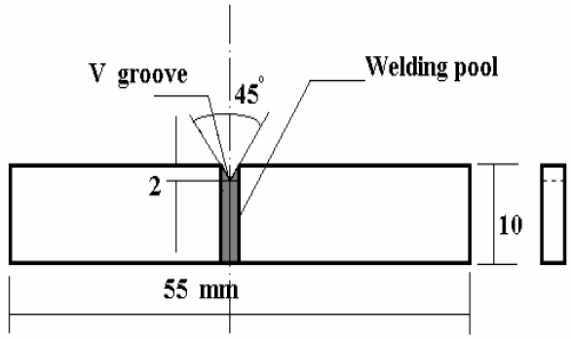

Fig 4.19: Schematic diagram of impact Sample [170]

Fig. 4.20: MAT21 universal pendulum impact machine

4.7 Micro-Study and Weld Pool Geometry Determination

4.7.1 Sample Preparation

A small sample was cut from each welded plate perpendicular to the welding line to study the weld pool shape and geometry. A Buehler Simplimet 2000 Mounting Press was used to mount the samples in Bakelite to allowing fixing of the samples during preparation and micro-studies. Buehler Motopol 2000 grinding and polishing wheel equipment were used during sample preparation for grinding and polishing. The grinding step for all samples were carried out by using Abrasive

silicon carbide papers of range (120, 240, 600, 800 and 1200) grain/cm^2, were used to grind the samples for four minutes for each grade, at a speed of 150 rpm using water for cooling. Polishing for ferrous materials was carried out using diamond suspensions with grain size of (6, 3 and 0.05 μm). The samples were ground for five minutes for each grain size. The samples were then cleaned by running under cool water followed by acetone cleaning and then dried using compressed air. For etching the ferrous dissimilar materials two different chemical solutions were used. The low carbon steel side of the weldment was etched in 4% Nital, and the rest of the regions of the weldment were etched in a solution containing 20 ml hydrochloric acid, 1.0 g sodium meta bisulphate and 100 ml distilled water. Also, an electrolytic etching in 10% (w/o) oxalic acid was employed to reveal the features of weld metal and the evolved interfaces. Keller's reagent (1% HF, 1.5% HCl, 2.5% HNO_3 and H_2O solution) was used as etchant for aluminum alloys of dissimilar joints and Reagent consisting of (10 ml HF and 5 ml HNO_3 in 85 ml of water) was used for etchant titanium parts of dissimilar joints.

4.7.2 Microstructure

The microstructures of dissimilar joints were inspected by means of optical microscopy coupled with a video camera, exhibited in Fig. 4.21. The microscopy lenses used for this study were a magnification of 16X for the eye-piece lens and 80X for objective.

4.7.3 Weld Pool Geometry

The area of the fusion welding zone (A) was measured by using the transverse sectioned specimens, the optical microscope and image analyzer software, exhibited in Fig. 4.21. Firstly, the image of the fusion welding zone was captured by using the MEIJI, EMZ-TR optical microscope, exhibited in Fig. 4.22, and then the image was exported to the image analyzer. Using the same procedure the welding pool width at the surface (W_1) and the welding pool width at the middle depth (W_2) of the specimens also were measured and analyzed as process responses. Fig. 4.23 shows the positions of welding pool geometries on the specimen. The average of three or

more results of weld-pool geometry were calculated for each sample for all dissimilar joints and tabulated for further analysis.

Fig. 4.21: The optical microscope connected to image analyzer software.

Fig. 4.22: The MEIJI, EMZ-TR optical microscope.

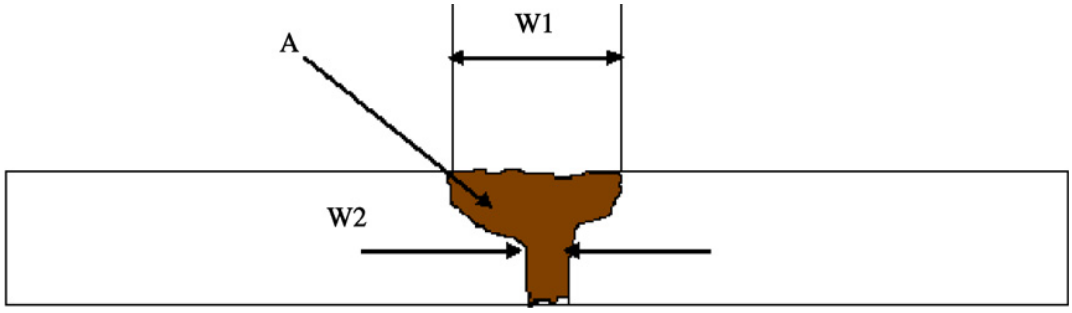

Fig. 4.23: Shows the positions of welding pool geometries on the specimen.

4.7.4 Microhardness

The Vickers Microhardness tests were measured by means of PMT-3 Microhardness tester at room temperature, exhibited in Fig. 4.24. A load of 100g was applied for fifteen minutes then the dimensions of the indentation were measured by means of the connected to the same microhardness test. An average of five measured readings were calculated for each location of weld transverse sample (base metal, HAZ and weld pool) and tabulated for further studies. The Vickers hardness number calculation is based on the following formula:

$$HV = 1.8544 \times \frac{p}{d^2} \quad \textbf{... (4.9)}$$

Where: p = load in Kgf , d = indentation in mm

Fig. 4.24: Photograph of Microhardness tester.

4.8 Cost Analysis

For optimizing the dissimilar laser welding process, the operation cost has to be carefully analyzed and calculated. For the laser welding machine system used in this study the operating cost in general fall within the classification listed in Table 4.7 [170]. The operating costs considered in the study included the scheduled and

preventive maintenance. The total operating cost per unit length per hour of the laser welding as a function of laser power and electric power cost per kW is presented in equation 4.10. The equations 4.11 and 4.12 were derivative for calculation of the welding cost of dissimilar joints for all specimens of non-ferrous and ferrous materials respectively.

$$\text{Welding cost} = \frac{5.455 + [(13.952 + 11.135\text{xP})\text{xEC}]/\text{h}}{\eta\text{xS[mm/min]x[60min/h]x[m/1000mm]}} \quad \textbf{... (4.10)}$$

$$\text{Welding cost}_{\text{(ferrous)}} = \frac{5.455 + [(13.952 + 11.135\text{xP})\text{xEC}]}{0.06x\eta x\text{S}} \quad \textbf{... (4.11)}$$

$$\text{Welding cost}_{\text{(nonferrous)}} = \frac{12.38 + [(13.952 + 11.135\text{xP})\text{xEC}]}{0.06x\eta x\text{S}} \quad \textbf{... (4.12)}$$

Where: EC = electric power cost per kW

EC = €0.1435 per kW, at the time of this study

P = laser power per kW

S = welding speed per mm/min

η = welding efficiency, when the efficiency = 100 %;

the efficiency η = 1

The equations (4.11, 4.12) could be rewritten in the following forms:

$$\text{Welding cost}_{\text{(ferrous)}} = \frac{7.455 + 1.60\text{xP}}{0.06\text{xS}} \quad \textbf{... (4.13)}$$

$$\text{Welding cost}_{\text{(nonferrous)}} = \frac{14.38 + 1.60\text{xP}}{0.06\text{xS}} \quad \textbf{... (4.14)}$$

Eq. 4.13 will be used for calculating welding cost of non-ferrous and when joining ferrous materials to non-ferrous materials. Eq. 4.13 and Eq. 4.14 were used in this study for calculation of the welding cost of dissimilar joints for all specimens of non-ferrous and ferrous materials respectively and used for further analysis

Table 4.7: Details of the Laser welding operation costs.

Element cost	Calculations	Welding Cost €/h
Laser electric power	(20.88kVA)(0.8pf)x(EC/kWA)x(P/1.5)	11.135xECxP
Chiller control power	(11.52kVA)(0.8pf)x(EC/kWA)	9.212xEC
Motion control power	(4.8kVA)(0.8pf)x(EC/kWA)	3.84xEC
Exhaust system power	(0.9 kWh)x(EC/kWA)	0.9xEC
Laser gas LASPUR208	[(€989.79/bottle)/(1500litter/bottle)]x[.1042 litter/h]	0.069
Gas bottle rental	€ 181.73/720h	0.252
Chiller additives	(€ 284.80 /year)/ (8760 h / year)	0.033
Shielding gas (Argon)	[(5) litter/ min]x[60 min / h]x[€ $8.62x10^{-3}$/ litter]	3.419
Shrouding Gas For non ferrous (Argon)	[(20) litter/ min]x[60 min / h]x[€ $8.62x10^{-3}$/ litter]	10.344
Nozzle tip	€5.60/50h	0.112
Exhaust system filter	€7/100h	0.07
Focus lens	(€ 240/lens)/(100h)	1.2
Maintenance labor (with overhead)	(12h/2000h operation) x (€ 50/h)	0.30
Total approximated operating cost (€) for ferrous materials per hour		5.455+[(13.952+ 11.135xP)x EC]/h
Total approximated operating cost (€) for nonferrous materials per hour		12.38+[(13.952+ 11.135xP)x EC]/h

CHAPTER 5

5. RESULTS AND DISCUTION OF DISSIMILAR FEROUS MATERIALS

This chapter is divided into three sections, in which the first two parts give the results and discussion of dissimilar butt laser welding between two plates of AISI 1008 low carbon steel and AISI 316 stainless steel with different plate thicknesses of 1.5 - 1.5 mm and 2 - 2 mm. Experiments for the first two parts of this chapter were designed using the Taguchi method with an L-25 orthogonal array. In the third part, the same stainless steel materials and Din: en 10131 low carbon steel plates of 3 - 3 mm in thickness were joined using butt welding. The experiments for the third part of this chapter were designed using the Taguchi method with an L-16 orthogonal array.

5.1 Joining of Low Carbon Steel AISI 1008 to Stainless Steel AISI 316 (1.5 mm Thickness)

For these dissimilar materials with 1.5 mm thickness pilot experiments were carried out by changing one parameter at a time to detect the operating range of the welding parameters under the study. Visual inspection of the welded joints under the criteria of absence of observable welding defects and full depth of penetration were used to determine the ranges of operation of the parameters. The selected welding parameters for these dissimilar materials are: Laser power, welding speed and focus point position. Welding seams of selected produced joints showing full penetration with no observed welding defects are exhibited in Figs. 5.1(a, b) face and bottom of the specimens respectively. Table 5.1 shows welding input variables and experiment design levels. The welding experiments were accomplished in the Mechanical School workshop following the Taguchi designed matrix in random order presented in Table 5.2. The welding pool geometry, mechanical destructive tests (impact strength and tensile strength) and cost per meter welded calculations were carried out in the

jointed specimens; the results are presented in Table 5.3. Each presented result in Table 5.3 is an average of at least of three readings.

Fig. 5.1a

Fig. 5.1b

Figs. 5.1 (a, b), Shows the welding seem (a, b face and bottom respectively) of a selected produced dissimilar joints.

Table 5.1: Process parameters and design levels used

Variables	Code	Unit	Level 1	Level 2	Level 3	Level 4	Level 5
Laser Power	P	kW	1.05	1.15	1.24	1.33	1.43
Welding Speed	S	mm/min	500	750	1000	1250	1500
Focus	F	mm	-1	-0.75	-0.5	-0.25	0

Table 5.2: Shows the Taguchi design matrix in actual values of studied welding parameters.

Std	Run	P, kW	S, mm/min	F, mm	Std	Run	P, kW	S, mm/min	F, mm
3	1	1.05	750	-0.5	13	14	1.24	750	0
2	2	1.05	625	-0.75	11	15	1.24	500	-0.5
19	3	1.33	875	-0.75	6	16	1.15	500	-0.75
18	4	1.33	750	-1	20	17	1.33	1000	-0.5
21	5	1.43	500	0	15	18	1.24	1000	-0.75
25	6	1.43	1000	-0.25	17	19	1.33	625	0
8	7	1.15	750	-0.25	14	20	1.24	875	-1
1	8	1.05	500	-1	7	21	1.15	625	-0.5
12	9	1.24	625	-0.25	23	22	1.43	750	-0.75
4	10	1.05	875	-0.25	16	23	1.33	500	-0.25
9	11	1.15	875	0	24	24	1.43	875	-0.5
5	12	1.05	1000	0	10	25	1.15	1000	-1
22	13	1.43	625	-1					

Table 5.3: Shows the welding pool geometry, tensile strength, impact strength and cost per meter welding calculations.

Exp. No.	A, mm^2	W_1, mm	W_2, mm	Impact strength, J	Tensile strength, MPa	Cost, €/m
1	2.1	1.075	0.967	14	620	0.248
2	1.332	2.805	0.572	15	524	0.198
3	1.2	3.073	0.613	14	575	0.165
4	0.977	1.635	0.565	7	477	0.141
5	0.963	2.172	0.304	4	393	0.124
6	2.452	2.296	1.183	8	544	0.253
7	1.774	2.649	0.689	10	561	0.202
8	1.354	1.739	1.034	15	586	0.169
9	1.012	1.497	0.898	6	563	0.144
10	1.186	0.454	0.302	12	505	0.126
11	2.273	2.905	2.021	22	630	0.258
12	1.693	2.89	0.766	18	599	0.206
13	1.202	1.998	0.729	17	487	0.172
14	0.999	1.464	0.709	16	552	0.147
15	0.891	1.389	0.692	5	527	0.129
16	2.278	4.112	1.659	22	618	0.262
17	1.541	2.47	0.784	24	562	0.21
18	1.157	1.62	0.882	18	532	0.175
19	1.045	1.52	0.98	12	530	0.15
20	0.728	1.142	0.784	12	506	0.131
21	2.592	3.41	2.124	16	562	0.268
22	1.996	0.8	0.404	17	358	0.214
23	1.251	1.893	1.008	18	503	0.179
24	1.037	1.088	0.657	17	522	0.153
25	1.093	1.464	0.587	10	549	0.134

5.1.1Orthogonal Array Experiment

In the present study, the interactions between the welding parameters are considered. Therefore, the degrees of freedom owing to the three sets of five-level welding process parameters for each response were analyzed. The degrees of freedom for the orthogonal array should be greater than or at least equal to those for the process parameters. In this study, an L25 orthogonal array with three columns

and 25 rows was used. Twenty-five experiments were required to study the welding parameters using the L25 orthogonal array.

5.1.2 Development Mathematical Models for Welding Pool Geometry

Specimens for measuring the welding pool geometries and further metallographic examinations were prepared by polishing successively in 120, 240, 600 and 800 emery grits, followed by a final disc polishing using 9, 6 and 3 micron diamond slurry. The carbon steel side of the weldment was etched in 4% Nital, and the rest of the regions of the weldment were etched in a solution containing 20 ml hydrochloric acid, 1.0 g sodium meta bisulphate and 100 ml distilled water. Also, an electrolytic etching in 10% (w/o) oxalic acid was employed to reveal the features of weld metal and the evolved interfaces. The average of at least three measured results of welding pool area was considered for each sample. Fig. 5.2 shows the effect of the welding parameters and the variation on the total weld pool (fusion area) 'A', welding widths at the specimen surface 'W_1' and welding widths at the middle specimen depth 'W_2' of a selected experiments listed in Table 5.3.

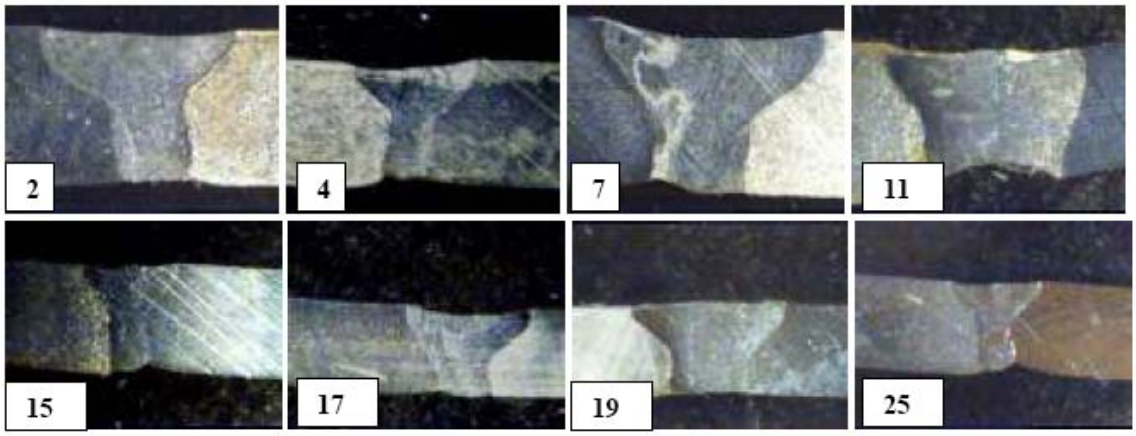

Fig. 5.2: Shows the effect of the welding parameters on the responses (A, W_1, W_2).

The fusion zone dimensions were measured by using the transverse sectioned specimens, optical microscope and image analyzer software. The measured responses are listed in the same Table 5.3. Design Expert 7 software was used for analyzing the measured responses.

The fit summary output indicates that the quadratic models which were developed by the software are statistically significant for the prediction of the responses (A, W_1 and W_2); therefore, they were used for further analysis. It was seen from the achieved results that the welding pool geometry, shape and penetration are controlled by the rate of heat input, which is a function of laser power and welding speed. Focusing position has also a strong effect on the responses.

5.1.2.1 The signal-to-noise (S/N) ratio analysis

In order to evaluate the influence of each selected factor on the responses: The signal-to-noise ratios S/N for each control factor were calculated. The signals had indicated that the effect on the average responses and the noises were measured by the influence on the deviations from the average responses, which would indicate the sensitiveness of the experiment output to the noise factors.

The appropriate formula for calculating S/N ratio must be chosen using previous knowledge, expertise, and understanding of the process.

When the target is fixed and there is a trivial or absent signal factor (static design), it is possible to choose the S/N ratio depending on the goal of the design. In this study, the S/N ratio was chosen according to the criterion the-smaller-the-better, in order to minimize the responses. The S/N ratio for the-smaller-the-better target for the responses (A, W_1, W_2) was calculated using Eqs 3.2 and 3.4 in which y is the average (of three or more) measured response.

The experimental layout for the welding process parameters using the L25 orthogonal array and test results are presented in Tables 5.2 and 5.3. The Taguchi experiment results, summarized in Table 5.4 and presented in Fig. 5.3, were obtained by means of MINITAB 13 statistical software The test results in Tables 5.2 and 5.3 were used with Eqs 3.2 and 3.4 to calculating S/N. It can be noticed from the S/N plot, that the travel speed ‘S’ is the most important factor affecting the responses; the minimum value of response is at the highest level of ‘S’. Focus position has a less relevant effect, while the laser power plots show the lowest effect among those factors. The main effects plot for S/N ratios suggest that those levels of variables would minimize the weld pool dimensions, and also produced welds that were robust against variability due to noise, as presented in Fig. 5.3.

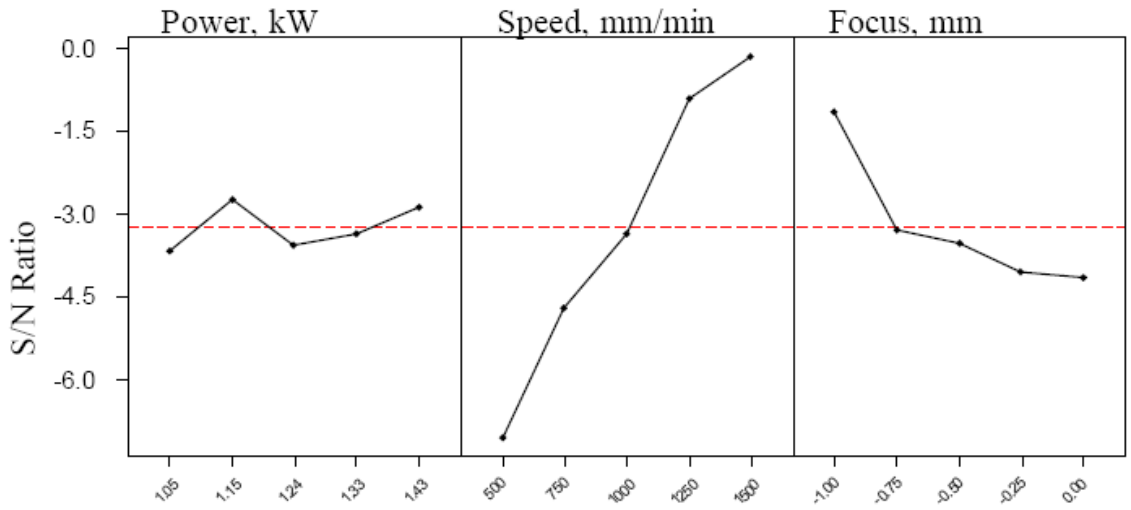

Fig. 5.3: Effects plot for S/N ratio of the (A, W_1 and W_2) on the responses with interactions considerations between the responses

Table 5.4: Response for signal-to-noise ratio (S/N)

Levels	1	2	3	4	5	Delta	Rank
P	1.35687	1.36793	1.50807	1.51347	1.42693	0.15660	3
S	2.22980	1.54433	1.38353	1.07220	0.94340	1.28640	1
F	1.07433	1.42060	1.50887	1.58973	1.57973	0.51540	2

5.1.2.2 Analysis of variance

The purpose of the ANOVA is to investigate which welding process parameters significantly affect the quality characteristic. This is accomplished by separating the total variability of the S/N ratios, which is measured by the sum of the squared deviations from the total mean of the S/N ratio, into contributions from each of the welding process parameter and also from error [114]. The test for significance of the regression model and the test for significance on individual model coefficients were performed using Design Expert 7 software. The backward elimination regression method; which eliminates the insignificant model terms automatically, was applied and the reduced suggested quadratic models are exhibited in the ANOVA Tables 5.5 to 5.7. The analyses of variances of the responses are summarized in Tables (5.5 to 5.7) and the significant models shown. The same Tables show also the other adequacy measures R^2, adjusted R^2 and adequate

precision. All adequacy measures were close to 1, which is reasonable and indicates an adequate model [159,171]. The adequate precision compares the range of the predicted value at the design points to the average predicted error. In this study the values of adequate precision for the A, W_1 and W_2 are significantly greater than 4. The adequate precision ratio above 4 indicates adequate model discrimination. The developed quadratic mathematical models in terms of coded factors and actual values are exhibited in Eqs. 5.1 to 5.6.

Final Equation for response 'A' in Terms of Coded Factors:

Fusion Area = 2.71+0.58*P-0.17*S -0.53*F -2.19*P*S +2.04*P*F+2.02*S*F -0.97 *P^2-0.58*S^2-1.01* F^2 **…(5.1)**

Final Equation for response 'A' in Terms of Actual Factors:

Fusion Area =-91.811 +103.438*P +0.037*S -39.850*F -0.023*P*S+ 21.526 * P* F +8.067E-003 * S * F -26.848* P^2 -2.3E-006* S^2 -4.023 F^2 **… (5.2)**

Table 5.5: ANOVA for response 'A'

Source	Sum of Squares	df	Mean Square	F_v Value	p-value Prob. > F_v	
Model	6.706	9	0.74511	31.7852	< 0.0001	significant
P	0.03421	1	0.03421	1.45941	0.2457	
S	0.00294	1	0.00294	0.12559	0.728	
F	0.02857	1	0.02857	1.21894	0.287	
PS	0.02953	1	0.02953	1.25988	0.2793	
PF	0.02582	1	0.02582	1.10156	0.3105	
SF	0.02627	1	0.02627	1.1207	0.3065	
P^2	0.02487	1	0.02487	1.0611	0.3193	
S^2	0.00858	1	0.00858	0.36605	0.5542	
F^2	0.02599	1	0.02599	1.10874	0.309	
Residual	0.35163	15	0.02344			
Cor. Total	7.05763	24				
R-Squared = 0.9502			Adeq. Precision = 17.485			
Adj. R-Squared = 0.9203						

Table 5.6: ANOVA for response W_1

Source	Sum of Squares	df	Mean Square	F_v Value	p-value Prob. > F_v	
Model	14.16920	8	1.771151	6.31649	0.0009	significant
P	1.82194	1	1.821936	6.497606	0.0214	
S	7.86075	1	7.86075	28.03395	< 0.0001	
F	5.17712	1	5.177118	18.46326	0.0006	
PS	1.32447	1	1.324469	4.723481	0.0451	
PF	1.68431	1	1.684313	6.0068	0.0261	
SF	2.65119	1	2.651188	9.454983	0.0073	
P^2	1.16524	1	1.165242	4.155626	0.0584	
S^2	1.17872	1	1.178717	4.203681	0.0571	
Residual	4.48642	16	0.280401			
Cor. Total	18.65562	24				
R-Squared = 0.7595			Adeq. Precision = 8.086			
Adj. R-Squared = 0.6393						

Final Equation for response W_1 in Terms of Coded Factors:

$W_1 = 1.21 - 0.54 * P - 1.11 * S + 0.85 * F + 1.12 * P * S - 1.45 * P * F - 1.79 * S * F + 0.77 * P^2 + 0.79 * S^2$ **… (5.3)**

Final Equation for response W_1 in Terms of Actual Factors:

$W_1 = 71.665 - 75.525 * P - 0.027 * S + 27.836 * F + 0.012 * P * S - 15.308 * P * F - 7.288E\text{-}003 * S * F + 21.461 * P^2 + 3.2E\text{-}006 * S^2$ **...(5.4)**

Table 5.7: ANOVA for response W_2

Source	Sum of Squares	df	Mean Square	F_v Value	p-value Prob. > F_v	
Model	3.8383	9	0.4265	5.2601	0.0024	significant
P	0.4329	1	0.4329	5.3387	0.0355	
S	0.2345	1	0.2345	2.8926	0.1096	
F	0.3301	1	0.3301	4.0711	0.0619	
PS	0.3833	1	0.3833	4.7274	0.0461	
PF	0.3758	1	0.3758	4.6345	0.0480	
SF	0.3634	1	0.3634	4.4818	0.0514	
P^2	0.3999	1	0.3999	4.9321	0.0422	
S^2	0.3126	1	0.3126	3.8550	0.0684	
C^2	0.4083	1	0.4083	5.0358	0.0403	
Residual	1.2162	15	0.0811			
Cor. Total	5.0544	24				
R-Squared = 0.7594			**Adeq. Precision** = 9.395			
Adj. R-Squared = 0.6150						

Final Equation for response W_2 in Terms of Coded Factors:

$W_2 = 6.52 + 2.08 * P + 1.53*S - 1.82*F - 7.88*P*S + 7.80*P*F + 7.50*S*F - 3.89*P^2 - 3.49*S^2 - 3.99* F^2$ **…(5.5)**

Final Equation for response W_2 in Terms of Actual Factors:

$W_2 = -364.106 + 401.8750* P + 0.149* S - 151.396* F - 0.083* P* S + 82.114*P*F + 0.0300*S*F - 107.646*P^2 - 1.4E-005*S^2 - 15.943*F^2$ **…(5.6)**

For the developed models of the three responses (A, W_1, and W_2), the analysis of variance indicates that the welding speed 'S' has the greatest affect on the responses. Focus position 'F' has a greater affect on the responses than laser power 'P'. The models indicate that all the studied parameters significantly affect the response. All the models indicate that the welding parameters have two level interactions, such as PS, PF and SF. For response 'A' the mathematical model including interactions between the parameters indicates that there are strong correlations between the considered welding parameters and their affect on the responses (A, W_1 and W_2). Interactions for response 'A' are exhibited in Fig 5.4 (a, b and c). Fig 5.4 (a) exhibits the interaction of the welding speed with laser power at focus position F= -0.5 mm. Fig 5.4 (b) exhibits the interaction of the laser power 'P' with focus 'F' at welding speed 'S' = 1000 mm/min. Fig. 5.4 (c) exhibits the interaction of the welding speed 'S' with focus position 'F 'at 'P' =1.24 kW.

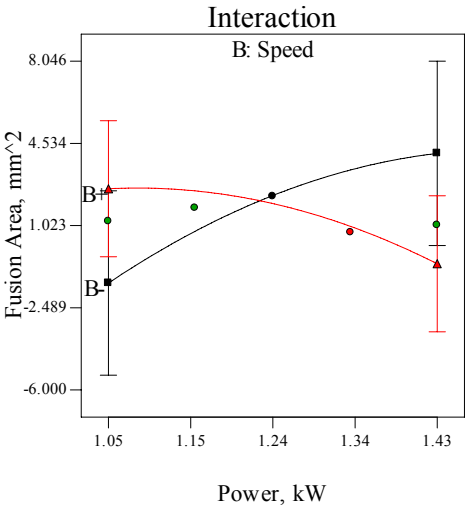

Fig 5.4 (a) at F= -0.5

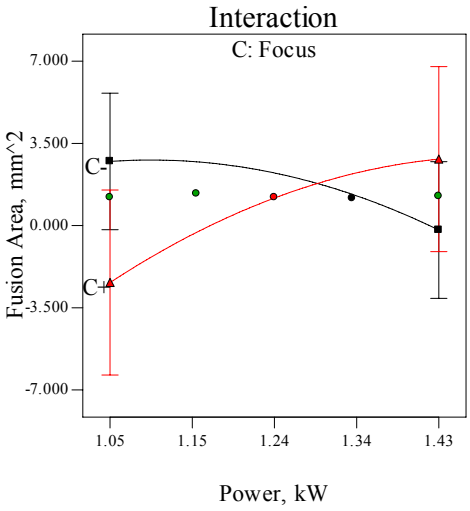

Fig 5.4 (b) at S=1000mm/min

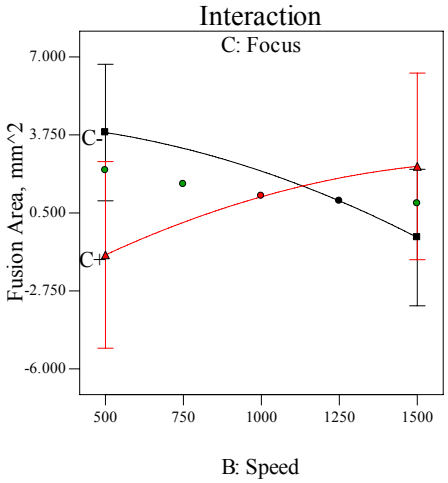

Fig. 5.4(c) at P= 1.24 kW

Fig 5.4 (a, b and c): Interactions between the welding parameters (P, S and F) with respect to the fusion area response.

The mathematical model for welding width at surface 'W_1' indicates interactions between the welding parameters that exhibited a strong relationship between the parameters and their effect on the response 'W_1'. Interactions for the response 'W_1' are exhibited in Fig 5.5 (a, b and c). Fig 5.5 (a) exhibits the intersection of the welding speed with laser power at focus position F= -0.5 mm. Fig 5.5 (b) exhibits the intersection of the laser power 'P' with focus 'F' at welding speed 'S' = 1000 mm/min. Fig. 5.5 (c) exhibits the intersection of the welding speed 'S' with focus position 'F 'at 'P' =1.24 kW.

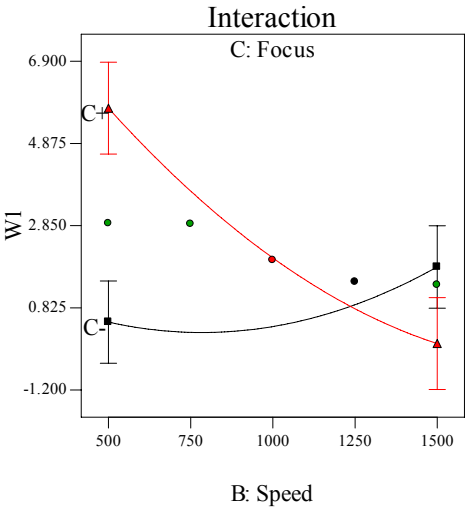

Fig 5.5 (a) at F= -0.5

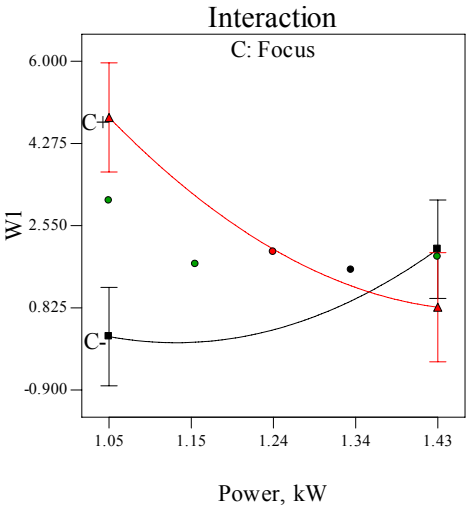

Fig 5.5 (b) at S=1000mm/min

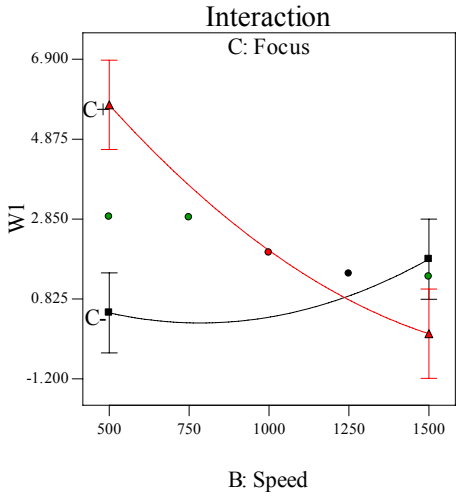

Fig. 5.5 (c) at P= 1.24 kW

Fig 5.5 (a, b and c): Interactions between the welding parameters (P, S and F) with respect to the welding width at surface 'W_1' response.

The quadratic mathematical model for welding width at the middle of specimen depth 'W_2' indicates interactions between the welding parameters that exhibited the strong relationship between the parameters and their effect on the response 'W_2'. Interactions for response 'W_2' are exhibited in Fig 5.6 (a, b and c). Fig 5.5 (a) exhibits the intersection of the welding speed with laser power at focus position F= -0.5 mm. Fig 5.6 (b) exhibits the intersection of the laser power 'P' with focus 'F' at welding speed 'S' = 1000 mm/min. Fig. 5.6 (c) exhibits the intersection of the welding speed 'S' with focus position 'F 'at 'P' =1.24 kW.

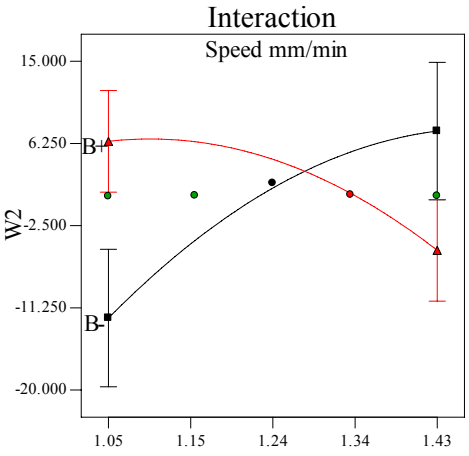

Fig 5.6 (a): at F= -0.5

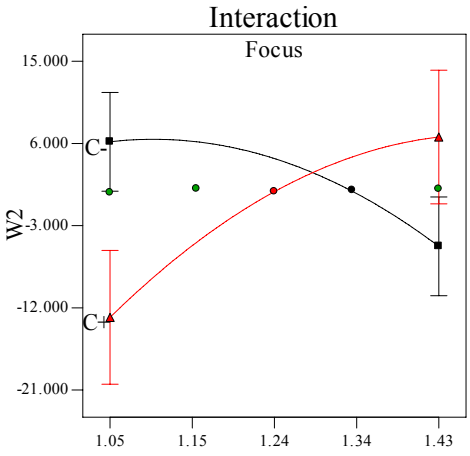

Fig 5.6 (b): at S=1000mm/min

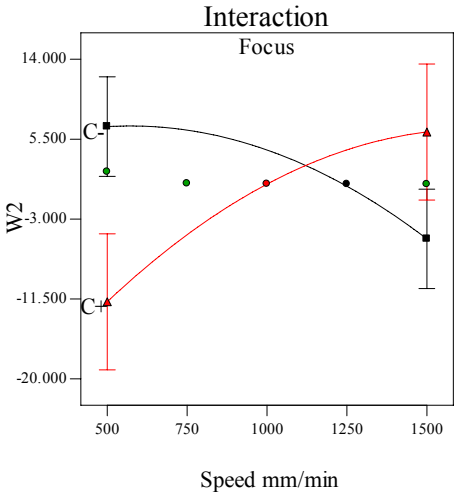

Fig. 5.6 (c): at P= 1.24 kW

Fig 5.6 (a, b and c): Interactions between the welding parameters (P, S and F) with respect to the welding width the middle of specimen 'W_2' response.

5.1.2.3 Model validation

The aim of this step is to predict and verify the improvement of the response using the optimal levels of the welding process parameters. Figs. 5.7 to 5.9 show the relationship between the actual and predicted values of A, W_1, and W_2, respectively. These figures indicate that the developed models are adequate because the residuals in prediction of each response are negligible, since the residuals tend to be close to the diagonal line.

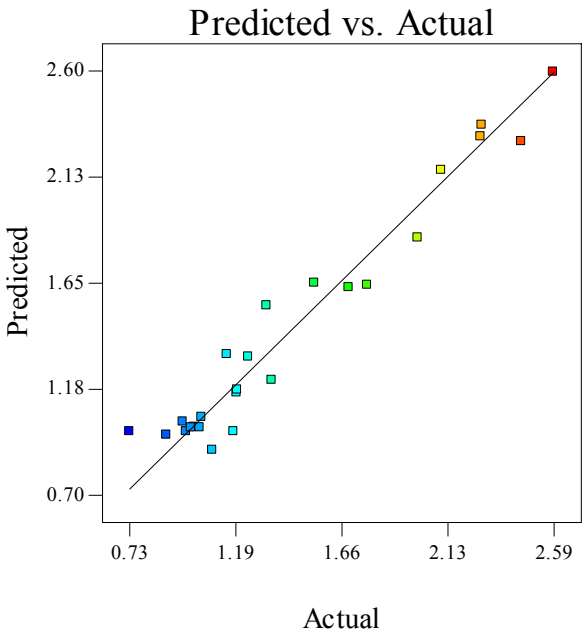

Fig 5.7: Exhibited predicted values of the fusion area vs. actual measured values.

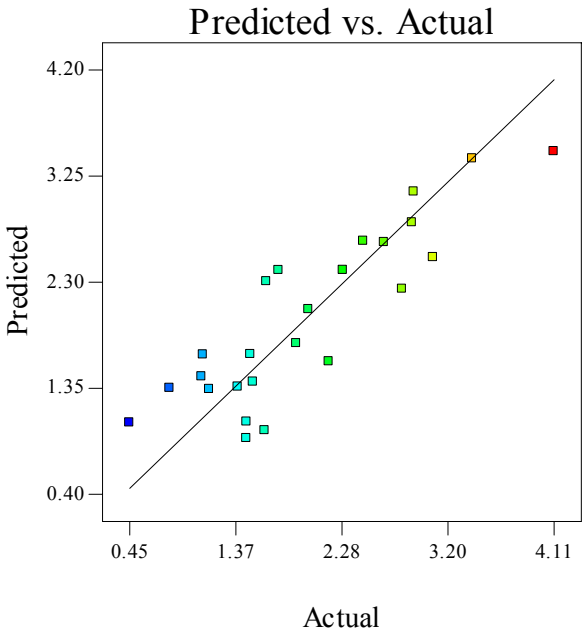

Fig 5.8: Exhibited predicted values of the W_1 vs. actual measured values.

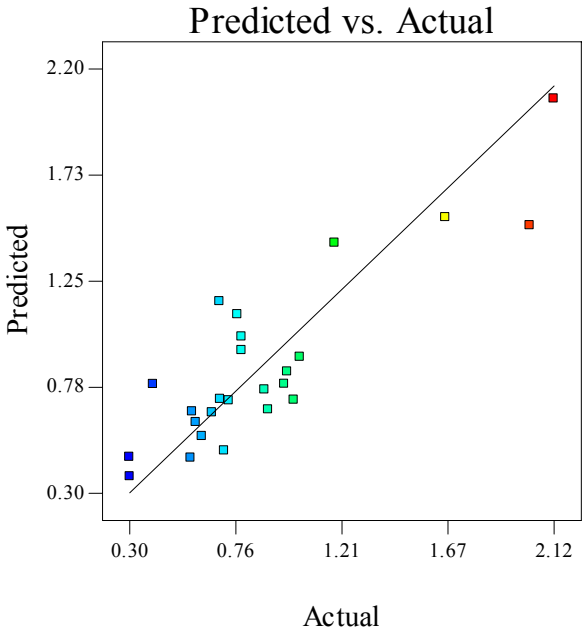

Fig 5.9: Exhibited predicted values of the W_2 vs. actual measured values.

Furthermore, to verify the satisfactoriness of the developed models, three confirmation experiments were carried out using new test conditions at different parameters conditions, obtained using the Design-Expert software and the developed mathematical models. The values of A, W_1 and W_2 for validation experiments were calculated using the Design-Expert software. Table 5.8 summarizes the experimental conditions, the actual experimental values, the predicted values and the percentages of absolute errors. It could be concluded that the models developed could predict the responses with a very small errors. A, W_1 and W_2 were greatly improved through this optimization.

Table 5.8: Confirmation experiments of the responses (A, W_1 and W_2)

Exp. No	**P, kW**	**S, mm/ min**	**F, mm**	**A, mm^2**		$\|E\|$ %	**W_1, mm**		$\|E\|$ %	**W_2, mm**		$\|E\|$ %
				Act.*	Pred.*		Act.	Pred.		Act.	Pred.	
1	1.15	1500	-1	1.023	0.941	8.7	1.130	1.061	6.5	0.289	0.302	4.3
2	1.07	1447	0	0.959	1.015	5.5	1.531	1.563	2.0	0.524	0.494	6.1
3	1.05	985	-.54	1.258	1.318	4.6	2.561	2.386	7.3	1.149	1.088	5.6

Act.* = Actual; Pred.* = Predicted

5.1.2.4: Effect of the parameters on responses

The reason for predicting the welding pool geometry is to develop a model which would include the optimizations step.

Welding pool area 'A'

The fusion area (welding pool) of dissimilar joints between stainless steel and low carbon steel was measured and is plotted in the contour graph in Figs. 5.10 (a, b). The graph shows that the welding speed has the most significant effect on the process. The increase in the welding speed rate, led to a decrease in the fusion area of welding pool. When S is at its maximum, at 1500 mm/min, the fusion area is at its minimum and equals 0.728 mm^2. This represents the optimal results.

It is also noted that changes in the laser power rate lead to a change in the response value. By increasing P the response tends to decrease to a lesser value at P equals 1.15 kW, then starts to increase to P equals 1.24 kW. Further increases of P value result in the response increasing again. The response has the least value at P equal to 1.33 kW these results are shown in Figs. 5.2 and 5.3. Fig. 5.10 (a) illustrates the relationship between S and P and the effect on the total welding pool area (A) at F = −0.5 mm. From Fig. 5.3, it is clear that the laser power has less effect on the process where by changing the laser power the response will not be consequentially changed and this is ensured in Table 5.4 in which the parameter has the greater value in S/N ratio ranking which is in agreement with findings of A. El-Batahgy [17].

The focus position parameter has a strong affect on welding pool volume and this is obvious from its S/N ratio ranking value in Table 5.4. Using a defocused beam, which is a wide beam, causes the laser power to spread to a wide area. Therefore, a wide area of the base metal will be melted leading to an increase in welding pool volume or vice versa, as is exhibited in Fig. 5.3. The relationship between the most effected welding parameters, S and F, and how they effect the fusion area is illustrated in contour graph in Fig 5.10 (b) at P = 1.24 kW.

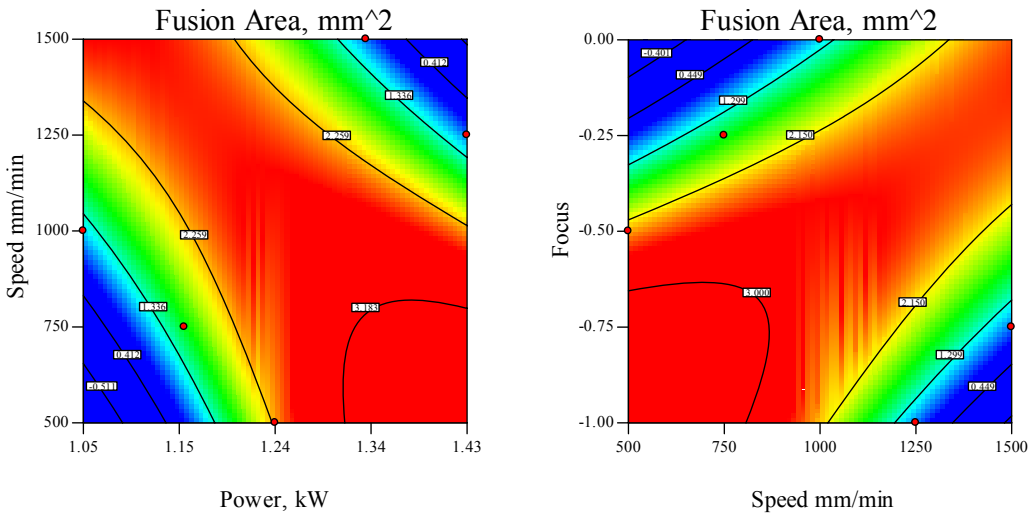

(a) Shows S vs. P at F = -0.5 mm (b) Shows S vs. F at P = 1.24 kW

Figs. 5.10 (a, b): Contour graphs exhibiting the effect of P, S and F parameters on the response A.

Welding Pool Width at the Work Piece surface 'W_1'

The results and the model obtained for the response indicate that the S and F are the most important factors affecting the W_1 value. An increase in S leads to a decrease in W_1. This is due to that the laser beam traveling at high speed over the welding line when S is increased. Therefore, the heat input decreases leading to less volume of the base metal being melted, consequently the width of the welded zone decreases. Moreover, a defocused beam, which is in a wider laser beam, results in spreading the laser power onto a wide area. Therefore, a wide area of the base metal will be melted leading to an increase in W_1 or vice versa. The result shows also that P contributes secondary effect in the response width dimensions. Increasing P results in a slight increase in W_1, due to the increase in the power density. Figs. 5.11 (a, b) shows contour plots for the effect of the process parameters on the W_1 width. Fig. 5.11 (a) illustrating the relationship between S and P with their impact on the total welding pool width (W_1) at F = -0.5 mm. The relationship between the welding parameters, S and F, and how they are effect W_1 is illustrated in contour graph in Fig 5.11 (b) at P = 1.24 kW.

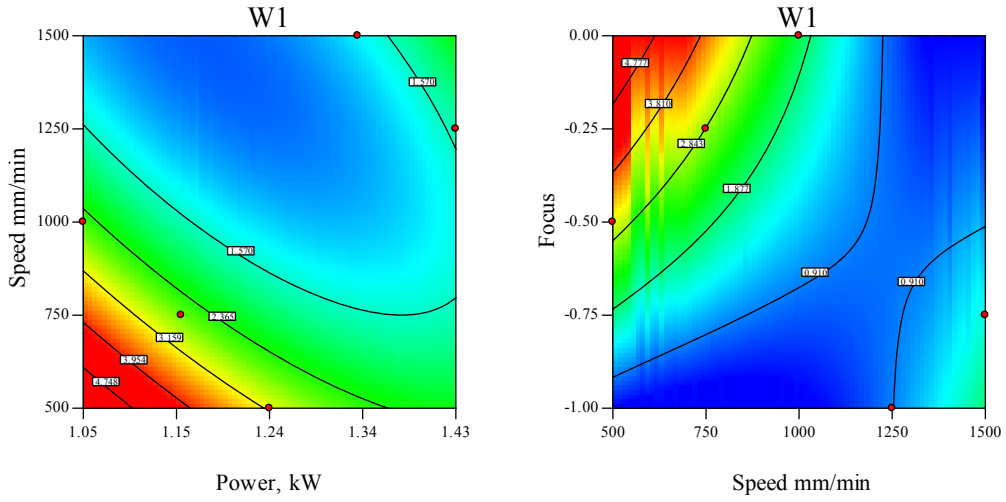

(a) Shows S vs. P at F = -0.5 mm (b) Shows S vs. F at P = 1.24 kW

Figs. 5.11 (a, b): Contour graphs exhibiting the effect of P, S and F parameters on the response W_1.

Welding Pool Width at the Middle of the Work Piece 'W_2'

From the results it is clear that the three welding parameters significantly affect the W_2 value with different rates. Using a focused beam results in an increase in the power density, this means that the heat will be localized in a small portion of the component being welded. This results in an increase in the power density, leading to an increase in the value of W_2. The model shows that the response is inversely proportional to F. The result shows that the changes in F parameter effects W_1, W_2 and effect A. As a result, as F is decreased, W_1 is increased and W_2 is decreased and vice versa. The increase in P leads to an increase in the heat input, therefore, more molten metal and consequently a wider W_2 will be achieved. However, the idea is reversed in the case of the S effect, because the S is inversely proportional to the heat input. The relationship between S and P with their effect on the welding pool width at the middle of specimen (W_2) is exhibited in Fig. 5.12 (a) at F = -0.5 mm. The relationship between the most effected welding parameters, S and F, and how they affect the response (W_2) is illustrated in contour graph in Fig 5.12 (b) at P = 1.24 kW.

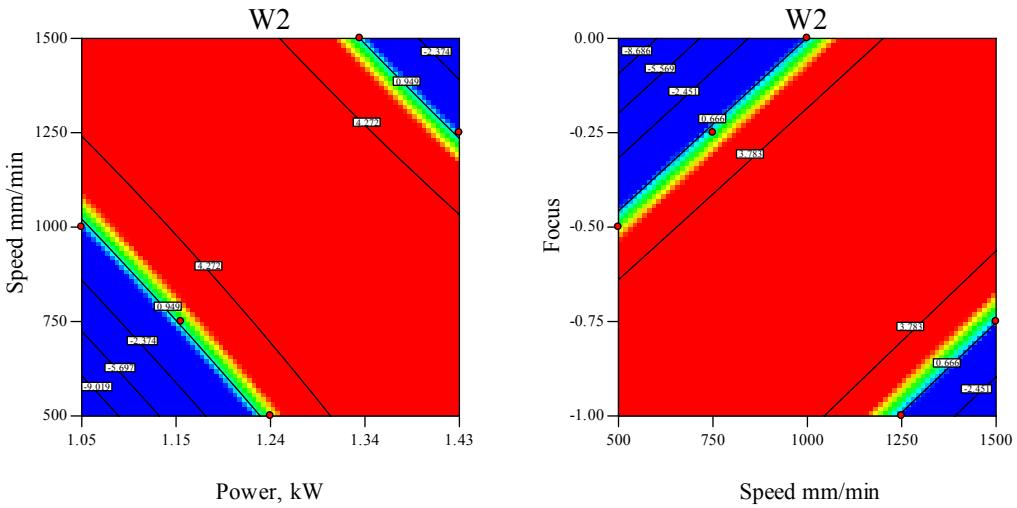

(a) S vs. P at F = -0.5 mm (b) S vs. F at P = 1.24 kW

Figs. 5.12 (a, b): Contour graphs exhibiting the effect of P, S and F parameters on the response W_2.

5.1.3 Development Mathematical Model for Impact Strength

The performance of the welded components in real life is sensitive to the service temperature. The welded components become very tough as the surrounding temperature decreases or vice versa. Hence, the most important mechanical property in this case is the impact strength resistance. The following section was carried out to study the effect of welding parameters and their relationships on the impact strength of the dissimilar joints.

5.1.3.1 The signal-to-noise (S/N) ratio analysis

The S/N ratio of the impact toughness was analyzed in accordance with the "larger is better" criterion to maximize the response. The impact strength was calculated by using Eqs 3.3 and 3.4 and the test results are presented in Table 5.3. The Taguchi experimental results for impact resistance were obtained using MINITAB 13 statistical software and are summarized in Table 5.9 and presented in Fig. 5.13. From the obtained result, it is obvious that the impact resistance is mainly affected by the laser power and welding speed, while the focal position has less effect on the response, as shown in Table 5.9. The rank "1" in Table 5.9 indicates that the power has a stronger effect on the process followed by rank "2" which means

that the welding speed parameter also has a strong effect on the process. Rank "3" in the same Table indicates that the focus position parameter has the minimum effect on the process.

Table 5.9: Response for signal-to-noise ratio (S/N).

Levels	1	2	3	4	5	Delta	Rank
P	19.6620	19.7461	22.9249	25.5172	23.6812	5.8552	1
S	23.7527	24.1681	24.2529	20.5480	18.8097	5.4431	2
F	23.6606	20.4504	24.1649	22.4755	20.7800	3.7145	3

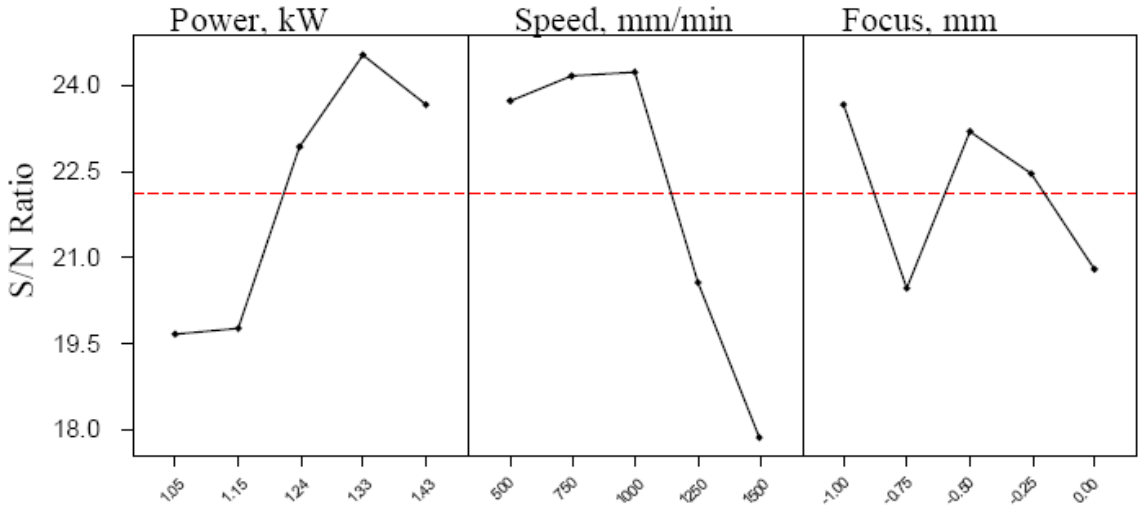

Fig. 5.13 Effects of the parameters on the impact test and S/N ratio.

5.1.3.2 Analysis of variance

To analyze the effects of the welding parameters in more detail, analysis of variance, using the backward elimination regression method ANOVA was conducted and the results are shown in Table 5.10 for the reduced cubic model. High F_v value for a parameter means that the effect of the parameters on the joints characteristics is large. The results show that the highest value F_v is at laser power of about 12.965, and at a speed and focus equal to 8.337 and 5.890 respectively. This means that speed and focus parameters have less effect on the process. The same Table shows the other adequacy measures R^2, Adjusted R^2 and Predicted R^2. All the adequacy measures indicate an adequate cubic model. The adequate precision is 10.688,

indicating adequate model discrimination. The developed cubic mathematical model in terms of coded factors and actual values are exhibited in Eqs 5.7 and 5.8.

Table 5.10: Shows the ANOVA for the impact strength.

Source	Sum of Squares	df	Mean Square	F_v Value	p-value Prob. > F_v	
Model	645.438	16	40.340	7.772	0.0031	significant
P	67.291	1	67.291	12.965	0.0070	
S	43.271	1	43.271	8.337	0.0203	
F	30.570	1	30.570	5.890	0.0414	
PS	38.429	1	38.429	7.404	0.0262	
PF	13.653	1	13.653	2.631	0.1435	
SF	29.767	1	29.767	5.735	0.0435	
P^2	38.843	1	38.843	7.484	0.0256	
S^2	28.369	1	28.369	5.466	0.0476	
F^2	42.872	1	42.872	8.260	0.0207	
P^2S	41.641	1	41.641	8.023	0.0221	
PS^2	42.149	1	42.149	8.121	0.0215	
PF^2	39.321	1	39.321	7.576	0.0250	
SF^2	44.717	1	44.717	8.616	0.0188	
P^3	61.150	1	61.150	11.782	0.0089	
S^3	37.343	1	37.343	7.195	0.0278	
F^3	45.849	1	45.849	8.834	0.0178	
Residual	41.522	8	5.190			
Cor. Total	686.960	24				
R-Squared = 0.9396				Adeq Precision = 10.688		
Adj R-Squared = 0.8187						

Final Equation in Terms of Coded Factors:

Impact Strength = -10.12+68.55* P +47.12* S +138.18* F +81.10 * P * S -11.66 * P * F -17.31 * S * F +38.56 * P^2 +34.85 * S^2 -24.08 * F^2 -121.65 * P^2 * S -135.24 * P * S^2 +133.49 * P * F^2 +130.06 * S* F^2 -53.35 * P^3 -43.05 * S^3 -86.84 * F^3 **…(5.7)**

Final Equation in Terms of Actual Factors:

Impact Strength = 30361.887-57938.750* P -19.474* S -4644.950* F +23.261* P* S +2687.717 * P * F +0.971 * S * F +36740.778* P^2 +4.70E-00* S^2-5663.735* F^2 6.739 * P^2* S-2.85E-003 * P* S^2 +2810.41629 * P* F^2 +1.040* S * F^2-7777.757* P^3-3.44E-007 * S^3-694.699 * F^3 **…(5.8)**

5.1.3.3 Validation of the model

Fig. 5.14 shows the actual response versus predicted response for impact strength. The measured values tend to be close to the diagonal line, indicating that the model adequately describes the response within the limits of the factors being investigated herein. To insure the results validation, three extra conformation experiments were carried out using test conditions, which are selected within the studied range of the parameters. Table 5.11 shows the actual and predicted values of the impact strength and the percentage of absolute error in the prediction. The impact strength of laser welded component has been increased by about 5 – 25 % from that of the base metal.

Table 5.11: Confirmation experiments of the impact strength

Exp. No	P, kW	S, mm/min	F, mm	Impact Strength, J		$\|E\|$ %
				Act.	Pred.	
1	1.05	1500	-0.25	31	33	6
2	1.17	1500	-1	31	30	3
3	1.05	1050	-0.3	28	30	6

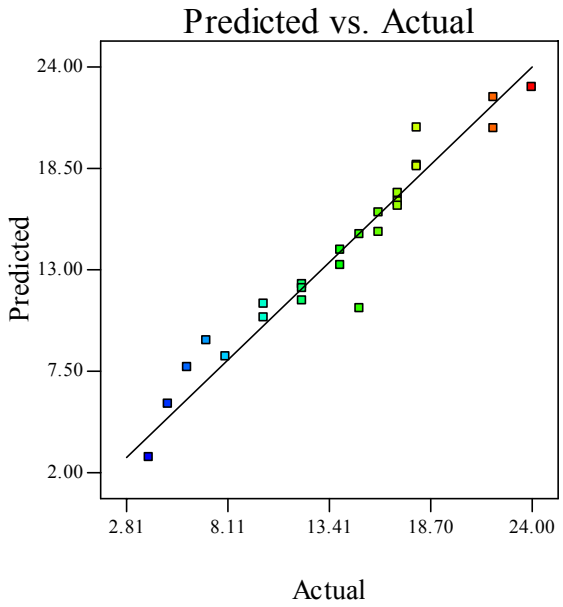

Fig 5.14: Exhibited predicted values of the impact strength resistance test vs. actual measured values

5.1.3.4 Effect of process parameters on the response

Laser Power: The results indicated that the laser power is the most significant factor associated with impact strength, as shown in Fig. 5.13. It is clear that the higher laser power resulted in higher impact strength, due to the fact that using high laser power results an increase in the power density, at a given focus point position, leading to more penetration and more heat input to work piece, which would improve the impact strength. The relationship between S and P and their effect on impact strength is exhibited in a contour graph exhibited in Fig. 5.15 at F = -0.5 mm.

Welding Speed: It is evident from the results that the welding speed also has a strong effect on the impact strength of the laser-welded joint, as shown in Fig. 5.13. The impact strength has the highest value at speed of 1000 mm/min; a further increase in speed will lead to a decrease in impact toughness.

Focus Point Position: The results indicate that the focus point position has a powerful effect on the impact strength. In general, using a focused laser beam means that the laser power will be localized onto a small area; this would result in an increase in the power density leading to better penetration and sound welds. Fig. 5.16 shows perturbation plots exhibiting the effect of welding parameters on the impact strength**.** The perturbation plot helps to compare the effect of all the factors at a particular point in the design space. The response is plotted by changing only one factor over its range while holding the other factors constant. By default, Design-Expert sets the reference point at the midpoint (coded 0) of all the factors. The midpoint can be changed to be any point.

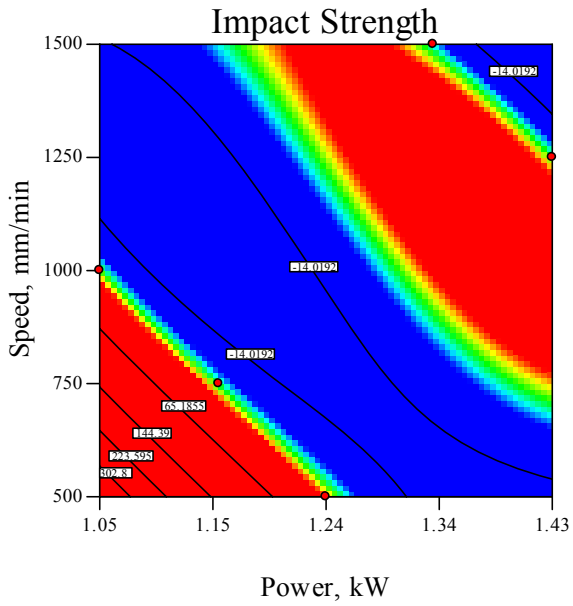

Fig. 5.15: Contour graphs exhibiting the effect of P, S and F parameters on the impact strength at F = -0.5 mm.

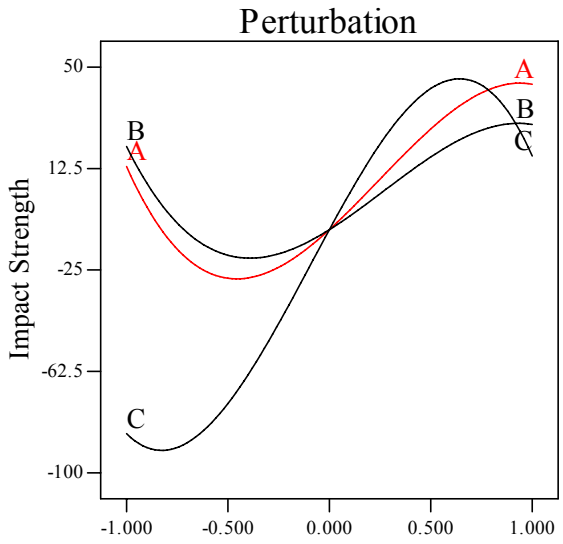

Fig.5.16 Perturbation plots exhibiting the effect of welding parameters on the impact strength.

5.1.4 Development of a Mathematical Model for Tensile Strength

The welded components become very tough as the surrounding temperature decreases or vice versa. Hence, tensile strength is one of the most important mechanical properties in this case especially in joining dissimilar components. Using Taguchi orthogonal design and designed welding parameters presented in Table 5.2, the joints strength for the specimens was determined using the notched tension strength (NTS) method using the NTS sample shown in Fig. 4.15. The average result of five or more NTS samples were tested and presented in Table 5.3. The tested result had been analyzed using Design Expert 7 software

The fit summary output indicates that the linear model which is developed by the software is statistically significant for the prediction of the tensile strength therefore it will be used for further analysis. It has been seen from the achieved results that the tensile strength is mostly affected by laser power and welding speed. Focusing position has also a strong effect on the responses.

5.1.4.1 The tensile strength signal-to-noise (S/N) ratio analysis

The average NTS tests appear to be mainly affected by the welding speed and laser power as shown in Table 5.2. For tensile strength, the S/N ratio was chosen according to the criterion the-bigger-the-better, in order to maximize the response. The S/N ratio for the-bigger-the-better target for the response was calculated using Eqs 3.3 and 3.4 in which y is the average (of three or more) measured responses. The results presented in Table 5.2 were used with Eqs 3.3 and 3.4 to calculate S/N. The Taguchi experiment results, which were obtained by means of MINITAB 13 statistical software, are summarized in Table 5.12. The rank 1 in Table 5.12 indicates that (1) welding speed has stronger effect on the process followed by rank (2) laser power parameter which has less effect, while rank (3) focus position has the minimum effect on the process.

Table 5.12: Shows the response for S/ N Ratio for tensile strength

levels	1	2	3	4	5	Delta	Rank
P	54.1772	54.8250	54.9122	54.6483	53.8497	1.0625	2
S	55.4722	54.1974	54.5703	54.4516	53.7210	1.7513	1
F	54.0697	54.4103	54.7873	55.0176	54.1276	0.9479	3

5.1.4.2 Analysis of variance

Analysis of the effects on the welding parameters in more detail was carried out using analysis of variance with implementing the backward elimination regression method (ANOVA) using Design Expert 7 software. The analysis results for the reduced linear model which is suggested by the software for the calculated tensile values are shown in Table 5.13. High F_v value for a parameter means that the parameter effect on the joints characteristics is large. The results show that the highest value F_v, is at a welding speed of about 11.498, but at the laser power and the focus are equal to 4.836 and 4.763 respectively, which means that power and focus parameters have less effect on the process. Other model adequacy measures R^2, Adjusted R^2 and Predicted R^2 are presented in the same table. All the adequacy measures indicate an adequate linear model. The adequate precision is 9.535, indicating adequate model discrimination. The developed liner mathematical model in terms of coded factors and actual values are exhibited in Eqs. 5.9 and 5.10.

Final Tensile Strength Equation in Terms of Coded Factors:

Tensile Strength =533.91-28.64*P -40.83*S +28.42*F +81.92*P*S -76.48*S*F **(5.9)**

Final Tensile Strength Equation in Terms of Actual Factors:

Tensile Strength = 2053.165 -1013.070*P -1.304*S +362.783*F +0.862*P*S -0.306*S* F **…(5.10)**

Table 5.13: Shows the ANOVA for the tensile strength

Source	Sum of Squares	d f	Mean Square	F Value	Prob. > F	
Model	64038	5	12808	7.0673	0.0007	significant
P	8764	1	8764	4.8362	0.0405	
S	20837	1	20837	11.4977	0.0031	
F	8631	1	8631	4.7626	0.0418	
PS	30828	1	30828	17.0112	0.0006	
SF	26872	1	26872	14.8282	0.0011	
Residual	34433	19	1812			
Cor. Total	98471	24				
R-Squared = 0.6503			Adeq Precision = 9.535			
Adj. R-Squared = 0.5583						

For the tensile strength the developed linear model, the analysis of variance indicates that welding speed ‘S’ is the stronger welding parameter affecting the responses. Laser power parameter ‘P’ has a greater effect on the responses than Focus position ‘F’. The model indicates that all the studied parameters significantly affect the response. The model indicates that the welding parameters have two level interactions, such as PS and SF. The mathematical model including interactions between the parameters indicates that there are strong relations between the considered welding parameters in their affect on the responses. Interactions on the response are exhibited in Fig 5.17 (a, b). Fig 5.17 (a) exhibits the interaction of the welding speed with laser power at focus position F= -0.5 mm, while Fig. 5.4 (b) exhibits the interaction of the welding speed ‘S’ with focus position ‘F ’at ‘P’ =1.24 kW.

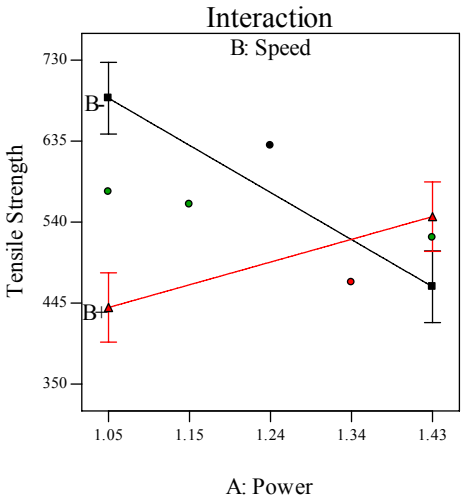

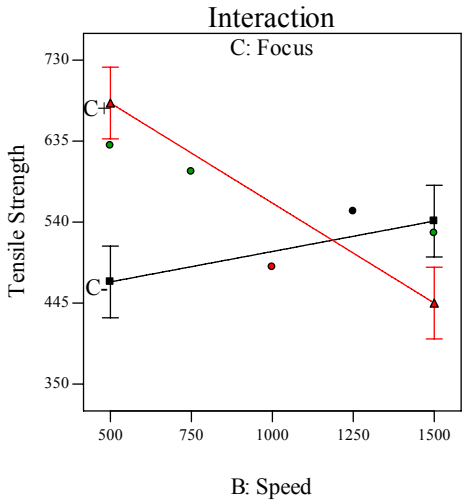

Fig 5.17 (a) at F= -0.5 mm Fig. 5.17(c) at P= 1.24 kW

Fig 5.17 (a, b): Interactions between the welding parameters (P, S and F) with respect to the tensile strength.

5.1.4.3 Model validation

Fig. 5.18 shows the actual measured tensile strength versus predicted tensile strength values. From the figure, it can be seen that the measured values tend to be close to the diagonal linear, indicating that the model can adequately describe the response within the limits of the factors being investigated herein. Furthermore, three extra experiment conformations were carried out using test conditions which are selected within considered range of the parameters. Table 5.14 shows the actual and predicted values of the response and the percentage of error in prediction. It can be seen that the NTS value obtained after laser welding is greater than the base metal value.

Table 5.14: Confirmation experiments of the tensile strength

Exp. No	P, kW	S, mm/min	F, Mm	Tensile Strength, J		$\|E\|$ %
				Act.	Pred.	
1	1.29	1500	-1	576	555	3.8
2	1.07	900	00	589	627	6.01
3	1.05	810	-.04	618	667	7.35

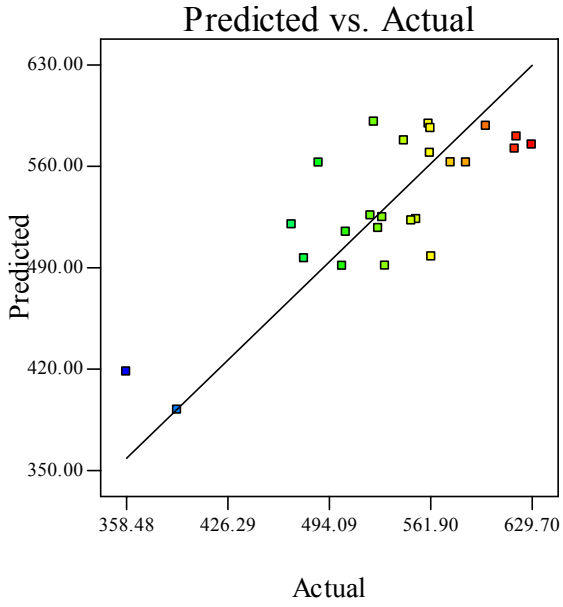

Fig. 5.18**:** Predicted values of the tensile strength resistance test vs. actual measured values.

5.1.4.4 Effect of the parameters on tensile strength

Laser Power: High power density at the workpiece is crucial to achieve keyhole welding and to control the formation of welds. It can be seen that the laser power also has a strong effect on the tensile strength of the laser-welded joint, as presented in Table 5.12. In fact, the higher laser power resulted in a higher response value, due to the fact that using high laser power would increase the power density. This leads to more penetration resulting in an improved response. Fig.19 shows a 3D graph of the effect of P and S on the tensile strength at F = -0.50 mm.

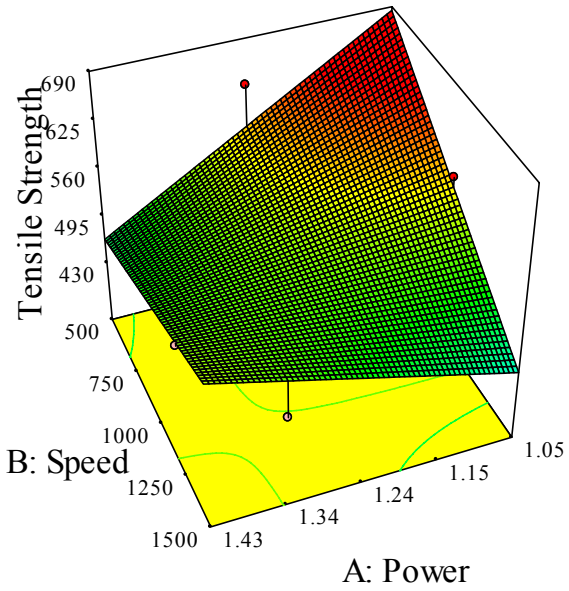

Fig.5.19: A 3D graph of the effect of P and S on the tensile strength at F = -0.50mm.

Welding speed: It is evident from the results that the welding speed is the most significant factor associated with the response, as presented in Table 5.12. The highest tensile strength value was observed to be at a speed of 500 mm/min. It is evident that by increasing welding speed the response would decrease. The tensile strength is inversely proportional to the welding speed.

Focus point position: The results indicate that the focus point position has an obvious effect on the response within the parameter range domain applied. Changing the focus point position significantly affects the tensile strength, causing it to decrease or increase. Fig. 5.20 (a, b) contours graph exhibits the effect of welding parameters (P, S, F) on tensile strength of dissimilar joints.

Fig.5.21 perturbation plotted shows the effect of all the considered welding parameters on the tensile strength at a midpoint in the design space. The response is plotted by changing only one factor over its range while holding of the other factors constant.

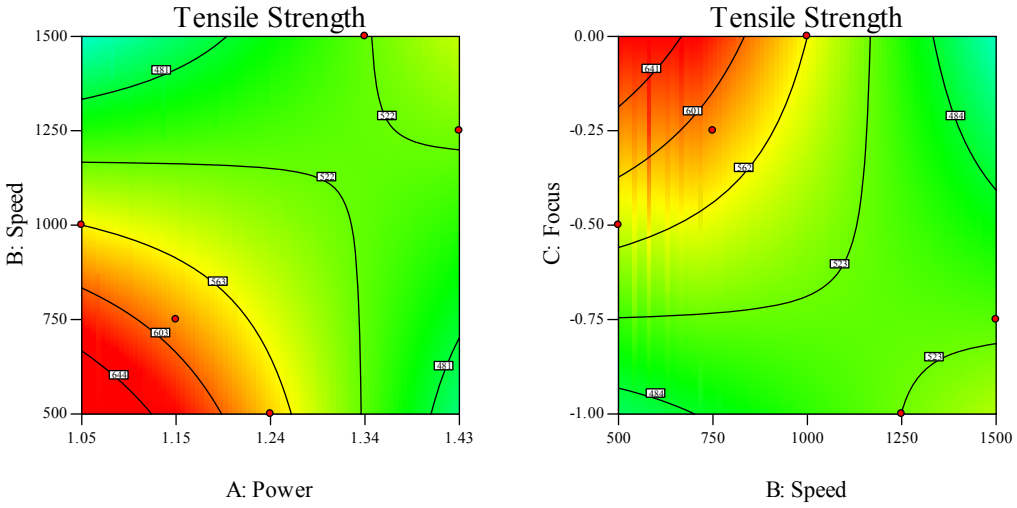

(a) The response F= -0.5mm (b) The response at P= 1.24 kW

Fig. 5.20 (a, b): Contours graph exhibiting the effect of welding parameters (P, S, and F) on tensile strength.

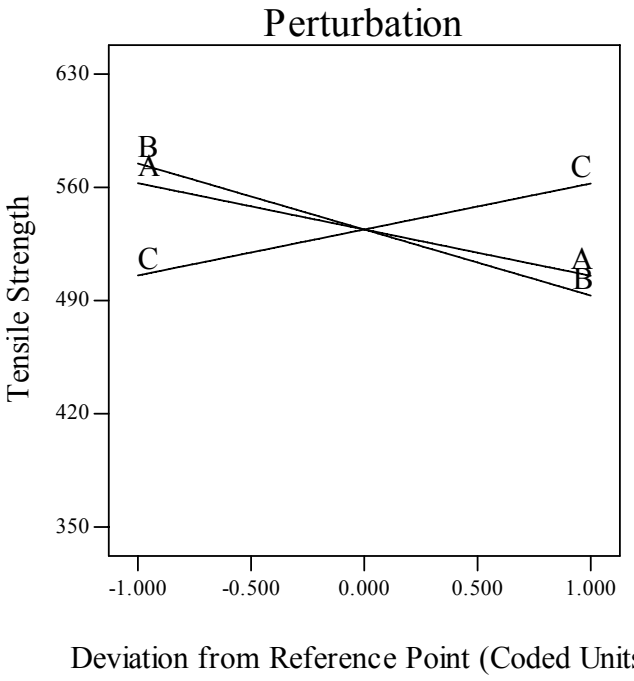

Fig.5.21: Perturbation plots exhibiting the effect of welding parameters on the tensile strength, where: A = power, B = Speed and C = Focus.

5.1.5 Operating Cost Modeling

The operating costs for joining the above mentioned dissimilar materials were calculated using Eq. 4.13. The mathematical model was developed to minimize the operating cost. Same procedure was followed to check the model adequacy. The analysis results are shown in Table 5.15 for the reduced quadratic model which is suggested by software for the received result of the welding operating cost. The same table shows the other adequacy measures R^2, Adjusted R^2 and Predicted R^2. All the adequacy measures indicate an adequate quadratic model. The adequate precision of 123.449 indicates adequate model discrimination. The developed quadratic mathematical model in terms of coded factors and actual values are exhibited in Eqs. 5.11 and 5.12.

Final Operating Welding Cost Equation in Terms of Coded Factors:

Operating Cost = 0.20 +0.018* P -0.052* S -0.011* F -0.047* P * S +0.044* P * F +0.043* S* F -0.021* P^2 -0.022* F^2 **…(5.11)**

Final Operating Welding Cost Equation in Terms of Actual Factors:

Operating Cost = -1.728 +2.273*P +5.899E-004*S -0.86187*F -4.906E-004*P*S +0.4681* P*F +1.727E-004*S*F -0.586* P^2-0.087* F^2 **…(5.12)**

Table 5.15: Shows the ANOVA for the welding operating cost

Source	Sum of Squares	df	Mean Square	F_v Value	p-value Prob. > F_v	
Model	0.0530	8	0.0066	1763	< 0.0001	significant
P	0.0021	1	0.0021	549	< 0.0001	
S	0.0199	1	0.0199	5287	< 0.0001	
F	0.0007	1	0.0007	197	< 0.0001	
PS	0.0017	1	0.0017	460	< 0.0001	
PF	0.0021	1	0.0021	553	< 0.0001	
SF	0.0015	1	0.0015	410	< 0.0001	
P^2	0.0009	1	0.0009	231	< 0.0001	
F^2	0.0009	1	0.0009	239	< 0.0001	
Residual	6E-05	16	3.8E-06			
Cor. Total	0.05305	24				
R-Squared = 0.9989			Adeq. Precision = 123.449			
Adj. R-Squared = 0.9983						

5.1.6 Models Optimization

5.1.6.1 Single -response optimization

The developed models were used for optimizing the welding input parameters. The optimizations were calculated for each model separately without taking the other responses into consideration. This is to convene practical demand for certain mechanical properties in industrial applications. The achieved results were based on the criteria presented in Table 5.16. In the same table, the selected importance of each factor is presented. The selected importance greatly affects the result and it is essential to select it correctly. The numerical optimization results based on individual response calculation are presented in Table 5.17.

Table 5.16: Shows the optimization criteria for input/output welding parameters

Parameter	**Power**	**Speed**	**Focus**	**Welding Pool geometry**			**Tensile Strength**	**Impact Strength**	**Cost**
Criteria	min	max	In range	A	W_1	W_2	max	max	min
				min	Min	In range			
Importance	+ + +	+ + +		+ + + +	+ + + +		+ + + + +	+ + + + +	+ + + +

Table 5.17: Shows the numerical optimization results based on individual response

parameter	**Power, min.**	**Speed, max.**	**Focus, in range**	**Response Value**			**Desirability**
Welding Pool	1.15	1500	-1.00	A	W_1	W_2	0.857
				0.941	1.061	0.302	
Tensile Strength	1.05	905.741	00	629			0.703
Impact Strength	1.05	1500	-0.26	32.464			1.000
Operating Cost	1.05	1500	0.00	0.12			0.998

5.1.6.2 Multiple -response optimization

In practical industrial applications a total optimization may be desired, for this reason a multiple-response could be a solution. Multiple-response (all input/output welding parameters) optimization can be achieved using the optimization process in the Design-Expert software in the search for a combination of factor levels that simultaneously satisfy the requirements placed (i.e. optimization criteria) on each one of the input/output welding parameters. The goals are combined into an overall desirability function and the optimization performed can be numerical and/or graphical optimization. Numerical and graphical optimization methods were used in this research by selecting the desired goals for each factor and response.

The numerical optimization process involves combining the goals into an overall desirability function (D). The numerical multiple-response optimization criterion is to reach maximum tensile strength, maximum impact strength and minimum welding pool geometry, minimum welding operating cost with minimizing laser power and maximizing welding speed, while focus position was kept in range. The importance for all input/output welding parameters was selected to be the same (+ + +). Table 5.18 presents the ten optimal solutions based on the chosen optimization criteria as determined by Design-Expert software using numerical multiple-response. The ramps view in Fig. 5.22 exhibits the first optimal solution in Table 5.18. However, the achieved values for the responses using multiple-response optimization are less than those values obtained by applying the single-response optimization.

In a graphical optimization with multiple responses, the software defines regions where requirements simultaneously meet the proposed criteria. Also, superimposing or overlaying critical response contours can be defined on a contour plot. Then, a visual search for the best compromise becomes possible. In the case of dealing with many responses, it is recommended to run numerical optimization first; otherwise it could be impossible to find out a feasible region. The graphical optimization displays the area of feasible response values in the factor space.

Regions that do not fit the optimization criteria are shaded [172]. The graphical optimization allows visual selection of the optimum welding conditions according to certain criterion. The result of the graphical optimization are the overlay plots, these type of plots are extremely practical for quick technical use in the workshop to choose the values of the welding parameters that would achieve a certain response value for this type of dissimilar materials. The yellow /shaded areas on the overlay plot in Fig. 5.23 are the regions that meet the proposed criteria.

Table 5.18: Shows the ten optimal solutions using numerical multiple-responses

No	Power, kW	Speed, mm/min	Focus, Mm	A, mm^2	W_1, mm	W_2, mm	Impact, J	Tensile, MPa	Cost €/m	D
1	1.16	1487	-0.99	0.931	1.070	0.300	14.7	517	0.13	0.70
2	1.16	1498	-0.98	0.933	1.093	0.300	14.7	516	0.13	0.70
3	1.2	1379	-1	0.915	0.966	0.300	16.4	524	0.13	0.69
4	1.23	1427	-0.87	0.875	1.256	0.300	17.3	524	0.13	0.68
5	1.24	1436	-0.83	0.865	1.317	0.300	17.6	524	0.13	0.68
6	1.26	1500	-0.71	0.847	1.441	0.300	17.4	520	0.13	0.67
7	1.21	1326	-1	0.956	0.925	0.426	15.1	525	0.14	0.66
8	1.29	1500	-0.64	0.832	1.465	0.300	17.7	521	0.13	0.65
9	1.29	1376	-0.76	0.852	1.413	0.300	19.2	527	0.14	0.65
10	1.27	1268	-0.9	0.919	1.183	0.300	19.6	525	0.14	0.65

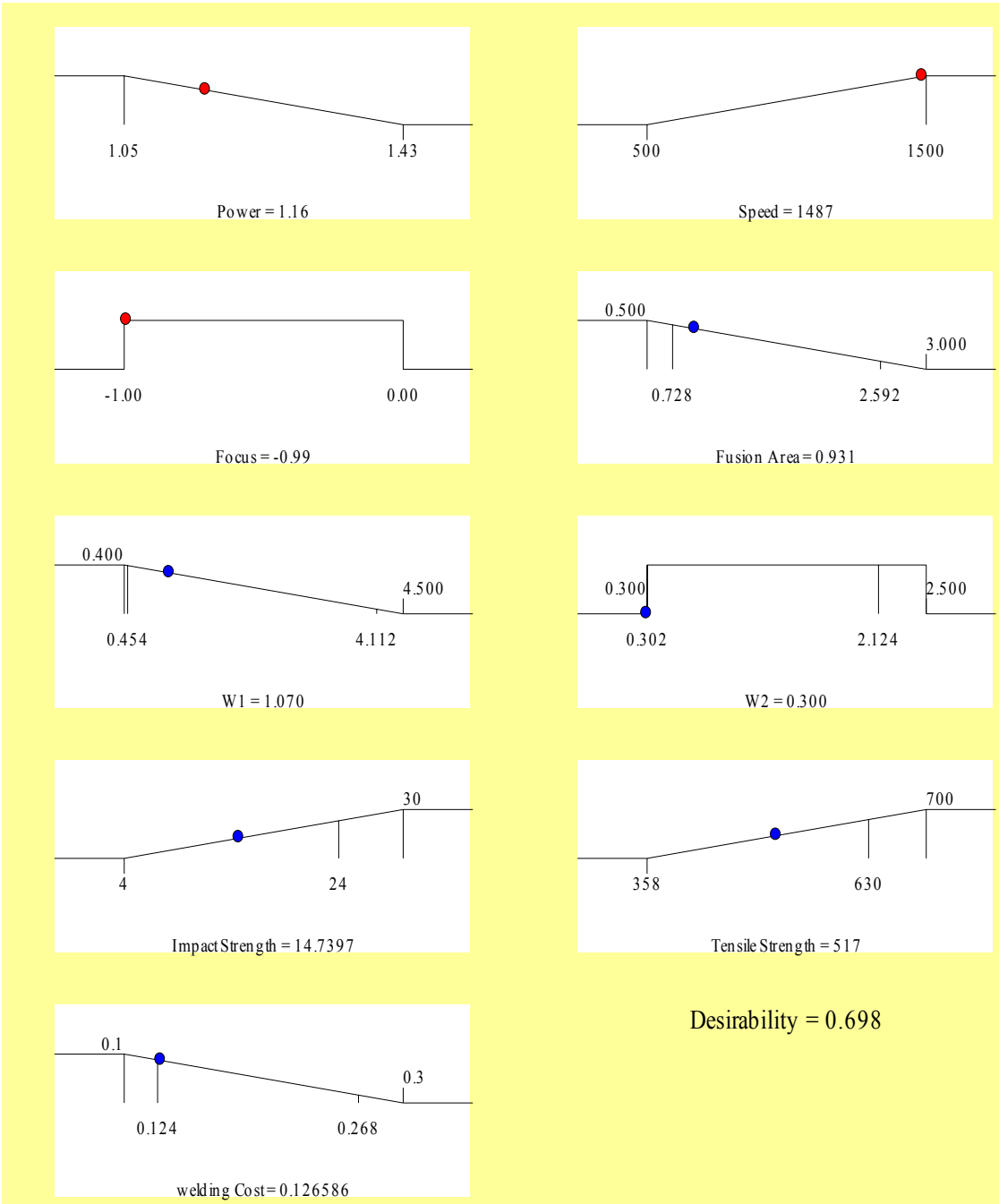

Fig. 5.22: The desirability for each factor and each response, as well as the combined desirability at the optimal point.

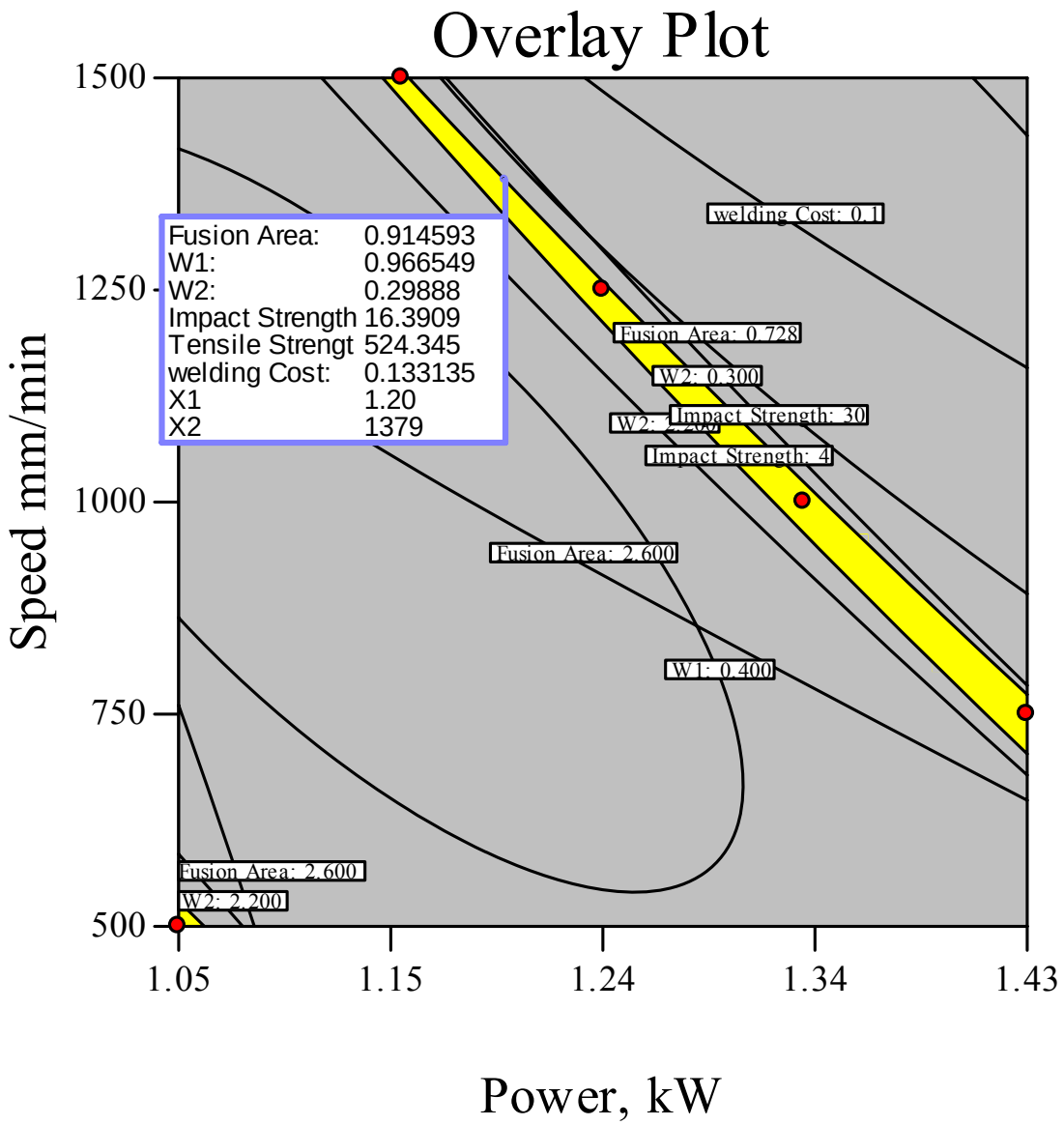

Fig. 5.23 Overlay plot shows the region (yellow color) of optimal welding condition at F =-0.2 mm.

5.2 Joining of Low Carbon Steel AISI1008 to Stainless Steel AISI 316 (2 mm Thickness)

5.2.1 Orthogonal Array Experiment

The above mentioned dissimilar materials were jointed using butt welding jointing design and the welding input parameters were studied. The operating range was determined using pilot experiments. The welding inputs variables and experiment design levels were then decided and are presented in Table 5.19. In this study of the dissimilar material joint with the above mentioned thickness, the interactions between the welding parameters are considered. An L25 orthogonal array with three columns and 25 rows was used. Twenty-five experiments were required to study the welding parameters using this array. The experiment was designed using Design Expert 7 software with random order and using the laser input variables presented in Table 5.20.

Table 5.19: Process parameters and design levels used

Variables	Code	Unit	Level 1	Level 2	Level 3	Level 4	Level 5
Laser Power	P	kW	1.05	1.15	1.24	1.33	1.43
Welding Speed	S	mm/min	500	625	750	875	1000
Focus	F	mm	-1	-0.75	-0.5	-0.25	0

Table 5.20: The Taguchi design matrix in actual values of the studied welding parameters and welding pool geometry, mechanical tests results and cost per meter welding calculations.

Std.	Run	Power, kW	Speed, mm/min	Focus, mm	A, mm^2	W_1, mm	W_2, mm	Impact St., J	Tensile St., MPa	Cost, €/m
1	8	1.05	500	-1	2.427	2.875	0.972	35	610	0.25
2	2	1.05	625	-0.75	1.953	2.264	0.780	29	611	0.20
3	1	1.05	750	-0.5	2.021	2.549	0.674	23	626	0.17
4	10	1.05	875	-0.25	2.058	2.198	0.639	19	614	0.14
5	12	1.05	1000	0	1.758	2.017	0.544	26	567	0.12
6	16	1.15	500	-0.75	2.115	1.758	1.032	24	619	0.25
7	21	1.15	625	-0.5	2.162	2.182	0.844	26	636	0.20
8	7	1.15	750	-0.25	2.190	2.094	0.763	27	599	0.17
9	11	1.15	875	0	2.237	2.010	0.679	24	609	0.14
10	25	1.15	1000	-1	1.872	1.825	0.616	28	649	0.13
11	15	1.23	500	-0.5	3.641	3.611	1.103	28	721	0.26
12	9	1.23	625	-0.25	2.205	2.674	0.931	26	716	0.21
13	14	1.23	750	0	1.742	2.134	0.756	29	698	0.17
14	20	1.23	875	-1	1.785	1.502	0.703	27	688	0.15
15	18	1.23	1000	-0.75	1.709	1.883	0.759	24	616	0.13
16	23	1.32	500	-0.25	3.100	2.056	1.426	31	711	0.26
17	19	1.32	625	0	2.707	2.297	0.946	30	653	0.21
18	4	1.32	750	-1	2.328	2.543	1.045	33	694	0.17
19	3	1.32	875	-0.75	1.784	2.297	0.718	27	673	0.15
20	17	1.32	1000	-0.5	1.598	1.939	0.719	27	682	0.13
21	5	1.43	500	0	2.877	2.552	1.153	36	705	0.27
22	13	1.43	625	-1	3.136	2.952	0.936	32	687	0.21
23	22	1.43	750	-0.75	2.261	2.416	0.680	30	674	0.18
24	24	1.43	875	-0.5	1.904	2.032	0.652	28	671	0.15
25	6	1.43	1000	-0.25	1.647	1.213	0.796	24	673	0.13

5.2.2 Development of Mathematical Models for Residual Stresses

Residual stresses of dissimilar welded components were evaluated during this study following the measurement procedure explained in paragraph 4.5.3 in the previous chapter in order to control and optimize the selected laser welding parameters. Residual stress was studied and analyzed through the depth of the welded joint at gradual levels to get a clear indication of the effect of welding

parameters on the distribution of the residual stress through the depth of HAZ and to optimize it. The strain gauge was bonded to the surface of the specimen (stainless-steel side) in the HAZ where the critical (serious) residual stresses in the joined component were present. A blind hole of incremental depth of 1.524 mm was drilled at 2-3 mm from the centre welded line in the middle of the specimen as presented in Fig.4.14 (a). "Design Expert 7" software was used for analyzing the measured responses. Depth levels at which the micro-strains were measured are presented in Table 5.21. The calculated stress (σ_i) at each level expressed in Table 5.22, were considered as responses and analyzed separately to predict the effect of the welding parameters through specimen depth. The effect of individual welding parameter on the residual stress at each level was investigated in this study.

Table 5.21: Shows the Depth at which the micro-strains were measured in the specimens.

Level (i)	*1*	*2*	*3*	*4*	*5*	*6*	*7*
Stress	σ_1	σ_2	σ_3	σ_4	σ_5	σ_6	σ_7
Depth in specimen, [mm]	0.127	0.254	0.508	0.762	1.016	1.27	1.524

Table 5.22: Shows the experimental assignments with random order and residual stresses in MPa.

Sp.	σ_1	σ_2	σ_3	σ_4	σ_5	σ_6	σ_7
1	273	166	121	87	79	73	70
2	230	121	111	82	82	75	73
3	138	106	89	70	70	66	63
4	143	108	86	68	64	61	61
5	142	82	67	48	51	50	51
6	138	103	92	75	77	72	70
7	183	133	104	80	77	74	72
8	222	156	118	86	75	74	73
9	173	103	86	71	71	68	66
10	146	95	77	65	64	64	60
11	209	160	119	85	83	82	77
12	192	141	116	82	78	72	67
13	203	138	100	77	74	61	55
14	195	121	91	71	66	59	52
15	159	96	78	63	59	54	52
16	330	202	141	98	89	79	74
17	255	157	96	69	69	70	64
18	188	114	81	63	66	65	59
19	184	121	94	69	65	60	56
20	100	92	74	65	60	58	60
21	238	177	134	102	98	89	82
22	206	154	106	77	77	77	73
23	217	150	96	73	77	77	76
24	178	120	87	76	74	74	72
25	152	95	66	55	59	58	59

5.2.2.1 The S/N ratio analysis

In order to evaluate the influence of each selected parameter on the responses: the S/N for each control factor had been calculated for each level separately. The

signals indicated that the effect on the average responses and the noises were measured by the influence on the deviations from the average responses, which would indicate the sensitivity of the experiment output to the noise factors. The appropriate S/N ratio must be chosen using previous knowledge, expertise, and understanding of the process. When the target is fixed and there is a trivial or absent signal factor (static design), it is possible to choose the S/N ratio depending on the goal of the design. In this study, the S/N ratio was chosen according to the criterion ***the-smaller-the-better***, in order to minimize the responses. The S/N ratio for the-smaller-the-better target was calculated using Eqs 3.2 and 3.4.

For the first response was the residual stresses at level 1, in the specimen. The data in Table 5.24 with the above formulas (Eqs 3.2, 3.4) were used for calculating S/N. The Taguchi experiment results, which were obtained by using MINITAB 13 statistical software, are presented in Fig. 5.24(a). The same procedure was applied for other responses for the levels from 2 to 7, which are expressed in Table 5.21, for calculating S/N and presented in Figs. 5.24(b-g). The effects of welding parameters vary between various depth levels. The welding parameters on all the levels are summarized by means of S/N ratio and presented in Fig. 5.24(h). From this figure, it is clear that the welding speed has the strongest effect on the residual stress development.

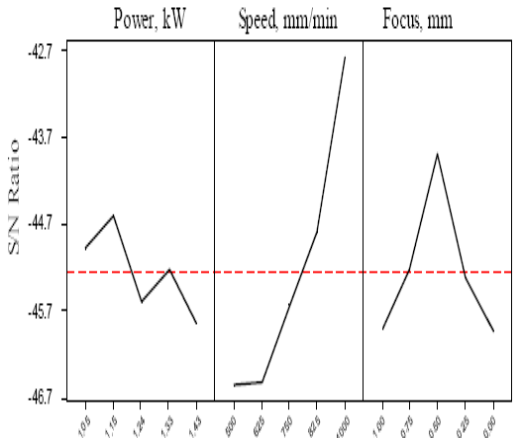

Fig. 5.24(a)

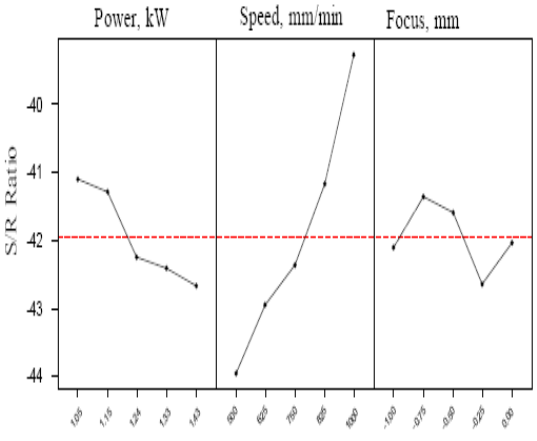

Fig. 5.24(b)

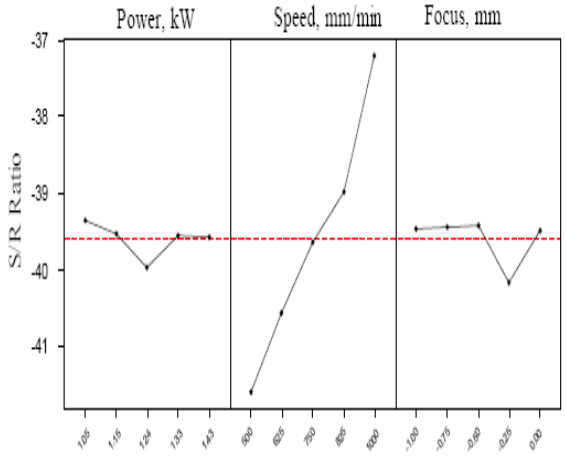

Fig. 5.24(c)

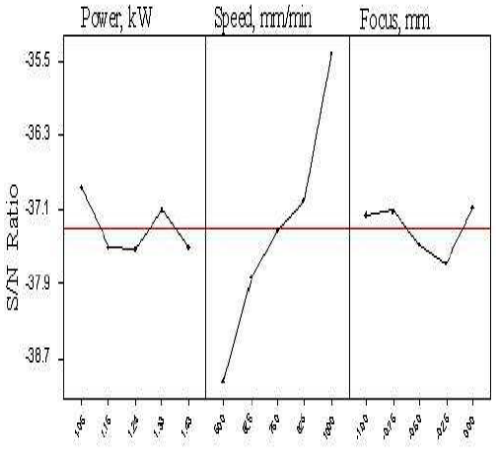

Fig. 5.24(d)

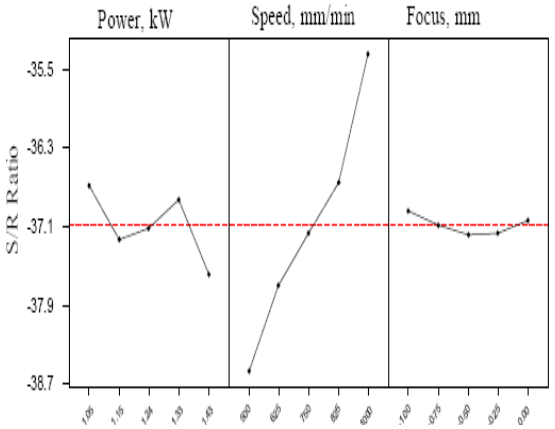

Fig. 5.24(e)

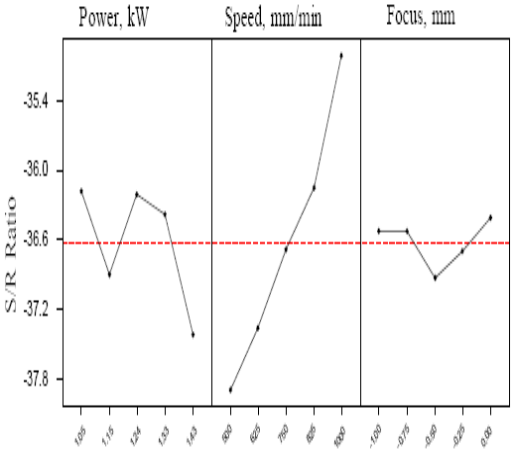

Fig. 5.24(f)

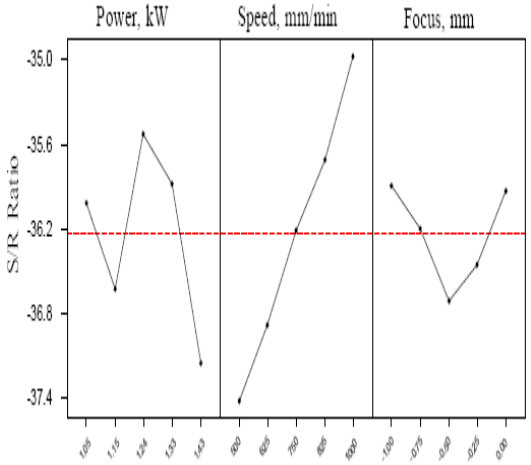

Fig. 5.24(g)

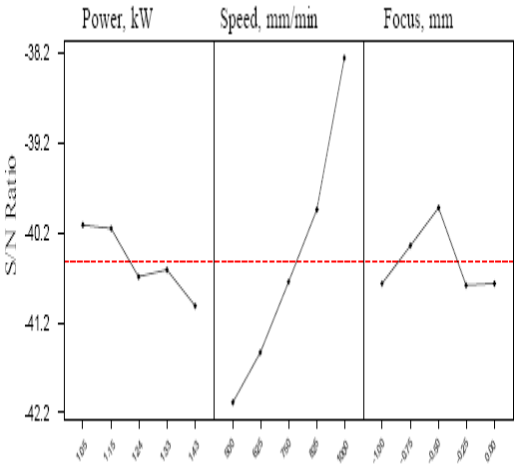

Fig. 5.24(h)

Figs. 5.24(a-h): Shows the average effect of welding parameters on residual stresses at HAZ

5.2.2.2 The ANOVA analysis

Further investigations for welding process parameters were carried out, using ANOVA, to identify which parameter is significantly affecting the welding quality. This is accomplished by separating the total variability of the S/N ratios, which is measured by the sum of the squared deviations from the total mean of the S/N ratio, into contributions by each welding process parameter and the error [173]. The test for significance of the regression model, the test for significance on individual model coefficients and the lack-of-fit test were performed using Design Expert 7 software. The backward regression method, which eliminates the insignificant model terms automatically, was applied for each level and exhibited in ANOVA Tables 5.23 to 5.29 for the models. The ANOVA Tables summarize the analysis of the variances of the responses and show the significant models. The same tables show also the other adequacy measures R^2, adjusted R^2, and adequacy precision for each response. The adequate precision compares the range of the predicted value at the design points to the average predicted error. In this study the values of adequate precision for all models developed were significantly greater than 4. All the adequacy measures in all ANOVA Tables indicate that adequate models have been obtained. The final mathematical models in terms of actual factors as determined by Design Expert software are shown below.

$$\sigma_1 = 332.619 - 0.188 * S \quad \textbf{…(5.13)}$$

$$\sigma_2 = 146.525 + 66.030* P - 0.134* S \quad \textbf{…. (5.14)}$$

$$\sigma_3 = 166.686 - 0.093* S \quad \textbf{.... (5.15)}$$

$$\sigma_4 = 2607.557 - 3593.719* P - 4.217 * S - 50.207* F + 4.735* P * S - 0.028* S * F + 1456.648* P^2 + 1.7E\text{-}003 * S^2 - 168.087* F^2 - 1.916* P^2 * S - 7.7E\text{-}007 * S^3 - 92.056* F^3 \quad \textbf{… (5.16)}$$

$$\sigma_5 = 281.134 - 252.328* P - 0.074* S + 38.307* F - 0.048* S * F + 103.223* P^2 \quad \textbf{… (5.17)}$$

σ_6 = 81.256 + 15.872* P - 0.043* S **… (5.18)**

σ_7 = -2806.843 + 7244.767 * P - 0.038 * S - 15.499 * F - 5999.662* P^2 - 17.386 * F^2 + 1645.974* P^3 **… (5.19)**

5.2.2.3 Effect of the parameters on the responses

The reason for predicting the residual stresses is to develop a model to control and to optimize them by controlling the welding parameters. Figs. 5.25 to 5.31 present 3D graphs of the effect of S, P and F on the response at each depth level.

At level 1 of the specimen depth, the analysis of variance presented in Fig. 5.25 and expressed in Table 5.23, indicates that the main effect on the residual stresses is the welding speed S as presented in Fig. 5.24(a); while the other parameters had an insignificant effect on the response. The analysis indicates also that the liner model developed was significant with an Adequate Precision of 9. Since depth level 1 is nearest to the specimen surface and the cooling rate is very fast; the response has the highest value at this level. The maximum response value was at experiment number 16 at 320 MPa and the lowest value was obtained at experiment number 5 at 142 MPa. The wide range of responses at all experiments settings (142- 320 MPa) reflects the strong effects of welding parameters on the process.

Table 5.23: ANOVA for residual stress at level 1

Source	**Sum of Squares**	**df**	**Mean Square**	**F_v Value**	**p-value Prob. > F_v**	
Model	27555	1	27555	19.589	0.0002	significant
S	27555	1	27555	19.589	0.0002	
Residual	32353	23	1407			
Cor. Total	59909	24				
R-Squared = 0.4600			Adeq. Precision = 9			
Adj. R-Squared = 0.4365						

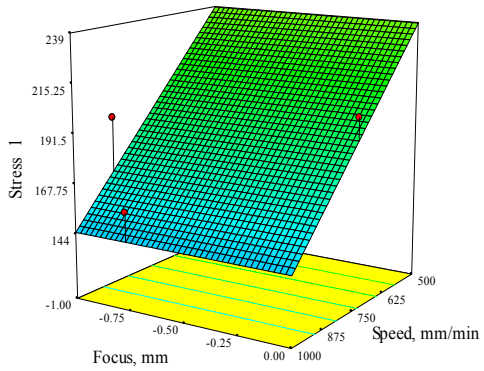

Fig. 5.25: 3-D plot for affected parameters against σ_1.

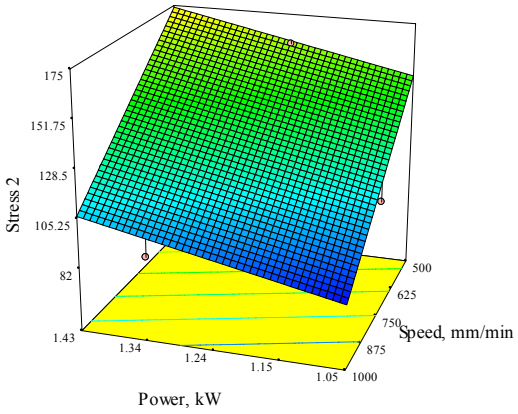

Fig. 5.26: 3-D plot for affected parameters against σ_2.

At level 2 of the specimen depth, the analysis of variance, presented in Fig. 5.26 and expressed in Table 5.24, indicates that the response is affected by laser power and welding speed. At this depth level, the liner model developed was significant and the Adequate Precision was 15. R^2 and Adjusted R^2 values emphasize the significance of the model developed. The model indicates that the depth level 2 results in lower response ranges (between 202 and 82 MPa) as expressed in Table 5.22 and presented in Fig. 5.24 (b). This is because depth level 2 is deeper than depth level 1 and thus has a slower cooling rate.

Table 5.24: ANOVA for residual stress at level 2

Source	**Sum of Squares**	**df**	**Mean Square**	**F_v Value**	**p-value Prob. > F_v**	
Model	15812	2	7906	25.350	< 0.0001	significant
P	2047	1	2047	6.562	0.0178	
S	13979	1	13979	44.823	< 0.0001	
Residual	6861	22	312			
Cor. Total	22673	24				
R-Squared = 0.6974			Adeq. Precision = 15			
Adj. R-Squared = 0.6699						

The ANOVA analysis presented in Fig. 5.27 and expressed in Table 5.25 for depth at level 3 indicates that the model developed was significant. At this depth level, only the welding speed parameter affected the response. The response values were further decreased in comparison to the third depth levels which had its minimum and maximum values at experiments numbers 5 and 16 respectively.

Table 5.25: ANOVA for residual stress at level 3

Source	**Sum of Squares**	**df**	**Mean Square**	**F_v Value**	**p-value Prob. > F_v**	
Model	6687	1	6687	57.823	< 0.0001	significant
S	6687	1	6687	57.823	< 0.0001	
Residual	2660	23	116			
Cor. Total	9347	24				
R-Squared = 0.7154			Adeq. Precision = 15			
Adj. R-Squared = 0.7031						

The model at depth level 4 is very complicated and is presented in Fig. 5.28. Since this level is located at the centre depth of the specimen, where the cooling rate will occur at both specimen sides at different rates; the resulting model is complex. At this depth level all the considered welding parameters had an effect on the response and second and third order parameters effects were observed. Interaction effects between welding speed and laser power and between welding speed and focus position are also included in the cubic model at this depth level. The ANOVA analysis, expressed in Table 5.26 indicates that the model is significant. Penetrating deeper into the specimen; the residual stress resulting due to welding operation decreases and this is presented in the above two depth levels whereby the response has decreased. Higher and lower values of this response were observed at experiments conducted at depth levels in experiments 5 and 16.

The model developed at a specimen depth of level 5 was statistically analyzed and is presented in Fig. 29 and expressed in Table 5.27, which indicate that the

quadratic model is significant. The ANOVA analysis expressed in Table 5.27 indicates that all welding parameters have an effect on the response at this depth level. The possibility for second order effects of laser power is presented and an interaction effect between welding speed and focus position is accounted for in the model developed. The response was further decreased in comparison to superficial depth levels and the range between the max and min response values was found to decrease. The range of values of this response varied between experiments numbers 4 and 16.

Table 5.26: ANOVA for residual stress at level 4

Source	Sum of Squares	Df	Mean Square	F_v Value	p-value Prob. > F_v	
Model	3205	11	291	11.014	< 0.0001	significant
P	13	1	13	0.474	0.5032	
S	29	1	29	1.104	0.3125	
F	232	1	232	8.773	0.0110	
P S	2	1	2	0.077	0.7851	
S F	33	1	33	1.254	0.2831	
P^2	2	1	2	0.064	0.8047	
S^2	0	1	0	0.008	0.9300	
F^2	140	1	140	5.307	0.0384	
P^2 S	371	1	371	14.041	0.0024	
S^3	160	1	160	6.030	0.0289	
F^3	141	1	141	5.332	0.0380	
Residual	344	13	26			
Cor. Total	3549	24				
R-Squared = 0.9031			Aeq. Precision =16			
Adj. R-Squared = 0.8211						

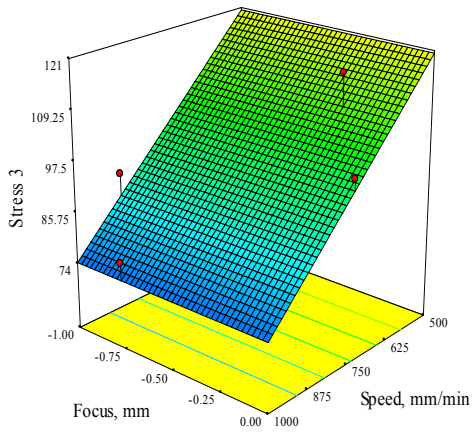

Fig. 5.27: 3-D plot for affected parameters against σ_3.

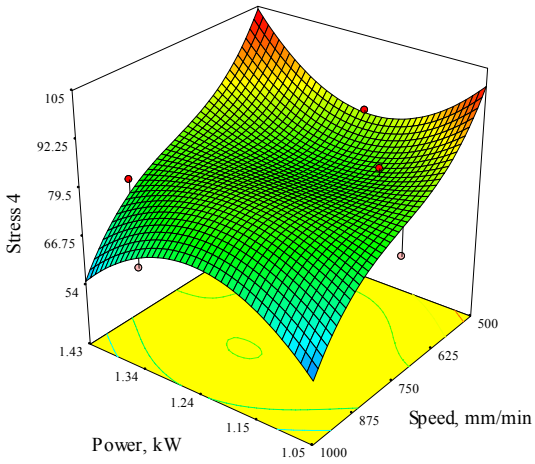

Fig. 5.28: 3-D plot for affected parameters against σ_4.

Table 5.27: ANOVA for residual stress at level 5

Source	Sum of Squares	df	Mean Square	F_v Value	p-value Prob. > F_v	
Model	2167	5	433	20.256	< 0.0001	significant
P	5	1	5	0.241	0.6288	
S	1953	1	1953	91.288	< 0.0001	
F	16	1	16	0.744	0.3991	
S F	160	1	160	7.467	0.0132	
P	52	1	52	2.436	0.1351	
Residual	407	19	21			
Cor. Total	2573	24				
R-Squared = 0.8420				Aeq. Precision =17		
Adj. R-Squared = 0.8005						

The model developed at depth level 6 was analyzed. The ANOVA is expressed in Table 5.28 and indicates that the liner model is significant. The laser power and welding speed parameters are found to affect the model while focus position has no significant effect, as shown in Fig. 5.24(f). The maximum response was observed at

experiment number 16 to be 79 MPa and the minimum were observed at experiment number 5 to be 50 MPa, as is presented in Fig. 5.30.

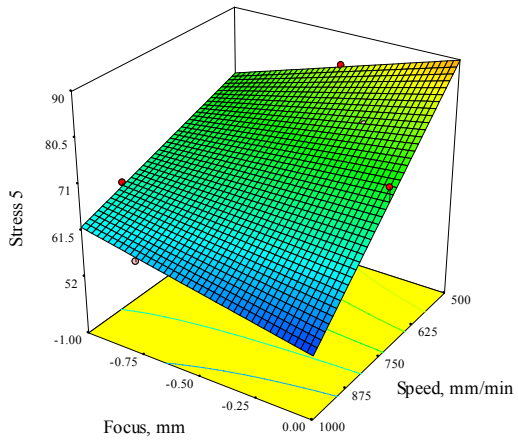

Fig. 5.29: 3-D plot for affected parameters against σ_5.

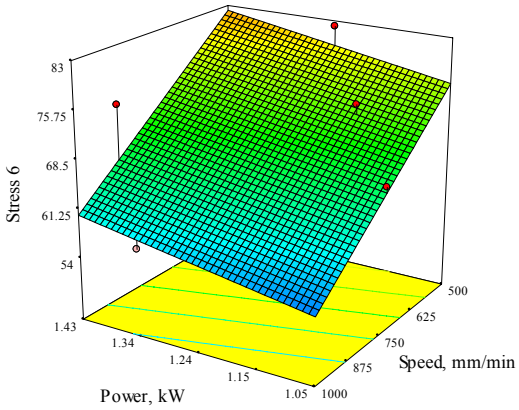

Fig. 5.30:3-D plot for affected parameters against σ_6.

Table 5.28: ANOVA for residual stress at level 6

Source	Sum of Squares	df	Mean Square	F_v Value	p-value Prob. > F_v	
Model	1577	2	789	29.390	< 0.0001	significant
P	118	1	118	4.407	0.0475	
S	1475	1	1475	54.990	< 0.0001	
Residual	590	22	27			
Cor. Total	2167	24				
R-Squared = 0.7277			Aeq. Precision =15			
Adj. R-Squared = 0.7029						

Similarly, the model developed at depth level 7, presented in Fig. 5.31, was analysed and is expressed in Table 5.29. The results indicate that the cubic model is significant and is affected by all welding parameters. Second order effects of laser power, focus position and third order effects of laser power are also found to affect the response. At this depth level, the maximum response value differed in comparison to all the other superficial levels (at the experiment number 23) while the minimum response value was similar to all other depth levels at experiment number 5. This is due to the depth level being far away from the surface and the heat source has a negligible affect on the welding process. Also, the response range has the

smallest changing range of all experiment settings (76 – 5 MPa). In all the above models, it is clear that the welding speed was the most significant parameter in the process, while the effect of the laser power and focus position factors were lower and varied between each depth level.

Table 5.29: Shows ANOVA for residual stress at level 7.

Source	Sum of Squares	df	Mean Square	F_v Value	p-value Prob. > F_v	
Model	1400	6	233	9.296	0.0001	significant
P	75	1	75	2.989	0.1009	
S	1094	1	1094	43.607	< 0.0001	
F	11	1	11	0.440	0.5154	
P^2	91	1	91	3.644	0.0724	
F^2	82	1	82	3.278	0.0869	
P^3	129	1	129	5.122	0.0362	
Residual	452	18	25			
Cor. Total	1851	24				
R-Squared = 0.7560			Aeq. Precision =10			
Adj. R-Squared = 0.6747						

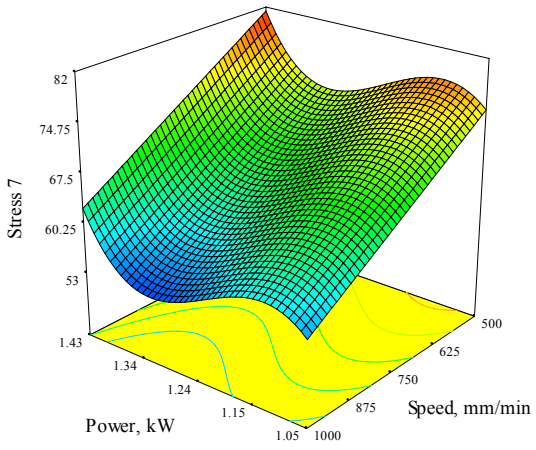

Fig. 5.31: 3-D plot for affected parameters against σ_7.

The fit summary output indicates that the models developed are statistically significant for the prediction of the responses therefore they will be used for further analysis and optimization. From the obtained results, it can be seen that the residual stresses are controlled by the rate of heat input, which is a function of laser power and welding speed. However, the focusing parameter has limited affect on the residual stress, especially at certain levels as indicated in the models developed in this research. Moreover, three confirmation experiments were carried out based on new random welding parameters to verify the developed models. The first experiment was carried out at a laser power of 1.05 kW, welding speed of 500 mm/min and focus of -1mm. The second experiment was at a laser power of 1.20 kW, welding speed of 1000 mm/min and focus of 0 mm. The last one was at a laser power of 1.40 kW, a welding speed of 750 mm/min and focus of 0 mm. After welding, the three specimens were subjected to residual stress measurements using the hole-drill method following the previously explained procedure for each measurement. The measured residual stress, the calculated (using the developed models) residual stress and the absolute error calculation are presented in Table 5.30. The average error for each model and the total error average are also presented in the same Table. Table 5.30 indicates that the error for each model is less than 9 % and the total average error is equal to 6.65 %. The received results in Table 5.30 indicate that the developed models, within the parameters domain, could be used adequately during the design stage to predict the residual stress that would result due to the welding operation.

Table 5.30: Confirmation experiments with absolute error calculation of the developed models

Stress Level	Welding Condition	Residual Stress		$\lvert Error \rvert$ %	Average Error %
		Measured	Predicted		
σ_1	1	254	239	6.28	8.48
	2	166	145	14.48	
	3	201	192	4.69	
σ_2	1	146	155	5.81	8.95
	2	103	91	13.19	
	3	151	140	7.86	
σ_3	1	113	120	5.83	7.17
	2	82	74	10.81	
	3	93	97	4.88	
σ_4	1	83	79	5.06	4.49
	2	56	55	1.82	
	3	71	76	6.58	
σ_5	1	79	82	3.66	4.86
	2	55	59	6.88	
	3	71	74	4.05	
σ_6	1	79	76	3.05	5.35
	2	52	57	8.77	
	3	68	71	4.22	
σ_7	1	71	72	1.39	6.86
	2	49	52	5.77	
	3	58	67	13.43	
Total Average Error % =				6.6014	

5.2.3 Development Mathematical Models for Welding Pool Geometry

The area of the fusion welding zone 'A' was measured by using the transverse sectioned specimens, the optical microscope and image analyzer software. Using the same procedure the welding pool width at surface W_1 and the welding pool width at the middle W_2 of the specimens were also measured and analyzed as process responses. The measured responses are listed in Table 5.20 and exhibited in Fig. 5.32. Design Expert 7 software was used for analyzing the measured responses.

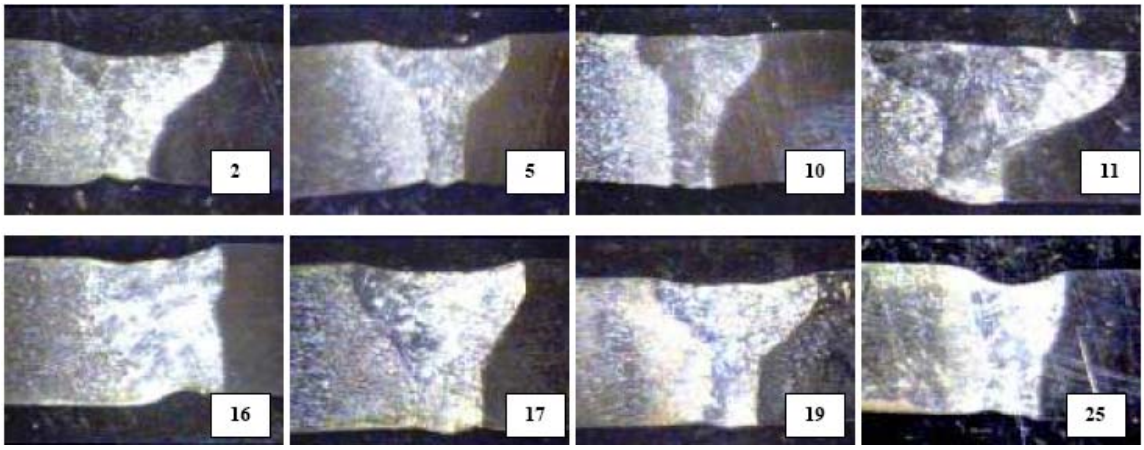

Fig. 5.32: The effect of the welding parameters on the responses (A, W_1, W_2), and the variation on weld bead geometry, X10.

5.2.3.1 The S/N ratio analysis

In order to evaluate the influence of each selected factor on the responses: The Signal-to-Noise ratios (S/N) for each control factor had to be calculated. The signals have indicated that the effect on the average responses and the noises were measured by the influence on the deviations from the average responses, which would indicate the sensitivity of the experiment output to the noise factors. The appropriate S/N ratio must be chosen using previous knowledge, expertise, and understanding of the process. When the target is fixed and there is a trivial or absent signal factor (static design), it is possible to choose the signal- to-noise (S/N) ratio depending on the goal of the design. In this study, the S/N ratio was chosen according to the criterion 'the-smaller-the-better', in order to minimize the responses. The S/N ratio for 'the-smaller-the-better' target for all the responses was calculated using Eqs 3.2 and 3.4.

Using the above-presented data with the selected above formula for calculating S/N, the Taguchi experiment results are summarized in Table 5.31 and presented in Fig. 5.33, which were obtained by means of MINITAB 13 statistical software. It can be noticed from main effects plot for S/N, that travel speed 'S' is the most important factor affecting the responses; the minimum is at the highest level of 'S'. Laser power has the lowest relevant effect. Focus point position plots show the less important effect of this factor as demonstrated in Fig. 5.33. Main effects plot for S/N ratios suggest that those levels of variables that minimised the weld pool dimensions were also robust against variability due to noises as presented in Fig. 5.33.

Table 5.31: The responses for signal-to-noise ratio (S/N).

levels	1	2	3	4	5	Delta	Rank
P, kW	-6.49	-6.52	-6.98	-7.22	-6.15	1.07	2
S, mm/min	-8.89	-7.59	-6.43	-5.78	-4.68	4.21	1
F, mm	-6.91	-6.82	-5.82	-6.74	-7.09	1.27	3

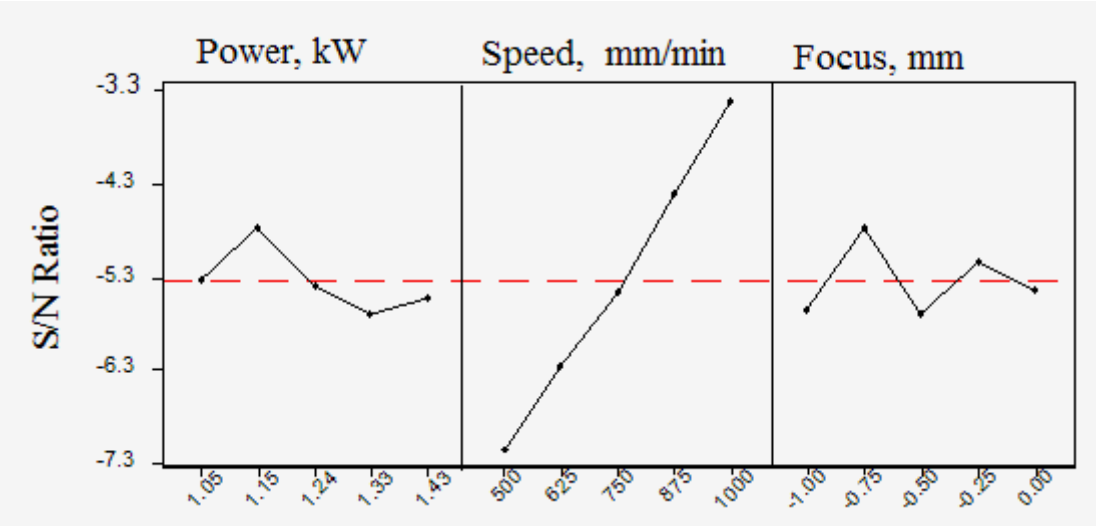

Fig. 5.33: Effects plot for S/N ratio of the responses.

5.2.3.2 Analysis of variance

The purpose of the ANOVA is to investigate which welding process parameters significantly affect the quality characteristic. The test for significance of the regression model, the test for significance on individual model coefficients and the lack-of-fit test were performed using Design Expert 7 software. Backward regression method was applied and exhibited in ANOVA Tables 5.32 to 5.34 for the reduction of the developed quadratic models. ANOVA Tables summaries the analysis of three variances of the responses and show the significant models. The same tables also show the other adequacy measures R^2, adjusted R^2 and adequacy precision R^2 for each response. The entire adequacy measures were close to 1, which are reasonable and indicate adequate models. The adequate precision compares the range of the predicted value at the design points to the average predicted error. In this study the value of adequate precision is significantly greater than 4.

The analysis of variance indicates that for the welding pool area 'A' model, the main effect was the welding speed, the second order effect was the laser power and the two level interaction of laser welding and welding speed (P, S), and the second order effect of welding speed (S^2) are the most significant model parameters. Secondly, for the welding pool width at the work piece surface 'W_1' model, the analysis indicated that there is a linear relationship between the main effects of the three parameters. Also, in case of welded pool width at the middle of work piece 'W_2' model the main effect of laser power, welding speed , focused position, the second order effect of (S^2, P^2, F^2) are significant model terms. However, the main effect of welding speed is the most important factor influencing the welding pool geometry.

The final mathematical models in terms of coded factors and actual factors as determined by Design Expert software are shown below in Eqs 5.20 to 5.25.

Final Equation in Terms of Coded Factors:

$$A = 2.02 +0.12*P -0.66*S +0.022* F -0.49* P*F -0.22*S*F +0.38* S^2 \quad \textbf{…(5.20)}$$

$$W_1 = 2.18 -0.085*P -0.46*S -0.21*F -0.30*P* F \quad \textbf{…(5.21)}$$

$$W_2 = 1.29 +0.22*P -0.032*S -0.23*F -0.73* P* S +0.68*P* F +0.74*S* F -0.43*P^2 - 0.22*S^2 -0.39*F^2 \quad \textbf{…(5.22)}$$

Final Equations in Terms of Actual Factors:

$$A = 10.582 -1.982*P -0.0127*S +7.775*F -5.179* P*F -1.75E\text{-}003*S*F +6E\text{-}006* S^2 \quad \textbf{...(5.23)}$$

$$W_1 = 5.866 -2.024* P -1.845E\text{-}003 * S +3.492*F -3.15723* P* F \quad \textbf{...(5.24)}$$

$$W_2 = -41.69514 +45.567*P +0.027*S -15.302*F -0.0153*P*S +7.138*P* F +5.93E\text{-}003*S*F -11.834*P^2 -3.4E\text{-}006* S^2 -1.54885*F^2 \quad \textbf{…(5.25)}$$

Table 5.32: ANOVA for 'A' response model

Source	Sum of Squares	df	Mean Square	F Value	p-value Prob > F	
Model	4.950	6	0.825	9.424	< 0.0001	significant
P	0.138	1	0.138	1.575	0.2256	
S	4.498	1	4.498	51.375	< 0.0001	
F	0.006	1	0.006	0.070	0.7941	
PF	0.829	1	0.829	9.474	0.0065	
SF	0.212	1	0.212	2.416	0.1375	
S^2	0.492	1	0.492	5.618	0.0291	
Residual	1.576	18	0.088			
Cor Total	6.526	24				
R-Squared= 0.7585			Adeq Precision = 10.293			
Adj R-Squared = 0.6780						

Table 5.33: ANOVA for 'W_1' response model

Source	Sum of Squares	df	Mean Square	F Value	p-value Prob. > F	
Model	2.985	4	0.746	6.789	0.0013	significant
P	0.086	1	0.086	0.785	0.3863	
S	2.354	1	2.354	21.413	0.0002	
F	0.557	1	0.557	5.065	0.0358	
P*F	0.479	1	0.479	4.362	0.0498	
Residual	2.199	20	0.110			
Cor. Total	5.184	24				
R-Squared = 0.5759			Adeq. Precision = 9.837			
Adj. R-Squared = 0.491						

Table 5.34: ANOVA for 'W_2 ' response model

Source	Sum of Squares	df	Mean Square	F Value	p-value Prob > F	
Model	0.5733	9	0.0637	7.337	< 0.0001	significant
P	0.0350	1	0.0350	0.214	0.0162	
S	0.0010	1	0.0010	10.428	0.6502	
F	0.0498	1	0.0498	4.902	0.0056	
PS	0.0234	1	0.0234	4.267	0.0427	
PF	0.0204	1	0.0204	5.223	0.0566	
SF	0.0249	1	0.0249	6.669	0.0373	
P^2	0.0318	1	0.0318	1.704	0.0208	
S^2	0.0081	1	0.0081	5.499	0.2114	
F^2	0.0262	1	0.0262	7.337	0.0332	
Residual	0.0716	15	0.0048			
Cor Total	0.6449	24				
R-Squared= 0.8890			Adeq Precision = 11.758			
Adj R-Squared = 0.8224						

5.2.3.3 Model validation

To predict and verify the improvement of the response using the optimal level of the welding process parameters the models are subjected to a model validation study. Figs. 5.34-5.36 show the relationship between the actual and predicted values of A, W_1, and W_2, respectively. These figures indicate that the developed models are adequate because the residuals in prediction of each response are negligible, since the residuals tend to be close to the diagonal line. Furthermore, to verify the satisfactoriness of the developed models, three confirmation experiments were carried out using new test conditions at optimal parameters conditions, obtained using the design expert software. The A, W_1 and W_2 of the validation experiments were carried out using new test conditions at different parameters conditions, obtained using the developed mathematical models. Table 5.35 summarizes the experiments conditions, the actual experimental values, the predicted values and the

percentages of error. It could be concluded that the models developed could predict the responses with a very small error. A, W_1 and W_2 were greatly improved through using the developed models. The fit summary output indicates that the models developed are statistically significant for the prediction of the responses; therefore, they will be used for parameters optimization.

Table 5.35: Confirmation experiments and base metal responses

Exp. No	P, kW	S, mm/min	F, mm	A, mm^2		$\|E\|$ %	W_1, mm		$\|E\|$ %	W_2, mm		$\|E\|$ %
				Actual	Pred.		Actual	Pred.		Actual	Pred.	
1	1.05	1000	-1	1.89	1.84	2.7	1.67	1.71	2.3	0.61	0.55	10.91
2	1.05	1000	-0.95	1.75	1.84	4.9	1.59	1.72	7.6	0.59	0.55	7.27
3	1.05	1000	-0.90	1. 90	1.84	3.3	1.84	1.73	6.4	0.53	0.55	3.64

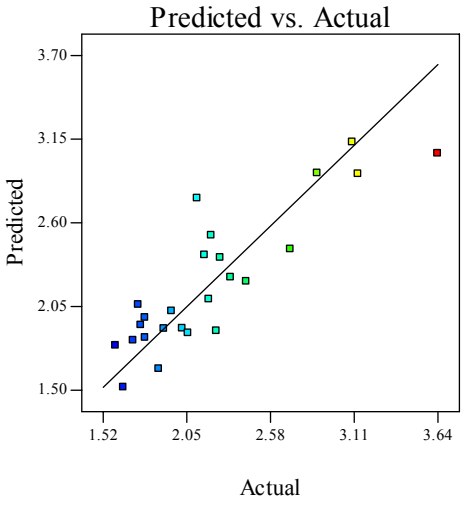

Fig. 5.34: The effect of actual welding parameters on the welding pool area 'A' response, against predicted

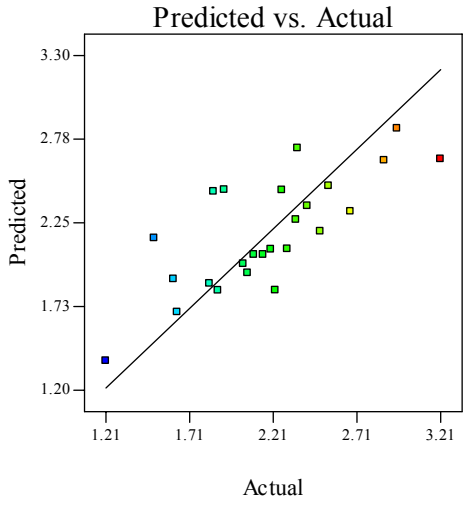

Fig. 5.35: The effect of actual welding parameters on the welding pool width 'W_1' against predicted

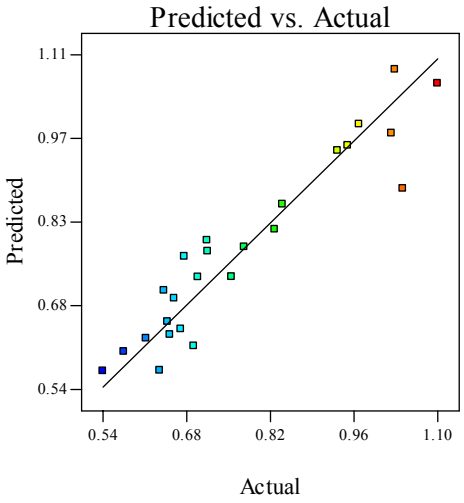

Fig. 5.36: The effect of actual welding parameters on the welding pool width at the middle of the spacemen 'W_2' response, against predicted

5.2.3.4 Effect of the parameters on responses

The reason for predicting the welding pool geometry is to develop a model which would include the optimizations step for future work. Fig. 5.37 contour graph shows the effect of P and F on the total welding pool area A at S = 750 mm/min. The contour graph in Fig. 5.38 shows the effect of P and F on the welding pool width at the work piece surface (W_1) at S = 750 mm/min. Fig. 5.39 contour graph shows the effect of P and S on the welding pool width at the middle of work piece (W_2) at F = -0.5 mm.

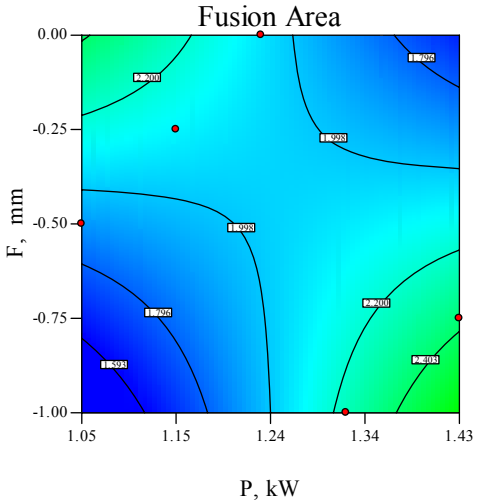

Fig. 5.37: The effect of 'P' and 'S' on the 'A' response, at focus value at 'F' = -0.5 mm

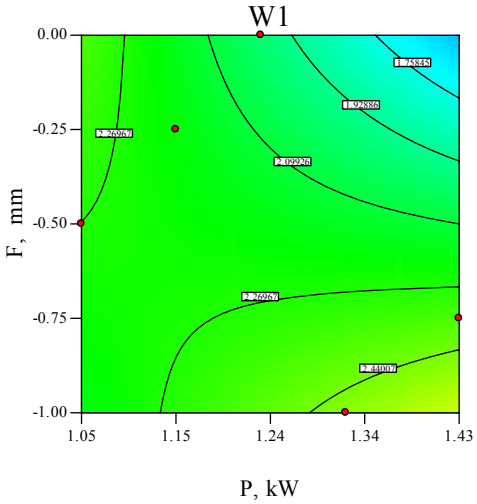

Fig. 5.38: The effect of 'P' and 'F' on the 'W_1' response, at 'S' = 750mm/min

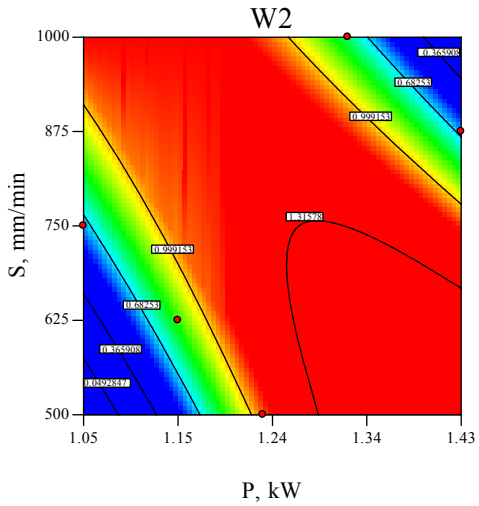

Fig. 5.39: The effect of 'P' and 'S' on the 'W_2' response, at focus value 'F' = -0.5 mm

Welding Pool Area 'A'

In the present study, the fusion area (welding pool) 'A' of dissimilar joints between stainless steel and low carbon steel was measured and plotted in the 3D graph as presented in Fig. 5.40, which demonstrates the relationship between the welding parameters (S and F) and the Fusion area at P = 1.24 kW. This figure shows that the welding speed has the most significant effect on the process. The increase in welding speed 'S' rate, lead to the reduction of the fusion area of the welding pool. When welding speed equals the maximum at 1000 mm/min, as presented in Table 5.20, the fusion area is at its minimum and equals 1.598 mm^2, which presents the best achieved results. It is also noted that changes in the laser power 'P' rate would lead to a change in the fusion area value. By increasing laser power the fusion area tends to decrease to a lower value at laser power equals 1.15 kW and then starts to increase up to laser power equal to 1.33 kW. Further increases of laser power value result in the fusion area increasing again. The fusion area has a minimum value at laser power equal 1.33 kW. These results are shown in Fig. 5.32 and 5.33. From Fig. 5.33 it is clear that the focusing position 'F' has an insignificant effect on the welding pool, whereby, changing the focusing position the welding pool will not be consequentially changed and this effect is shown in Table 5.31 in which the focusing position has the greater S/N ratio (rank = 3).

Welding Pool Width at the Work Piece Surface (W_1)

The results and the model obtained for the response indicate that the S and F are the most important factors affecting the W_1 value. An increase in S leads to a decrease in W_1. This is due to the laser beam traveling at high speed over the welding line when S is increased. Therefore, the heat input decreases leading to less volume of the base metal being melted, consequently the width of the welded zone decreases. Moreover, a defocused beam, which has a wide laser beam, results in spreading the laser power onto wide area. Therefore, a wider area of the base metal will be melted leading to an increase in W_1 or vice versa. The result also shows that P contributes secondary effect in the response width dimensions. Increases in P will result in slight increases in W_1, due to the increase in the power density. Fig. 5.41 shows 3D plots for the effect of process parameters (P and F) at S = 750 mm/min on the W_1 width.

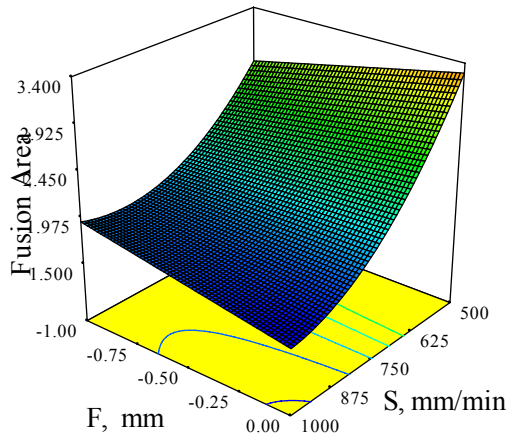

Fig. 5.40: 3D graph shows the effect of 'S' and 'F' on 'A' response, at 'P' = 1.24 kW.

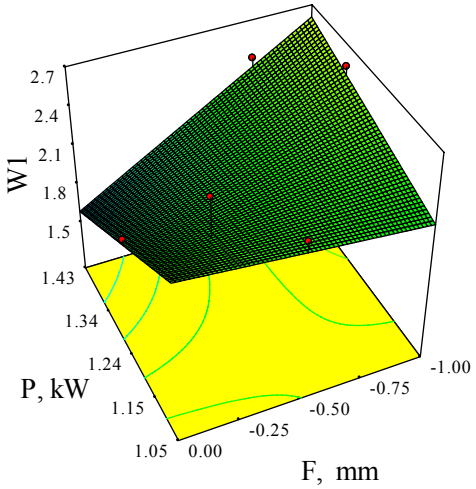

Fig. 5.41: 3D graph shows the effect of 'P' and 'F' on 'W1' response, at 'S' = 750mm/min.

Welding Pool Width at the Middle of the Work Piece (W_2)

From the results it is clear that the three parameters significantly affect the W_2 value. Using a focused beam results in an increase in the power density, which indicates that the heat will be localize in a small metal portion, resulting in an increase in the power density leading to an increase in the W_2 value. The model shows that the response is inversely proportional to F. The result shows that the

changes in F parameter effects W_1 and W_2 and does not effect A. This may be interpreted that as F decreased, W_1 increased and W_2 decreased, so the total area A will not be affected by changing F. The increase in P leads to an increase in the heat input, therefore, more molten metal and consequently wider W_2 will be achieved. However, the idea is reversed in the case of the S effect, because the S is inversely proportional to the heat input. Fig. 5.42 shows 3D plots to present the effect of process parameters (P and S) on the W2 value at F = -0.5 mm.

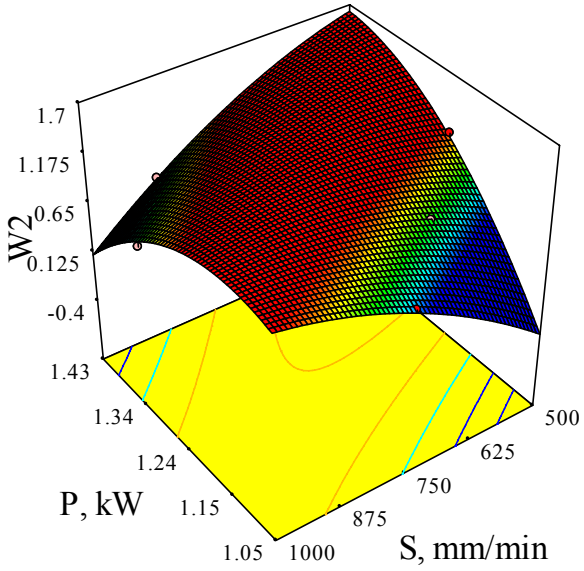

Fig. 5.42: 3D graph shows the effect of 'P' and 'S' 'W_2' response, at 'F' = -0.5 mm.

5.2.4 Development of a Mathematical Model for Tensile Strength

A butt joint was applied for joining the two dissimilar plates, mentioned above, together. The experiments were carried out according to the design matrix given in Table 5.20. They were performed in random order to avoid any systematic error. The notched tensile strength (NTS) samples, mentioned in chapter four, were tested at room temperature (20 ºC).

5.2.4.1 Analysis of the result

The raw data, the average tensile strength and the S/N ratio of the tensile test results are shown in Table 5.20. The average tensile strength and S/N ratio of the

tensile test results are plotted for each of the welding parameters in Fig 5.43. The average NTS tests appear to be mainly affected by the laser power and welding speed as shown in Table 5.36. The rank 1 in Table 5.36 indicates that power parameter (1) has a stronger effect on the process followed by rank (2) speed which has less effect, while rank (3) has the minimum or no effect on the process. To analyze the effects of the welding parameters in detail, ANOVA was conducted; these results are shown in Table 5.37.

Table 5.36: Shows the tensile strength response for S/ N Ratio.

Levels	**1**	**2**	**3**	**4**	**5**	**Delta**	**Rank**
P	55.64	55.88	56.74	56.68	56.67	1.10	1
S	56.54	56.38	56.35	56.26	56.07	0.47	2
F	56.45	56.09	56.47	56.40	56.18	0.38	3

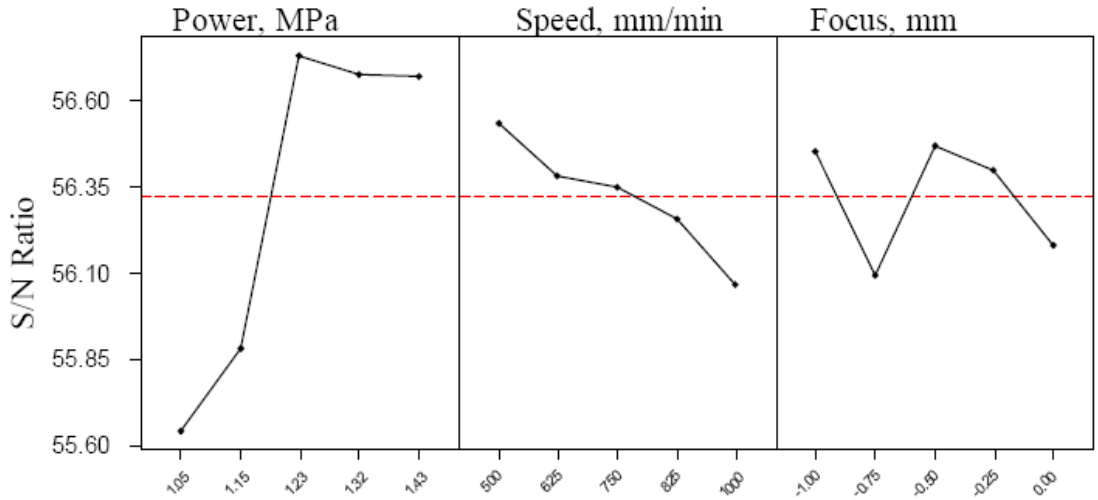

Fig. 5.43: The effect of the laser welding parameters on the tensile strength and S/N ratio.

Table 5.37: ANOVA for selected factorial model

Source	Sum of Squares	df	Mean Square	F Value	p-value Prob. > F	
Model	25011	2	12505	14.60	< 0.0001	significant
P	21714	1	21714	25.35	< 0.0001	
S	3297	1	3297	3.85	0.0626	
Residual	18847	22	857			
Cor. Total	43858	24				
R-Squared = 0.5703				Adeq. Precision = 11.580		
Adj. R-Squared = 0.5312						

In the ANOVA table, Table 5.37, the F_v is used to test the significance of a factor by comparing model variance with residual (error) variance, which is calculated by dividing the model mean square by the residual mean square. If the variance values are close to each other, the ratio will be close to one and it is less likely that any of the factors have a significant effect on the response. A high F_v value for a parameter means that the effect of the parameter on the characteristics is large. The result in Table 5.37 shows that the highest F_v value in the process was obtained for laser power 'P' equal to 25.35. The F_v value for the speed 'S' was equal to 3.85, which indicates that the speed has a relatively small effect on the process. Adequate Precision compares the range of the predicted values at the design points to the average prediction error. Ratios greater than 4 indicate adequate model discrimination. For this model it was equal to 11.580, as shown in Table 5.36. The same table also shows the other adequacy measures R^2 and Adjusted R^2. All the adequacy measures indicate that an adequate model has been obtained. The final mathematical model for predicting the tensile strength of a dissimilar F/A joint in terms of coded factors and actual factors as determined by Design Expert software are shown below.

Final Equation in Terms of Coded Factors:

Tensile Strength = 657.35 +42.47*P -16.24*S **…(5.26)**

Final Equation in Terms of Actual Factors:

Tensile Strength= 428.917+ 223.514* P - 0.065* S **…(5.27)**

5.2.4.2 Validation of the model

Fig. 5.44 shows the actual response versus the predicted response for NTS. From this Fig., it can be seen that the model adequately describes the response within the limits of the factors being investigated herein, as the data points are close to the diagonal line. Furthermore, three extra confirmation experiments were carried out using different test conditions, which are presented in Table 5.38 along with the resulting percentage error. It can be noticed that the NTS value obtained after laser welding is greater than the base metals value specially when compared to the low carbon steel side.

Table 5.38: Confirmation experiments of the responses compared with model results.

Exp. No	P, kW	S, mm/ min	F, mm	Tensile strength, MPa		$\|E\|$ %
				Actual	predicted	
1	1.05	500	-0.75	589	631	7.1
2	1.20	750	0	658	648	1.5
3	1.28	1000	-0.29	603	650	7.7

5.2.4.3. Effect of Process Parameters on the Response:

Laser power: It can be seen that the laser power is the most significant factor associated with the response, as shown in Fig. 5.43. It is clear that the higher laser power resulted in a higher response value, due to the fact that using high laser power would increase the power density. This leads to more penetration resulting in an improved response. Fig.5.45 shows a 3D graph of the effect of P and S on the response at F = -0.92 mm.

Welding speed: It is evidence from the results that the welding speed also has a strong effect on the tensile strength of the laser-welded joint, as shown in Fig. 5.43. The highest tensile strength value was observed to be at a speed of 500 mm/min. It is evidence that by increasing welding speed, with or without changing focus position, the response would decrease.

Focus point position: The results indicate that the focus point position has no obvious effect on the response within the parameter range domain applied. By changing the focus point position the response will not be effected.

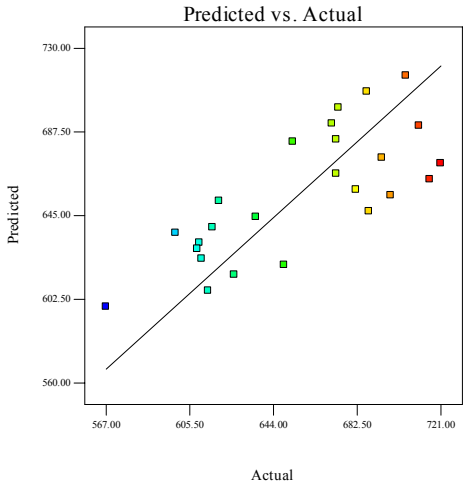

Fig. 5.44: Predicted Vs Actual for notched tensile strength NTS, MPa.

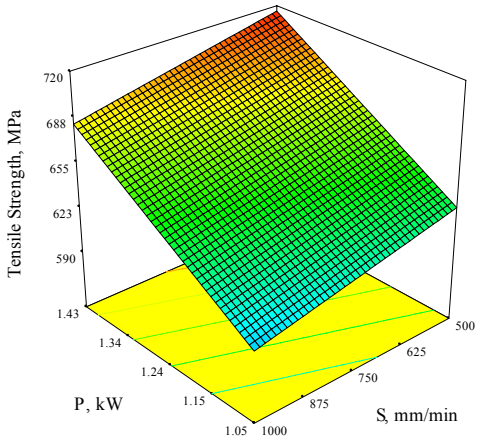

Fig. 5.45: 3D graph shows the effect of P and S on the tensile strength of the dissimilar joints at F = -0.92 mm.

5.2.5 Development of the Mathematical Model for Impact Strength

The impact resistance was measured and is listed in Table 5.20 and exhibited in Fig. 5.46. Design Expert 7 software had been used for analysing the measured response. The fit summary output indicates that the model developed is statistically significant for the prediction of the response and therefore they will be used for further analysis

5.2.5.1 The S/N ratio analysis

The signals have indicated that the effect on the average responses and the noises were measured by the influence on the deviations from the average responses, which would indicate the sensitivity of the experiment output to the noise factors. In this study, the S/N ratio was chosen according to the criterion the-bigger-the-better in order to maximize the impact resistance. Eqs 3.2 and 3.4 were applied for calculating the S/N ratio. The Taguchi experiment results presented in Fig. 5.46 were obtained using MINITAB 13 statistical software.

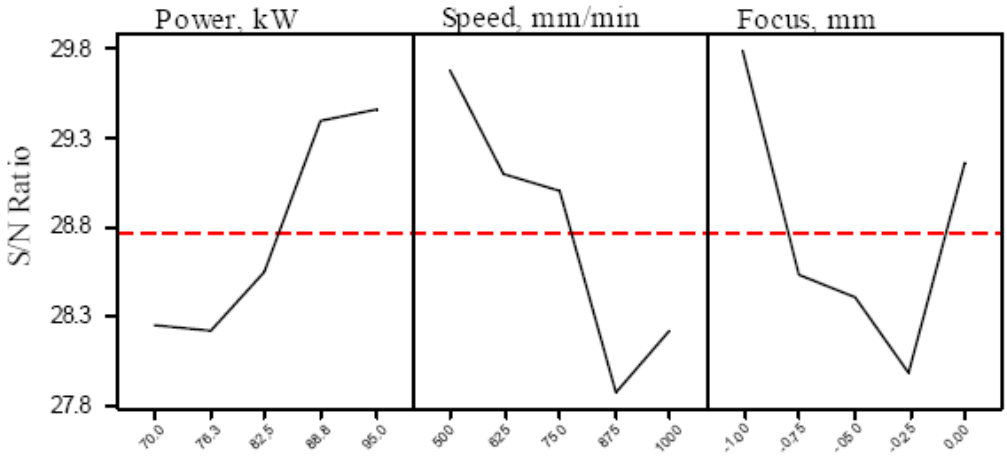

Fig. 5.46: Effects of the parameters on the impact test and S/N ratio.

5.2.5.2 Analysis of variance

The test for significance of the regression model, the test for significance on individual model coefficients and the lack-of- fit test were performed using Design Expert 7 software. The backward regression method; which eliminates the insignificant model terms automatically was applied and exhibited in the ANOVA Table 5.39 for the reduced quadratic model. ANOVA Table summarizes the analysis of the variance of the response and shows the significant model. The same table shows also the other adequacy measures R^2, adjusted R^2, and adequacy precision for each response. The Model F_v-value of 5.332 implies the model is significant. Values of "Prob > F_v " of less than 0.0500 indicates that the model terms are significant. In this case P, S and F are significant model terms. Another indicator value is "Adeq Precision" which measures the signal to noise ratio. In this study a ratio of 8.956

indicates an adequate signal. This model can be used to navigate the design space. The analysis of variance indicates that for the impact resistance model, the main effect was the laser power P, the second order effect was the focused position parameter F, while welding speed S has a less significant effect to the response. The final mathematical model in terms of coded factor and actual factors as determined by Design Expert software is shown below. The developed model indicates that the welding parameters have two level interactions, such as PS, PF and SF.

Final Equation in Terms of Coded Factors:

Impact Strength = 27.81 +3.00*P -1.81*S -2.01*F -4.50*P*S +4.45*P*F +3.18*S*F **…(5.28)**

Final Equation in Terms of Actual Factors:

Impact Strength = -115.126 +110.339 *P +0.123*S -81.164*F -0.095* P* S+46.836*P*F +0.025*S*F **…(5.29)**

Table 5.39: ANOVA for selected parameters model

Source	**Sum of Squares**	**d f**	**Mean Square**	**Fv-value**	**Prob. > F_v**	
Model	228.489	6	38.081	5.332	0.0026	significant
P	85.241	1	85.241	11.936	0.0028	
S	33.257	1	33.257	4.657	0.0447	
F	40.835	1	40.835	5.718	0.0279	
PS	51.476	1	51.476	7.208	0.0151	
PF	50.218	1	50.218	7.032	0.0162	
SF	26.645	1	26.645	3.731	0.0693	
Residual	128.551	18	7.142			
Cor. Total	357.040	24				
R-Squared = 0.6400				Adeq. Precision = 8.956		
Adj. R-Squared = 0.5199						

5.2.5.3 Model validation

The final step is to predict and verify the improvement of the response using the optimal level of the welding process parameters. Fig. 5.47 shows the relationship between the actual and predicted values of the response, which indicates that the developed model is adequate because the residuals in prediction of each response are

negligible, since the residuals are distributed around the diagonal line. To insure the results validation, three extra conformation experiments were carried out using test conditions, which were selected within studied range of the parameters. Table 5.40 shows the actual and predicted values of the impact strength and the percentage of absolute error in prediction.

Table 5.40: Confirmation experiments of the responses compared with model results.

Exp. No	P, kW	S, mm/min	F, mm	Impact Strength, J		$\|E\|$ %
				Act.	Pred.	
1	1.05	590	-0.59	23	25	8
2	1.21	642	-1	28	32	12.5
3	1.31	1000	0	29	28	3.57

5.2.5.4 Effect of process parameters on the responses

The results indicate that the laser power also has the major effect on the impact strength, as shown in Fig. 5.48. It is clear that the higher laser power results in higher impact strength. This is due to the fact that using high laser power results in increased power density, at a given focus point position, leading to greater penetration, which would improve the impact strength. It is evidence from the results that the welding speed has a significant effect on the impact strength among the studied welding parameters of the laser-welded joint. Fig. 5.48 shows the contour graph of the relationship between the welding speed, laser power and the energy absorbed by the joint. It is evident that the impact strength has the highest value at a speed of 750 mm/min. Further increases in speed will lead to a decrease in impact toughness. The results indicate that the focus point position has a great effect on the toughness of the material within the domain range of the study. In general, using a focused laser beam means that the laser power will be localized onto a small area. This would increase heat input which increases the power density leading to better penetration and sound welds. The relationship between P and F and their effect on impact strength is exhibited in a contour graph shown in Fig. 5.49 at S = 750 min/mm.

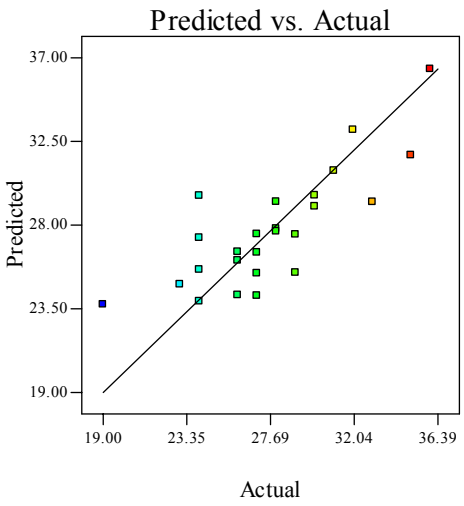

Fig.5.47: Scatter diagram of actual response predicted.

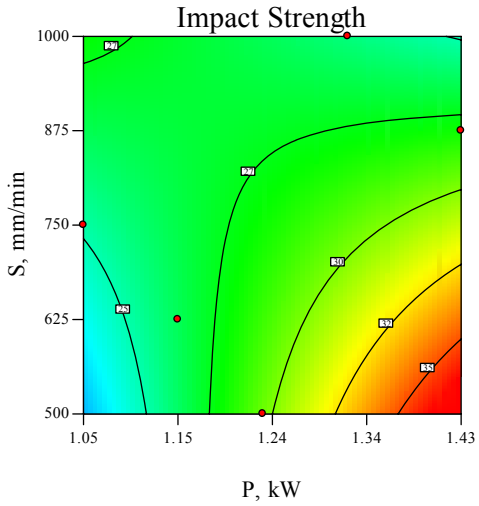

Fig. 5.48: Contour graph shows against the relationship between P and S at F =-0.5 mm

Fig.5.50 shows the perturbation plot exhibiting the effect of the three welding parameters on the impact strength**.** The perturbation plot helps to compare the effect of all the factors at a particular point in the design space. The response is plotted by changing only one factor over its range while holding the other factors constant. The reference point is at the midpoint (coded 0) of all the factors. The reference point can be changed to be any point.

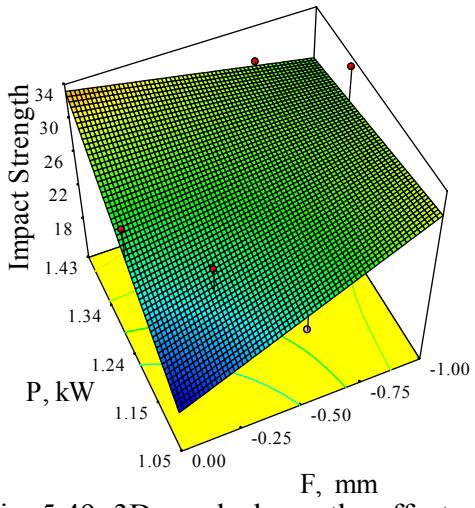

Fig. 5.49: 3D graph shows the effect of P and S on Impact strength at F=-.5mm.

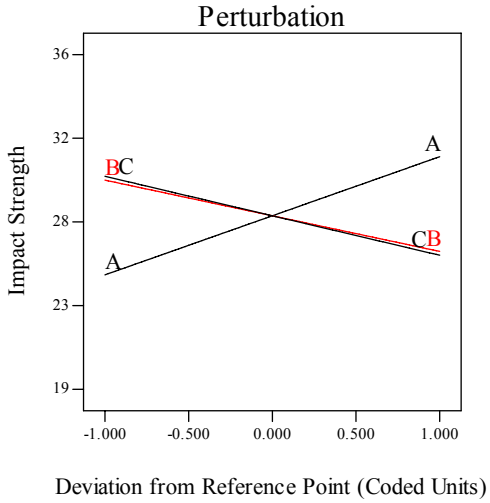

Fig 5.50: Perturbation plot exhibiting the effect of welding parameters on the impact strength.

5.2.6 Operating Cost Modeling

The operating cost for joining the above mentioned dissimilar materials were calculated using Eq. 4.13 and presented in Table 5.20. The mathematical model was developed to minimize the operating cost. The same procedure was followed to check the model adequacy. The analysis results are presented in Table 5.41 for the backward reduced quadratic model for the welding operating cost. The same table shows the other adequacy measures R^2, Adjusted R^2 and predicted R^2. All the adequacy measures indicate an adequate quadratic model. The adequate precision is 177.1, indicating adequate model discrimination. The developed quadratic mathematical model in terms of coded factors and actual values, exhibited in Eqs 5.30 and 5.31, will be used for optimization calculations.

Final Operating Welding Cost Equation in Terms of Coded Factors:

Welding Cost = 0.17 +7.162E-003*P -0.063*S -2.487E-003*P*S +0.022*S^2 **…(5.30)**

Final Operating Welding Cost Equation in Terms of Actual Factors:

Welding Cost= 0.461+0.070* P -7.09E-004*S -5.24E-005*P*S+3.473E-007*S^2

…(5.31)

Table 5.41: Shows the ANOVA for the welding operating cost.

Source	**Sum of Squares**	**df**	**Mean Square**	**F_v Value**	**p-value Prob. > F_v**	
Model	0.0527	4	0.01317	4158.07	< 0.0001	significant
P	0.0006	1	0.00062	194.90	< 0.0001	
S	0.0500	1	0.05001	15782.68	< 0.0001	
PS	0.0000	1	3.7E-05	11.75	0.0027	
S^2	0.0021	1	0.00206	650.70	< 0.0001	
Residual	0.0001	20	3.2E-06			
Cor. Total	0.0528	24				
R-Squared = 0.9988				Adeq. Precision = 177.1		
Adj. R-Squared = 0.9986						

5.2.7 Models (multiple –response) Optimization

5.2.7.1 Numerical Optimization

For numerically optimizing the input/output welding parameters, three optimization criteria were selected. For each criterion a multiple-response optimization was considered to optimize all the input/output welding parameters. Each optimization criteria is made to be different from the other by changing the parameters weight, giving each parameter a certain weight (from 0.1 to 10) to emphases a parameter influence on the process optimization, as detailed in chapter 3, or by changing the parameters important which is ranged between (+ to + + + + +). The numerical multiple-response optimization criterion is to reach maximum tensile strength, maximum impact strength and minimum welding pool geometry, minimum welding operating cost with minimizing laser power and maximizing welding speed while focus position was kept in range.

In first optimization criteria all the parameters received the same importance (+ + +) and same weight (1) as per the Design Expert software default. In the second criteria a different weight was assigned for each parameter as presented in Table 5.42, while the importance for each parameter was kept same as (+ + +). The importance was changed for welding parameters in the third criteria while the weight was kept as per the software default. All the decided welding optimization criteria and the resultant optimizations are presented in Table 5.42. The result presented in Table 5.42 at each criterion is selected from the ten or more different optimum result calculated by software based on the selected criterion.

The effect of changing the criteria on the optimization result is obvious in Table 5.42. For example by applying in the third criteria tensile strength value will reach up to 668 MPa while by applying the second criteria the tensile strength will be around 674 MPa. If the target is only to maximize the tensile strength regarding less the other parameters than the response value will be greater than the received values and this is true for each response individually optimized.

Referring to the studied residual stress at different depth levels, level 1 was chosen for a multiple-response optimization, it is well-known that most of the cracks are started at the surface of the work piece therefore the level 1 is the most critical

level among the studied levels. The residual stress at level 1 depth of the specimen does not change (145 MPa for all optimization criteria results) because the residual stress in this level is dependent only on welding speed as it obvious in the developed model (Eq. 5.13). Impact strength was affected by changing the optimization criterion, its value is between (26 J – 30 J) depending on its assigned weight and the importance it received in each criterion.

The welding geometries were not assigned high weight or high important since they are not direct targets for the optimization, they are indirectly effected by the welding quality. W_2 was kept as 'in range' in all optimization criteria to avoid applying more constraints which are affecting the optimization processes and negatively affecting the important responses (mechanical properties). This will lead to decreasing welding quality.

The welding cost was reduced to around 13 cent in the three criteria comparing to the values presented in Table 5.20, in which a maximum of 27 cent was reached. Also, the welding speed is maximum or nearly maximum (1000 mm/min) in all optimization criteria which leads to increasing production rate. The welding cost is almost the same in all the criteria because it received the highest importance rate and highest weight at all three criteria. However, the achieved values for the responses using multiple-response optimization is less then those values obtained by applying the single-response optimization. A ramps view of the results of first optimal criterion presented in Table 5.42 is exhibit in Fig. 5.512.

5.2.7.2 Graphical optimization

In a graphical optimization with multiple responses, the software defines regions where requirements simultaneously meet the proposed criteria. Also, superimposing or overlaying critical response contours can be defined on a contour plot. Then, a visual search for the best compromise becomes possible. The graphical optimization displays the area of feasible response values in the factor space. The overlay plots in Figs. 5.51 to 5.53 shows that the graphical optimization allows visual selection of the optimum welding conditions according to certain criterion. The result of the graphical optimization are the overlay plots, these type of plots are extremely practical for quick technical use in the workshop to choose the values of the welding parameters that would achieve certain response value for this type of dissimilar

materials. The yellow /shaded areas on the overlay plot in Figs. 5.51-5.53 are the regions that meet the proposed criteria.

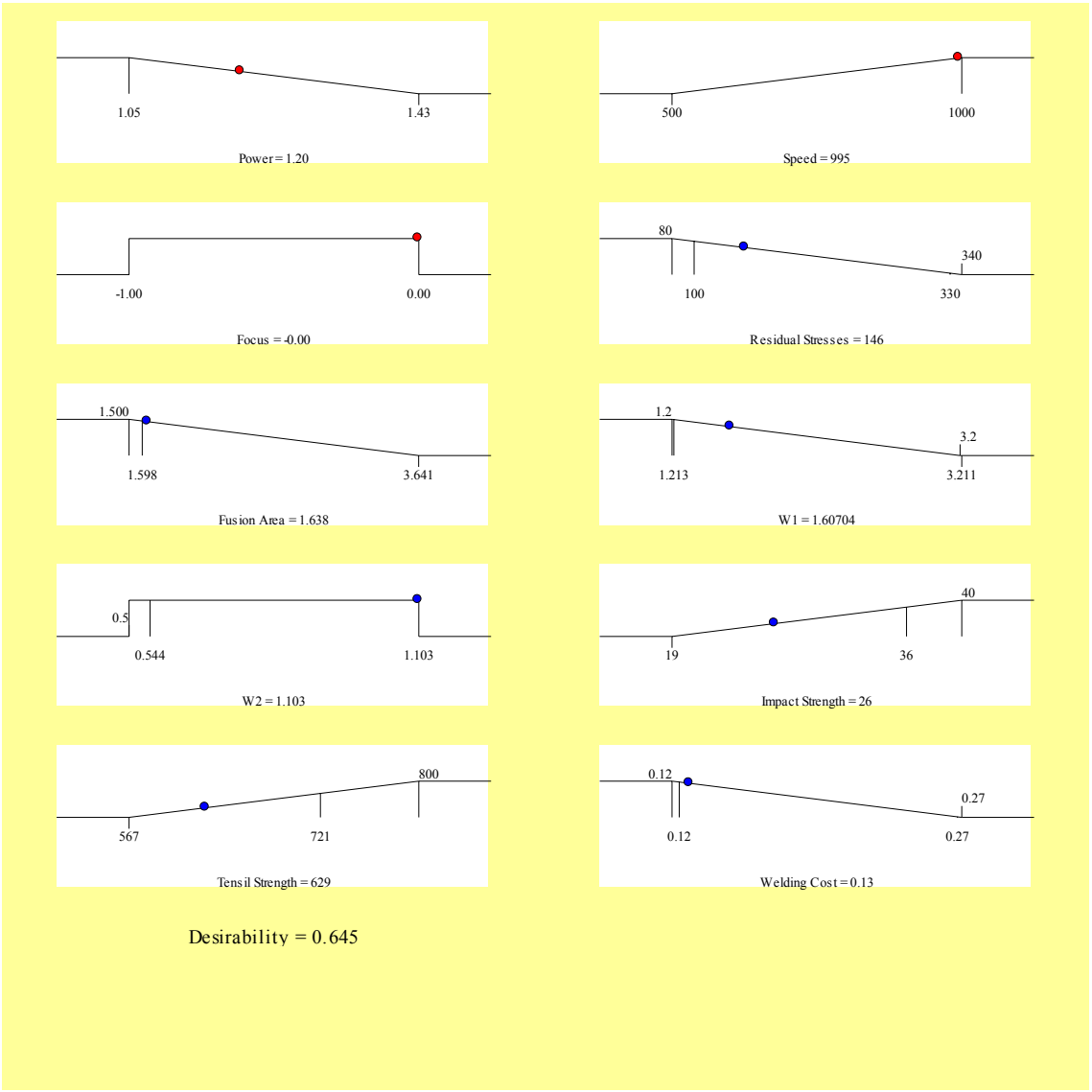

Fig 5.51: Ramps view of the first optimal criterion shows the desirability for each factor and each response, as well as the combined desirability at the optimal point

Table 5.42: Three optimization criteria with the optimization results using numerical multiple-response

Welding Parameters	**Power**		**Speed**		**Focus**		**Residual Stresses**		**A**		**W_1**		**W_2**		**Impact Resistance**		**Tensile Strength**		**Cost**		**D*.**
Goal	Min		Max.		In range		Min		Min.		Min.		In range		Max.		Max.		Min.		
Criteria	Wt.*	Imp.*	Wt.	Imp.	Wt.	Imp.	Wt.	Imp.	Wt.	Imp.	Wt.	Imp.	-	-	Wt.	Imp.	Wt.	Imp.	Wt.	Imp.	
First Criteria	1	+++	1	+++	-	-	1	+++	1	+++	1	+++	-	-	1	+++	1	+++	1	+++	
Result	1.20		995		0		145		1.638		1. 607		1.103		26		629		0.13		0.645
Second Criteria	0.5	+++	5	+++	-	-	0.5	+++	0.5	+++	0.5	+++	-	-	5	+++	5	+++	0.5	+++	
Result	1.440		1000		0.00		145		1.235		1.189		1.018		30		674		0.13		0.354
Third Criteria	1	+	1	+++	-	-	1	+++ ++	1	+++	1	++	-	-	1	+++ ++	1	+++ ++	1	+++ ++	
Result	1.37		1000		0.00		145		1.284		1.239		1.082		29		668		0.13		0.125

Imp.* = Important, Wt*.= Weight, D.* = Desirability

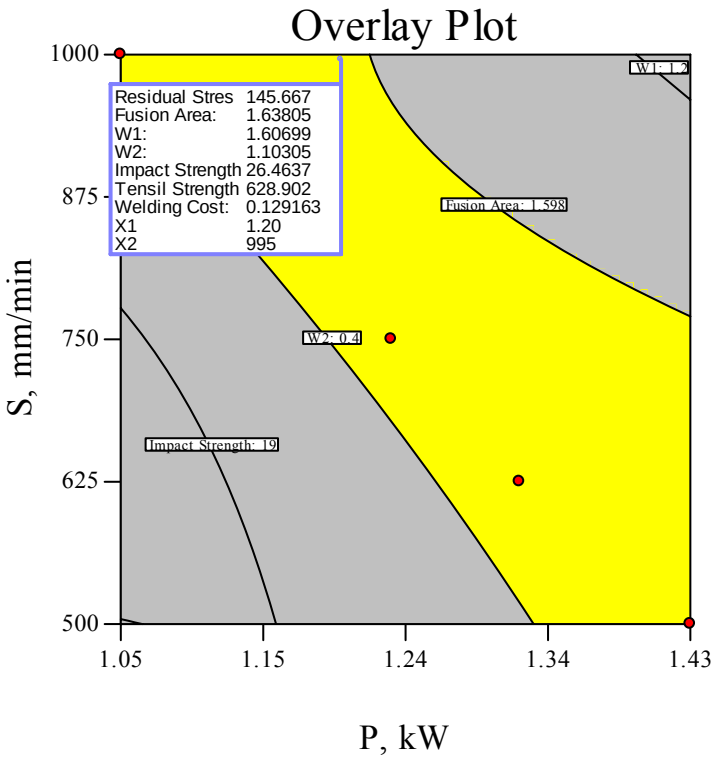

Fig 5.52: Exhibiting the feasible solution in the yellow shaded area for the first optimization criteria.

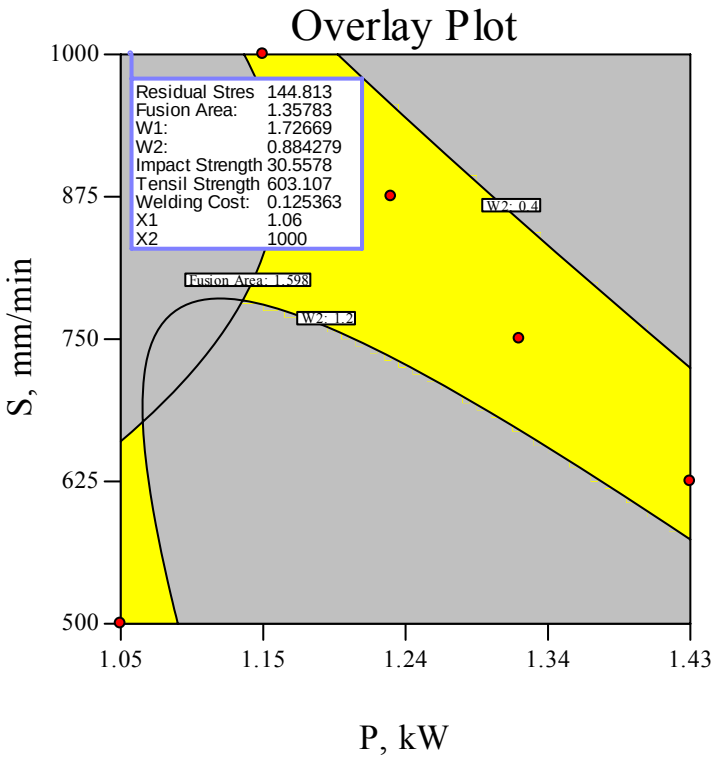

Fig 5.53: Exhibiting the feasible solution in the yellow shaded area for second optimization criteria.

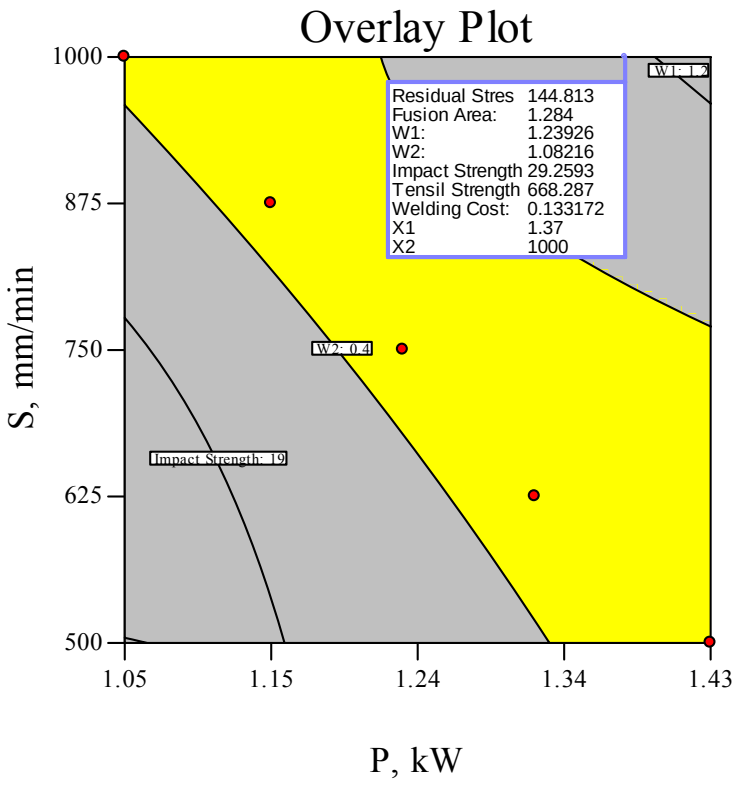

Fig 5.54: Exhibiting the feasible solution in yellow shaded area for third optimization criteria.

5.2.8 Micro Harness and Microstructure Studies

5.2.8.1 Solidification in the fusion zone

As Pb is insoluble in molten steel, and austenite / ferrite have a low capacity for dissolving S and P, all of these elements are vigorously segregated in the liquid during solidification. The resulting high impurity concentrations in the last liquid to solidify in the interdendritic regions have much lower melting points than those of the primary solidifying phase. The melting point of Pb is only 327–502°C and the melting point of the sulphides (MnS, FeS, CrS) is about 1100 –1200°C, i.e. much lower than that of Fe (1538°C). If sufficiently high stresses are generated before final solidification, the boundaries with segregated Pb and sulfides may separate to form solidification cracks in the fusion zone, which providentially was not observed in this experimental study. Figs. 5.55(a, b) and 5.56 (a, b) shows the base metal (BM) / HAZ of AISI1008 and AISI316 respectively.

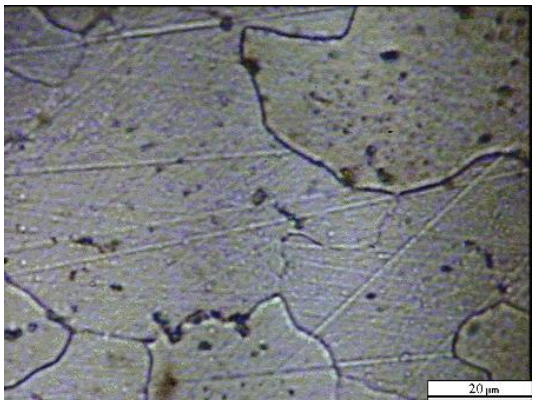

Fig 5.55(a): AISI1008 base metal

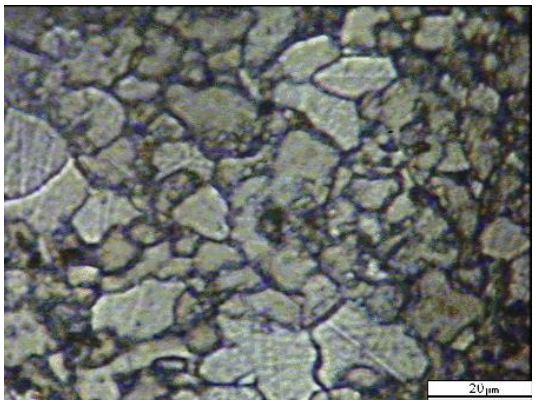

Fig 5.55(b): LCS1008 HAZ

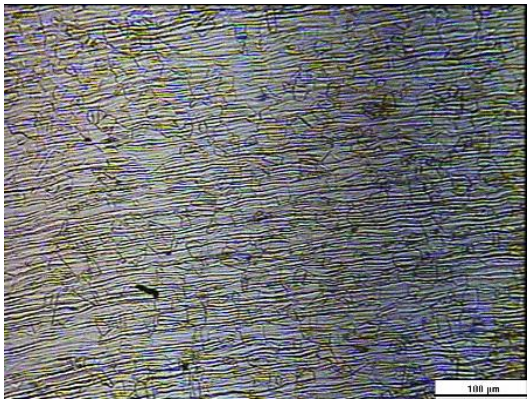

Fig 5.56(a): SST 316 base metal

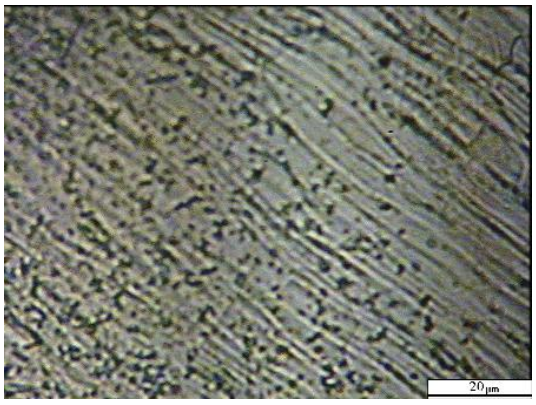

Fig 5.56(b): SST 316 HAZ

5.2.8.2 Microstructure in the HAZ

Owing to the epitaxial nature of solidification, the grain boundary in the HAZ can link up with the solidification grain boundary in the fusion zone. Segregation of S, Pb, Mn and P during solidification means that these elements are able to diffuse into the HAZ from the fusion zone along the grain boundaries. The impurities and dissolved elements diffuse more rapidly along the grain boundaries than through the crystal lattice, and this results in a local depression of the melting temperature [174]. As a consequence, the grain boundary may melt during welding thermal cycles, but the local stress (as studied above in this chapter) is insufficiently high to impose the melted grain boundary to separate in the HAZ.

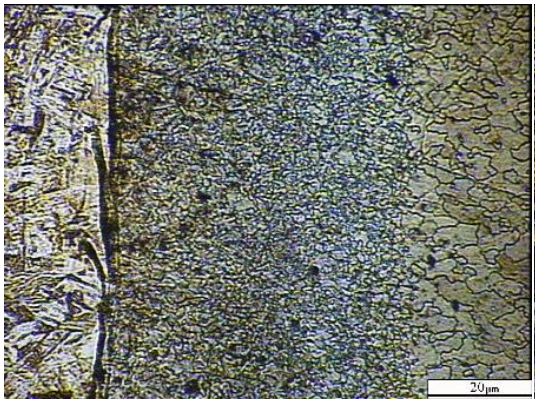

Fig 5.57(a): Weld pool, HAZ and BM of AISI1008.

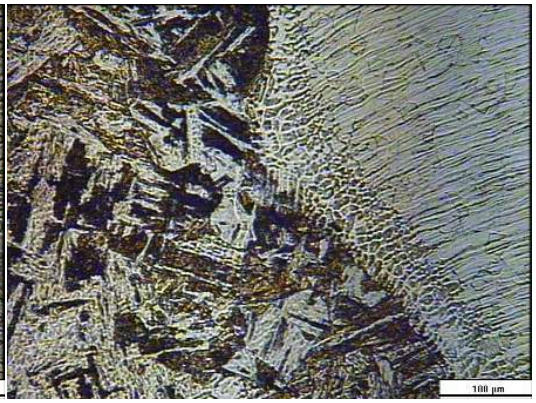

Fig 5.57(b): Weld pool, HAZ and BM of AISI316.

The microstructures in the fusion zone are a result of solidification behaviour and subsequent solid-phase transformation, which are controlled by composition and weld cooling rates. Moreover, the composition in the fusion zone of a dissimilar joint depends on the melting ratio of the two materials to be jointed, which in turn is related to the welding parameters. Figs. 5.58 (a, b) shows the redistribution of elements in the fusion zone of a butt weld joining AISI316 to AISI1008, corresponding to the welding parameters given in Table 5.19 of the specimens number 1 and 25 respectively . As is obvious from Figs. 5.57 (a, b) the HAZ of AISI1008 width is about 300 to 400 μm while the HAZ of AISI316 width is about 20 to 40 μm, this is due that the thermal expansion coefficient of austenite being higher than that of ferrite, and the heat conductivity of austenite is lower than that of ferrite, these features resulted in a higher level of thermally-generated stresses.

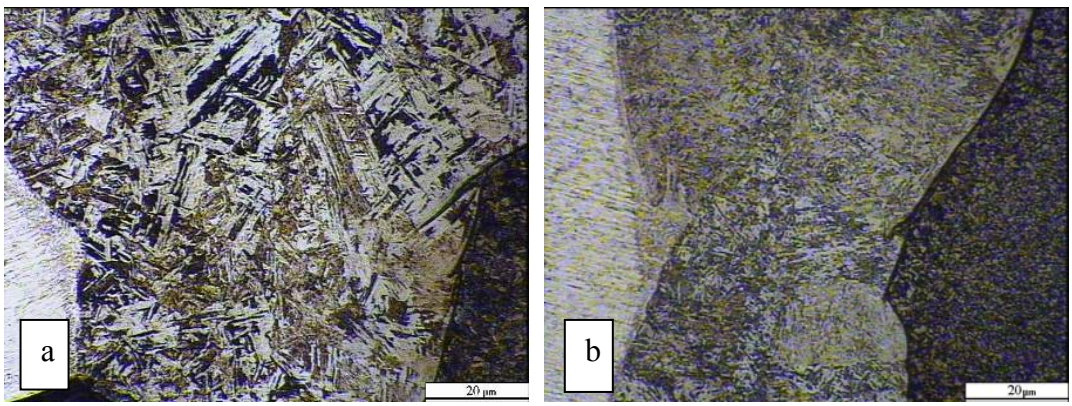

Figs. 5.58 (a, b): The redistribution of elements in the fusion zone of a butt weld joining AISI316 to AISI1008.

5.2.8.3 Microhardness

Since AISI316 is an austenitic base material and AISI1008 is a ferritic base material, the microstructures of the fusion zone must contain a variety of complex austenite–ferrite structures. Fig. 5.59 shows the microhardness profile of the joint in seven different points of selected specimens. The specimens selected for microhardness studies were based on heat input calculations (P x S). The microhardness of the fusion zone is greater than that of both the AISI316 and AISI1008 base materials; this may result from the effect of rapid solidification. The microhardness gradient correlates with the gradient of the redistribution of the elements Cr, Fe, and Ni, which may be a particular phenomenon of dissimilar fusion joints. The cooling rate in the fusion zone of laser keyhole welds is roughly between 10^4 and 10^6 °C s^{-1} [4]. Rapid solidification not only increases under cooling and nucleation probability, which leads to very fine structures but also extends the solutes solubility, which thus prevents marked segregation and results in a supersaturated solid solution, and then new microstructures [175]. The microhardness of the weld HAZ interface in both sides is less than that measured in the weld pool but it is higher than the HAZ and base metals. This is due to the reasons mentioned above.

The strength of the laser welds is higher than both the tensile strength and impact strength of AISI316 / AISI1008 under the test conditions adopted in this research. The greater mechanical properties of the laser welds demonstrate the beneficial effect of rapid solidification in the fusion zone and of a small HAZ. The microstructures in the fusion zone call for further research using TEM.

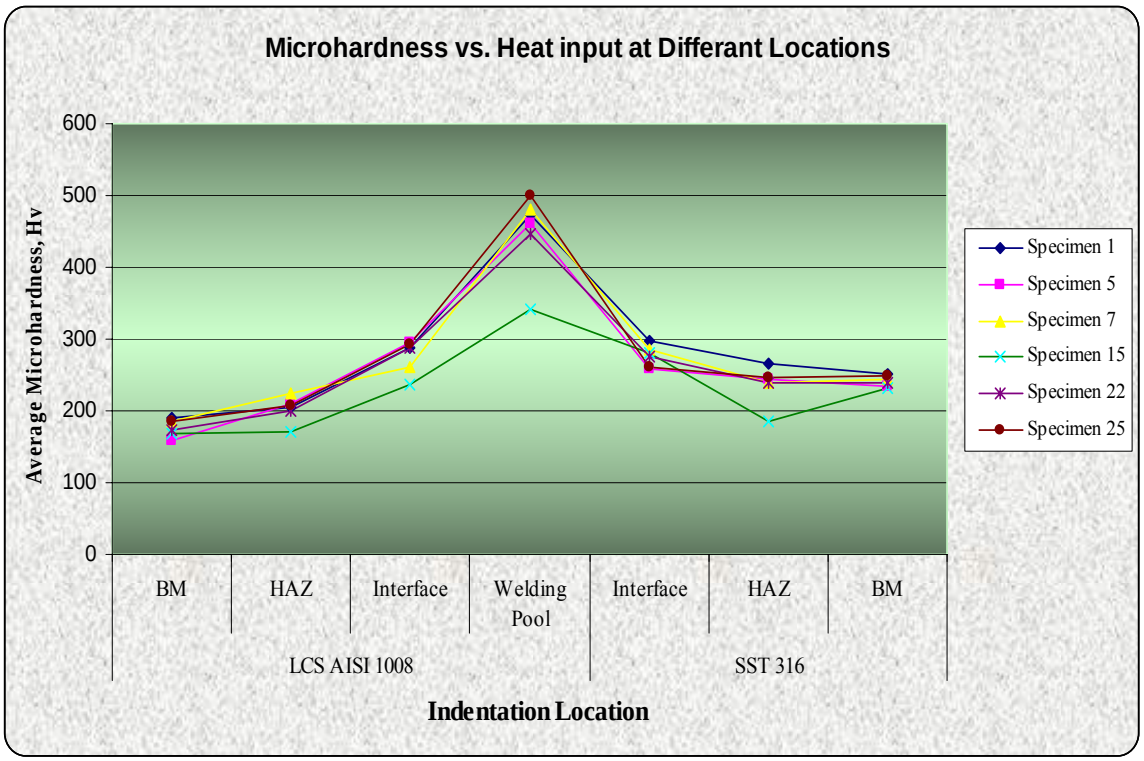

Fig. 5.59: The microhardness profile of the dissimilar joint for the specimens (1, 5, 7, 15, 22 and 25)

5.3 Joining of Low Carbon Steel Din: en 10131 to Stainless Steel AISI 316 (3 mm Thickness)

5.3.1 Orthogonal Array Experiment

The dissimilar materials low Carbon steel Din: en 10131 and stainless steel AISI 316 plates of 3 mm thicknesses were jointed using the butt welding jointing design. The welding input parameters used were studied. The operating range was determined by pilot experiments, the welding inputs variables and experiment design levels, presented in Table 5.43, were then decided. In this study of the dissimilar material joint with the above mentioned thickness, the interactions between the welding parameters are considered. An L16 orthogonal array with four columns and 16 rows was used. Sixteen experiments runs were required to study the welding parameters using an L16 orthogonal array. The experiments were designed using Design Expert 7 software. The welding input variables used are as presented in Table 5.44. The experiments were run in random order.

Table 5.43: Process parameters and design levels used

Variables	Code	Unit	Level 1	Level 2	Level 3	Level 4
Laser Power	P	kW	1.00	1.15	1.30	1.45
Welding Speed	S	mm/min	200	533	867	1200
Focus	F	mm	-1	-0.67	-0.33	0
Gap	G	mm	0	0.05	0.1	0.15

Table 5.44: The Taguchi design matrix with the actual values of the studied welding parameters and welding pool geometry, mechanical tests results and cost per meter welding calculations.

Std.	Run	Power, kW	Speed, mm/min	Focus, mm	Gap, mm	A, mm^2	W_1, mm	W_2, mm	Impact St., J	Tensile St., MPa	Cost, €/m
1	9	1.00	200	-1.00	0.00	9.469	4.839	2.761	33	757	0.61
2	8	1.00	533	-0.67	0.05	3.628	2.586	3.483	30	643	0.23
3	10	1.00	867	-0.33	0.1.0	2.469	1.733	0.821	27	603	0.14
4	16	1.00	1200	0.00	0.15	1.636	1.168	0.734	16	559	0.10
5	11	1.15	200	-0.67	0.10	11.956	5.170	3.374	33	731	0.63
6	4	1.15	533	-1.00	0.15	3.492	1.936	1.124	31	659	0.24
7	1	1.15	867	0.00	0.00	2.660	1.584	0.944	26	617	0.15
8	3	1.15	1200	-0.33	0.05	2.033	1.499	0.854	4	544	0.11
9	15	1.30	200	-0.33	0.15	12.567	5.555	3.396	31	835	0.65
10	2	1.30	533	0.00	0.1	3.902	2.506	0.956	37	629	0.24
11	14	1.30	867	-1.00	0.05	2.872	1.834	0.979	35	692	0.15
12	13	1.30	1200	-0.67	0.00	2.083	1.588	0.797	7	613	0.11
13	5	1.45	200	0.00	0.05	10.747	3.529	3.730	31	842	0.67
14	6	1.45	533	-0.33	0.00	3.971	2.332	1.005	37	710	0.25
15	12	1.45	867	-0.67	0.15	2.604	1.898	0.934	16	646	0.16
16	7	1.45	1200	-1.00	0.10	2.018	1.172	0.742	12	570	0.11

5.3.2 Development Mathematical Models for Welding Pool Geometry

The area of the fusion welding zone 'A' was measured by using the transverse sectioned specimens, the optical microscope and image analyzer software. Using the same procedure the welding pool width at surface, W_1, and the welding pool width at the middle, W_2, of the specimens, was also measured and analyzed. The measured responses are listed in Table 5.44 and selected experiments runs are exhibited in Fig.

5.60 to illustrate the effect of welding parameters on the weld bead geometries. Design Expert 7 software was used for analyzing the measured responses.

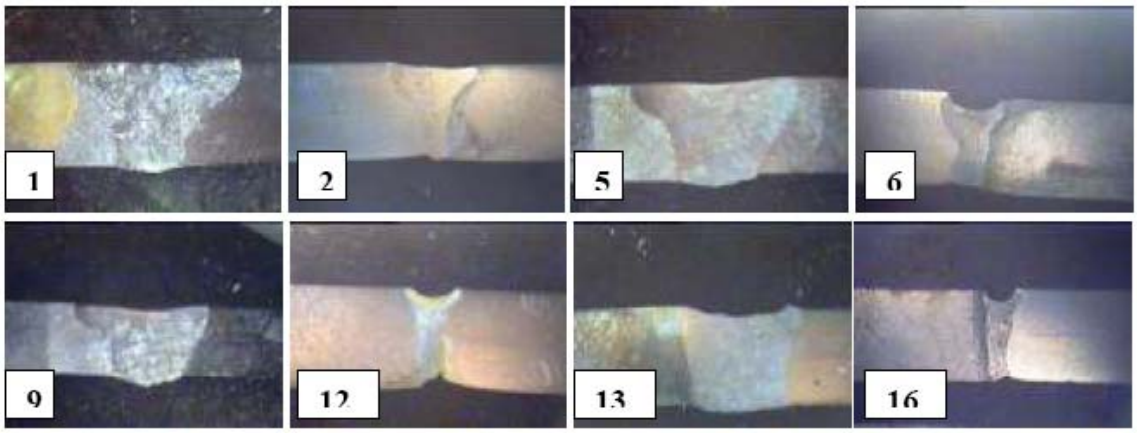

Fig. 5.60: Shows the effect of the welding parameters on the responses (A, W_1, W_2), and the variation on weld bead geometry, X10.

5.3.2.1 The S/N ratio analysis

In order to evaluate the influence of each selected factor on the responses: The Signal-to-Noise ratios (S/N) for each control factor had to be calculated. The signals indicated that the effect on the average responses and the noises were measured by the influence on the deviations from the average responses. The level of deviation indicates the sensitivity of the experiment output to the noise factors. The appropriate S/N ratio must be chosen using previous knowledge, expertise, and understanding of the process. When the target is fixed and there is a trivial or absent signal factor (static design), it is possible to choose the signal- to-noise (S/N) ratio depending on the goal of the design. In this study, the S/N ratio was chosen according to the criterion the-smaller-the-better, in order to minimize the responses. The S/N ratio for the-smaller-the-better target for all the responses was calculated using Eqs 3.2 and 3.4.

The above-presented data was used with the selected above formula to calculate S/N. The Taguchi experiment results are summarized in Table 5.45 and presented in Fig. 5.61, which were obtained by means of MINITAB 13 statistical software. It can be noticed from the main effects plot for S/N that travel speed ‘S’ is the most important factor affecting the responses; the minimum is at the highest level of ‘S’. Laser power and Focus point position plots show a less relevant effect. The

gap between the jointed plates show the least important effect of this factor as demonstrated in Fig. 5.61. Main effects plot for S/N ratios suggest that those levels of variables that minimised the weld pool dimensions were also robust against variability due to noises as presented in Fig. 5.61.

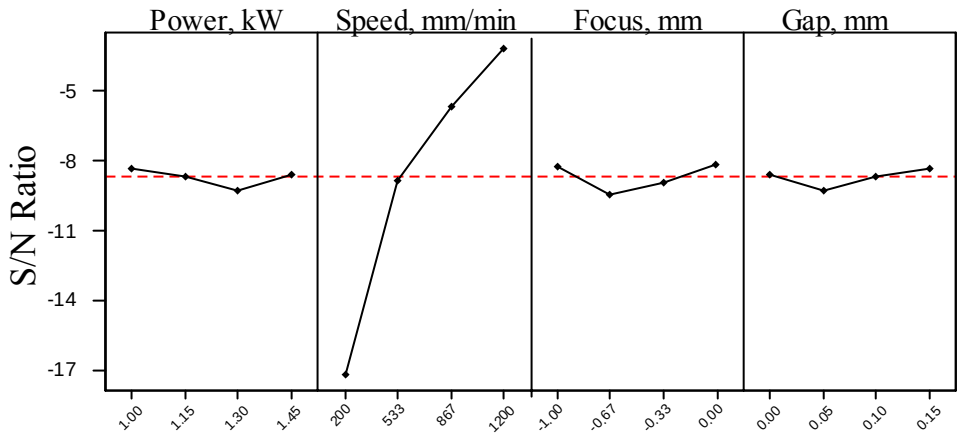

Fig. 5.61: Effects plot for S/N ratio of the responses.

Table 5.45: The responses for signal-to-noise ratio (S/N).

Levels	**1**	**2**	**3**	**4**	**Delta**	**Rank**
P, kW	-8.32	-8.84	-9.30	-8.55	0.97	3
S, mm/min	-17.21	-8.82	-5.63	-3.14	14.07	1
F, mm	-8.21	-9.45	-8.95	-8.19	1.26	2
Gap, mm	-8.54	-9.25	-8.67	-8.35	0.90	4

5.3.2.2 Analysis of variance

The test for significance of the regression model, the test for significance of the individual model coefficients and the lack-of-fit test were performed using Design Expert 7 software. The backward regression method was applied and exhibited in ANOVA Tables 5.46-5.48 for the reduction of the developed quadratic models.

ANOVA Tables summaries the analysis of three variances of the responses and show the significant models. The same tables also show the other adequacy measures, R^2, adjusted R^2, and adequacy precision, for each response. All adequacy measures were close to 1, which are reasonable and indicate adequate models. The adequate precision compares the range of the predicted value at the design points to the average predicted error. In this study the value of adequate precision in each case is significantly greater than 4.

The analysis of variance indicates that for the welding pool area 'A' model, the welding pool width at the work piece surface 'W_1' model and welded pool width at the middle of work piece 'W_2' model the main effect was the welding speed, the second order effects were the focused position and the laser power. The final mathematical models in terms of coded factors and actual factors as determined by Design Expert software are shown below.

Final equation for fusion area in terms of coded factors:

$$A = 4.88 - 4.32*S \quad \textbf{…(5.32)}$$

Final equation for fusion area in terms of actual factors:

$$A = 10.93479 - 8.647E\text{-}003* S \quad \textbf{…(5.33)}$$

Final equation for W_1 in terms of coded factors:

$$W_1 = 2.56 - 1.62*S \quad \textbf{…(5.34)}$$

Final equation for W_1 in terms of actual factors:

$$W_1 = 4.83167 - 3.248E\text{-}003* S \quad \textbf{…(5.35)}$$

Final equation for W_2 in terms of actual factors:

$$W_2 = 1.66 - 1.25*S \quad \textbf{…(5.36)}$$

Final equation for W_2 in terms of actual factors:

$$W_2 = 3.41263 - 2.497E\text{-}003* S \quad \textbf{…(5.37)}$$

Table 5.46: The ANOVA for 'A' response model

Source	Sum of Squares	df	Mean Square	F_v Value	p-value Prob > F_v	
Model	166.16	1	166.16	39.87	< 0.0001	significant
S	166.16	1	166.16	39.87	< 0.0001	
Residual	58.35	14	4.17			
Cor. Total	224.52	15				
R-Squared.= 0.7401			Adeq Precision = 11.980			
Adj. R-Squared = 0.7215						

Table 5.47: The ANOVA for 'W_1' response model

Source	Sum of Squares	df	Mean Square	F_v Value	p-value Prob > F_v	
Model	23.44	1	23.44	44.06	< 0.0001	significant
S	23.44	1	23.44	44.06	< 0.0001	
Residual	7.45	14	0.53			
Cor. Total	30.89	15				
R-Squared = 0.7589			Adeq Precision = 12.594			
Adj. R-Squared = 0.7416						

Table 5.48: The ANOVA for 'W_2' response model

Source	Sum of Squares	df	Mean Square	F_v Value	p-value Prob > F_v	
Model	13.86	1	13.86	26.11	0.0002	significant
S	13.86	1	13.86	26.11	0.0002	
Residual	7.43	14	0.53			
Cor. Total	21.29	15				
R-Squared = 0.6510			Adeq Precision = 9.695			
Adj R-Squared = 0.6260						

5.3.2.3 Model validation

To predict and verify the improvement of the response using the optimal level of the welding process parameters the models are subjected to a model validation

study. Figs. 5.62-5.64 show the relationship between the actual and predicted values of A, W_1, and W_2, respectively. These figures indicate that the developed models are adequate because the residuals in prediction of each response are negligible, since the residuals tend to be close to the diagonal line. Furthermore, to verify the satisfactoriness of the developed models, three confirmation experiments were carried out using new test conditions at optimal parameters conditions, obtained using the Design Expert software. The A, W_1 and W_2 of the validation experiments were carried out using new test conditions at different parameters conditions, obtained using the developed mathematical models. Table 5.49 summarizes the experiments conditions, the actual experimental values, the predicted values and the percentages of error. It could be concluded that the models developed could predict the responses with a very small error. A, W_1 and W_2 were greatly improved through using the developed models. The fit summary output indicates that the models developed are statistically significant for the prediction of the responses therefore they will be used for parameters optimization.

Table 5.49: The confirmation experiments and base metal responses

Exp. No	**P, kW**	**S, mm/min**	**F, mm**	**G, mm**	**A, mm^2**		$\|E\|$ %	**W_1, mm**		$\|E\|$ %	**W_2, mm**		$\|E\|$ %
					Act.	**Pred.**		**Act.**	**Pred.**		**Act.**	**Pred.**	
1	1.01	846	0.69	.073	3.425	3.623	5.5	2.54	2.085	21.8	1.146	1.301	11.9
2	1.00	1073	-0.98	.018	1.847	1.658	11.4	1.216	1.347	9.7	0.656	0.734	10.6
3	1.00	1200	-0.18	.140	0.632	0.558	13.3	1.038	0.934	11.1	0.471	0.416	13.2

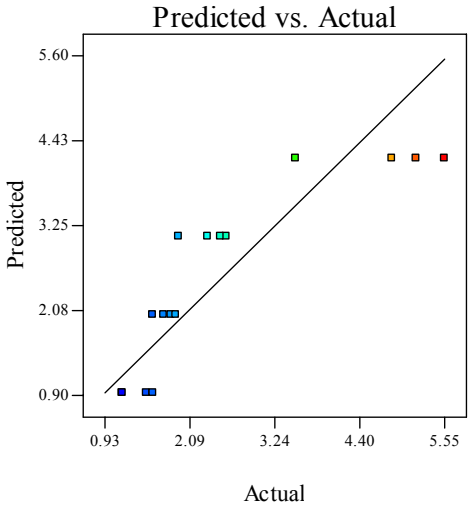

Fig. 5.62: The effect of actual welding parameters on the welding pool area 'A' response, against predicted.

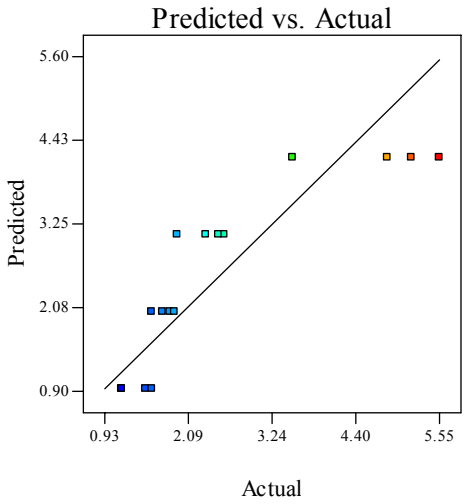

Fig. 5.63: The effect of actual welding parameters on the welding pool width at the serves of the specimen 'W_1'response, against predicted.

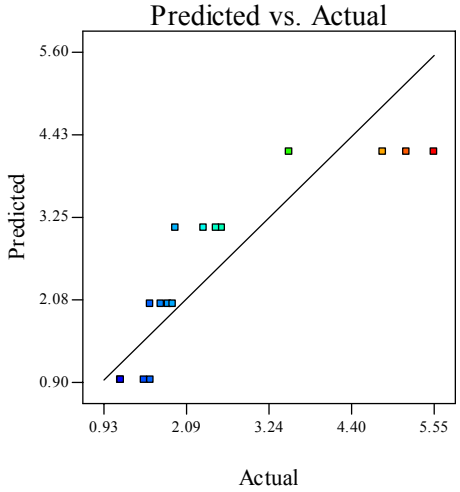

Fig. 5.64: The effect of actual welding parameters on the welding pool width at the middle of the spacemen 'W_2' response, against predicted

5.3.2.4 Effect of the parameters on responses

Welding Pool Area 'A'

In the present study, the fusion area 'A' of dissimilar joints between stainless steel and low carbon steel was measured and plotted in the 3D graph, as presented in Fig. 5.65. The figure shows the relationship between the welding parameters (S and F) and the Fusion area at P = 1.23 kW. Fig 5.65 shows that the welding speed has the

most significant effect on the process. The increase in welding speed 'S' rate, led to the reduction of the fusion area of the welding pool. When welding speed is at its maximum (1200 mm/min), as presented in Table 5.65, the fusion area is at its minimum and equals 1.636 mm^2, which presents the best achieved results. It is also noted that changes in the laser power 'P' rate would lead to changes in the fusion area value. The fusion area has the minimum value at a laser power of 1kW these results are shown in Fig. 5.61, it is clear that the focusing position 'F' and gap between the jointed plates 'G' have an insignificant effect on the welding pool, whereby changing the focusing position and/or gap the welding pool will not be consequentially changed and this effect is shown in Table 5.45.

Welding Pool Width at the Work Piece Surface (W_1)

The results and the model obtained for the response indicate that the S and F are the most important factors affecting W_1 value. An increase in S leads to a decrease in W_1. This is due to the laser beam travelling at high speed over the welding line when S is increased. Therefore, the heat input decreases leading to less volume of the base metal being melted, consequently the width of the welded zone decreases. Moreover, defocused beam, i.e. a wide laser beam, results in the spreading the laser power over a wide area. Therefore, a wide area of the base metal will be melted leading to an increase in W_1 or vice versa. The result shows also that P has a secondary effect on the response width dimensions. Increases in P will results in slight increases in W_1, due to the increase in the power density. Fig. 5.66 shows a 3D plot of the effect of process parameters (P and F) at F = -.05 mm/min and G = 0.075 mm on the W_1 width. The gap between the jointed plates 'G' has insignificant effect on the welding pool, whereby changing the gap the welding pool will not be consequentially changed. This effect is shown in Table 5.45 in which the parameter 'G' has the highest value (4).

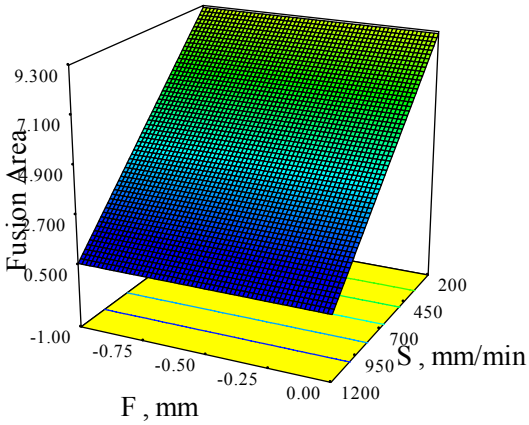

Fig. 5.65: 3D graph shows the effect of 'S' and 'F' on 'A' response, at 'P' = 1.23 kW and G = 0.075mm.

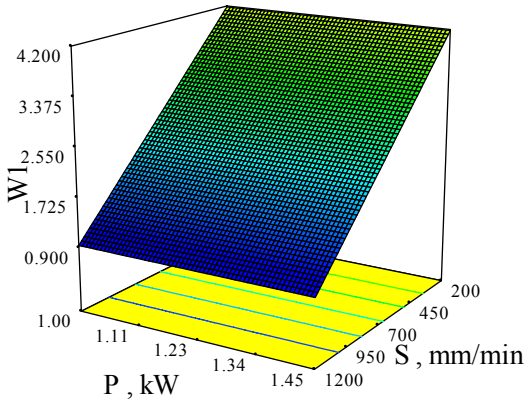

Fig. 5.66: 3D graph shows the effect of 'P' and 'S' on 'W1' response, at 'F' = -0.5 mm and G = 0.075 mm.

Welding Pool Width at the Middle of the Work Piece (W_2)

From the results it is clear that the four parameters significantly affect the W_2 value. Using a focused beam results in an increase in the power density, which indicates that the heat will be localize in a small metal portion, resulting in an increase in the power density leading to increasing W_2 value. The model shows that the response is proportioned inversely to F. The result shows that the changes in F parameter affects W_1, W_2 and doesn't affect A. This may be interpreted that as F decreased, W_1 increased, W_2 decreased and vice versa, so the total area A will not be affected by changing F. The increase in P leads to an increase in the heat input, therefore, more molten metal and consequently a wider W_2 will be achieved. However, the idea is reversed in the case of the S effect, because the S is inversely proportional to the heat input. Fig. 5.67 shows a 3D plots presenting the effect of process parameters (P and S) on the W_2 value at F = -0.5 mm and G = 0.075 mm. The result also shows that G contributes to a secondary effect in the response width dimensions.

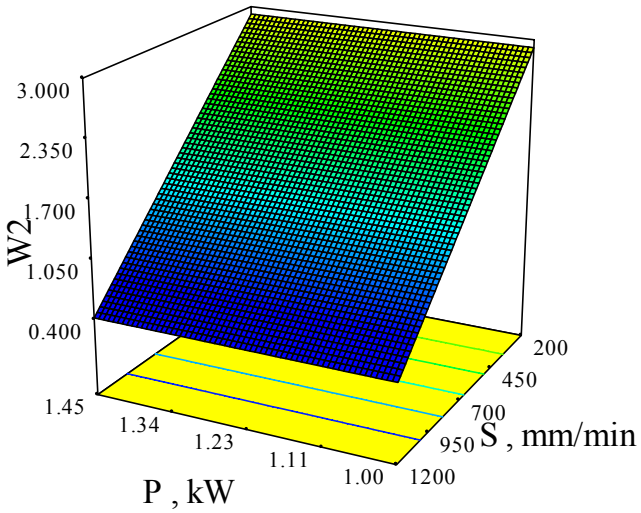

Fig. 5.67, 3D graph shows the effect of 'P' and 'S' 'W_2' response, at 'F' = −0.5 mm and G = 0.075 mm.

5.3.3 Development of a Mathematical Model for Tensile Strength

The experiments were carried out according to the design matrix given in Table 5.44. They were performed in random order to avoid any systematic error. The notched tensile strength 'NTS' samples mentioned in chapter four were tested at room temperature (20 ºC). Each tensile test result listed in table 5.44 is an average of at least three or more samples.

5.3.3.1 Analysis of the result

The raw data, the average tensile strength and the S/N ratio of the tensile test results are shown in Table 5.44. The average tensile strength and S/N ratio of the tensile test results are plotted for each of the welding parameters in Fig 5.68. The average NTS tests appear to be mainly affected by the welding speed and laser power as shown in Table 5.50. The rank 1 in Table 5.50 indicates that speed has a stronger effect on the process followed by rank 2, power, which has also a strong effect, while rank 3 for gap parameter has less on the process. The minimum affect on the process, at rank 4, focus position, has an insignificant effect on the process. To analyze the effects of the welding parameters in detail, ANOVA was conducted; these results are shown in Table 5.51.

Table 5.50: Shows the tensile strength response for S/ N Ratio.

Levels	1	2	3	4	Delta	Rank
P	640.50	637.75	692.25	692.00	54.50	2
S	791.25	660.25	639.50	571.50	219.75	1
F	669.50	658.25	673.00	661.75	14.75	4
G	674.25	680.25	633.25	674.75	47.00	3

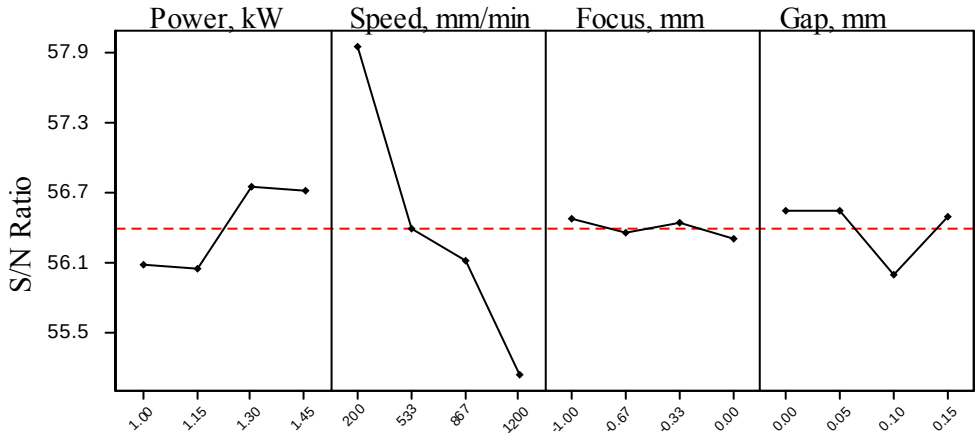

Fig. 5.68: The effect of the laser welding parameters on the tensile strength and S/N ratio.

In the ANOVA Table 5.51, the F_v is used to test the significance of a factor by comparing model variance with residual (error) variance, which is calculated by dividing the model mean square by the residual mean square. A high F_v value for a parameter means that the effect of the parameter on the characteristics is large. The result in Table 5.51 shows that the highest F_v value in the process was obtained for speed 'S' equal to 58.61. The F_v value for the laser power 'P' was equal to 5.54, which indicates that the laser power has relatively less of an effect on the process. Adequate Precision compares the range of the predicted values at the design points to

the average prediction error. For this model it was equal to 15.506, as shown in Table 5.51. The same table also shows the other adequacy measures R^2 and Adjusted R^2. All the adequacy measures indicate that an adequate model has been obtained. The final mathematical models for predicting the tensile strength of dissimilar F/A joint in terms of coded factors and actual factors as determined by Design Expert software are shown below in Eqs (5.38 and 5.39).

Final Equation in Terms of Coded Factors:

Tensile Strength = 665.63 +31.35 * P -102.00 * S **…(5.38)**

Final Equation in Terms of Actual Factors:

Tensile Strength = 637.74167 +139.33333* P -0.20400* S **…(5.39)**

Table 5.51: Shows the ANOVA for selected factorial model.

Source	**Sum of Squares**	**df**	**Mean Square**	**F_v Value**	**p-value Prob. > F_v**	
Model	1.0 E+005	2	50608.1	32.07	< 0.0001	significant
P	8736.20	1	8736.2	5.54	0.0350	
S	92480.00	1	92480.0	58.61	< 0.0001	
Residual	1.2E+005	13	1577.8			
Cor. Total	43858	15				
R-Squared = 0.8315				Adeq. Precision = 15.506		
Adj. R-Squared = 0.8056						

Fig. 5.69 shows the actual response versus the predicted response for NTS. From this Fig., it can be seen that the model adequately describes the response within the limits of the factors being investigated herein, as the data points are close to the diagonal line. Furthermore, three extra confirmation experiments were carried out using different test conditions, which are presented in Table 5.52 along with the resulting percentage error. It can be noticed that the NTS value obtained after laser welding is greater than the base metals value, especially when compared to low carbon steel side.

Table 5.52: Confirmation experiments of the responses compared with model results.

Exp. No	P, kW	S, mm/ min	F, mm	G, mm	Tensile strength, MPa		$\|E\|$ %
					Actual	predicted	
1	1.30	304	-0.33	0.129	802	756	6.1
2	1.37	1119	-0.61	0.141	579	600	3.5
3	1.00	236	-0.04	0.146	754	729	3.4

5.3.3.2. Effect of process parameters on the Response:

***Welding speed*:** It can be seen that the welding speed is the most significant factor associated with the response, as shown in Fig. 5.68. The highest tensile strength value (842 MPa) was observed to be at a speed of 200 mm/min. It is evidence that by increasing welding speed with or without changing focus position the response would decrease. Fig.5.70 shows a 3D graph of the effect of P and S on the response at F = -0.5 mm and G = 0.075 mm.

Laser power: It is evident from the results that the laser power also has a strong effect on the tensile strength of the laser-welded joint, as shown in Fig. 5.68. It is clear that the higher welding speed laser power resulted in a higher response value, due to the fact that using high laser power increases the power density. This leads to more penetration resulting in an improved response.

Gap parameter: The result indicates that the gap between the two jointed dissimilar plates has an insignificant effect on the process. The result in Fig. 5.68 indicates that the stronger effect of the parameter is at 0.1 mm.

Focus point position: The results indicate that the focus point position has no obvious effect on the response within the parameter range domain applied. Changing the focus point position does not affect the response.

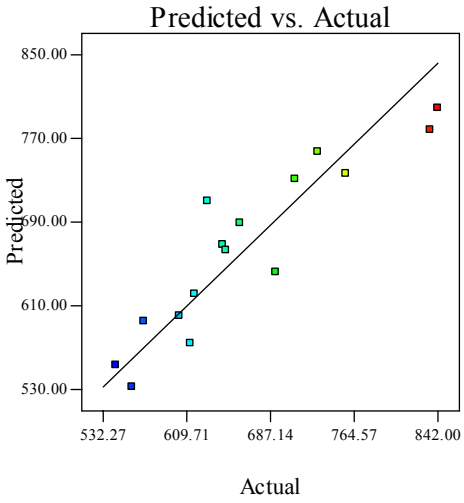

Fig. 5.69: Predicted Vs Actual for notched tensile strength NTS, MPa.

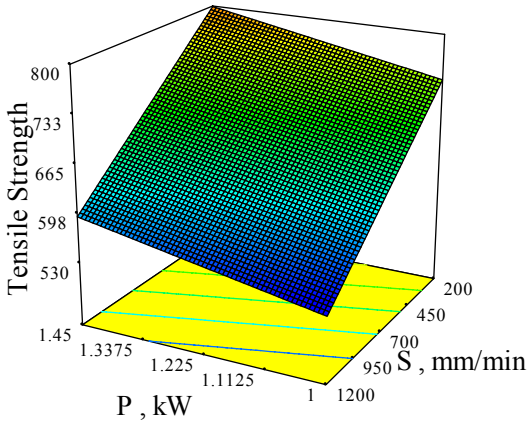

Fig. 5.70: 3D graph shows the effect of P and S on the tensile strength of the dissimilar components at F = -0.5mm and G = 0.075 mm.

5.3.4 Development Mathematical Model for Impact Strength

Robust Design using an L-16 orthogonal array which is composed of 4 columns and 16 rows was used for the analysis of impact strength. The design was selected based on a four welding parameters with four levels each. The selected welding parameters for this study are: welding power, welding speed, focus point position, and gap between the plates to be jointed. Table 5.43 show the laser input variables and experiment design levels. The experiments were carried out according to the design matrix given in Table 5.44. They were performed in random order to avoid any systematic error. The impact samples, mentioned in chapter four, were tested at room temperature (20 ºC). Each impact tested result listed in table 5.44 was an average of at least three or more samples. From the impact test it was noted that fractures generally occurred in HAZ or base metal (Low carbon steel side) which indicates that the produced joints were stronger than the low carbon steel plate

The Taguchi method using the statistical software “Design-expert 7”was applied for designing the experiments, analyzing and optimizing the experimental data. Regardless of the category of the quality characteristic, a larger S/N ratio corresponds to a better quality characteristic. Therefore, the optimal level of the

process parameters is the level with the highest S/N ratio. The signals have indicated that the effect on the average responses and the noises were measured by the influence on the deviations from the average responses, which would indicate the sensitivity of the experiment output to the noise factors. In this study, the S/N ratio was chosen according to the criterion the-bigger-the-better, in order to maximize the impact resistance, Eqs 3.2 and 3.4 were applied to calculate S/N. The Taguchi experiment results are presented in Table 5.53 and exhibited in Fig. 5.71. From the obtained result, its' obvious the impact resistance is mainly affected by the welding speed and focal position, while the laser power and gap have less affect on the response as shown in Table 5.53 and exhibited in Fig. 5.71. The rank 1 in Table 5.53 indicates that the welding speed has a stronger effect on the process followed by rank 2 which indicates that the focal position parameter also has a strong effect on the process. Rank 3 in the Table indicates that the laser power parameter has less effect on the process. Rank 4 in the same Table indicates that the gap parameter has a minimal effect on the process.

Table 5.53: Shows the impact strength response for S/ N Ratio.

Levels	**1**	**2**	**3**	**4**	**Delta**	**Rank**
P	28.1969	25.2967	27.2425	26.7335	2.9002	3
S	30.0775	30.5636	28.0192	18.8093	11.7542	1
F	28.1666	25.2664	25.6220	28.4146	3.1482	2
G	26.7785	25.7119	27.9840	26.9952	2.2721	4

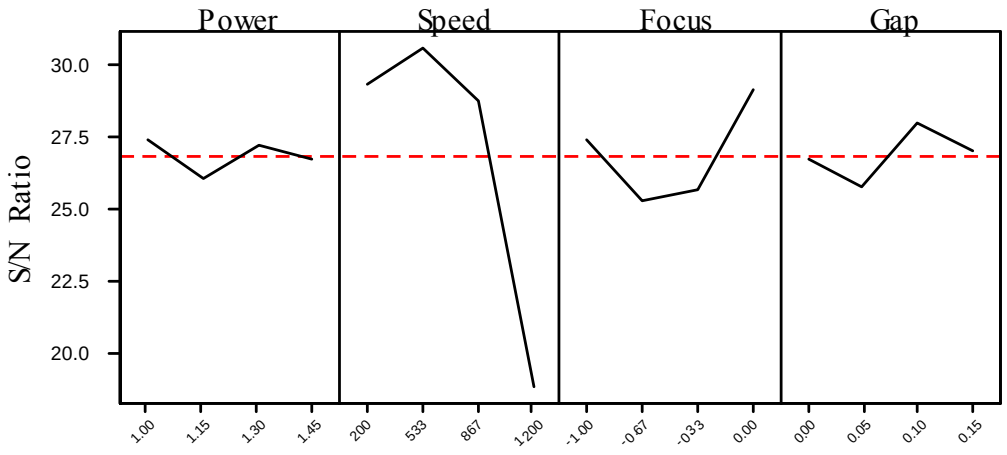

Fig. 5.71: Exhibited the effect of the laser welding parameters on the impact strength and S/N ratio.

Furthermore, a statistical analysis of variance (ANOVA) is performed and presented in Table 5.54 to see which process parameters are statistically significant. The optimal combination of the process parameters can then be predicted. The result shows that the highest F_v value obtained is 156.462 for the welding speed, but the focus and gap parameters F_v values were equal to 0.842 and 11.095 respectively which means that gap and focus have less effect on the process. The lowest F_v value was 0.360 for laser power this is due to effect of the gap parameter on the process. The same table shows also the other adequacy measures R-Squared, Adjusted R-Squared and Adequate precision. All the adequacy measures indicate that an adequate model has been developed. The final mathematical models in terms of actual factors as determined by Design Expert software are shown below in Eqs (5.40 and 5.41).

Final Equation in Terms of Coded Factors:

Impact Strength = 29.44 +0.43*P -16.19*S -0.64*F -2.73*G -7.58*P*F -3.96*P*G +3.90*F*G -12.21* S^2 +5.02 *F^2 **…(5.40)**

Final Equation in Terms of Actual Factors:

Impact Strength= 48.725-14.167* P +0.036*S +93.503* F +303.293* G -67.364* P* F -234.939* P* G +103.87649* F* G -4.885E-005* S^2 +20.06246 * F^2 **…(5.41)**

Finally, confirmation experiments were conducted to verify the optimal process parameters obtained from the design. They are presented in Table 5.55.

Table 5.54: Shows the ANOVA for impact strength response model.

Source	Sum of Squares	df	Mean Square	F_v Value	p-value Prob. > F_v	
Model	1706.427	9	189.603	49.801	< 0.0001	significant
P	1.369	1	1.369045	0.360	0.5707	
S	595.688	1	595.6877	156.462	< 0.0001	
F	3.206	1	3.205679	0.842	0.3942	
G	42.242	1	42.24206	11.095	0.0158	
PF	63.444	1	63.44368	16.664	0.0065	
PG	65.112	1	65.1117	17.102	0.0061	
FG	53.352	1	53.35217	14.013	0.0096	
S^2	384.933	1	384.933	101.106	< 0.0001	
F^2	79.507	1	79.50665	20.883	0.0038	
Residual	22.843	6	3.807228			
Cor. Total	1729.270	15				
R-Squared = 0.9868			Adeq. Precision = 22.691			
Adj. R-Squared = 0.9670						

Table 5.55: Confirmation experiments of the responses compared with model results.

No.	P	S	F	G	Impact strength		$\lvert Error \rvert$ %
					Actual	Predicted	
1	1	906	0	0.15	39	37	4.9
2	142	963	-1.00	0	42	40	4.9
3	1	886	0	0.15	37	38	3.3

5.3.4.1 Model validation

This step is to predict and verify the improvement of the response using the optimal level of the welding process parameters. Fig. 5.72 shows the relationship between the actual and predicted values of impact strength. This figure indicates that the developed model is adequate because the residual in prediction of response is negligible, since the residuals tend to be close to the diagonal line. It could be concluded that the model developed could predict the response with a very small error. Furthermore, to verify the satisfactoriness of the developed models, three confirmation experiments were carried out using new test conditions at optimal parameters conditions, obtained using the design expert software. Table 6 summarizes the experiments conditions, the actual experimental values, the predicted values and the percentages of error. It could be concluded that the developed model could predict the response with a very small error. Impact strength was greatly improved through this optimization.

5.3.4.2 The effect of the parameters on the response

The impact strength of dissimilar joints between stainless steel and low carbon steel was measured and plotted in 3D in Fig. 5.73; which shows that the welding speed parameter and laser power effect on the process at focus equal -0.5 mm and gap distance equal 0.75 mm.

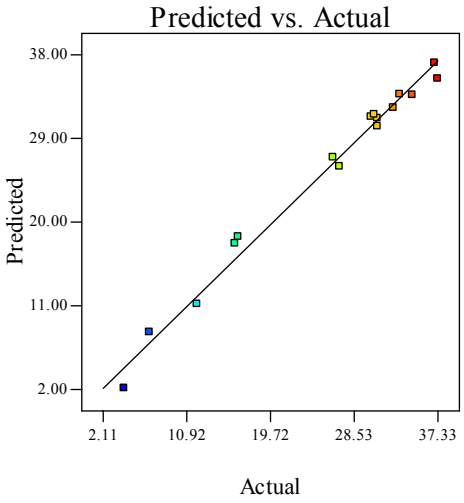

Fig. 5.72: The relationship between the actual and predicted values of the response.

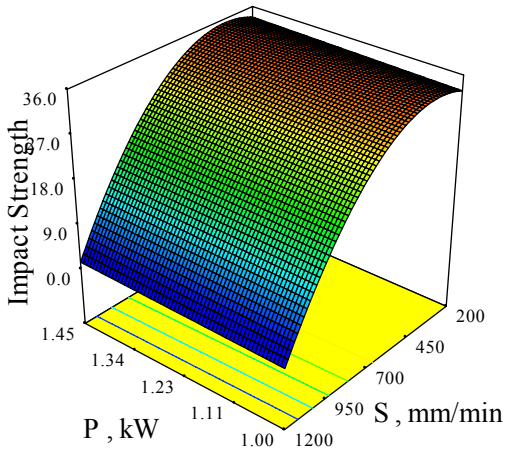

Fig.5.73: The effect of welding parameters on the Impact Strength.

Welding Speed

The signal-to-noise (S/N) ratio analysis and ANOVA analysis indicates that the welding speed parameter has the most significant effect on the process. The increase in welding speed, leads to decreases in impact strength. When speed is at its highest value (1200 mm/min), the impact strength is at its lowest and equals 4.3 [176]. This is due to the increase of welding speed, which results in decreased the heat input, and the cooling rate, which result in formation of a brittle joint particularly at heat affected zone.

Focusing Position

This factor has a strong effect on the response as it is indicated in S/N ratio analysis and ANOVA analysis. The focus parameter in this study interacts with the laser power parameter and influences its affect on process. The interaction between the focus position parameter and laser power parameter at a speed of 750 mm/min and gap of .075 mm is presented in Fig. 5.74.

Laser Power

In presence of the effect of focus and the gap parameters in the welding process the laser power parameter has an insignificant effect, whereby changing the laser power input, the response will not be consequentially changed.

Gap Width between the Welded Plates

The presence of gap between jointed plates is an important factor to decrease the residual stresses resulting from heat input due to the welding process particularly when joining dissimilar materials. In this study, signal-to-noise (S/N) ratio analysis and ANOVA analysis indicates that the gap parameter has a strong effect on the process. The study shows that the gap parameter interacts with laser power at a speed of 750 mm/min and a focus of -0.05 mm as presented in Fig. 5.75 and decreasing its affect on the process.

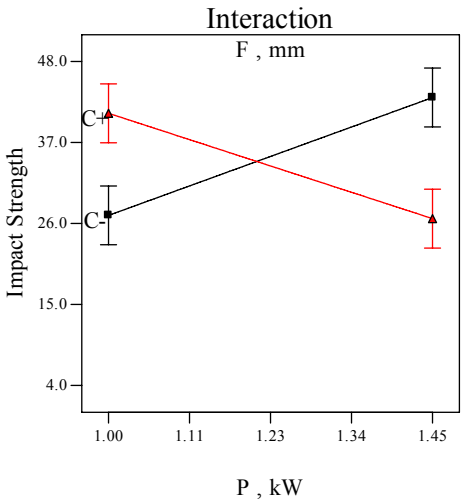

Fig. 5.74: The interaction between the Laser power and the focusing position

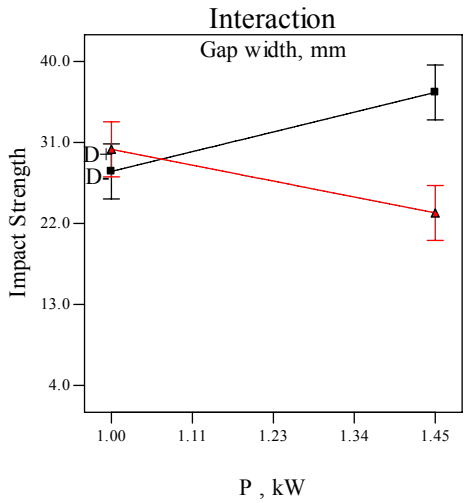

Fig. 5.75: The interaction between the Laser power and the gap parameter

To compare the effect of all the considered welding parameters on the impact strength at a midpoint point position in the design space, a perturbation plotted is exhibited in Fig.5.76. The response is plotted by changing only one factor over its range while holding of the other factors constant.

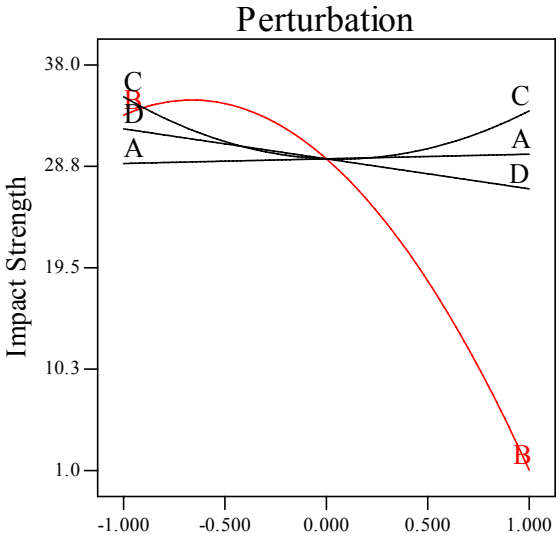

Fig.5.76: Perturbation plots exhibiting the effect of welding parameters on the tensile strength, where: A = power, B = Speed, C = Focus and D = Gap.

5.3.5 Operating Cost Modeling

The operating cost for joining the above mentioned dissimilar materials were calculated using Eq. 4.13; the mathematical model was developed to minimize the operating cost. The same procedure was followed to check the model adequacy. The cost calculation for the reduced linear model which is suggested by software for the results of the welding operating cost is presented in Table 5.44 and the analysis results are shown in Table 5.56. The same Table shows the other adequacy measures R^2, Adjusted R^2 and adequate precision. All the adequacy measure indicates an adequate quadratic model. The adequate precision 14.138 is indicating adequate model discrimination. The developed quadratic mathematical models in terms of coded factors and actual values are exhibited in Eqs 5.11 and 5.12.

Final Equation in Terms of Coded Factors:

Operating Cost = 0.28 -0.25 * S **…(5.42)**

Final Equation in Terms of Actual Factors:

Operating Cost = 0.64110 -5.0938E-004* S **…(5.43)**

Table 5.56: Shows the ANOVA for the welding operating cost.

Source	Sum of Squares	df	Mean Square	F Value	p-value Prob > F	
Model	0.58	1	0.58	55.52	< 0.0001	significant
S	0.58	1	0.58	55.52	< 0.0001	
Residual	0.15	14	0.010			
Cor. Total	0.72	15				
R-Squared = 0.7986			Adeq Precision = 14.138			
Adj. R-Squared = 0.7842						

5.3.6 Models (multiple –response) Optimization

5.3.6.1 Numerical optimization

The numerical multiple-response optimization criterion is to reach maximum tensile strength, maximum impact strength and minimum welding pool geometry, minimum welding operating cost with minimizing laser power and maximizing welding speed while focus position was kept in range.

In first optimization criteria all the parameters received the same importance (+ + +) and same weight (1) as per the Design Expert software default. In the second criteria a different weight was assigned for each parameter as presented in Table 5.57, while the importance for each parameter was kept same as (+ + +). The importance was changed for welding parameters in the third criteria while the weight was kept as per the soft ware default. All the decided welding optimization criteria and the resultant optimizations are presented in Table 5.57. The result presented in the Table 5.57 at each criterion is selected from one of ten or more different optimum result calculated by the software.

The effect of changing the criteria on the optimization result is obvious in Table 5.57. For example by applying in the third criteria the tensile strength value will reach up to 633 MPa while if applying the second criteria it will be around 657 MPa. If the target is only to maximize the tensile strength regardless of the other

parameters then the response value will be greater than the received values and this is true for each response individually optimized.

Impact strength was affected by changing the optimization criteria; its value is between (37J to 44J) depending on its assigned weight and importance it received in each criterion.

The welding geometries were not assigned high weight or high important since they are not a direct target for the optimization, they indirectly affect the welding quality. W_2 was kept as 'in range' in all optimization criteria to avoid applying more constraints which would affect the optimization processes and negatively affect the important responses 'mechanical properties' which lead to decreased welding quality, also the value W_2 before optimization was acceptable.

The welding cost was significantly reduced up to 85% in the second criteria compared to the maximum values presented in Table 5.44 at experiment run number 13. Also, the welding speed is relatively high, in range of (848 - 943 mm/min), in the optimization criteria which leads to increased production rate. The desirability bar graph of all the three optimization criteria is presented in Table 5.57 and exhibited in Figs. 5.77 to 5.79.

Table 5.57: Shows three optimization criteria with the optimization results using numerical multiple-response.

Welding Parameters	Power		Speed		Focus		Gap		A		W_1		W_2		Impact Resistance		Tensile Strength		Cost € / m		D*.
Goal	Min.		Max.		In range		In range		Min.		Min.		In range		Max.		Max.		Min.		
Criteria	Wt.*	Imp.*	Wt.	Imp.	Wt.	Imp.	Wt.	Imp.	Wt.	Imp.	Wt.	Imp.	-	-	Wt.	Imp.	Wt.	Imp.	Wt.	Imp.	
First Criteria	1	+++	1	+++	-	-	-	-	1	+++	1	+++	-	-	1	+++	1	+++	1	+++	
Result	1.01		897		0.00		0.15		3.180		1.919		1.173		37.3		595		0.18		0.686
Second Criteria	0.5	+++	5	+++	-	-	-	-	0.5	+++	0.5	+++	-	-	5	+++	5	+++	0.5	+++	
Result	1.388		848		-1.00		0.00		3.605		2.078		1.296		44		657		0.21		0.351
Third Criteria	1	+	1	+++	-	-	-	-	1	+++	1	++	-	-	1	+++ ++	1	+++ ++	1	+++ ++	
Result	1.34		943		-1.00		0.00		2.778		1.768		1.057		37.3		633		0.16		0.671

Imp.* = Important, Wt*.= Weight, D.* = Desirability

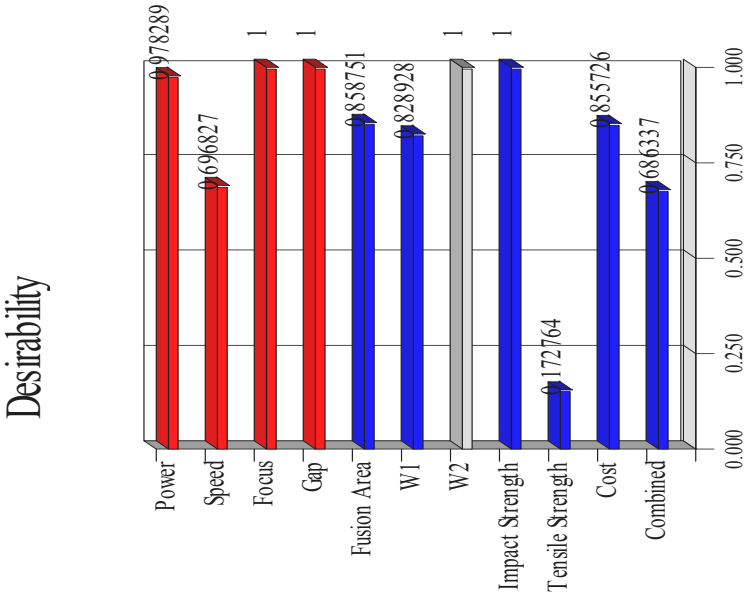

Fig.5.77: The desirability bar graph of first optimization criteria.

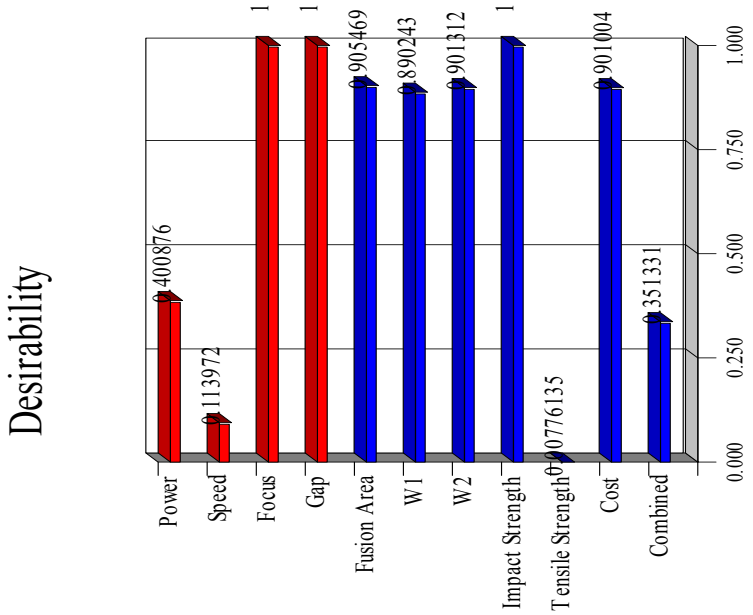

Fig.5.78: The desirability bar graph of second optimization criteria.

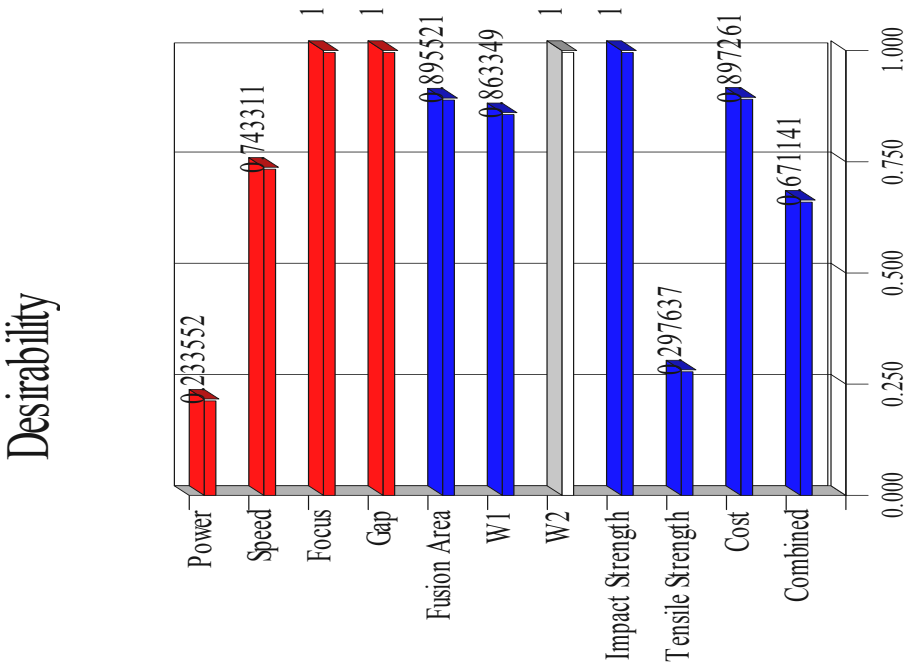

Fig.5.79: The desirability bar graph of third optimization criteria.

5.3.6.2 Graphical optimization

The graphical optimization displays the area of feasible response values in the factor space. From the overlay plots in Figs. 5.80 to 5.82 it is obvious that the graphical optimization allows visual selection of the optimum welding conditions according to certain criterion. The result of the graphical optimization are the overlay plots, these type of plots are extremely practical for quick technical use in the workshop to choose the values of the welding parameters that would achieve certain response value for this type of dissimilar materials. The yellow /shaded areas on the overlay plot in Figs. 5.80-5.82 are the regions that meet the proposed criteria.

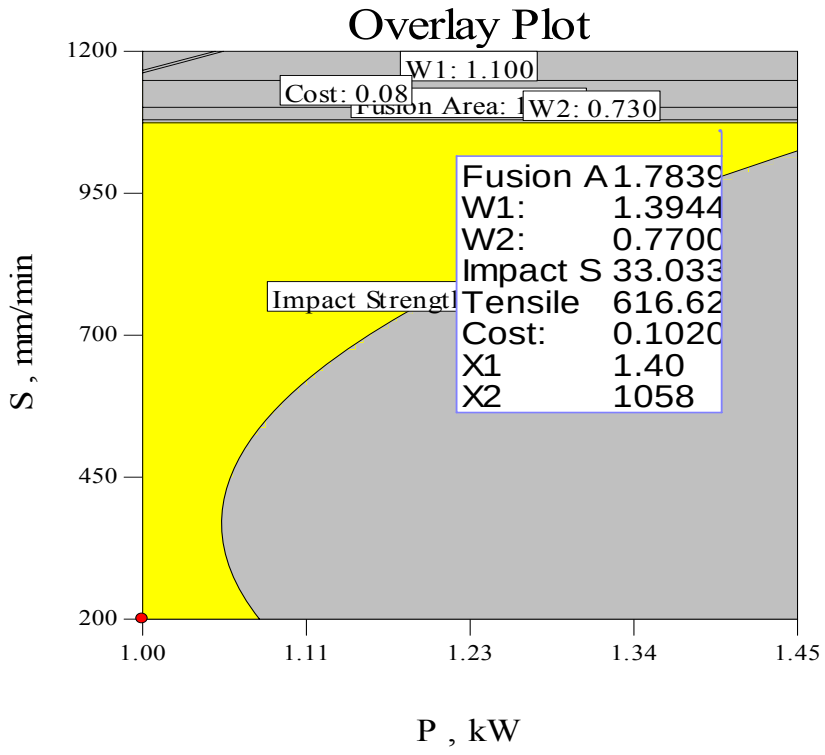

Fig 5.80: The feasibel solution in yallow shaded area for first optimization criteria.

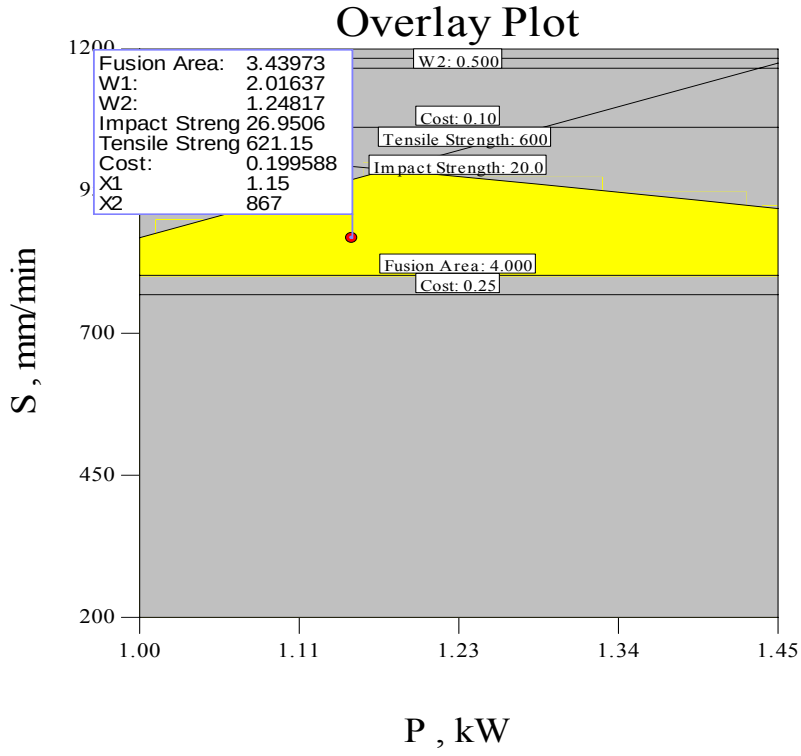

Fig 5.81: The feasible solution in yellow shaded area for second optimization criteria.

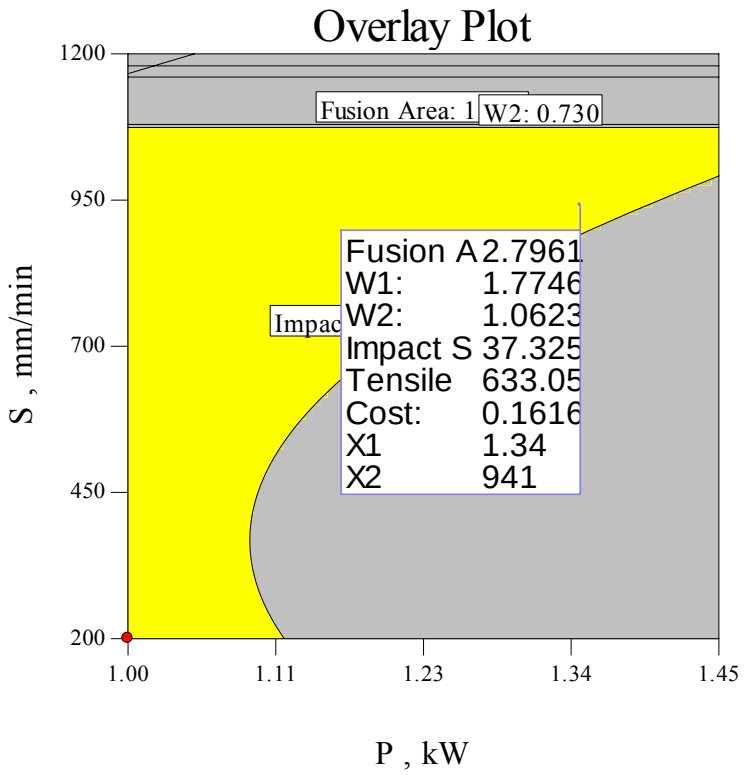

Fig 5.82: The feasibel solution in yallow shaded area for third optimization criteria.

5.3.7 Microharness and Microstructure Studies

5.3.7.1 Microstructure of dissimilar jointed materials

Figs. 5.83(a, b) shows the Base metal (BM) / HAZ and 5.84 (a, b) shows the welding pool of Low Carbon Steel Din: en 10131 and stainless steel AISI316 respectively.

Owing to the epitaxial nature of solidification, the grain boundary in the HAZ can link up with the solidification grain boundary in the fusion zone. Segregation of S, Pb, Mn and P during solidification means that these elements are able to diffuse into the HAZ from the fusion zone along the grain boundaries lines. The impurities and dissolved elements diffuse more rapidly along the grain boundaries than through the crystal lattice, and this result in a local depression of the melting temperature. As a consequence, the grain boundary may melt during welding thermal cycles, but the local stress (as it was studied above in this chapter) is insufficiently high to cause the melted grain boundary to separate in the HAZ.

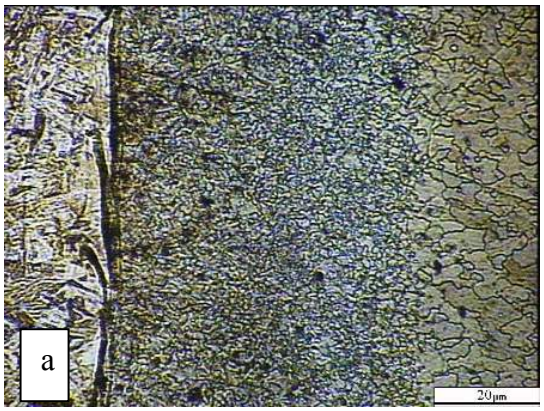

Fig 5.83(a): Weld pool, HAZ and BM of Low Carbon Steel Din: en 10131.

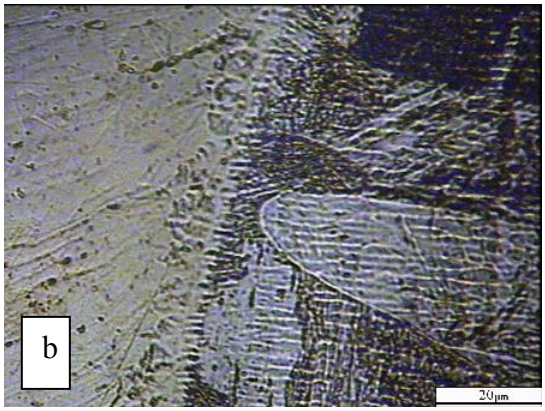

Fig 5.83(b): BM, HAZ and weld pool of AISI316.

The microstructures in the fusion zone are a result of solidification behavior and subsequent solid-phase transformation, which are controlled by composition and weld cooling rates. Moreover, the composition in the fusion zone of a dissimilar joint depends on the melting ratio of the two materials to be jointed, which in turn is related to the welding parameters. Figs. 5.84 (a, b) shows the redistribution of elements in the fusion zone of a butt weld joining AISI316 to Din: en 10131, corresponding to the welding parameters given in Table 5.44 of the specimens number 10 and 1 respectively . As it is obvious from Figs. 5.83 (a, b) the HAZ of Din: en 10131 width is about (350 to 450) µm while the HAZ of AISI316 width is about (30 to 50) µm, this is due that the thermal expansion coefficient of austenite is higher than that of ferrite, and the heat conductivity of austenite is lower than that of ferrite, these features resulting in a higher level of thermally-generated stresses. Fig 5.85 (a, b) exhibits a comparison of the grain size of BM and HAZ respectively due to welding operation and the effect of rapid solidification in the fusion zone in the LCS.

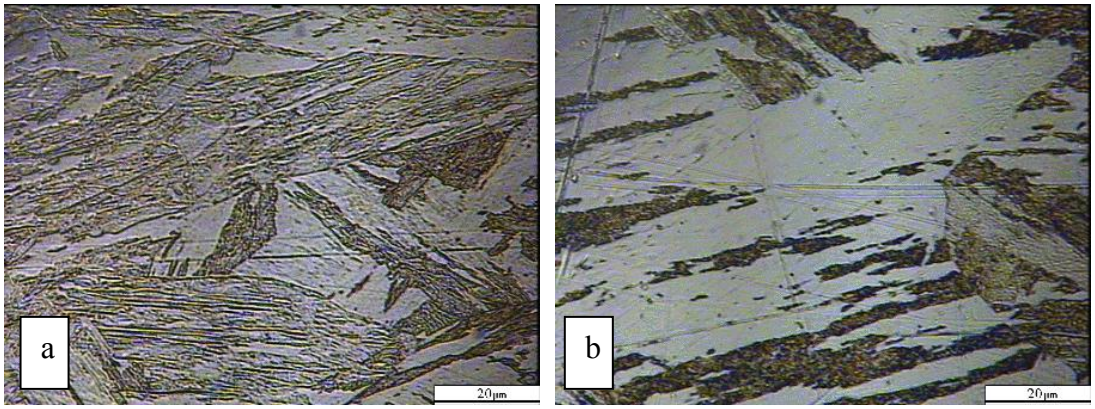

Figs. 5.84 (a, b): The redistribution of elements in the fusion zone of a butt weld joining AISI316 to Din: en 10131.

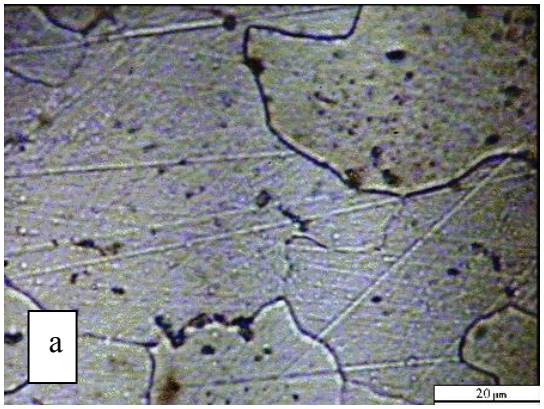

Fig. 5.85 (a): The grain size of BM of Din: en 10131.

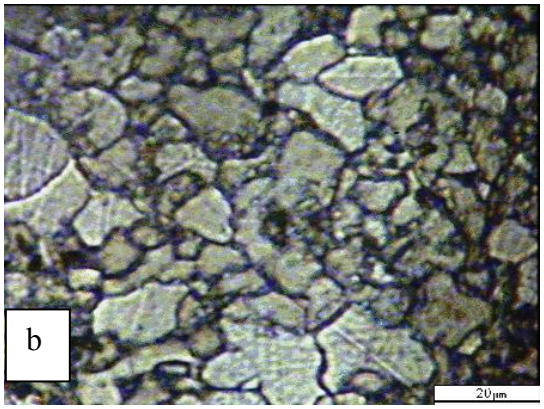

Fig. 5.85 (b): Shows the grain size of HAZ of Din: en 10131.

5.3.7.2 Microhardness

The specimens selected for microhardness studies were based on heat input calculation (P x S). The microhardness of the fusion zone is greater than that of both the AISI316 and Din: en 10131 base materials; this resulted from the effect of rapid solidification. Fig. 5.86 shows the microhardness profile of the joint at seven different points on the selected specimens. The microhardness gradient correlates with the gradient of the redistribution of the elements Cr, Fe, and Ni, which may be a particular phenomenon of dissimilar fusion joints. The microhardness of the weld HAZ interface in both sides is less than that measured in weld pool but it is higher than that in the HAZ and base metals, this is due to the same two reasons mentioned above.

The strength of the laser welds is higher than both the tensile strength and impact strength of AISI316 / Din: en 10131 under the test conditions adopted in this

research. The greater mechanical properties of the laser welds demonstrate the beneficial effect of rapid solidification in the fusion zone and of a small HAZ. The microstructures in the fusion zone call for further research using TEM.

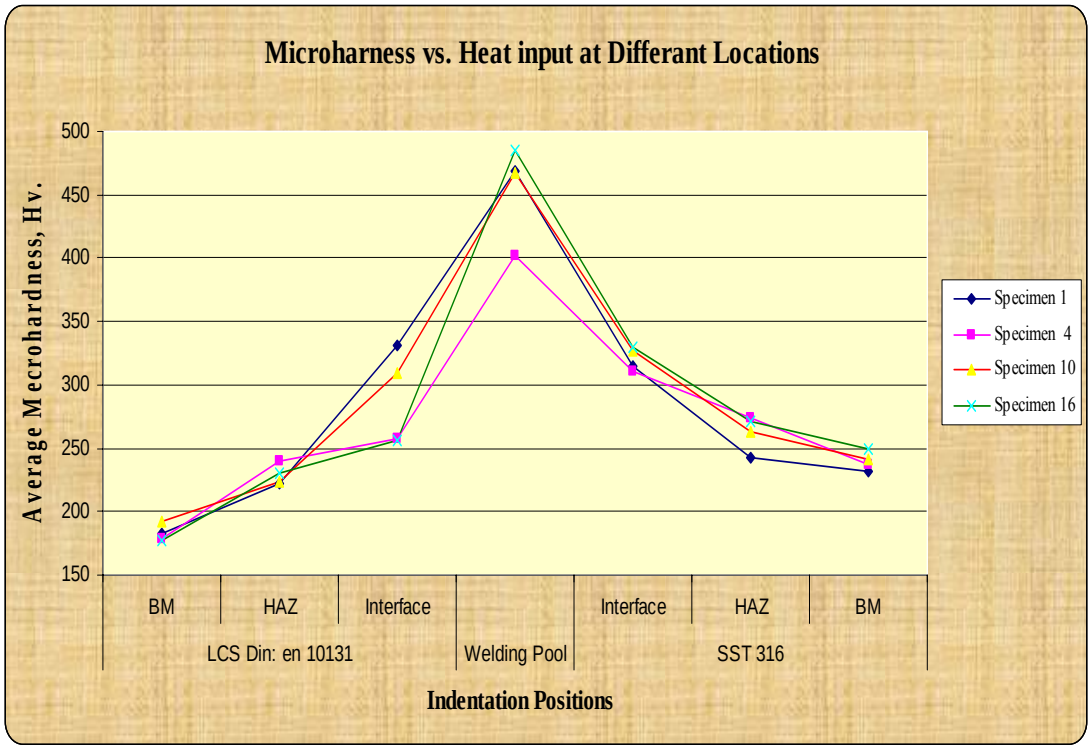

Fig. 5.86: The microhardness profile of the dissimilar joint (AISI316 / Din: en 10131) for the specimens (1, 4, 10 and 16).

CHAPTER 6

6. RESULTS AND DISCUTION OF DISSIMILAR FEROUS WITH NONFERROUS JOINED MATERIALS

In this chapter the results and discussion of dissimilar lap laser welding between ferrous and nonferrous materials will be presented. Low carbon steel Din en: 10131 as a ferrous material was jointed with aluminium of different grades and different thicknesses. The low carbon steel has a less reflectivity than aluminium plate which permit a better absorption of laser power (as a heat input source) and for economic purposes the steel plate was at the top in direct contact with laser beam during the welding process. Furthermore, a study of joining low carbon steel with titanium G2 using laser welding was carried out. Experiments for the joining of the dissimilar materials (ferrous / nonferrous) in this chapter were performed using Design of Experiment and the Taguchi approach with L-16 orthogonal arrays. Mathematical models for the responses of the jointed material were developed, analyzed and verified.

6.1 Joining of Aluminium (6082) to Low Carbon Steel Din: en 10131

Two plates of dimensions (160 x 80 x 2) mm of the above mentioned material were lap jointed as exhibited in Fig. 4.16 (a). For these materials pilot experiments were carried out by changing one parameter at a time to detect the operating range of the welding parameters under investigation. Visual inspection of the welded joints was carried out in order to determine a suitable range of operation for the parameters. The criterion used for selecting a good weld seam was the absence of observable welding defects. The selected welding parameters for these dissimilar materials are: Laser power, welding speed and focus point position. Table 6.1 shows the welding input variables and experiment design levels. The welding experiments were carried out in the Mechanical School workshop following the Taguchi designed matrix in random order, as presented in Table 6.2. Welding pool geometry measurements, mechanical destructive tests (tensile shear strength) and cost per meter welded calculations were carried out in the jointed specimens and the results are presented in

Table 6.2. Each of the results presented in Table 6.2 is an average of at least of three readings.

Table 6.1: Process parameters and design levels used

Variables	Code	Unit	Level 1	Level 2	Level 3	Level 4
Laser Power	**P**	**kW**	1.05	1.125	1.200	1.275
Welding Speed	**S**	**mm/min**	600	800	1000	1200
Focus	**F**	**mm**	-1.0	-0.67	-0.33	0.00

Table 6.2: Welding input variables, experiment design levels, residual stress, welding pool geometry, tensile shear strength and cost per meter welding calculations.

Std	Run	P, kW	S, mm/min	F, mm	R S MPa	W_1, µm	L_1, µm	A_1, µm	Shear St, N/mm	Cost € / m
16	1	1.275	1200	-1.00	134	616	696	291.9	138	0.23
7	2	1.125	1000	0.00	62	436.6	329	93.5	134	0.27
15	3	1.275	1000	-0.67	129	727	597	185.3	91	0.27
5	4	1.125	600	-0.67	124	750.1	609.4	273.7	135	0.45
6	5	1.125	800	-1.00	122	566	856	406.2	146	0.34
1	6	1.050	600	-1.00	76	666.7	701.1	409.641	215	0.45
12	7	1.200	1200	-0.67	110	725	678	207.1	139	0.23
14	8	1.275	800	-0.33	124	760	608	352.6	108	0.34
8	9	1.125	1200	-0.33	116	543	430	179.8	183	0.22
11	10	1.200	1000	-1.00	106	607	637	167.4	109	0.27
3	11	1.050	1000	-0.33	128	540	597.4	202.7	270	0.27
4	12	1.050	1200	0.00	68	548	468.1	179	310	0.22
13	13	1.275	600	0.00	65	804.6	617	273.8	203	0.46
9	14	1.200	600	-0.33	83	756	688	395.8	166	0.45
10	15	1.200	800	0.00	107	799	497	292.3	199	0.34
2	16	1.050	800	-0.67	156	483.6	647.4	388.8	269	0.33

6.1.1 Development of Mathematical Models for Residual Stresses

The large difference of the thermal conductivity and thermal expansion between the two jointed materials indicates the necessity to study the residual stress of the joints. Residual stress control during the welding process can easily protect welded components without any additional procedure after welding. Residual stresses of ferrous / nonferrous dissimilar welded components were evaluated during this study following the measurement procedure explained in paragraph 4.5.3 in the previous chapter in order to control and optimize the selected laser welding parameters. Residual stress was studied and analyzed through the depth of the welded joint at gradual levels to get a clear indication of the effect of welding parameters on the distribution of the residual stress through the depth of HAZ and to allow it to be optimized. The strain gauge was bonded to the surface of the specimen (aluminium side) in the HAZ were the present of the critical (serious) residual stresses in the joined component and a blind hole of incremental depth of 1.27 mm was drilled at 1-2 mm from the centre welded line in the middle of the specimen as presented in Fig.4.14 (a). "Design Expert 7" software was used for analysing the measured responses. The depth levels at which the micro-strains were measured are presented in Table 6.3. The calculated stress (σ_i) at each level, expressed in Table 6.4, were considered as responses and analysed separately to predict the effect of the welding parameters through the specimen depth. The effect of the individual welding parameters on the residual stress was also investigated in this study.

Table 6.3: Depths at which the micro-strains were measured in the specimens

Level (i)	*1*	*2*	*3*	*4*	*5*	***6***
Stress	σ_1	σ_2	σ_3	σ_4	σ_5	σ_6
Depth in specimen, [mm]	0.127	0.254	0.508	0.762	1.016	1.27

Table 6.4: The experimental calculated for Al 6082 residual stresses in MPa

Std	σ_1	σ_2	σ_3	σ_4	σ_5	σ_6
1	75.98	37.87	18.84	8.57	5.31	3.65
2	156.40	85.62	44.64	24.55	14.73	6.78
3	128.26	57.95	31.35	15.81	9.16	4.68
4	68.32	34.92	16.08	7.85	4.45	2.63
5	123.99	52.30	26.79	14.65	10.49	6.50
6	121.74	56.03	29.72	15.13	9.36	4.17
7	62.29	28.85	17.38	7.63	4.08	1.87
8	115.61	58.48	25.26	10.89	5.25	2.94
9	83.34	37.28	20.25	12.31	7.13	2.05
10	106.87	63.20	26.85	9.50	2.69	2.32
11	106.49	47.38	15.10	14.95	9.50	4.90
12	110.16	48.97	27.59	15.02	9.36	3.89
13	64.56	28.93	16.94	10.44	7.11	3.66
14	123.50	51.94	28.92	17.43	11.86	7.02
15	129.24	59.01	27.02	13.18	7.27	2.89
16	134.10	56.11	30.38	15.83	9.55	4.42

6.1.1.1 The ANOVA analysis

Further investigations for welding process parameters were carried out, using ANOVA, to identify which parameters significantly affect the welding quality. The test for significance of the regression model, the test for significance of individual model coefficients and the lack-of-fit test were performed using Design Expert 7 software. The backward regression method was applied for the critical levels, as observed in the first and second levels (σ_1 and σ_2) in Table 6.4 and exhibited in ANOVA Tables 6.5 and 6.6 for the models. The ANOVA Tables summaries the analysis of variance of the responses and show the significant model at level 1. The model at level 2 is not significant and can not be used for predicting the residual stress at that level. The same tables also show the other adequacy measures R^2,

adjusted R^2, and adequacy precision for each response. The adequate precision compares the range of the predicted value at the design points to the average predicted error. The adequacy measures in the ANOVA Table for model 1 indicate that an adequate model has been obtained. The final mathematical models in terms of actual factors as determined by Design Expert software are shown below in Eqs.6.1 and 6.2.

Table 6.5: ANOVA for residual stress at level 1

Source	Sum of Squares	df	Mean Square	F_v Value	p-value Prob. > F	
Model	8054.012	4	2013.503	5.910441	0.0086	significant
S	314.9598	1	314.9598	0.924534	0.3569	
F	2854.451	1	2854.451	8.378962	0.0146	
S^2	1574.462	1	1574.462	4.62168	0.0547	
F^2	3310.139	1	3310.139	9.716588	0.0098	
Residual	3747.357	11	340.6688			
Cor. Total	11801.37	15				
R-Squared = 0.6825			Adeq. Precision = 7.796			
Adj. R-Squared = 0.5670						

Final Equation in Terms of Coded Factors:

R S at σ_1 = -1128.969+1.345*S -29.867*F -3.6E-004*S^2 -89.897*F^2 **…(6.1)**

Final Equation in Terms of Actual Factors:

R S at σ_1 = -684.583 +0.80139*S-10.295*F -2.14E-004*S^2-38.379*F^2 **…(6.2)**

Table 6.6: ANOVA for residual stress at level 2

Source	Sum of Squares	df	Mean Square	F_v Value	p-value Prob. > F	
Model	1557.3	4	389.325	2.645721	0.0908	not significant
S	49.1916	1	49.1916	0.334289	0.5748	
F	339.1557	1	339.1557	2.304787	0.1572	
S^2	565.6436	1	565.6436	3.843921	0.0757	
F^2	603.3093	1	603.3093	4.099885	0.0679	
Residual	1618.68	11	147.1527			
Cor. Total	3175.98	15				
R-Squared = 0.4903			Adeq. Precision = 5.242			
Adj. R-Squared = 0.3050						

6.1.1.2 Model validation

To predict and verify the improvement of the response using the optimal level of the welding process parameters the model is subjected to a model validation study. Fig. 6.1 shows the relationship between the actual and predicted values residual stress at level 1(σ_1). The figure indicates that the developed model is adequate because the residuals in prediction of the response are negligible, since the residuals tend to be close to the diagonal line.

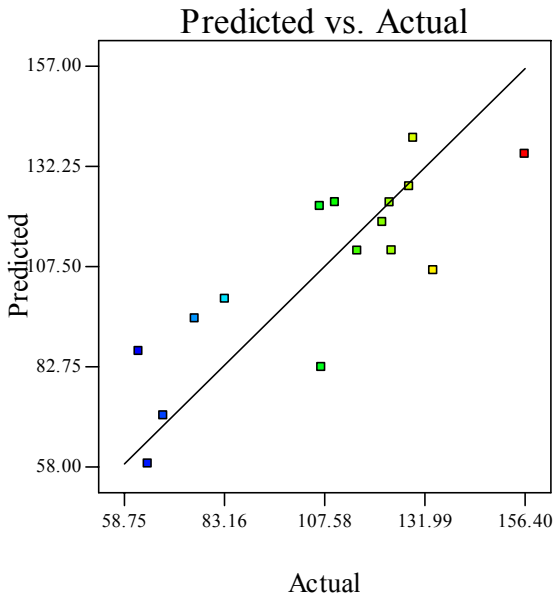

Fig. 6.1: The actual vs. predicted values residual stress at level 1(σ_1)

Moreover, three confirmation experiments were carried out based on new random welding parameters to verify the significance of the developed model at σ_1. After welding the three specimens were subjected to residual stress measurements using the hole-drill method following the previously explained procedure for each measurement. The measured residual stress, the calculated (using the developed model) residual stress and the absolute error calculation are presented in Table 6.7. Table 6.7 indicates that the error for the model is less than 15 %. The received results in Table 5.30 indicate that the developed model, within the parameters domain, could be used adequately during the design stage to predict the residual stress that would result due to a welding operation.

Table 6.7: Confirmation experiments of the residual stress at σ_1

Exp. No.	P, kW	S, mm/min	F, mm	σ_1, MPa		$\|E\|$ %
				Act.*	Pred.*	
1	0.90	2100	0.60	79	71	11.2
2	1.23	1636	0.60	75	66	13.6
3	1.13	1618	-0.60	84	98	14.2

Act.* = Actual; Pred.* = Predicted

6.1.1.3 Effect of the parameters on the responses

The reason for predicting the residual stresses is to develop a model to control and to optimize them by controlling the welding parameters. Fig. 6.2 presents a 3D graph of the effect of S, P and F on the response at depth level 1.

At level 1 of the specimen depth, the analysis of variance, presented in Fig. 6.2 and expressed in Table 6.5, indicates that the main effect on the residual stresses is the focus position F. Welding speed has a great effect on the response at level 1 while the laser power parameter had an insignificant effect on the response. The analysis indicates also that the quadratic model developed was significant with an Adequate Precision of 7.796. Since depth level 1 is nearest to the specimen surface and the cooling rate is very fast; the response has the highest value at this level. The maximum response value was at experiment number 2 at 156 MPa which is greater than yield stress (140 MPa) of the aluminium 6082 and the lowest value was obtained at experiment number 7, at 62 MPa. The wide range of responses at all experiments settings (156- 62 MPa) reflects the strong effects of welding parameters on the process.

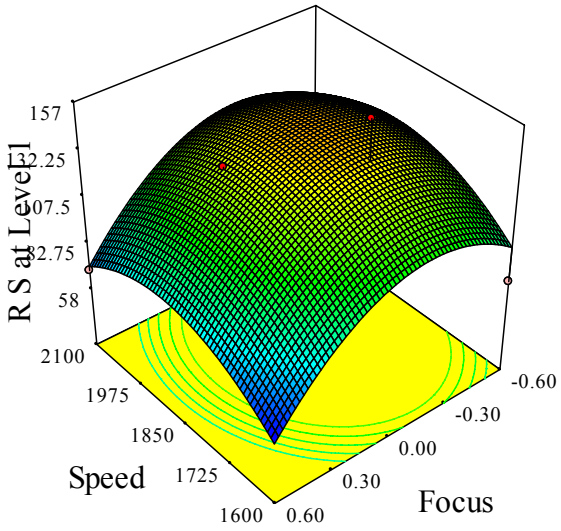

Fig. 6.2: A 3D graph of the effect of S and F at P = 0.9kW on the response at depth level 1.

6.1.2 Development Mathematical Models for Welding Pool Geometry

Specimens for measuring the welding pool geometries and further metallographic examinations were prepared by polishing successively using 120, 240, 600, 800 and 1200 SiC paper polishing, followed by a final disc polishing using 3 µm, 1 µm diamond suspension and finished with a SiO_2 suspension to a mirror-like surface finish. The carbon steel side of the weldment was etched in 4% Nital, and the rest of the regions of the weldment were etched with Keller's reagent (1% HF, 1.5% HCl, 2.5% HNO_3 and H_2O solution). The measured results of welding pool area for each sample are presented in Table 6.2. Fig. 6.3 shows the effect of the welding parameters and the variation on the total weld pool (fusion area) 'A_1' at aluminum plate only, welding widths at the specimen surface of aluminium 'W_1' and welding widths at the penetration of welding depth in aluminum plat 'L_1' of a selected experiments listed in Table 6.2.

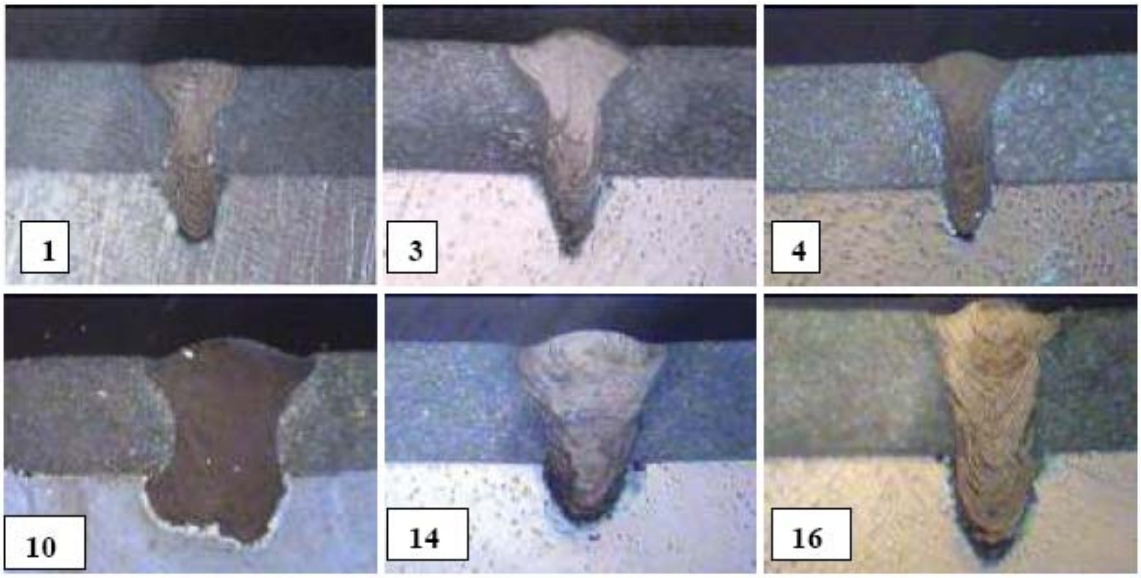

Fig. 6.3: The effect of the welding parameters on the responses (A_1, W_1, L_1).

The fusion zone dimensions in the aluminium plate were measured by using the transverse sectioned specimens, optical microscope and Image Analyser software. The measured responses are listed in Table 6.2. Design Expert 7 software was used for analysing the measured responses.

The fit summary output indicates that the quadratic models which are developed by the software are statistically significant for the prediction of the responses (A_1, W_1 and L_1); therefore, they were used for further analysis. It can be seen from the achieved results that the welding pool geometry, shape and penetration are controlled by the rate of heat input, which is a function of laser power and welding speed. Focusing position also has a strong effect on the responses.

6.1.2.1 Analysis of variance

The test for significance of the regression model and the test for significance on individual model coefficients were performed using Design Expert 7 software. The backward elimination regression method was applied for the reduction of the suggested quadratic models. The results are exhibited in the ANOVA Tables 6.8 to 6.10. Tables 6.8 to 6.10 summarize the analysis of variances of the responses and show the significant models. The same Tables show also the other adequacy measures R^2, adjusted R^2 and adequacy precisions. All adequacy measures were close to 1, which is reasonable and indicates an adequate model [159,171]. The

adequate precision compares the range of the predicted value at the design points to the average predicted error. In this study the values of adequate precision for the A_1, W_1 and L_1 are significantly greater than 4. The adequate precision ratio above 4 indicates adequate model discrimination. The developed quadratic models in terms of coded factors and actual values are exhibited in Eqs. 6.3 to 6.8.

Table 6.8: ANOVA for response 'W_1'

Source	Sum of Squares	df	Mean Square	F_v Value	p-value Prob. > F_v	
Model	131212.1	2	65606.06	11.07594	0.0016	significant
P	84448.01	1	84448.01	14.25693	0.0023	
S	46764.12	1	46764.12	7.894951	0.0148	
Residual	77002.83	13	5923.295			
Cor. Total	208215	15				
R-Squared = 0.6302			**Adeq. Precision** =10.202			
Adj. R-Squared = 0.5733						

Final Equation in Terms of Coded Factors:

$W_1 = 645.54+97.47 * P -72.53* S$ **…(6.3)**

Final Equation in Terms of Actual Factors:

$W_1 =-144.05500+866.40* P -0.24177 * S$ **…(6.4)**

Table 6.9: ANOVA for response 'L_1'

Source	Sum of Squares	df	Mean Square	F_v Value	p-value Prob. > F_v	
Model	172616.4	4	43154.1	7.858349	0.0030	significant
P	4315.922	1	4315.922	0.785928	0.3943	
S	27313.44	1	27313.44	4.973769	0.0475	
F	98957.95	1	98957.95	18.02021	0.0014	
PS	17317.79	1	17317.79	3.153564	0.1034	
Residual	60406.47	11	5491.498			
Cor. Total	233022.9	15				
R-Squared = 0.7408			**Adeq. Precision** = 8.943			
Adj. R-Squared = 0.6465						

Final Equation in Terms of Coded Factors:

L_1 =+603.52 +22.04* P -55.43* S-177.84* F -99.81* P* S **…(6.5)**

Final Equation in Terms of Actual Factors:

L_1 = -2729.918 +2857.548*P +3.253*S -355.681* F -2.957* P * S **…(6.6)**

Table 6.10: ANOVA for response 'A_1'

Source	Sum of Squares	df	Mean Square	F_v Value	p-value Prob. > F_v	
Model	83799.09	2	41899.55	8.284635	0.0048	significant
P	64776.27	1	64776.27	12.80796	0.0034	
S	19022.82	1	19022.82	3.761309	0.0745	
Residual	65747.51	13	5057.5			
Cor. Total	149546.6	15				
R-Squared = 0.5604			**Adeq. Precision** = 8.549			
Adj. R-Squared = 0.4927						

Final Equation in Terms of Coded Factors:

A_1 = 268.72 -85.37* S -46.26* F **…(6.7)**

Final Equation in Terms of Actual Factors:

A_1 = 478.55804-0.28455* S -92.52172* F **…(6.8)**

For the developed models of the responses (W_1, and A_1), the analysis of variance indicates that welding speed 'S' and laser power 'P' are the stronger welding parameters affecting the responses. Focus position 'F' has a greater affect on the developed model of the response (L_1) among the studied laser power parameters. The W_1 and A_1 models indicate that all the studied parameters (P, S) significantly affecting the response but the model L_1 indicates that the F parameter has the greater effect on the response. The L_1 model indicates that the welding parameters have interactions between P and S exhibited in Fig. 6.4. Fig 6.4 exhibits the interaction of the welding speed with laser power at focus position F= -0.5 mm.

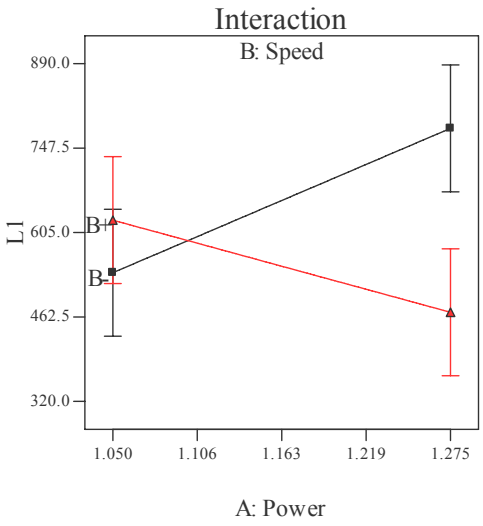

Fig. 6.4: Interactions between the welding parameters (P, S) with respect to the depth of penetration response.

6.1.2.2 Model validation

The aim of this step is to predict and verify the improvement of the response using the optimal levels of the welding process parameters. Figs. 6.5 to 6.7 show the relationship between the actual and predicted values of W_1, L_1 and A_1, respectively. These figures indicate that the developed models are adequate because the residuals in prediction of each response are negligible, since the residuals tend to be close to the diagonal line.

Furthermore, to verify the satisfactoriness of the developed models, three confirmations experiments were carried out using new test conditions at different parameters conditions, obtained using the Design-Expert software and the developed mathematical models. The values of W_1, $L_1$and A_1 for validation experiments were calculated using Design-Expert software. Table 6.11 summarizes the experimental conditions, the actual experimental values, the predicted values and the percentages of absolute errors. It could be concluded that the models developed could predict the responses with a very small errors. W_1, $L_1$and A_1 were greatly improved through this optimization.

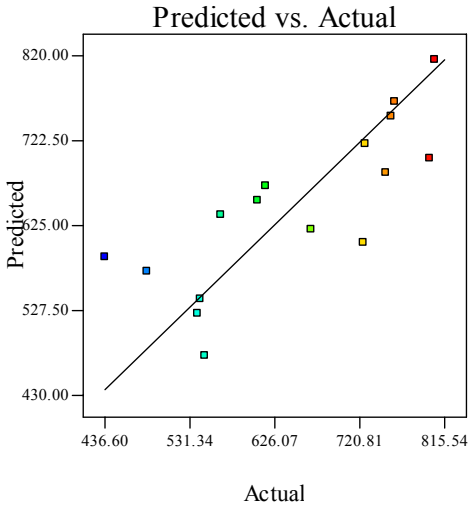

Fig. 6.5: Exhibited predicted values of the W_1 vs. actual measured values.

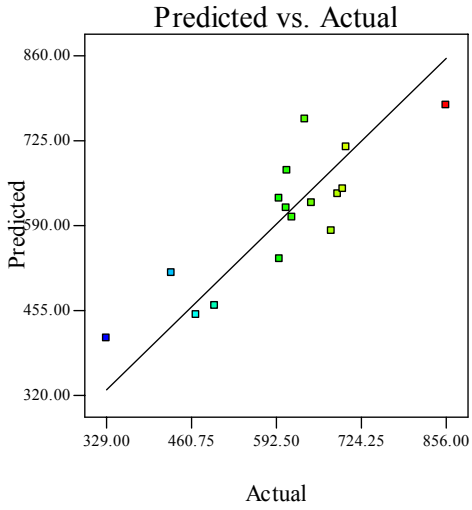

Fig. 6.6: Exhibited predicted values of L_1 vs. actual measured values.

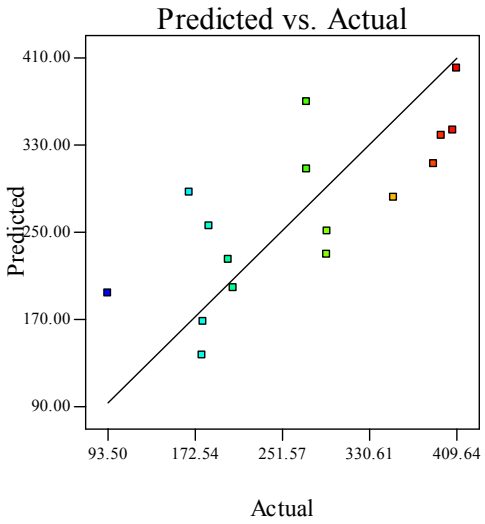

Fig. 6.7: Exhibited predicted values of the A_1 vs. actual measured values.

Table 6.11: Confirmation experiments of the responses (W_1, L_1 and A_1)

Exp. No	P, kW	S, mm/ min	F, mm	W_1, mm		$\|E\|$ %	L_1, mm		$\|E\|$ %	A_1, mm^2		$\|E\|$ %
				Act.	Pred.		Act.	Pred.		Act.	Pred.	
1	1.050	1200	0.00	423	475.5	11	378	448	15.6	216	137	57.7
2	1.050	1090	-1	567	502	12.9	832	788	5.6	302	261	15.7
3	1.119	839	-.79	584	623	6.2	638	701	9	341	313	8.9

Act* = Actual; Pred.* = Predicted

6.1.2.3 Effect of the parameters on responses

The reason for measuring the welding pool geometry is to develop models which can be included in the optimization step.

- **Welding Pool Width at the Work Piece surface (W_1).**

The results and the model obtained for the response indicate that the S and P are the most important factors affecting the W_1 value. An increase in S leads to a decrease in W_1 and the increase of P leads to increase in W_1. This is due to the laser beam traveling at high speed over the welding line when S is increased. Therefore, the heat input decreases leading to less volume of the base metal being melted, consequently the width of the welded zone decreases. Moreover, a defocused beam, which is in a wider laser beam, results in spreading the laser power onto a wide area. Therefore, a wide area of the base metal will be melted leading to an increase in W_1 or vice versa. The result shows also that P contributes a secondary effect in the response width dimensions. Increasing P results in a slight increase in W_1, due to the increase in the power density. Fig. 6.8 shows contour plots for the effect of the process parameters on the W_1 width. The contour graph illustrates the relationship between S and P with their impact on the total welding pool width (W_1) at F = -0.5 mm.

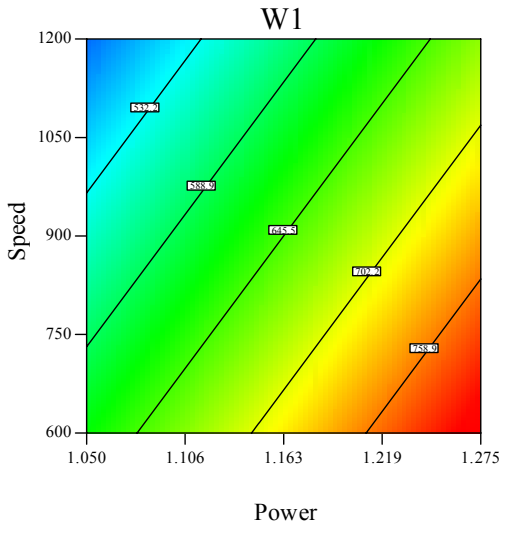

Fig. 6.8: Contour graphs exhibiting the effect of P, S parameters at F = -0.5 mm on the response W_1

- **Welding Pool Width at the Middle of the Work Piece (L_1)**

From the results it is clear that the three welding parameters significantly affect the L_1 value with different rates. Using a focused beam results in an increase in the power density, this means that the heat will be localized in a small portion of the component being welded. This results in an increase in the power density, leading to an increase in the value of L_1. The model shows that F is the most important factor affecting the response and is inversely proportional to it. The result shows that the changes in F parameter effects only L_1. As a result, when F is decreased, L_1 is increased and vice versa. The increase in P leads to an increase in the heat input, therefore, more molten metal and consequently a deeper L_1 will be achieved. However, the idea is reversed in the case of the S effect, because the S is inversely proportional to the heat input. The relationship between S and P with their effect on the welding pool depth of specimen (L_1) is exhibited in Fig. 6.9 at F = -0.8 mm. The relationship between the most effected welding parameters, S and F, and how they affect the response (L_1) is illustrated in contour graph in Fig 6.9.

- **Welding pool area (A_1)**

The fusion area (welding pool) of dissimilar joints in aluminium plate was measured and is plotted in the contour graph in Fig. 6.8. The graph shows that the welding speed has a strong affect on the process. The increase in the welding speed rate, lead to a decrease in the fusion area of welding pool.

The model shows that the P parameter has the most significant effect on welding pool volume and this is obvious in Table 6.2. It is also noted that changes in the laser power rate would lead to a change in the response value. Fig. 6.10 illustrates the relationship between S and F and the effect on the total welding pool area (A_1) at P = 1.163 kW. From Fig. 6.10, it is clear that focus position has less effect on the process whereby changing the focus position the response will not be consequentially changed. This is shown in Table 6.2.

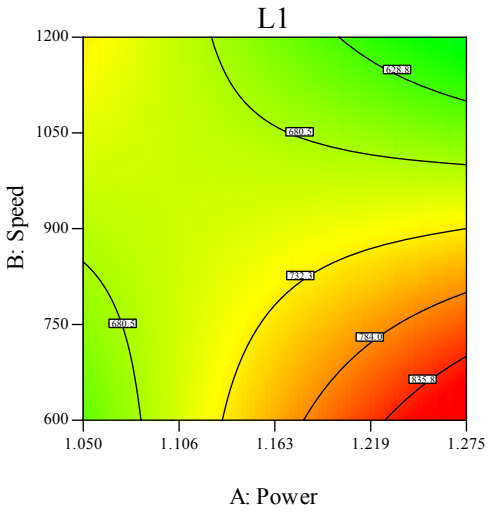

Fig. 6.9: Contour graphs exhibiting the effect and S parameters on the response L_1 at F = -0.8 mm.

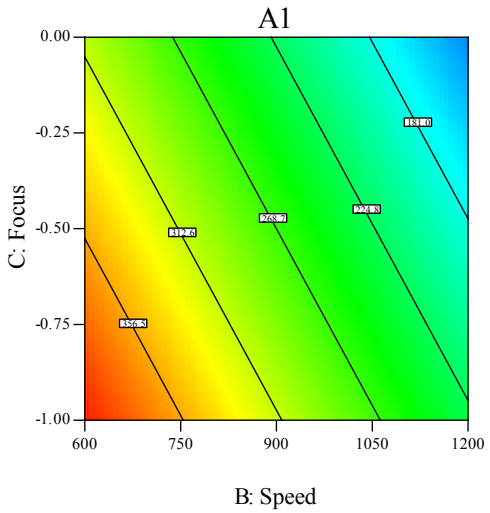

Fig. 6.10: Contour graphs of P exhibiting the effect of F and S parameters on the response A_1 at P = 1.163 kW.

6.1.3 Development of a Mathematical Model for Tensile Strength

A lap joint was applied for joining the ferrous / nonferrous dissimilar plates, mentioned above, together. The experiments were carried out according to the design matrix given in Table 6.2. They were performed in random order to avoid any systematic error. The tensile shear strength samples, as exhibited in Figs. 4.16 (a, b), mentioned in chapter four, were tested at room temperature (20 ºC). Tensile tests were carried out at a constant travel speed of 1 mm/min, with stress applied in the sheet plane in a perpendicular direction to the weld line. Since the welding penetration of the jointed sheets are not the same, the ultimate strength is obtained by dividing the force at fracture of the specimen by the length of the weld line (6 mm) and termed as resistance (N/mm). Rupture was found to mainly occur in the heat-affected zone (HAZ) of the aluminium or in the welding pool. The fracture occurring at the seam/aluminium interface could be initiated by the Al–Fe–Si inclusions that are generally present in the 6xxx aluminium alloys. Most of these intermetallic phases of Al–Fe–Si composition are short rods perpendicularly oriented to the laser welding direction as it is exhibited in Fig. 6.15 (c).

6.1.3.1 Analysis of the result

The raw data of the average tensile shear strength test results is shown in Table 6.2. To analyze the effects of the welding parameters in detail, ANOVA was conducted; these results are shown in Table 6.12. In the ANOVA table, Table 6.12, the F_v is used to test the significance of a factor by comparing model variance with residual (error) variance, which is calculated by dividing the model mean square by the residual mean square. As mentioned in the previous chapter the high F_v value for a parameter means that the effect of the parameter on the characteristics is large. The average tensile shear tests appear to be mainly affected by the laser power and focus position, as shown in Table 6.12. The result in Table 6.12 shows that the highest F_v value in the process was obtained for laser power 'P' equal to 30.20. The F_v value for the focus position 'F' was equal to 9.45, which indicates that the 'F' has a relatively small effect on the process. The F_v value for the welding speed 'S' was equal to 0.018, which indicates that the speed has an insignificant effect on the process. Adequate Precision compares the range of the predicted values at the design points to the average prediction error. For tensile shear model adequate precision value was equal to 10.595, as shown in Table 6.12. The same table also shows the other adequacy measures R^2 and Adjusted R^2. All the adequacy measures indicate that an adequate model has been obtained. The final mathematical model for predicting the tensile strength of a dissimilar joint in terms of coded factors and actual factors as determined by Design Expert software are shown below in Eqs 6.9 and 6.10.

Table 6.12: ANOVA for selected tensile shear model

Source	Sum of Squares	df	Mean Square	F_v Value	p-value Prob. > F	
Model	53375.87	5	10675.17	12.38778	0.0005	Significant
P	26022.24	1	26022.24	30.19696	0.0003	
S	15.42939	1	15.42939	0.017905	0.8962	
F	8139.268	1	8139.268	9.445043	0.0118	
SF	5161.54	1	5161.54	5.989602	0.0344	
P^2	9638.331	1	9638.331	11.1846	0.0074	
Residual	8617.502	10	861.7502			
Cor. Total	61993.37	15				
R-Squared = 0.8610			Adeq. Precision = 10.595			
Adj. R-Squared = 0.7915						

Final Equation in Terms of Coded Factors:

Tensile St. = 145.16 -91.20*P +1.32*S +30.26*F -54.49*S*F +55.22*P^2 **…(6.9)**

Final Equation in Terms of Actual Factors:

Tensile St. = 7173.945 -10955.384*P -0.177*S+387.471*F -0.363*S*F +4363.33*P^2

…(6.10)

6.1.3.2 Validation of the model

Fig. 6.11 shows the actual response versus the predicted response for tensile shear testing result. From this Fig., it can be seen that the model adequately describes the response within the limits of the factors being investigated herein, as the data points are close to the diagonal line. Furthermore, three extra confirmation experiments were carried out using different test conditions, which are presented in Table 6.13 along with the resulting percentage error. It can be noticed that the percentage error is less than 15%. The obtained tensile shear stress after laser welding is greater than the base metals value particularly when compared to the aluminium side. The mechanical strength values are compatible with the specifications relative to these assemblies in the automotive industry.

Table 6.13: Confirmation experiments of the responses compared with model results.

Exp. No	P, kW	S, mm/ min	F, mm	Tensile strength, MPa		$\lvert E\% \rvert$
				Actual	predicted	
1	1.091	827	-0.64	234	213	9.9
2	1.119	1200	-0.45	173	188	8
3	1.200	600	0.00	231	204	13.2

6.1.3.3 Effect of process parameters on the response:

1) Laser power**:** It is evident from the results that the laser power is the most significant factor associated with the response, and it is inversely proportional with the response as shown in a perturbation in Fig. 6.12. The highest tensile strength value was observed to be at a power of 1.05 kW as presented in Table 6.2.

2) Focus point position: The results indicate that the focus point position also has a strong effect on the tensile strength of the laser-welded joint, as shown in Fig. 6.12. The model developed indicates that there is an interaction between the two

welding parameters (the welding speed and the focus position). The interaction between the focus position and welding power is exhibited in Fig 6.13.

3) Welding speed**:** It can be seen that the welding speed has no obvious effect on the response within the parameter range domain applied. Therefore, changing welding speed will not affect the response which is clear in Fig. 6.12.

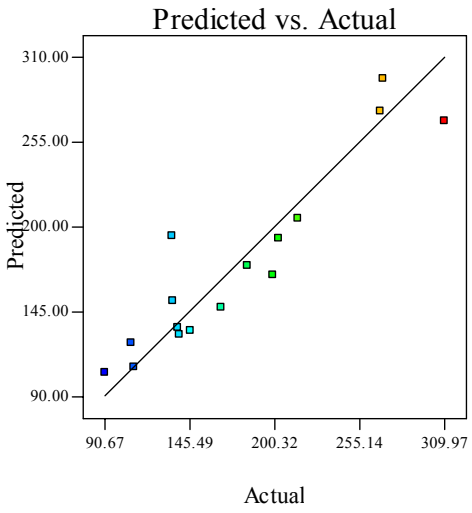

Fig. 6.11: Predicted Vs Actual for tensile shear strength.

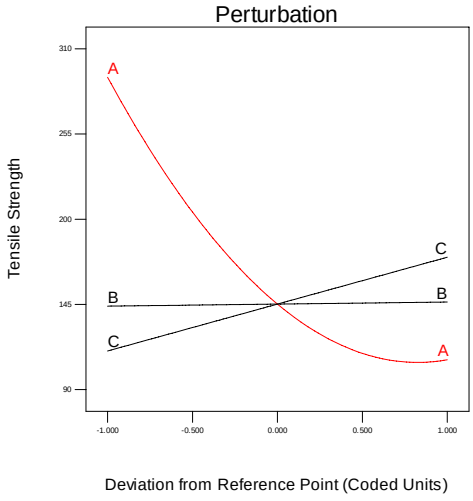

Fig. 6.12: Shows P, F and S parameters and their effect on the tensile strength of the dissimilar components.

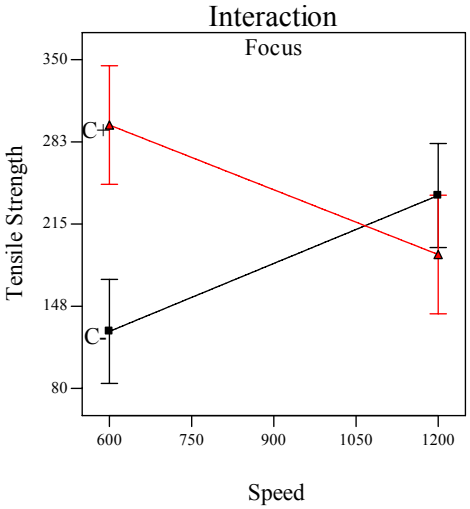

Fig 6.13: The interaction between S and F at P = 1.1kW

6.1.4 Operating Cost Modeling

The operating costs for joining the above mentioned dissimilar materials were calculated using Eq. 4.13 and presented in Table 6.2. The mathematical model was developed to minimize the operating cost. The same procedure was followed to check the model adequacy. The results for the reduced quadratic model which was suggested by software for the received result of the welding operating cost are shown in Table 6.14. The same table shows the other adequacy measures R^2, Adjusted R^2 and Predicted R^2. All the adequacy measures indicate an adequate quadratic model. The adequate precision of 152 indicates adequate model discrimination. The developed quadratic mathematical models in terms of coded factors and actual values are exhibited in Eqs 6.11 and 6.12.

Final Equation in Terms of Coded Factors:

$$\text{Cost} = 0.30 + 3.56E\text{-}003 * P - 0.1 * S + 0.038 * S^2 \quad \textbf{…(6.11)}$$

Final Equation in Terms of Actual Factors:

$$\text{Cost} = +0.94097 + 0.032 * P - 1.13E\text{-}003 * S + 4.2E\text{-}007 * S^2 \quad \textbf{…(6.12)}$$

Table 6.14: ANOVA for operating welding cost

Source	**Sum of Squares**	**df**	**Mean Square**	**F_v Value**	**p-value Prob. > F_v**	
Model	0.115498	3	0.038499	4214.004	< 0.0001	Significant
P	0.000113	1	0.000113	12.34807	0.0043	
S	0.110806	1	0.110806	12128.49	< 0.0001	
S^2	0.004579	1	0.004579	501.1771	< 0.0001	
Residual	0.00011	12	9.14E-06			
Cor. Total	0.115608	15				
R-Squared = 0.9991			Adeq. Precision = 152			
Adj. R-Squared = 0.9988						

6.1.5 Microharness and Microstructure Studies

6.1.5.1 Microstructure of dissimilar jointed materials

The effect of welding speed, focus position and laser power on the appearance of laser-welded joints and welding pool shape are shown in Fig. 6.3 of low carbon steel-on-aluminium 6082. Figs. 6.14(a, b) shows the Base metal (BM) low carbon steel Din: en 10131 and aluminium 6082 respectively.

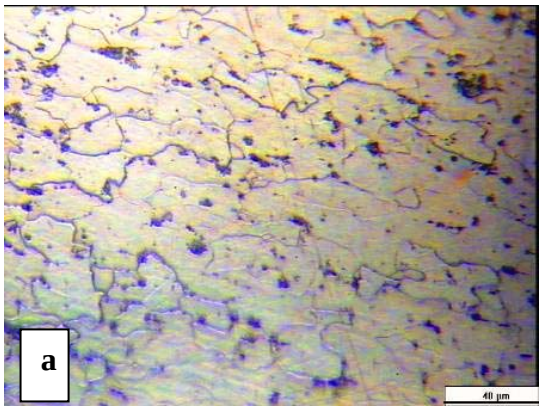

Fig 6.14(a): BM of low carbon steel Din: en 10131.

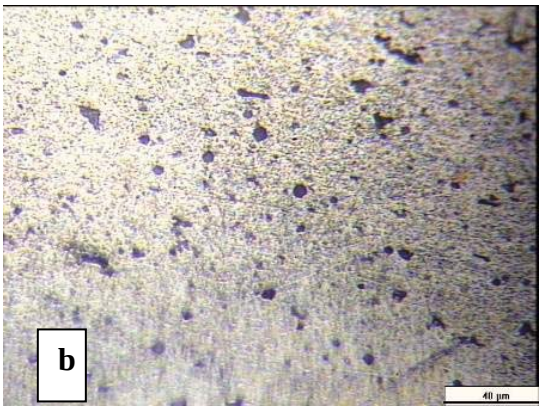

Fig 6.14(b): BM of aluminium 6082

Microstructures of the dissimilar joints are clearly exhibited on micrographics in Fig. 6.15(a, b, c), showing columnar grains oriented from steel–weld interfaces to the weld centre (which are controlled by composition and weld cooling rates). This well-known solidification microstructure of low carbon steel weld was observed for all welding parameters, showing no effect of cooling rate on weld microstructure. Some “white solute bands” were observed at the bottom of the weld pool, seeming to cross the columnar grains. These “solute bands” following the weld–aluminium interface shape were more frequent when steel penetration increased. The low carbon steel penetration increase was combined with a rise in the volume of melted aluminium producing bigger aluminium–steel dilution, which in turn multiplied the quantity of solute bands. Following this, during cooling, entrapped aluminium in steel could form: (i) local affluence of aluminium Fe–Al alloys, (ii) Fe-Al intermetallic phases, (iii) solidified as pure aluminium. The laser steel–aluminium dissimilar joining resulted in a complex and heterogeneous microstructures

composed of columnar grains and “white solute bands” in the base of the welding pool. Adjacent to the weld, a small grain size (10 μm versus 50 μm in the base material) heat affected zone was evidenced in the low carbon steel due to a re-crystallization phenomenon (for steel, between the melting point and the austenite transformation temperature).The liquation zones, observed in aluminium partially melted zones are due to the presence of low fusion point elements (magnesium) at the grain boundaries.

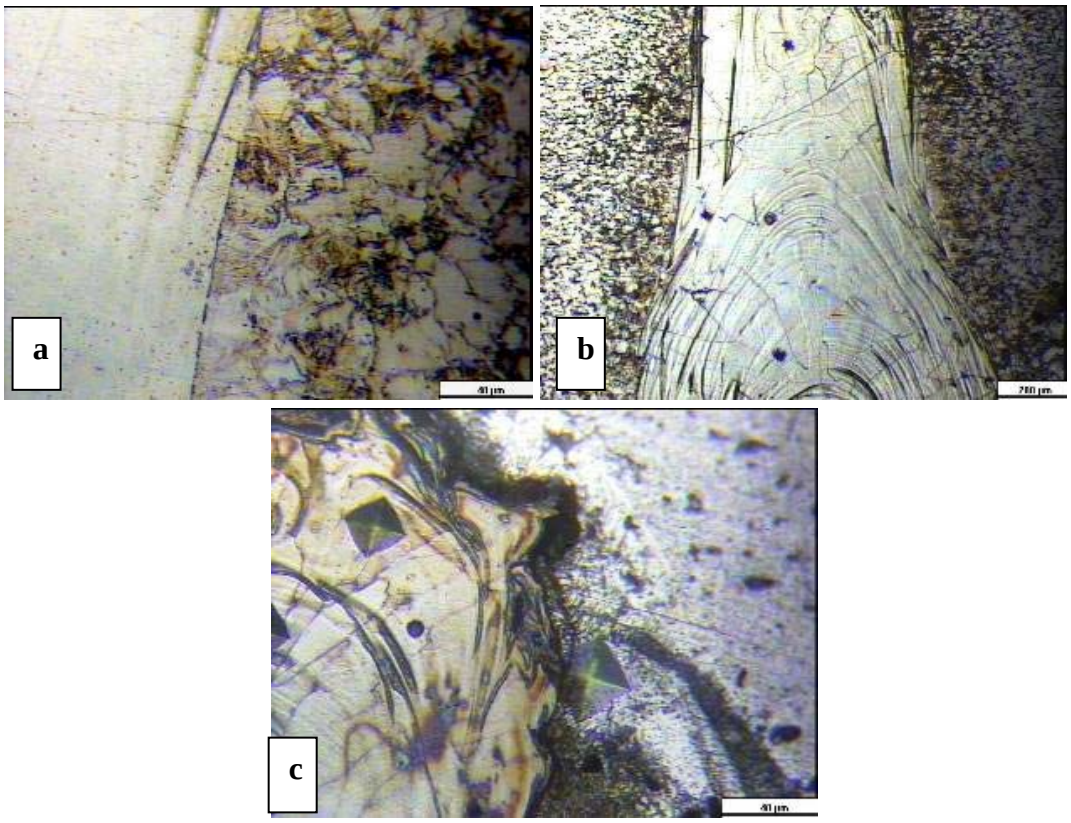

Figs. 6.15 (a, b, c): The redistribution of elements in the fusion zone of an overlap welding joint of aluminium 6082 to LCS Din: en 10131.

6.1.5.2 Microhardness of dissimilar jointed materials

The specimens selected for microhardness studies were based on heat input calculation (P x S). Vickers microhardness measurements with a 50 g loading force test were applied to the elected specimens shown in Fig 6.3. For each specimen three different positions were subjected to the study (BM, HAZ, and WZ) for each plate of

the dissimilar joint as presented in Table 6.15 and exhibited in microhardness profile of the dissimilar joint Fig. 6.16. It is well known that in the case of solid steel to liquid aluminium interaction, resulting layers consist of a thin $FeAl_3$ layer on the aluminium side and a thicker Fe_2Al_5 layer directed on the way to the steel side of the joint. On the other hand, limited data is available on the liquid steel to liquid aluminium interaction during high solidification rate key-hole laser welding. In the HAZ of the steel side, the microhardness increase (328 – 372 Hv) as presented in Table 6.16 was evidenced and could be related to the grain refining during re-crystallization, and to the quenching effect resulting in a fine acicular microstructure. The microhardness of the WZ (320 – 257 Hv) in steel sides exhibited in Fig 6.15 is less than that measured in HAZ but it is higher than that in the BM (175 – 145 Hv) this is due to rapid solidification rate as mentioned above.

Table 6.15: Microhardness test result of dissimilar ferrous to nonferrous materials

Sp No.	**LCS 10131**			**AL6082H24**		
	BM	**HAZ**	**WZ**	**WZ**	**HAZ**	**BM**
3	158.9	371.85	319.7	326.53	160.5	127.79
7	175.29	340.8	256.76	377.98	148.91	140.01
12	170.36	316.98	278.38	474.27	128.65	107.72
16	145.38	328.3	321.58	472.17	131.05	101.1

Compared to the hardening effect detected in the weld–aluminium interfaces by intermetallic compound generation, the steel–weld interfaces were not expected to be the weakest point of the assemblies. The microhardness profile of the dissimilar joints are presented in Table 6.15 and exhibited in Fig 6.16. The tensile test shows that the fracture mostly occurred at the HAZ or WZ in the aluminium side. The fracture could be attributed to the Al–Fe–Si inclusions that are generally present in the 6xxx aluminium alloys [4]. Most of these intermetallic phases of Al–Fe–Si compositions are short rods perpendicularly oriented to the laser welding direction (Fig. 6.16). Referring to Fig. 6.16 there are insignificant effects due the difference in heat input among the selected specimens, in terms of microhardness achieved values, excluding the WZ at the aluminum side were the difference is vary between 474 Hv and 326 Hv.

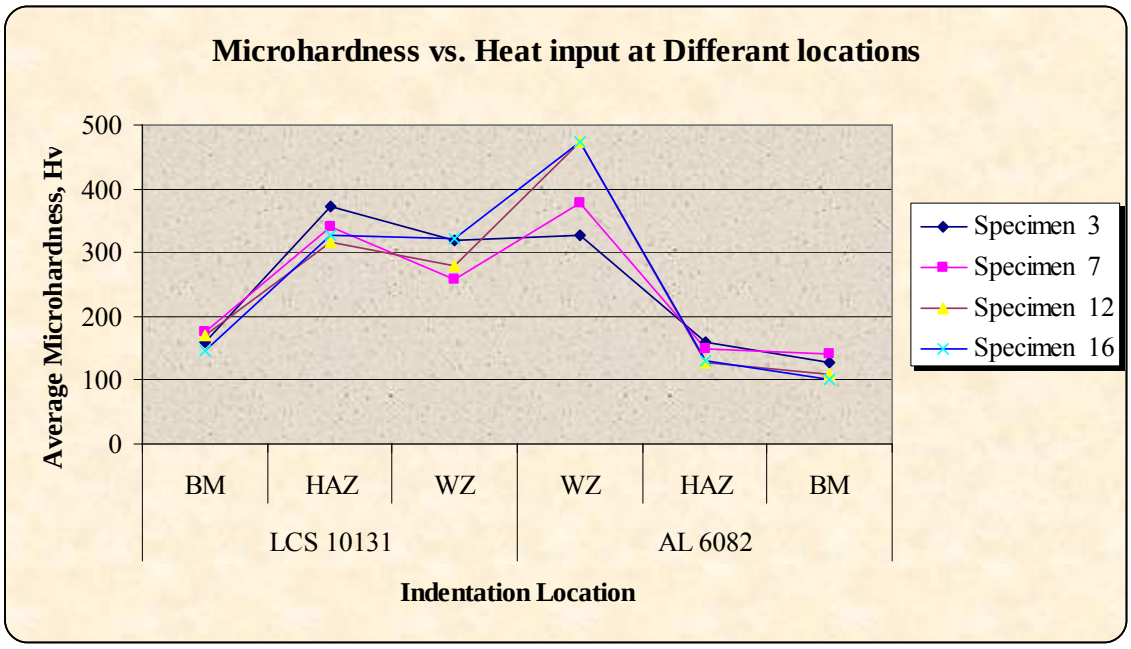

Fig. 6.16: The microhardness profile of the dissimilar joint (Al 6082 / Din: en 10131).

6.1.6 Models (multiple –response) Optimization

6.1.6.1 Numerical optimization

The numerical multiple-response optimization criterion is to reach maximum tensile shear strength, minimum residual stresses and minimum welding pool geometry, improve penetration, minimum welding operating cost while minimizing laser power and maximizing welding speed. Focus position value was kept in range (between -1 and 0).

Three different optimization criteria were decided and presented in Table 6.16. In the first optimization criteria all the parameters received the same importance (+ + +) and same weight (1) as per the Design Expert software default. In the second criteria a different weight was assigned (as presented in Table 6.16) for each parameter while the importance for each parameter was kept as per the software default. The importance was changed for welding parameters in the third criteria. The optimization result presented in the Table 6.16 at each criterion is selected from one of ten or more different optimum result calculated by the software.

The effect of changing the criteria on the optimization result is obvious in Table 6.17. For example, by applying the second or third criteria the tensile strength (resistance) value will reach up to 317 N/mm, while if applying the first criteria it will be around 269 N/mm. If the target is only to maximize the tensile strength regardless of the other parameters then the response value will be greater than the received values and this is true for each response individually optimized. The mechanical strength values obtained by this method of optimization are compatible with the specifications relative to these assemblies in the automotive industry. The welding geometries were not assigned high weight or high importance since they are not a direct target for the optimization; they indirectly affect the welding quality. The welding cost was significantly reduced up to 52 % in all the selected criteria compared to the values presented in Table 6.2, in which a maximum cost of 46 cent was reached. Also, the welding speed is at its maximum (1200 mm/min) in all the optimization criteria which leads to increased production rate.

Comparing the second and third criterion they are same in the input / out put values but the only difference is at the desirability. The third criterion in which the importance and the weight of the input / output parameters is different than in the second criterion leads to a change in desirability value (0.85) compared to the desirability value in second criterion (0.89).

6.1.6.2 Graphical optimisation

The graphical optimization displays the area of feasible response values in the factor space. From the overlay plots in Figs. 6.17 and 6.18 it is obvious that the graphical optimisation allows visual selection of the optimum welding conditions according to certain criterion. The result of the graphical optimisation are the overlay plots, these type of plots are extremely practical for quick technical use in the workshop to choose the values of the welding parameters that would achieve certain response value for this type of dissimilar materials. The yellow /shaded areas on the overlay plot in Figs. 6.17 and 6.18 are the regions that meet the proposed criteria.

Table 6.16: Shows three optimization criteria with the optimization results using numerical multiple-response.

Welding Parameters	Power		Speed		Focus		W_1		L_1		A_1		Residual stresses		Tensile Strength		Cost € / m		D*.
Goal	Min.		Max.		In range		Min.		Max.		Min.		Min.		Max.		Min.		
Criteria	Wt.	Imp.	Wt.	Imp.	-	-	Wt.	Imp.	Wt.	Imp.	Wt.	Imp.	Wt.	Imp.	Wt.	Imp.	Wt.	Imp.	
First Criteria	1	+++	1	+++	-	-	1	+++	1	+++	1	+++	1	+++	1	+++	1	+++	
Result	1.08		1200		-1.00		500.84		783.52		229.62		107		269		0.22		0.55
Second Criteria	.05	+++	5	+++	-	-	0.5	+++	0.5	+++	0.5	-	5	+++	5	+++	0.1	+++	
Result	1.05		1200		-1.00		476		804		230		107		317		0.22		0.89
Third Criteria	1	+++	1	+++	-	-	1	+	1	++	1	+	1	+++ ++	1	+++ ++	1	+++ ++	
Result	1.05		1200		-1.00		476		804		230		107		317		0.22		0.85

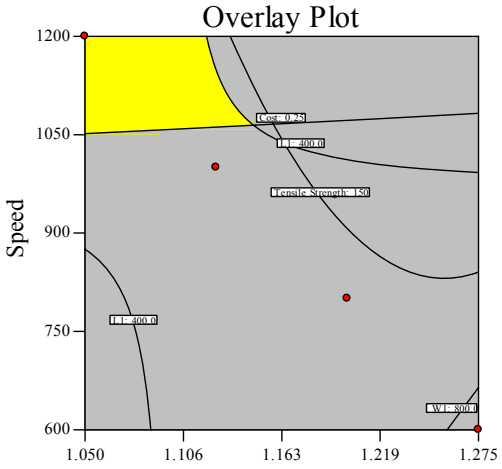

Fig 6.17: The graphical feasible solution in yellow shaded area for first optimisation criteria at F = 0.00 mm.

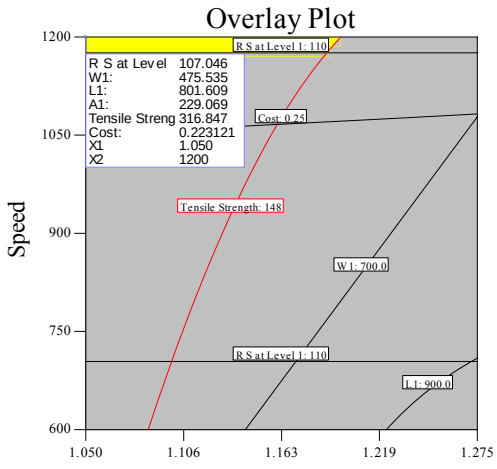

Fig 6.18: The graphical feasible solution in yellow shaded area for second optimisation criteria at F = -1.00 mm.

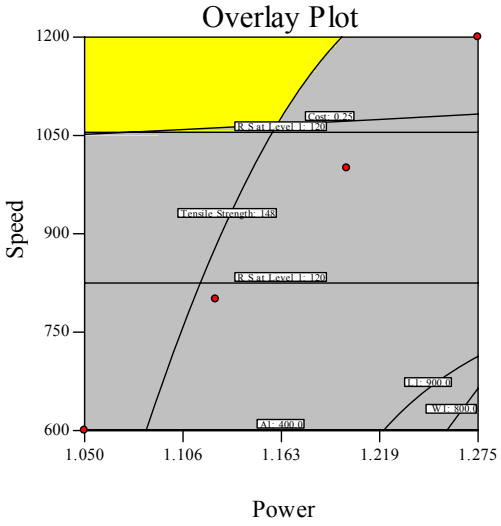

Fig 6.19: The feasibel solution in yellow shaded area for third optimisation criteria at F = -0.99 mm

6.2 Joining of Aluminium (1050 H24) to Low Carbon Steel Din: en 10131

Aluminium 1050 H24 plates with a thickness of 2mm were welded to Low Carbon Steel Din: en 10131 plates of the same thickness using lap joint design, exhibited in Fig. 4.16 (a), and pilot experiments were carried out by changing one parameter at a time to detect the operating range of the welding parameters under investigation. Visual inspection of the welded joints was carried out in order to determine a suitable range of operation for the parameters. The criterion used for selecting a good weld seam was the absence of observable welding defects. The selected welding parameters for these dissimilar materials are: Laser power, welding speed and focus point position. Table 6.17 shows the welding inputs variables and experiment design levels. The welding experiments were accomplished in the Mechanical School workshop following the Taguchi designed matrix in random order presented in Table 6.18. The mechanical destructive tests (tensile shear test specimens) and cost per meter welded calculations were carried out for the jointed specimens and the results are presented in Table 6.18. Each presented result in Table 6.18 is an average of at least of three readings.

Table 6.17: Process parameters and design levels used

Variables	Code	Unit	Level 1	Level 2	Level 3	Level 4
Laser Power	**P**	**kW**	0.90	1.05	1.20	1.35
Welding Speed	**S**	**mm/min**	1500	1700	1900	2100
Focus	**F**	**mm**	-0.6	-0.2	0.2	0.6

Table 6.18: Shows the Taguchi design matrix in actual values of studied welding parameters, tensile shear test and cost per meter welded

Std	Run	Power, kW	Speed, mm/min	Focus, mm	Tensile Strength, MPa	Cost, €/m
13	1	1.35	1500	0.6	109.29	0.18
5	2	1.05	1500	-0.2	80.00	0.18
8	3	1.05	2100	0.2	98.57	0.13
2	4	0.9	1700	-0.2	89.29	0.16
11	5	1.2	1900	-0.6	59.29	0.14
10	6	1.2	1700	0.6	78.57	0.16
7	7	1.05	1900	0.6	96.43	0.14
6	8	1.05	1700	-0.6	62.86	0.16
12	9	1.2	2100	-0.2	76.43	0.13
15	10	1.35	1900	-0.2	106.43	0.15
1	11	0.9	1500	-0.6	72.14	0.18
16	12	1.35	2100	-0.6	77.14	0.13
3	13	0.9	1900	0.2	86.43	0.14
4	14	0.9	2100	0.6	82.86	0.13
9	15	1.2	1500	0.2	97.86	0.18
14	16	1.35	1700	0.2	102.14	0.16

6.2.1 Development of Mathematical Models for Residual Stresses

The study of the residual stress is very important when two dissimilar materials are jointed together especially if there is a large difference in the thermal conductivity and thermal expansion of the two jointed materials. Residual stresses of Low carbon steel / Al 1050 H24 dissimilar welded components were evaluated during this study following the measurement procedure explained in paragraph 4.5.3 in the previous chapter in order to control and optimize the selected laser welding parameters. Residual stresses were studied and analyzed through the depth of the welded joint at gradual levels to get a clear indication of the effect of welding parameters on the distribution of the residual stress through the depth of HAZ. This also allowed the optimisation of residual stress. The strain gauge was bonded to the surface of the specimen (aluminium side) in the

HAZ were the present of the critical (serious) residual stresses in the joined component and a blind hole of incremental depth of 1.27 mm was drilled at 1-2 mm from the centre welded line in the middle of the specimen as presented in Fig.4.14 (a). "Design Expert 7" software has been used for analyzing the measured responses. Depth levels at which the micro-strains were measured are presented in Table 6.3. The calculated stress (σ_i) at each level expressed in Table 6.19, were considered as responses and analysed separately to predict the effect of the welding parameters through the specimen depth. The effect of individual welding parameter on the residual stress was also investigated in this study.

Table 6.19: The experimental calculated for Al 1050 H24 residual stresses in MPa.

Std	σ_1	σ_2	σ_3	σ_4	σ_5	σ_6
1	17.0	10.6	8.6	9.4	8.4	6.9
2	21.7	10.6	24.5	22.6	18.6	18.3
3	21.3	18.2	15.8	15.8	12.6	11.4
4	12.0	8.9	7.9	8.1	7.6	6.0
5	29.1	16.0	14.7	13.4	11.5	11.3
6	18.7	18.7	15.1	14.9	12.3	10.9
7	7.7	8.2	7.6	8.7	6.3	5.5
8	13.7	10.5	10.9	12.7	12.9	10.3
9	33.4	14.1	12.3	10.3	8.0	7.3
10	27.0	13.8	9.5	13.5	13.9	13.1
11	22.4	18.8	15.0	13.3	10.3	9.5
12	17.8	18.5	15.0	14.0	10.6	9.8
13	34.6	14.1	10.4	8.6	6.2	5.7
14	32.7	16.6	17.4	14.7	11.2	10.8
15	23.9	14.4	13.2	13.7	12.8	11.4
16	20.1	19.0	15.8	15.4	12.2	11.9

6.2.1.1 The ANOVA analysis

The investigations for welding process parameters were carried out, using ANOVA, to identify which parameters significantly affect the welding quality. The study of the residual stress of the aluminium plate presented in Table 6.19 shows that the produced stresses due to the dissimilar joining process using the laser welding method are not serious and may have no negative effect on the welding quality of the joint. According to the achieved result in Table 6.19, only the results for level 1 (σ_1) will be subjected to ANOVA analysis The test for significance of the regression model, the test for significance on individual model coefficients and the lack-of-fit test were performed using Design Expert 7 software. The backward regression method was applied for the critical level as observed in Table 6.19 first level only (σ_1) and exhibited in ANOVA Table 6.20 for the model. The ANOVA Table summarizes the analysis of the variances of the responses and shows the significant model at level 1. The same table also shows the other adequacy measures R^2, adjusted R^2, and adequacy precision for each response. The adequate precision compares the range of the predicted value at the design points to the average predicted error. The adequacy measures in the ANOVA Table for model 1 indicate that an adequate model has been obtained. The final mathematical models in terms of actual factors as determined by Design Expert software are shown below in Eqs.6.13 and 6.14.

Table 6.20: ANOVA for residual stress at level 1

Source	**Sum of Squares**	**df**	**Mean Square**	**F_v Value**	**p-value Prob. > F**	
Model	670.8918	2	335.4459	17.69654	0.0002	Significant
P	279.7229	1	279.7229	14.75686	0.0020	
S	391.1689	1	391.1689	20.63622	0.0006	
Residual	246.4209	13	18.95545			
Cor. Total	917.3126	15				
R-Squared = 0.7314			Adeq. Precision = 12.989			
Adj. R-Squared = 0.6900						

Final Equation in Terms of Coded Factors:

RS at Level 1 = 22.08 +5.61*P -6.63*S **…(6.13)**

Final Equation in Terms of Actual Factors:

RS at Level 1 = 33.83514 +24.93204* P -0.0221* S **…(6.14)**

6.2.1.2 Validation of the model

Fig. 6.20 shows the actual response versus the predicted response for residual stress result at level 1. From this Fig., it can be seen that the model adequately describes the response within the limits of the factors being investigated herein, as the data points are close to the diagonal line.

6.2.1.3 Effect of process parameters on the response:

1) Welding speed**:** It is obvious from the results that the welding speed is the most significant factor associated with the response, as shown in a contour graph in Fig. 6.21. The lowest residual stress value for level 1 was observed to be at a speed of 1900 mm/min as presented in Table 6.19.

2) Laser power**:** It can be seen that the laser power has an important effect on the response, as shown in Table 6.19. It is clear that the higher laser power resulted in a higher response value, due to the fact that using high laser power would increase the power density. This leads to more penetration resulting in an improved response. Fig.6.21 shows a contour graph of the effect of P and S on the response at F = 0 mm.

3) Focus point position: From the ANOVA analysis it can be seen that the focus position has no significant effect on the response within the parameter range domain applied. By changing focus point the response will not be affected.

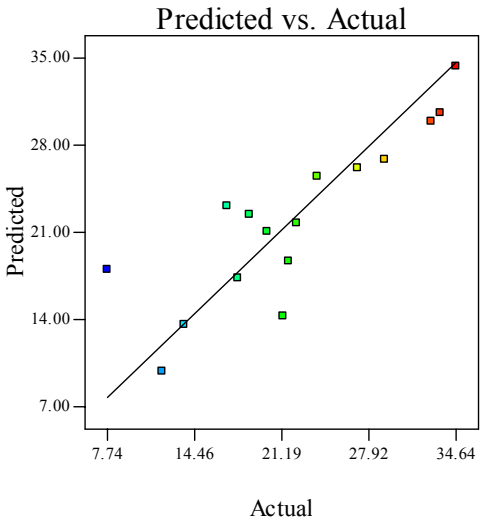

Fig. 6.20: Predicted Vs Actual for residual stresses

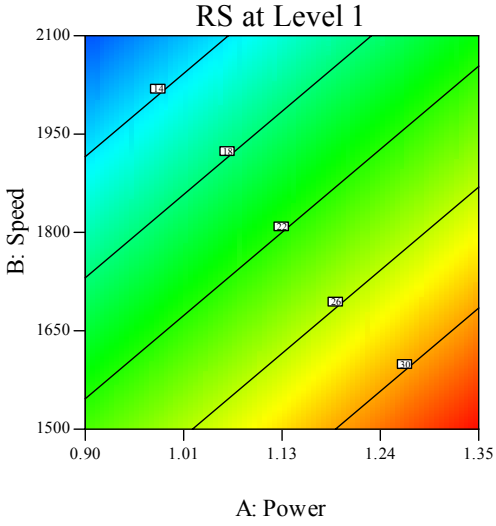

Fig. 6.21: Presents contour graph of the effect of S, P at F = 0.0 mm on the response at depth level 1.

6.2.2 Development of a Mathematical Model for Tensile Shear Strength

A lap joint was applied for joining the low carbon steel / Aluminium 1050 dissimilar plates together. The experiments were carried out according to the design matrix given in Table 6.18. They were performed in random order to avoid any systematic error. The tensile shear strength samples, as exhibited in Figs. 4.16 (a, b), mentioned in chapter four, were tested at room temperature (20 ºC). Tensile tests were carried out at a constant travel speed of 1 mm/min, with stress applied in the sheet plane in a perpendicular direction to the weld line. Since the welding penetration of the jointed sheets are not the same, the ultimate strength is obtained by dividing the force at fracture of the specimen by the length of the weld line (6 mm) and termed as resistance (N/mm). The rupture mainly occurs in the heat-affected zone (HAZ) of the aluminium or in the welding pool.

6.2.2.1 Analysis of the result

The raw data, the average tensile shear strength test results are shown in Table 6.18. To analyze the effects of the welding parameters in detail, ANOVA with backward

elimination regression method; which eliminates the insignificant model terms automatically, was conducted; these results are shown in Table 6.21. In the ANOVA table, Table 6.22, the F_v is used to test the significance of a factor by comparing model variance with residual (error) variance, which is calculated by dividing the model mean square by the residual mean square. As mentioned in the previous chapter the high F_v value for a parameter means that the effect of the parameter on the characteristics is large. The average tensile shear tests appear to be mainly affected by the focus position and laser power, as shown in Table 6.21. The result in Table 6.21 shows that the highest F_v value in the process was obtained for focus position, 'F' equal to 18.62. The F_v value for the laser power 'P' was equal to 5.08, which indicates that the laser power has a relatively small effect on the process, The F_v value for the speed 'S' was automatically eliminated by the applied regression method mentioned above, which indicates that the speed has an insignificant effect on the process. Adequate Precision compares the range of the predicted values at the design points to the average prediction error. For this model it was equal to 9.595, as shown in Table 6.21. The same table also shows the other adequacy measures R^2 and Adjusted R^2. All the adequacy measures indicate that an adequate model has been obtained. The final quadratic mathematical model for predicting the tensile strength of a dissimilar F/A joint in terms of coded factors and actual factors as determined by Design Expert software are shown below.

Table 6.21: ANOVA for selected tensile shear model

Source	Sum of Squares	df	Mean Square	F_v Value	p-value Prob. > F	
Model	2594.77	4.00	648.69	9.44	0.0015	Significant
P	349.21	1.00	349.21	5.08	0.0456	
F	1280.00	1.00	1280.00	18.62	0.0012	
P^2	358.29	1.00	358.29	5.21	0.0433	
F^2	607.27	1.00	607.27	8.83	0.0127	
Residual	756.12	11.00	68.74			
Cor. Total	3350.89	15.00				
R-Squared = 0.7744			Adeq. Precision = 9.956			
Adj. R-Squared = 0.6923						

Final Equation in Terms of Coded Factors:

Tensile Strength =87.77 +6.27*P +12.00* F+10.65*P^2 -13.8 *F^2 **…(6.15)**

Final Equation in Terms of Actual Factors:

Tensile Strength = 322.612-445.357*P +20.00* F +210.317* P^2 -38.504*F^2 **…(6.16)**

6.2.2.2 Validation of the model

Fig. 6.22 shows the actual response versus the predicted response for tensile shear testing result. From this Fig., it can be seen that the model adequately describes the response within the limits of the factors being investigated herein, as the data points are close to the diagonal line. Furthermore, three extra confirmation experiments were carried out using different test conditions, which are presented in Table 6.22 along with the resulting percentage error. It can be noticed that the percentage error is less than 12%. The obtained tensile shear stress after laser welding is greater than the base metals value particularly when compared to the aluminium side.

Table 6.22: Confirmation experiments of the responses compared with model results.

Exp. No	P, kW	S, mm/ min	F, mm	Tensile strength, MPa		$\lvert E\% \rvert$
				Actual	predicted	
1	0.90	2100	0.26	84	95	11.6
2	1.35	2100	0.26	98	107	8.4
3	0.90	1800	0.50	101	92	9.8

6.2.2.3 Effect of process parameters on the response:

Focus point position: It is evident from the results that the focus point position is the most significant factor associated with the response, as shown in a 3D graph Fig. 6.23. The model developed indicates that there is an interaction between the two welding parameters (the focus position and the welding speed).

Laser Power: The results indicate that the laser power also has a strong effect on the tensile strength of the laser-welded joint, as shown in Table 6.21. The highest tensile strength value was observed to be at a laser power of 1.35 kW as presented in Table 6.18.

Welding speed: From the ANOVA analysis it can be seen that the welding speed has no obvious effect on the response within the parameter range domain applied. By changing the welding speed the response will not be affected.

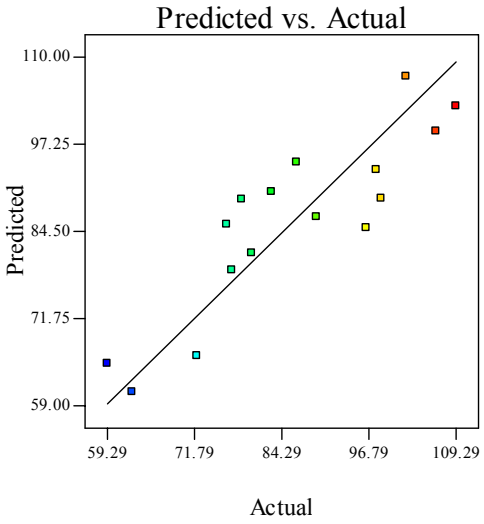

Fig. 6.22: Predicted Vs Actual for tensile shear strength, n/mm.

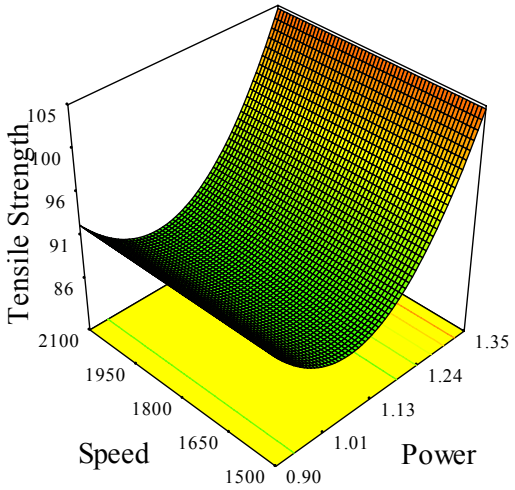

Fig. 6.23: 3D graph shows the effect of P and S parameters on the ensile strength of the dissimilar components at F = 0mm.

6.2.3 Operating Cost Modeling

The operating costs for joining the above mentioned dissimilar materials were calculated using Eq. 4.13. The mathematical model was developed to minimize the operating cost. The same procedure was followed to check the model adequacy. The analysis results are shown in Table 6.23 for the reduced quadratic model which is suggested by software for the received result of the welding operating cost. The same table shows the other adequacy measures R^2, Adjusted R^2 and Predicted R^2. All the adequacy measures indicate an adequate quadratic model. The adequate precision of 590

indicates adequate model discrimination. The developed quadratic mathematical model in terms of coded factors and actual values are exhibited in Eqs. 6.17 and 6.18.

Final Equation in Terms of Coded Factors:

$$\text{Cost} = 0.15 + 3.386E{-}003*P - 0.026*S - 5.700E{-}004*P*S + 4.294E{-}00*S^2 \quad \textbf{…(6.17)}$$

Final Equation in Terms of Actual Factors:

$$\text{Cost} = 0.42406 + 0.030*P - 2.476E{-}004*S - 8.445E{-}006*P*S + 4.77E{-}008*S^2 \quad \textbf{…(6.18)}$$

Table 6.23: ANOVA for operating welding cost

Source	Sum of Squares	df	Mean Square	F_v Value	p-value Prob. > F_v	
Model	0.005996	4	0.001499	48522.46	< 0.0001	Significant
P	0.000102	1	0.000102	3299.163	< 0.0001	
S	0.005834	1	0.005834	188852.6	< 0.0001	
PS	1.6E-06	1	1.6E-06	51.93959	< 0.0001	
S^2	5.83E-05	1	5.83E-05	1886.11	< 0.0001	
Residual	3.4E-07	11	3.09E-08			
Cor. Total	0.005996	15				
R-Squared = 0.9999			Adeq. Precision = 590			
Adj. R-Squared = 0.9999						

6.2.4 Microhardness and Microstructure Studies

6.2.4.1 Microstructure of dissimilar jointed materials

The microstructures of the dissimilar (aluminium 1050 H24 / low carbon steel 10131) joints are exhibited in the micrographs in Fig. 6.24 (a, b, c and d). The micrographs show columnar grains oriented from steel–weld interfaces to weld centre (which are controlled by composition and weld cooling rates). This well-known solidification microstructure of low carbon steel weld was observed whatever the welding parameters, showing no effect of cooling rate on weld microstructure. Some "white solute bands" were observed at the bottom of the weld pool, seeming to cross the columnar grains which are clearly evident in Figs. 6.24 (c, d). At the weld–aluminium

interfaces, new phases were generated by steel to aluminium reaction. These phases; which ensured bonding between aluminum (BM) and weld pool (WZ) as exhibited in Fig. 6.24 d, were composed of a compact and uniform layer of intermetallic compounds with thicknesses in the (0–30µm) range.

Needle-like precipitated phases were observed in Figs.6.24 (c, d) in aluminium plate in the aluminium HAZ. According to the microstructure shown in the Figs. 6.24, intermetallic compounds are anticipated to be $FeAl_2$, $Fe2Al_5$ or $FeAl_3$ phases as predicted by the Fe–Al equilibrium diagram [177]. Due to the large difference in chemical composition and in mechanical properties, the weld–aluminium and weld–steel interfaces were expected to be the weak points of the steel–aluminium assemblies.

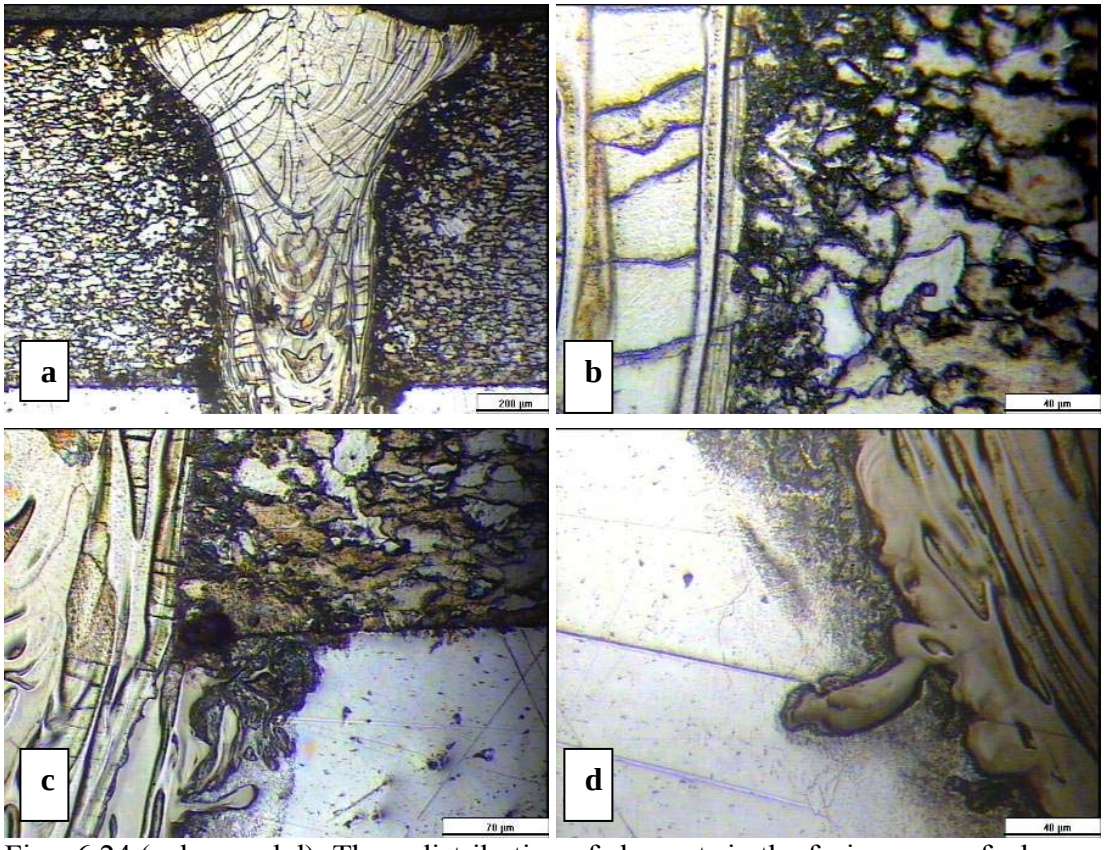

Figs. 6.24 (a, b, c and d): The redistribution of elements in the fusion zone of a lap weld joining aluminium 1050 H24 to LCS Din: en 10131.

6.2.4.2 Microhardness of dissimilar jointed materials

The specimens selected for microhardness studies were based on heat input calculation (P x S). Vickers microhardness measurements with a 50 g loading force test were applied to the elected specimens shown in Fig 6.6.24. For each specimen three different positions were subjected to the study (BM, HAZ, and WZ) for each plate of the dissimilar joint as presented in Table 6.24 and exhibited in microhardness profile of the dissimilar joint in Fig. 6.25. In the HAZ of the steel, some microhardness increase from 174 HV at the BM up to 308 HV was observed and could be attributed to the grain refining during re-crystallization, and to the quenching effect resulting in a fine acicular microstructure. The microhardness of the WZ (382 Hv) in steel sides exhibited in Fig 6.25 was due to the formation of intermetallic compounds of Fe_xA_y in the welding pool.

It is well-known that in the case of solid steel to liquid aluminium interaction, the resultant layers consist of a thin $FeAl_3$ layer on the aluminium side and a thicker Fe_2Al_5 layer towards the steel side of the joint. On the other hand, limited data is available on the liquid steel to liquid aluminium interaction during high solidification rate key-hole laser welding. In the HAZ of the steel side, the microhardness increase (328 – 372 Hv) as presented in Table 6.24 was observed and could be related to the grain refining during re-crystallization, and to the quenching effect resulting in a fine acicular microstructure. The microhardness of the WZ (320 – 257 Hv) in steel sides exhibited in Fig 6.25 is less than that measured in HAZ but it is higher than that in the BM (175 – 145 Hv). This is due to the same reasons mentioned above.

For the aluminium plate the measured microhardness in the HAZ (ranges from 64 up to 137 Hv) is greater that that in BM (53 Hv) exhibited in Fig. 6.25. The microhardness results achieved, showing the microhardness profile of the aluminium are presented in Table 6.24 and exhibited in Fig 6.25. The WZ (up to 592 Hv) composition domain intermetallic compounds seem to be rich in $FeAl_2$, Fe_2Al_5 or $FeAl_3$ phases as predicted by the Fe–Al equilibrium diagram. These intermetallic regions always exhibited severe cracking which seems to be detrimental to the assembly resistance. Most of the tensile testing cracks seem to take place in this region. Referring to Fig. 6.26 there are insignificant effects due the difference in heat input among the selected

specimens, in terms of microhardness measured values, except in WZ at the aluminum side were the difference is 592 – 365 Hv.

Table 6.24: Microhardness test result of dissimilar ferrous to nonferrous materials

Sp No.	LCS 10131			AL1050H24		
	BM	HAZ	WZ	WZ	HAZ	BM
1	173.5	308.6	360.8	592.33	117.7	52.51
4	167.51	282.11	331.43	447.75	137.4	52.81
10	174.7	308.2	332.41	365.64	63.93	51.46
16	180.2	291.52	381.93	475.45	89.16	57.81

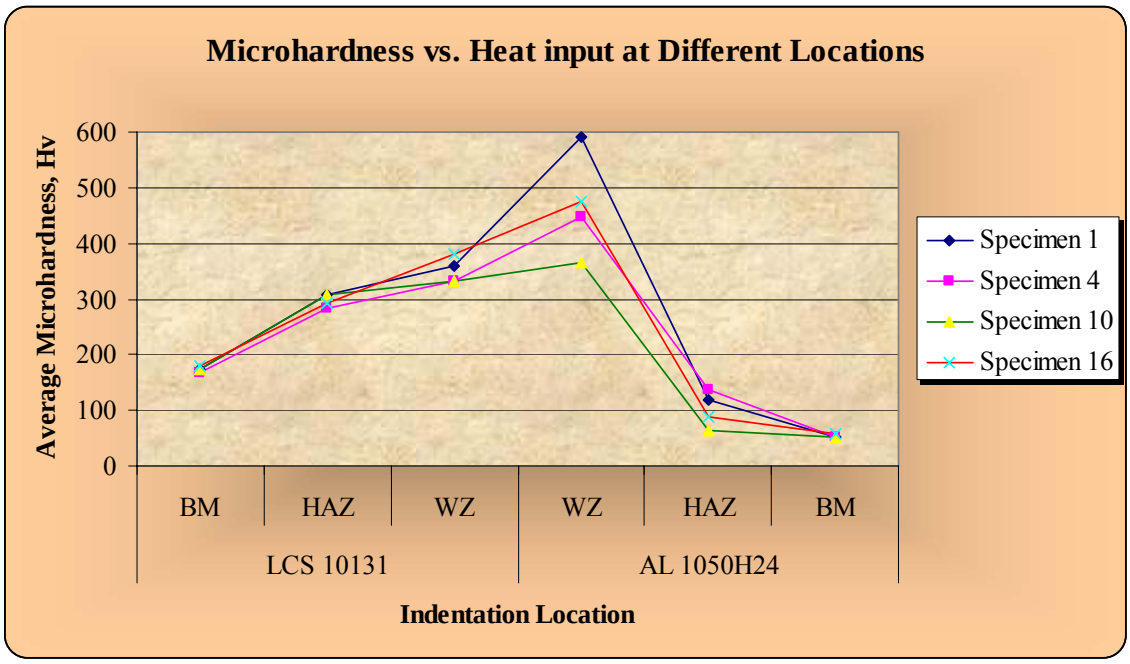

Fig. 6.25: The microhardness profile of the dissimilar joint (Al 1050 H24 / Din: en 10131).

6.2.4.3 Defects of dissimilar jointed materials

Local defects, such as weld cracks, were identified in steel-on-aluminium joints, as it is clear in Fig 6.24 c, sometimes propagating along weld–aluminium interfaces. Due to the great difference in melting temperatures between steel and aluminium, an aluminium fusion zone was detected just around the bottom of the weld. This region also presented

some defects such as circular porosities and liquation zones, exhibited in Fig. 6.26. The porosities could be attributed to hydrogen occlusion in the melt-pool at high temperature with a possible contribution of Argon gas shielding.

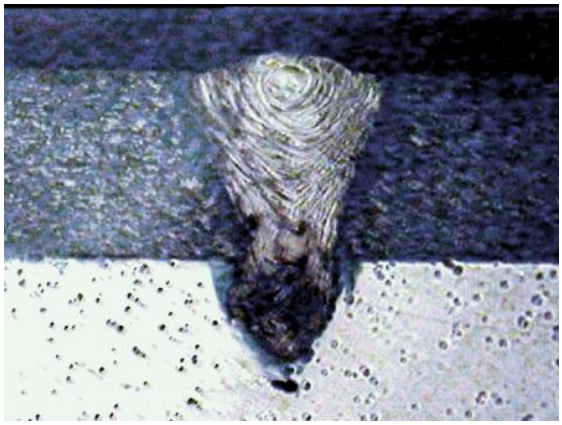

Fig 6.26: Defects of dissimilar (steel 10131 /aluminium 1050 H24) joints

6.2.5 Models (multiple –response) Optimisation

6.2.5.1 Numerical optimisation

For optimizing the dissimilar laser joint of the AL1050 H24 / LCS 10131, three different optimisation criteria were selected. They are presented in Table 6.25. In the first optimisation criteria the Design Expert software default was applied in which all the parameters received the same importance (+ + +) and same weight (1). In the second criteria a different weight was assigned for each parameter, as presented in Table 6.26, while the importance for each parameter was kept as the Design Expert software default at (+ + +). The importance of the input / output welding parameters was changed in the third criteria. The optimization result achieved and presented in the Table 6.25. Each optimum result presented in the Table 6.25 was selected from one of ten or more different optimum results calculated by the software for each criterion.

The effect of changing the criteria on the optimisation result is obvious in Table 6.25. For example comparing between the second and third criteria the tensile strength (resistance) value will change from 107 N/mm in the second optimisation criterion to 90

N/mm in the third criterion, while if applying the first criteria it would be about 95 N/mm. If the target is only to maximize the tensile strength regardless of the other parameters then the response value will be greater than the received values and this is true for each response individually optimized. The welding geometries were not assigned high weight or high importance since they are not a direct target for the optimisation; they indirectly affect the welding quality. The welding cost was unchanged by applying any one of the decided criterion, it was around € 0.13, but it was significantly improved compared to the result achieved in Table 6.18. Also, the welding speed is at a maximum (2100 mm/min) in all the selected optimisation criteria which leads to increased production rate and the laser power was at minimum (0.9 kW) value when the first criterion was selected.

6.2.5.2 Graphical optimisation

The graphical optimisation displays the area of feasible response values in the factor space. From the overlay plots in Fig. 6.27 for the first criterion it is obvious that the graphical optimisation allows visual selection of the optimum welding conditions according to certain criterion. The result of the graphical optimisation are the overlay plots, these type of plots are extremely practical for quick technical use in the workshop to choose the values of the welding parameters that would achieve certain response value for this type of dissimilar materials. The yellow /shaded area on the overlay plot in Fig. 6.27 is the region that meets the proposed criteria.

Table 6.25: Three optimization criteria with the optimization results using numerical multiple-response

Welding Parameters	Power		Speed		Focus		Residual stresses		Tensile Strength		Cost € / m		D.
Goal	Min		Max.		In range		Min.		Max.		Min.		
Criteria	Wt.	Imp.	Wt.	Imp.	Wt.	Imp.	Wt.	Imp.	Wt.	Imp.	Wt.	Imp.	
First Criteria	1	+++	1	+++	-	-	1	+++	1	+++	1	+++	
Result	0.90		2100		0.26		10		95		0.13		0.883
Second Criteria	0.1	+++	5	+++	-	-	0.1	+++	5	+++	0.1	+++	
Result	1.35		2100		0.26		21		107		0.13		0.700
Third Criteria	1	+	1	+++++	-	-	1	+++	1	+++ ++	1	+++ ++	
Result	1.00		2100		0.26		12		90		0.13		0.808

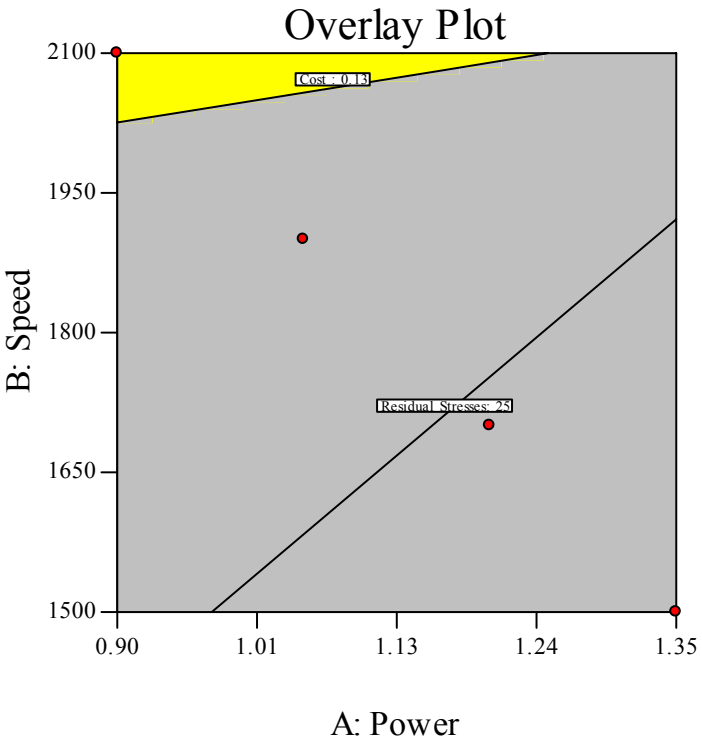

Fig. 6.27: The feasibel for third optimization criteria at F = 0.6 mm.

6.3 Joining Titanium G2 to Low Carbon Steel Din: en 10131

Dissimilar joints to weld two different materials with entirely different physical and mechanical properties can be prepared by either fusion or solid state welding depending on the dissimilar materials and the desired properties for the application. In this section of this chapter, two dissimilar (Titanium G2 / Low Carbon steel 10131) materials with dimensions 75 x 125 x 1 mm as (ferrous /nonferrous materials) dissimilar joining were lap jointed, as exhibited in Fig. 4.16 (a), using CO_2 Laser welding. For these materials a pilot experiment was carried out by changing one parameter at a time to detect the operating range of the welding parameters under investigation. Visual inspection of the welded joints under the criteria of absence of observable welding defects and good weld seam and color (a grey seam color was obtained) were used to determine the ranges of operation of the parameters. The selected welding parameters for these dissimilar materials are: Laser power, welding speed and focus point position. Table 6.26 shows welding input variables and experiment design levels. The welding experiments were completed in the Mechanical School workshop following the Taguchi designed matrix in random

order. Molten titanium weld metal was totally protected from contamination by air. Also, hot heat-affected zones and root side of titanium welds were shielded until temperatures dropped below 800°F (427°C) using a shrouding system especially designed and produced in Mechanical School workshop for this purpose. The above dissimilar joints were produced by fusion laser welding methods as they produce joints with desired physical and mechanical properties.

The mechanical destructive tests (tensile shear strength) and residual stresses measurements were carried out in the jointed specimens. The residual stress results present a good result comparing to the yield stress of both materials. The maximum residual stress value was 91 MPa at level 1 (0.127 mm under the specimen surface). The maximum tensile shear test results were not more than 35 N/mm which is very low compared to the base materials tensile shear values. The interpretation of the tensile result is due to the titanium carbides compounds formed in welding pool during the welding process which are very brittle components. The achieved result indicates that the fusion (key-hole laser) welding is not a successful process for titanium / steel dissimilar welding.

Table 6.26: Process parameters and design levels used for titanium / steel

Variables	Code	Unit	Level 1	Level 2	Level 3	Level 4
Laser Power	**P**	**kW**	0.75	0.9	1.05	1.20
Welding Speed	**S**	**mm/min**	2500	3000	3500	4000
Focus	**F**	**mm**	-1.0	-0.67	-0.33	0.00

6.4 Chapter Summary

Heterogeneous steel–aluminum for overlap assembly components have been achieved by CO_2 laser welding. The laser welding process presents several advantages compared to the conventional assembly processes such as riveting or spot welding. Notably, the work speed is raised and the laser process can be automated and controlled, this agrees with results achieved by Mathieu et al. [178].

By completing a ‘‘Design of Experiment’’ inspired by Taguchi approaches, it was possible to find the best operating welding parameters. Under the optimal

conditions, the mechanical performances of the steel/aluminum assemblies were reached, fracture strengths superior to 317 N/mm for Al 6082 joints and 107 N/mm for Al 1050H24 joints, which are greater than the strength of base metal in both joints were achieved. In certain conditions, the fracture occurs in the heat-affected zone (HAZ) of the aluminum or in the steel sheet itself. The mechanical strength values were compatible with the specifications relative to these assemblies in the automotive industry. Residual stress distribution in aluminum plate at HAZ of the lap-welded joint was measured by means of by the hole-drilling method. The result shows that the highest residual stresses were at the level 1 and 2. Detailed AVONA analysis was conducting to those levels and mathematical models were developed in order to control and optimize welding parameters affects the residual stress distribution. The effect of individual welding parameter on the residual stress has been investigated in this study. A study of microstructures and microhardness was conducted and used to interpret the change in the mechanical properties of the welding operation. Fe–Al intermetallic compound phases were formed at the interface between the steel and the weld metal. The thickness and the composition of the intermetallic compound layer varied with weld heat input. Despite the formation of the intermetallic compound phases, the interface between steel and weld metal is not the weakest location of the joints. Tensile tests of the joints caused fractured in the Al HAZ, even when the intermetallic compound layer thickness exceeded 40 μm. Two optimization strategies were applied in this chapter, numerical optimization which is recommended when dealing with many responses and graphical optimization which is allows visual selection of the optimum welding conditions according to certain criterion. Operating welding cost per meter also was optimized through controlling welding parameters.

Taguchi optimization approach could be used to optimize any mechanical property individually or combine mechanical properties together to produce components for different engineering applications.

A similar welding process model for materials other than steel/aluminum dissimilar, such as aluminum alloys and stainless steel dissimilar or any other ferrous/nonferrous dissimilar materials, could be developed through the same approach as proposed here with same experimental procedure.

CHAPTER 7

7. RESULTS AND DISSUSSION OF DISSIMILAR NONFEROUS WITH NONFERROUS JOINED MATERIALS

In this chapter, welding of two different components dissimilar nonferrous materials is studied. Lap joint design and CO_2 laser welding process were applied as the joining process. The first joint component is aluminum 6082 / titanium G2 and the second jointed component is aluminum 5251H22 / titanium G2. Experiments for the joining of the dissimilar materials (nonferrous / nonferrous) in this chapter were performed using design of experiment and Taguchi approach with L-16 orthogonal arrays. Mathematical models for the responses of the jointed material were developed, analysed and verified.

7.1 Joining of Aluminum (6082) to Titanium G2

A dissimilar heterogeneous lap joint between two plates of Al 6082 and Ti G2, of dimensions (160 x 80 x 2 and 160 x 80 x 1) mm respectively, was made using the single pass laser welding process. The titanium plate was the upper plate and exposed to the laser beam to avoid the high reflectivity of aluminium. Before conducting the experiment to study the joint quality and develop the process models, pilot experiments were carried out by changing one parameter at a time to identify the operating range of the welding parameters used in the study. The criterion used to identify the operating range of the welding parameters involved a visual inspection of the welded joints using the principle of absence of observable welding defects and presence of a good weld seam. The selected welding parameters for these dissimilar materials are: Laser power, welding speed and focus point position. Table 7.1 shows the welding input variables and experiment design levels. The welding experiments were carried out in the Mechanical School workshop following the Taguchi designed matrix in random order generated by Design Expert software, as presented in Table 7.2. The welding pool geometry, mechanical destructive tests (tensile shear strength)

and cost per meter welded calculations were carried out in the jointed specimens and the results are presented in Table 7.2. Each presented result in Table 7.2 in each column is an average of at least of three readings.

Table 7.1: Process parameters and design levels used

Variables	Code	Unit	Level 1	Level 2	Level 3	Level 4
Laser Power	**P**	**kW**	0.675	0.850	1.025	1.200
Welding Speed	**S**	**mm/min**	2000	2333	2667	3000
Focus	**F**	**mm**	-1.0	-0.67	-0.33	0.00

Table 7.2: Welding input variables, experiment design levels, the welding pool geometry, tensile shear strength and cost per meter welding calculations.

Std	Run	P, kW	S, mm/min	F, mm	W_1, µm	L_1, µm	A_1, µm	Shear St, N/mm	Cost € / m
16	1	1.200	3000	-1	644	451	155.2	235.8	0.09
7	2	0.850	2667	0.00	392	362	114.1	114.2	0.10
15	3	1.200	2667	-0.67	619	354	171.8	180.2	0.10
5	4	0.850	2000	-0.67	317	267	71.3	114.6	0.13
6	5	0.850	2333	-1.00	341	257	67.7	174.3	0.11
1	6	0.675	2000	-1.00	508	362	131.8	131.2	0.13
12	7	1.025	3000	-0.67	527	312	88.6	374.4	0.09
14	8	1.200	2333	-0.33	449	407	144.3	235.4	0.12
8	9	0.850	3000	-0.33	394	215	33.7	349.2	0.09
11	10	1.025	2667	-1.00	252	491	122.7	237.9	0.10
3	11	0.675	2667	-0.33	597	165	63.3	89.6	0.10
4	12	0.675	3000	0.00	478	251	78.1	128.2	0.09
13	13	1.200	2000	0.00	474	281	155.2	248.2	0.14
9	14	1.025	2000	-0.33	422	297	31.2	165.0	0.13
10	15	1.025	2333	0.00	248	280	24.8	242.4	0.11
2	16	0.675	2333	-0.67	552	272	103.9	52.1	0.11

7.1.1 Development of Mathematical Models for the Welding Pool Geometry

The welded specimens were prepared for measuring the welding pool geometries and further metallographic examinations by polishing successively in 120, 240, 600, 800 and 1200 SiC paper polishing, followed by a final disc polishing using 3 μm, 1 μm diamond suspension and finished with a SiO_2 suspension to a mirror-like surface aspect. The titanium side of the weldment was etched in Reagent consisting of (10 ml HF and 5 ml HNO_3 in 85 ml of water), and the rest of the regions of the weldment were etched with Keller's reagent (1% HF, 1.5% HCl, 2.5% HNO_3 and H_2O solution). The measured results of welding pool area for each sample are presented in Table 7.2. Fig. 7.1 (a, b, c and d) shows the effect of the welding parameters and the variation on the total weld pool (fusion area) 'A_1' at aluminum plate only, welding widths at the specimen surface of aluminium 'W_1' and welding widths at the penetration of welding depth in aluminum plate 'L_1' of some experiments selected from Table 7.2.

The fusion zone dimensions in the aluminum plate were measured by using the transverse sectioned specimens, optical microscope and image analysis software. The measured responses are listed in the same Table 7.2. Design Expert 7 software was used for analysing the measured responses. The fit summary output indicates that the quadratic models which are developed by the software are statistically significant for the prediction of the responses (W_1 and L_1); therefore, they will be used for further analysis. It has been seen from the achieved results that the welding pool geometry, shape and penetration are controlled by the rate of heat input, which is a function of laser power and welding speed. Focusing position has also a strong effect on the responses.

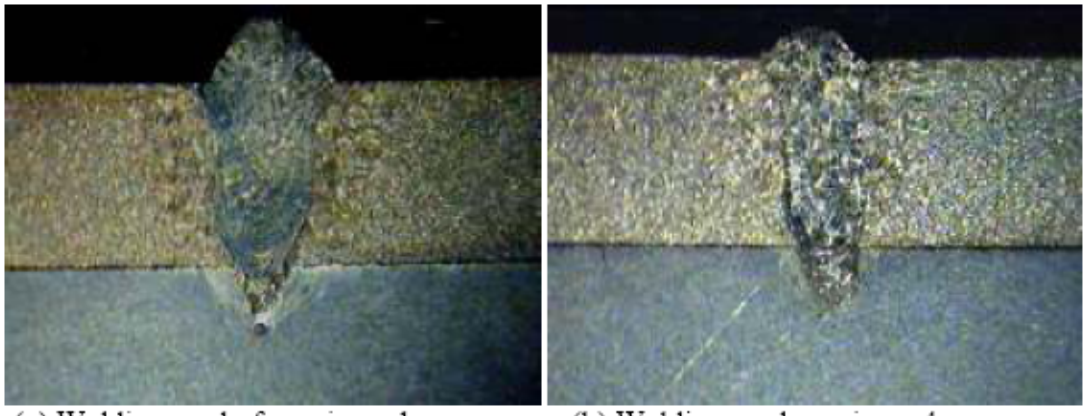

(a) Welding pool of specimen 1 (b) Welding pool specimen 4

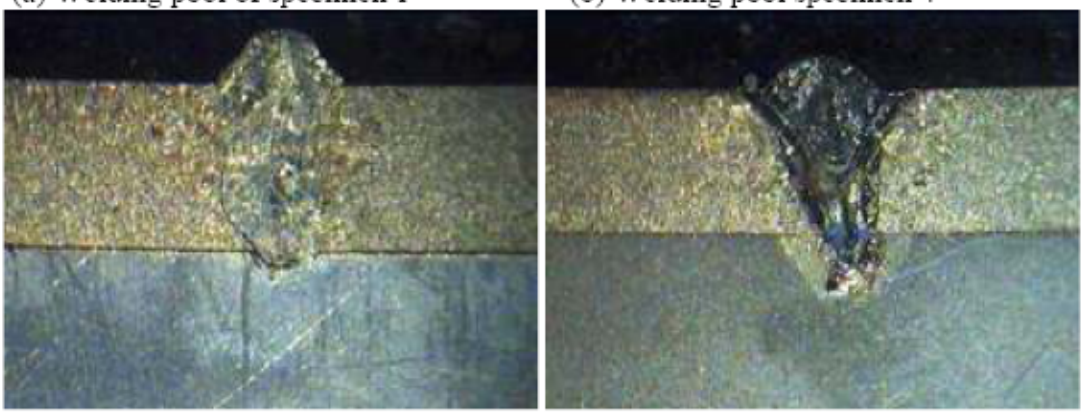

(c) Welding pool specimen 8 (d) Welding pool specimens 14

Figs. 7.1 (a, b, c and d): Exhibit the effect of the welding parameters and the variation on the total weld pool dimensions.

7.1.1.1 Analysis of variance

The test for significance of the regression model and the test for significance on individual model coefficients were performed using Design Expert 7 software. The backward elimination regression method was applied and exhibited in ANOVA Tables (7.3 and 7.4) for the reduced the suggested quadratic models. Table 7.3 and Table 7.4 summarize the analysis of variances of the responses and show the significant models. The same tables also show the other adequacy measures R^2, adjusted R^2 and adequacy precisions. All adequacy measures were close to 1, which is reasonable and indicates an adequate model. The adequate precision compares the range of the predicted value at the design points to the average predicted error. In this study the values of adequate precision for the W_1 and L_1 are significantly greater than 4. The adequate precision ratio above 4 indicates adequate model discrimination. The

developed quadratic models in terms of coded factors and actual values are exhibited in Eqs. 7.1 to 7.4.

Final Equation in Terms of Coded Factors:

$W_1 = 381.50 + 5.92*P + 46.35*S - 22.95*F + 200.81*P^2 - 75.94*F^2$ **…(7.1)**

Final Equation in Terms of Actual Factors:

$W_1 = 2591.086 - 5441.714*P + 0.093*S - 349.65*F + 2914.286*P^2 - 303.75*F^2$ **…(7.2)**

Final Equation in Terms of Coded Factors:

$L_1 = 279.16 + 60.30*P + 8.32*S - 21.60*F + 44.13*P*S + 62.72*F^2$ **…(7.3)**

Final Equation in Terms of Actual Factors:

$L_1 = 851.344 - 610.87*P - 0.299*S + 207.682*F + 0.336*P*S + 250.875*F^2$ **…(7.4)**

Table 7.3: ANOVA for response 'W_1'

Source	Sum of Squares	df	Mean Square	F_v Value	p-value Prob. > F_v	
Model	169764.1	5	33952.81	6.068453	0.0078	Significant
P	312.05	1	312.05	0.055773	0.8181	
S	19096.2	1	19096.2	3.413101	0.0944	
F	4681.8	1	4681.8	0.836787	0.3818	
P^2	127449	1	127449	22.77921	0.0008	
F^2	18225	1	18225	3.25739	0.1013	
Residual	55949.7	10	5594.97			
Cor. Total	225713.8	15				
R-Squared = 0.7521			Adeq. Precision = 6.799			
Adj. R-Squared = 0.6282						

Table 7.4: ANOVA for response 'L_1'

Source	Sum of Squares	df	Mean Square	F_v Value	p-value Prob. > F_v	
Model	69298.46	5	13859.69	3.34876	0.0491	Significant
P	32320.8	1	32320.8	7.809308	0.0190	
S	616.05	1	616.05	0.148849	0.7077	
F	1459.354	1	1459.354	0.352607	0.5658	
PS	3385.314	1	3385.314	0.817955	0.3870	
F^2	12432.25	1	12432.25	3.003863	0.1137	
Residual	41387.54	10	4138.754			
Cor. Total	110686	15				
R-Squared = 0.6261			Adeq. Precision = 6.842			
Adj. R-Squared = 0.4391						

For the response W_1 the developed model, the analysis of variance indicates that the welding speed 'S' and focus position 'F' are the stronger welding parameters affecting the responses. Focus position 'F' has a greater affect on the response W_1 than laser power 'P'. The W_1 model indicates that the studied parameters (S, F) significantly affect the response. For the response L_1 the developed model, the analysis of variance indicates that the laser power 'P' and focus position 'F' are the stronger welding parameters affecting the responses. Focus position 'F' has a greater affect on the response W_1 than welding speed 'S'. The L_1 model indicates that the studied parameters (P, F) significantly affect the response. The L_1 model indicates that the welding parameters have interactions between P and S exhibited in Fig. 7.2. The figure exhibits the interaction of the welding speed with laser power at focus position F= -0.5 mm.

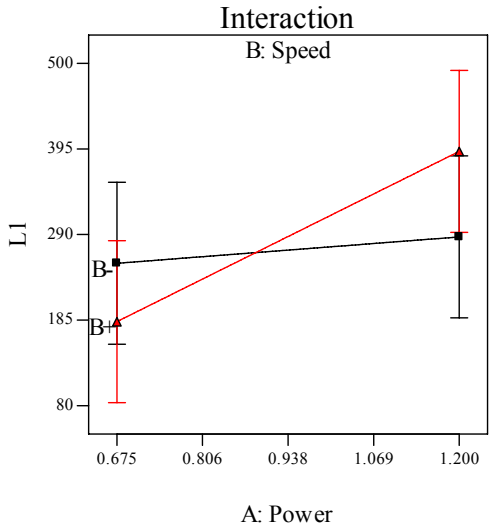

Fig. 7.2: Interactions between the welding parameters (P, S) with respect to the depth of penetration response at F = -0.5 mm.

7.1.1.2 Model validation

The aim of this step is to predict and verify the improvement of the response using the optimal levels of the welding process parameters. Figs. 7.3, 7.4 show the relationship between the actual and predicted values of W_1 and L_1, respectively. These figures indicate that the developed models are adequate because the residuals

in prediction of each response are negligible, since the residuals tend to be close to the diagonal line.

Furthermore, to verify the satisfactoriness of the developed models, three confirmations experiments were carried out using new test conditions at different parameters conditions, obtained using the Design-Expert software and the developed mathematical models. The values of W_1 and L_1 for validation experiments were calculated using Design-Expert software. Table 7.5 summarizes the experimental conditions, the actual experimental values, the predicted values and the percentages of absolute errors. It could be concluded that the models developed could predict the responses with a very small errors. W_1 and L_1 were greatly improved through this optimization.

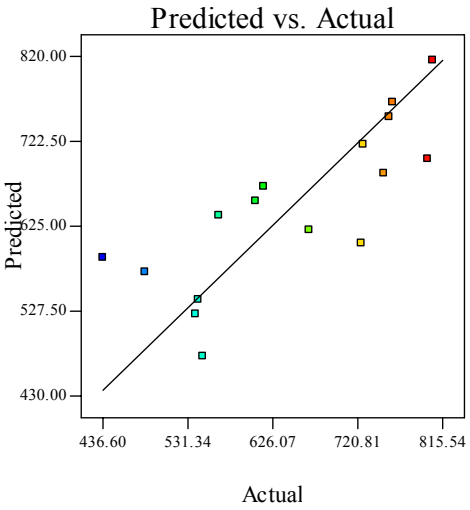

Fig. 7.3: Exhibited predicted values of the W_1 vs. actual measured values.

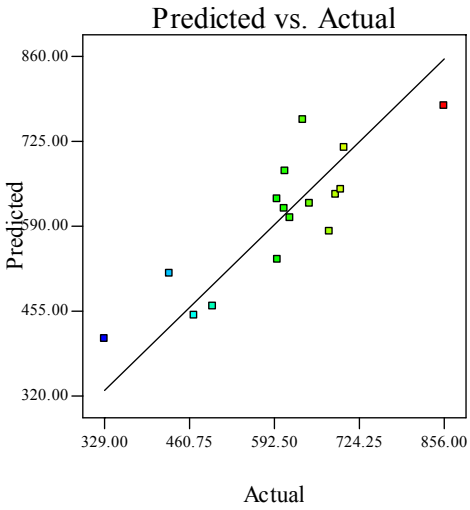

Fig. 7.4: Exhibited predicted values of depth of penetration L_1 vs. actual measured values.

Table 7.5: Confirmation experiments of the responses (W_1 and L_1)

Exp. No	P, kW	S, mm/ min	F, mm	W_1, mm		$\|E\|$ %	L_1, mm		$\|E\|$ %
				Act.	Pred.		Act.	Pred.	
1	1.134	2000	0.00	382	408	6.37	299	327	8.56
2	1.134	2500	0.00	501	399	25.56	323	365	11.51
3	0.871	3000	-1.00	388	386	0.52	401	345	16.23

Act* = Actual; Pred.* = Predicted

7.1.1.3: Effect of the parameters on responses

The reason for predicting the welding pool geometry is to develop a model which would include the optimization step.

- **Welding Pool Width at the Work Piece surface (W_1).**

The results and the model obtained for the response indicate that the S and F are the most important factors affecting the W_1 value. An increase in S leads to a decrease in W_1 and the increase of F leads to increase in W_1. This is due to the laser beam traveling at high speed over the welding line when S is increased. Therefore, the heat input decreases leading to less volume of the base metal being melted, consequently the width of the welded zone decreases. Moreover, a defocused beam, which is a wider laser beam, results in spreading the laser power over a wide area. Therefore, a wide area of the base metal will be melted leading to an increase in W_1 or vice versa. The result shows also that P contributes a secondary effect in the response width dimensions. Increasing P results in a slight increase in W_1, due to the increase in the power density. Fig. 7.5 shows contour plots for the effect of the process parameters on the W_1 width. Fig. 7.5 illustrates the relationship between S and P with their impact on the welding pool width at the surface of the aluminum plate (W_1) at F = - 0.5 mm.

- **Welding Pool Width at the Middle of the Work Piece (L_1)**

The results and the model obtained for the response indicate that the P and F are the most important factors affecting the W_1 value. An increase in P leads to an increase in W_1 and the increase in F leads to increase in W_1. This is due to the fact that an increase in the amount of laser power P that is transfer to the work piece leads to an increase in the response. Therefore, the heat input increases leading to an increase in the amount that the base metal melts, consequently the penetration of the welded zone increases. Moreover, a defocused beam, which is in a wider laser beam, results in spreading the laser power over a wide area. Therefore, a wide area of the base metal will be melted leading to an increase in L_1 or vice versa. The result also shows that S contributes in a secondary effect in the response width dimensions. S is inversely proportional to the heat input. Increasing S results in a slight decrease in

L_1, this is due to the decrease in the heat input. Fig. 7.6 shows contour plots for the effect of the process parameters on the L_1 width. Fig. 7.6 illustrates the relationship between S and P with their impact on the welding pool depth of the aluminum plate (L_1) at F = -0.5 mm.

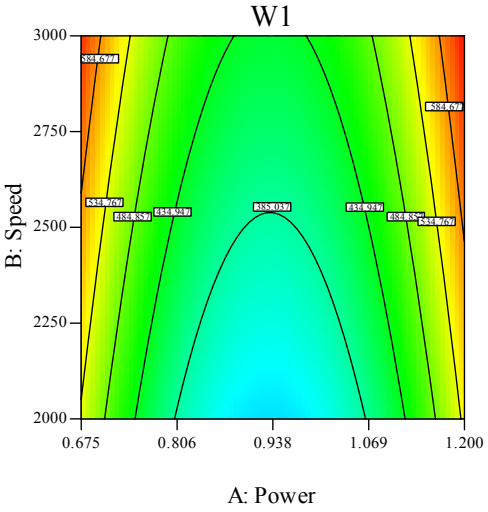

Fig. 7.5: Contour graphs exhibiting the effect of P, S parameters at F = -0.5 mm on the response W_1

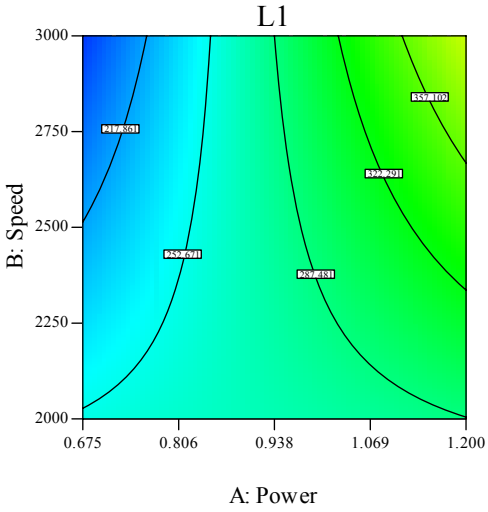

Fig. 7.6: Contour graphs exhibiting the effect of P, S parameters at F = -0.5 mm on the response L_1

7.1.2 Development of a Mathematical Model for Tensile Strength

A lap joint was applied for joining the nonferrous / nonferrous dissimilar plates, mentioned above, together. The experiments were carried out according to the design matrix given in Table 7.2. They were performed in random order to avoid any systematic error. The tensile shear strength samples, as exhibited in Figs. 4.16 (a, b), mentioned in chapter four, were tested at room temperature (20 ºC). Tensile tests were carried out at a constant travel speed of 1 mm/min, with stress applied in the sheet plane in a perpendicular direction to the weld line. Since the welding penetration of the jointed sheets are not the same, the ultimate strength is obtained by dividing the force at fracture of the specimen by the length of the weld line (6 mm) and termed as resistance (N/mm). The rupture mainly occurs in the heat-affected zone (HAZ) of the aluminum or in the welding pool. The accelerated growth of the

grain size due to heating and fast cooling in the HAZ and WZ led to deterioration of the tensile strength of the weldment.

7.1.2.1 Analysis of the result

The raw data, the average tensile shear strength test results are shown in Table 7.2. To analyze the effects of the welding parameters in detail, ANOVA was conducted; these results are shown in Table 7.6. In the ANOVA table, Table 7.6, the F_v is used to test the significance of a factor by comparing model variance with residual (error) variance. As mentioned in the previous chapter the high F_v value for a parameter means that the effect of the parameter on the characteristics is large. The average tensile shear tests appear to be mainly affected by the laser power and welding speed 'S' as shown in Table 7.6. The result in Table 7.6 shows that the F_v value in the process obtained for laser power 'P' equal to 48.6 which indicates that the parameter has a strong effect on the process. The F_v value for the welding speed 'S' was equal to 62.1, which indicates that the welding speed has the strongest effect on the process. The F_v value for the focus 'F' was equal to 0.007, which indicates that the focus position has insignificant effect on the process. Adequate Precision compares the range of the predicted values at the design points to the average prediction error. For this model it was equal to 10.595, as shown in Table 7.6. The same table also shows the other adequacy measures R^2 and Adjusted R^2. All the adequacy measures indicate that an adequate model has been obtained. The final mathematical model for predicting the tensile strength of a titanium G2 / aluminum 6082 dissimilar joint in terms of coded factors and actual factors as determined by Design Expert software are shown below in Eqs 7.5 and 7.6.

Final Equation in Terms of Coded Factors:

Tensile Strength = 196.02 +66.12*P +125.97*S -0.80*F +134.74*P*F -66.28*P^2 +59.13*S^2 **…(7.5)**

Final Equation in Terms of Actual Factors:

Tensile Strength = -519.319 +2568.788*P -0.931*S -964.051*F +1026.623*P* F -961.905*P^2 +2.365E-004*S^2 **…(7.6)**

Table 7.6: ANOVA for selected tensile shear model

Source	Sum of Squares	df	Mean Square	F_v Value	p-value Prob. > F_v	
Model	113465.7	6	18910.95	23.65587	< 0.0001	Significant
P	38866.81	1	38866.81	48.61881	< 0.0001	
S	49651.84	1	49651.84	62.10991	< 0.0001	
F	5.629784	1	5.629784	0.007042	0.9350	
PF	31560.11	1	31560.11	39.47881	0.0001	
P^2	13884.69	1	13884.69	17.36848	0.0024	
S^2	11048.35	1	11048.35	13.82047	0.0048	
Residual	7194.771	9	799.419			
Cor. Total	120660.5	15				
R-Squared = 0.9404			Adeq. Precision = 16.795			
Adj. R-Squared = 0.9006						

7.1.2.2 Validation of the model

Fig. 7.7 shows the actual response versus the predicted response for tensile shear testing result. From this Fig., it can be seen that the model adequately describes the response within the limits of the factors being investigated herein, as the data points are close to the diagonal line. Furthermore, three extra confirmation experiments were carried out using different test conditions, which are presented in Table 7.7 along with the resulting percentage error. It can be noticed that the percentage error is equal to or less than 10 %. The obtained tensile shear stress after laser welding in some cases is greater than the base metals value especially when compared to the aluminum side.

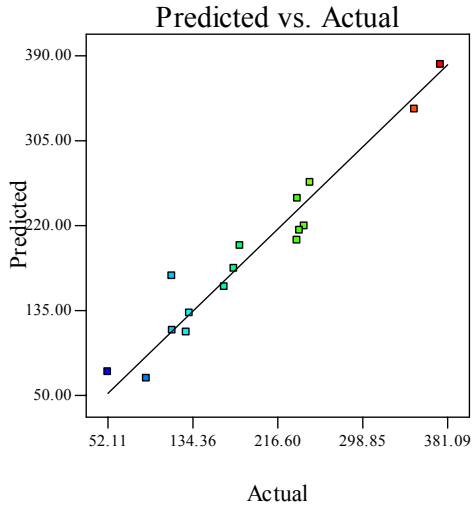

Fig. 7.7: Predicted Vs Actual for tensile shear strength.

Table 7.7: Confirmation experiments of the responses compared with model results.

Exp. No	P, kW	S, mm/ min	F, mm	Tensile strength, MPa		$\|E\%\|$
				Actual	predicted	
1	1.134	2000	0.00	271	256	5.86
2	1.134	2500	0.00	339	308	10
3	0.871	3000	-1.00	378	395	4.3

7.1.2.3 Effect of process parameters on the response:

1) Welding speed**:** It is evident from the results that the welding speed is the most significant factor associated with the response, as shown in contour graph Fig. 7.8. The highest tensile strength value was observed to be at a speed of 3000 mm/min as presented in Table 7.2.

2) Laser power**:** The results indicate that the laser power has also a very strong effect on the tensile strength of the laser-welded joint, as shown in Fig. 7.8. The model developed indicates that there is an interaction between the two welding parameters the laser power and the focus position. The interaction between the focus position and laser power is exhibited in Fig 7.9.

3) Focus point position**:** It can be seen that the focus position has no obvious effect on the response within the parameter range domain applied. Changing the

focus point position will not affect the response. Fig.7.10 shows a 3D graph of the effect of F and P on the response at S = 2700 mm/min.

To compare the effect of all the considered welding parameters on the tensile strength at a midpoint position in the design space, a perturbation plotted is exhibited in Fig.7.11. The response is plotted by changing only one parameter over its range while holding the other parameters constant.

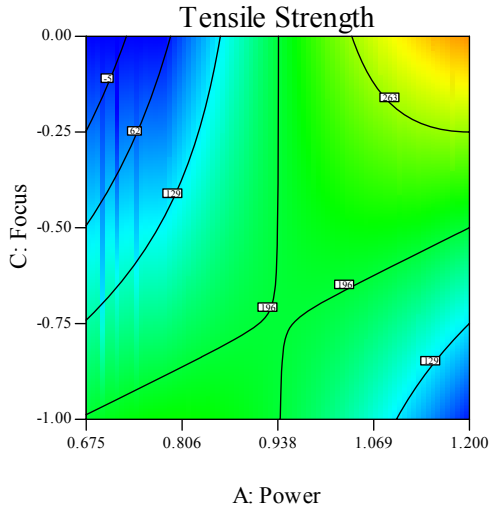

Fig. 7.8: Contour graph shows the effect welding parameters At S = 2700 mm/min.

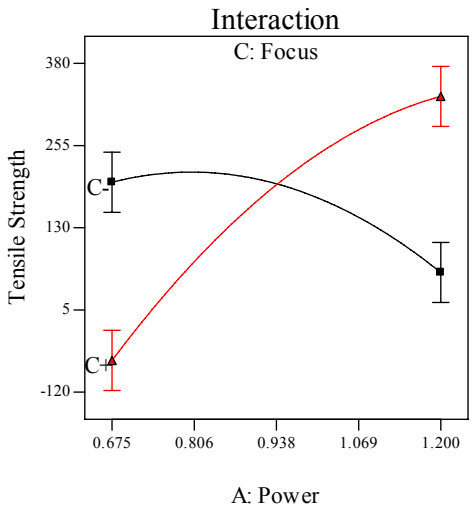

Fig 7.9: Shows the interaction between the laser power and focus at S = 2500 mm/min.

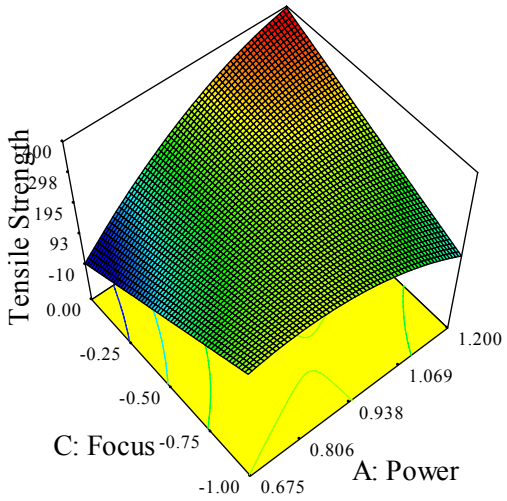

Fig. 7.10: 3D graph shows the effect of P and F At S = 2700 mm/min

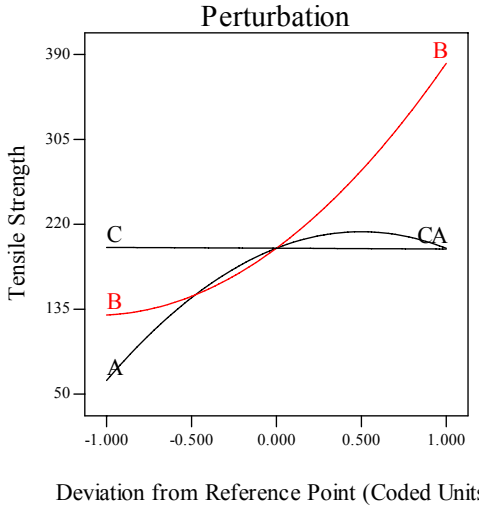

Fig.7.11: Perturbation plots exhibiting the effect of welding parameters on the tensile strength, where: A = power, B = Speed and C = Focus.

7.1.3 Operating Cost Modeling

The operating costs for joining the above mentioned dissimilar materials were calculated using Eq. 4.13. The mathematical model was developed to minimize the operating cost. The same procedure was followed to check the model adequacy. The analysis results are shown in Table 7.8 for the reduced quadratic model which is suggested by the software for the received welding operating cost results. The same table shows the other adequacy measures R^2, Adjusted R^2 and Predicted R^2. All the adequacy measures indicate an adequate quadratic model. The adequate precision of 409 indicates adequate model discrimination. The developed quadratic mathematical model in terms of coded factors and actual values are exhibited in Eqs 7.7 and 7.8.

Final Equation in Terms of Coded Factors:

$$Cost = 0.11 + 2.865E\text{-}003*P - 0.022*S - 5.812E\text{-}004*P*S + 4.431E\text{-}003*S^2 \quad \textbf{…(7.7)}$$

Final Equation in Terms of Actual Factors:

$$Cost = 0.30589 + 0.021984*P - 1.28418E\text{-}004*S - 4.42857E\text{-}006*P*S + 1.77232E\text{-}008*S^2 \quad \textbf{…(7.8)}$$

Table 7.8: ANOVA for operating welding cost

Source	**Sum of Squares**	**df**	**Mean Square**	**F_v Value**	**p-value Prob. > F_v**	
Model	0.00443	4	0.001107	23396.23	< 0.0001	Significant
P	7.29E-05	1	7.29E-05	1540.961	< 0.0001	
S	0.004293	1	0.004293	90697.88	< 0.0001	
PS	1.67E-06	1	1.67E-06	35.247	< 0.0001	
S^2	6.2E-05	1	6.2E-05	1310.815	< 0.0001	
Residual	5.21E-07	11	4.73E-08			
Cor. Total	0.00443	15				
R-Squared = 0.9999			Adeq. Precision = 408.5			
Adj. R-Squared = 0.9998						

7.1.4 Microharness and Microstructure Studies

7.1.4.1 Microstructure of dissimilar jointed materials

The same specimens prepared for weld pool measurements of Al6082 / Ti G2 and mentioned above in section 7.1.1 were used for microhardness and microstructure studies. The microstructure of titanium G2 is exhibited in Fig. 7.12 (a). Different grain textures can be clearly observed in Figs. 7.1(a-d) between the upper WZ and the lower WZ due to the diversity of heat transfer direction. When welding started but before penetration, the heat transferred along cross-direction and depth direction, consequently generated the columnar grains whose orientation was perpendicular to the boundary between the fusion zone and the HAZ in titanium plate as it exhibited in Figs. 7.12 (b and c). The input heat mostly transferred along the cross-direction, and thus generated coarse equiaxed grains. No obvious second phase was observed in the WZ at upper part of welding pool and just the solidification crystals were apparent. The microstructure feature is mainly caused by the different weld thermal cycles at two different zones. The optical microscopy micrograph exhibited in Fig. 7.12 (c) shows that the HAZ in the vicinity of molten boundary of titanium consists of mainly ά martensite. The cooling rate which is estimated to be 10^4 °C/s [4] is responsible for the martensite structure formation. The martensitic structure in WZ and HAZ is the main reason for improving the tensile strength of the welded titanium components. The circular ά in the HAZ was attributed to rapid cooling of the weld metal. The grain size of the β matrix has been increased greatly by the thermal cycle of the welding as it exhibited in Fig. 7.12(b). The laser titanium–aluminium dissimilar joining resulted in a complex and heterogeneous microstructure composed of columnar grains and “white solute bands” in the base of welding pool. The liquation zones, evident in aluminium partially melted zones are due to the presence of low fusion point elements (magnesium) at the grain boundaries. Also, it was noted that the reduction in porosity that may be attributed to the following two main reasons:

1. Increased average power (and hence power density) at the specimen. The increased power density at the specimen maintained the stable keyhole during the

welding process. The keyhole stayed open during the welding, and the solidification time was increased, allowing the pores to escape on both sides of the seam.

2. Improved gas shielding system design with a coaxial argon shield on the top and bottom of the welded specimen.

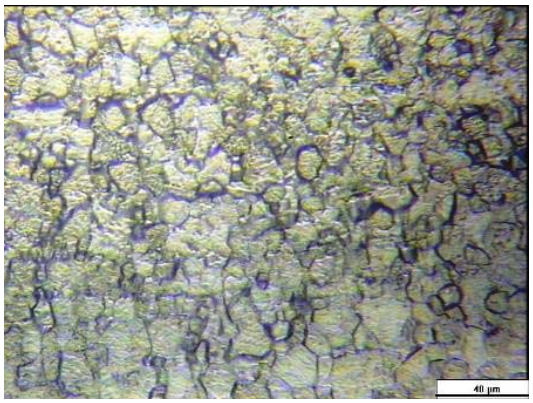

Fig. 7.12(a): Titanium G2 BM

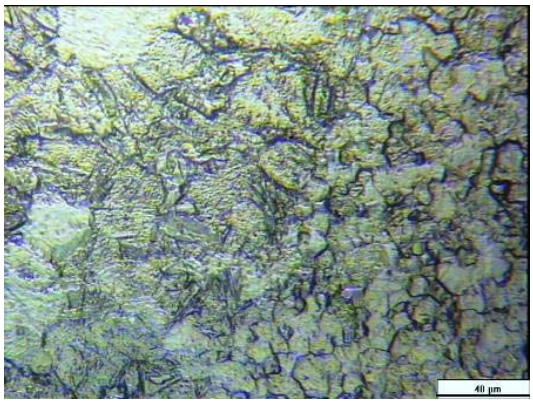

Fig. 7.12(b): Titanium G2 BM, HAZ

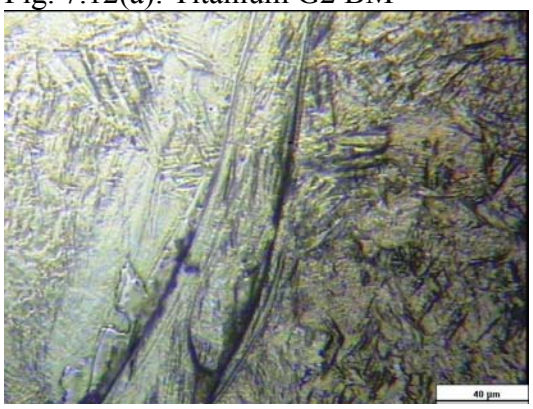

Fig. 7.12(c): Titanium G2 WZ, HAZ

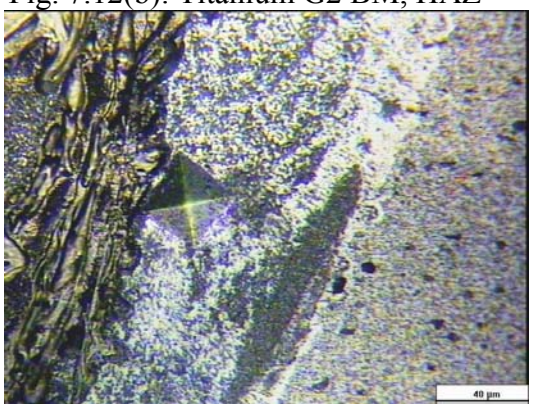

Fig. 7.12(d): A6082 –WZ, HAZ and BM

Figs. 7.12 (a-d): The redistribution of elements in the fusion zone of a lap weld joining aluminium 6082 to titanium G2.

7.1.4.2 Microhardness of dissimilar jointed materials

The specimens selected for microhardness studies were based on heat input calculation (P x S). Vickers microhardness measurements with a 50 g loading force test were applied to the selected specimens shown in Fig 7.1. For each specimen, three different positions were subjected to the study (BM, HAZ, and WZ) for each side of the dissimilar joint as presented in Table 7.9 and exhibited in microhardness profile of the dissimilar joint Fig. 7.13. The data on the liquid titanium to liquid aluminium interaction during high solidification rate key-hole laser welding is very

limited. In the HAZ of the titanium side, there was an increase in the microhardness (255 – 309 Hv) and a dramatic increase in WZ up to (418- 509 Hv) as presented in Table 7.9. This could be related to the quenching effect resulting in a martensitic ά microstructure.

Table 7.9: Microhardness test result of dissimilar ferrous to nonferrous materials

Sp No.	**Al 6082**			**Ti G2**		
	BM	**HAZ**	**WZ**	**WZ**	**HAZ**	**BM**
1	139.45	126.06	537.4	503.96	309.32	224.34
4	129.63	139.69	430.69	418.06	273.41	241.76
14	131.43	150.24	669.4	504.27	255.62	219.93
15	96.59	135.37	308.77	536.00	280.78	241.59

Compared to the hardening effect observed in the weld–aluminium interfaces by intermetallic compound generation, the titanium–weld interfaces were not expected to be the weakest point of the assemblies. The fractures were mostly occurred at the aluminum WZ and referring to the microhardness result measured and presented in Table 7.9. Fig 7.13 presents the microhardness profile the aluminum WZ (up to 670 HV). The fracture could be interpreted as being due to a loss in the ductility of aluminium and due to the brittle components formed during solidification stage in WZ at aluminium side.

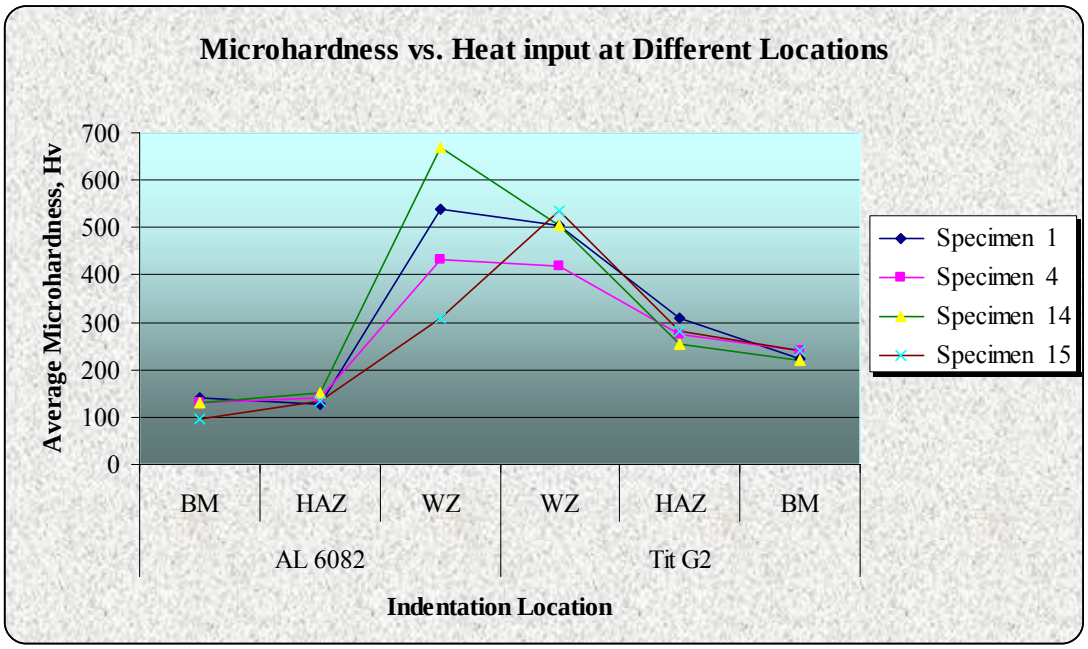

Fig. 7.13: The Microhardness profile of the dissimilar joint (Al 6082 / Ti G2).

7.1.5 Models (multiple –response) Optimization

7.1.5.1 Numerical optimization

The numerical multiple-response optimization criterion is to reach maximum tensile shear strength and minimum welding pool geometry, improve penetration, minimum welding operating cost with minimum laser power and maximum welding speed while focus position was kept in range.

The optimization criteria was chosen and presented in Table 7.10. In the optimization criteria all the parameters received the same importance (+++) and same weight (1) as per the Design Expert software default. The optimization result presented in Table 7.10 is selected from one of more than ten different optimum result calculated by the software.

The effect of the selected criteria on the optimization result is obvious in Table 7.10. For example by applying the decided criteria the tensile strength (resistance) value will reach up to 395 N/mm. If the target is only to maximize the tensile strength regardless of the other parameters then the response value will be greater than the received values and this is true for each response individually optimized. The mechanical strength value obtained by this method of optimization is compatible

with the specifications relative to these assemblies in the automotive industry. The welding geometries were not assigned high weight or high important since they are not a direct target for the optimization, they indirectly affect the welding quality. The welding cost was significantly reduced up to 38% in all the decided criteria compared to the values presented in Table 7.2 in which reached a maximum of 14 cent /m. Also, the welding speed is maximum (3000 mm/min), in the optimization criteria which leads to increased production rate.

7.1.5.2 Graphical optimization

The graphical optimization displays the area of feasible response values in the factor space. From the overlay plot in Fig. 7.14 it is obvious that the graphical optimization allows visual selection of the optimum welding conditions according to certain criterion. The result of the graphical optimization are the overlay plots, these type of plots are extremely practical for quick technical use in the workshop to choose the values of the welding parameters that would achieve certain response value for this type of dissimilar materials. The yellow /shaded area on the overlay plot in Fig. 7.14 is the region that meets the proposed criteria.

Table 7.10: Shows three optimization criteria with the optimization results using numerical multiple-response.

Welding Parameters	Power, kW		Speed, mm/min		Focus, mm		W_1, µm		L_1, µm		Tensile Strength		Cost € / m		D*.
Goal	Min.		Max.		In range		Min.		Max.		Max.		Min.		
Criteria	Wt.	Imp.	Wt.	Imp.	Wt.	Imp.	Wt.	Imp.	Wt.	Imp.	Wt.	Imp.	Wt.	Imp.	
First Criteria	1	+++	1	+++	-	-	1	+++	1	+++	1	+++	1	+++	
Result	0.871		3000		-1.00		386.2		345.4		395		0.09		0.704

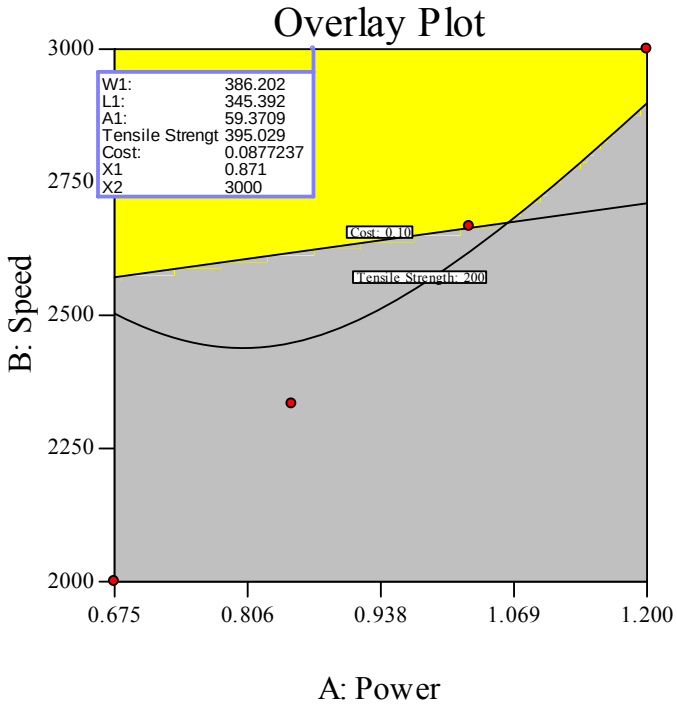

Fig. 7.14: The feasible solution in yellow shaded area for optimisation criteria at F = -1 mm

7.2 Joining of Aluminum (5251 H22) to Titanium G2

Two plates of dissimilar materials mentioned above with their chemical compositions and mechanical properties presented in Tables (4.2 to 4.5) are welded together using the CO_2 laser welding process. Lap joint design was applied to joint the plates of aluminum and titanium with dimensions of (160 x 80 x 1.5 and 160 x 80 x 1) mm respectively. The titanium plate was positioned above the aluminum plate in direct contact with laser beam during the welding process. A heterogeneous single pass was carried out to joint the two plates. Pilot experiments were applied to determine the input welding parameters range. The pilot experiments were carried out by changing one parameter at a time to identify the operating range of the welding parameters under the study.

The criterion for identification of the operating range of the welding parameters was the approval by visual inspection of the welded joints under the principle of absence of observable welding defects and the presence of a good weld

seam. The selected welding parameters for these dissimilar materials are presented in Table 7.11. The same table shows welding input variables and experiment design levels. The welding experiments were carried out in the Mechanical School workshop following the Taguchi design matrix generated by Design Expert V7 software, presented in Table 7.12, in random order. An L16 orthogonal array with three columns and 16 rows was used. Sixteen experiments were required to study the welding parameters using an L16 orthogonal array. Residual stresses, mechanical destructive tests (tensile shear strength) and cost per meter welded calculations of the jointed specimens were carried out and the results are presented in Table 7.12.

Table 7.11: Process parameters and design levels used

Variables	**Code**	**Unit**	**Level 1**	**Level 2**	**Level 3**	**Level 4**
Laser Power	**P**	**kW**	0.9	1.05	1.200	1.35
Welding Speed	**S**	**mm/min**	1600	1767	1933	2100
Focus	**F**	**mm**	-1.0	-0.67	-0.33	0.00

Table 7.12: Welding input variables, experiment design levels, the residual stresses, tensile shear strength and cost per meter welding calculations.

Std	Run	P, kW	S, mm/min	F, mm	Residual Stresses, MP	Shear St, N/mm	Cost € / m
4	1	0.9	2100	0	19	181	0.13
13	2	1.35	1600	0	4	38	0.17
7	3	1.05	1933	0	2	164	0.14
1	4	0.9	1600	-1	20	135	0.16
2	5	0.9	1767	-0.67	2	172	0.15
6	6	1.05	1767	-1.00	6	137	0.15
11	7	1.2	1933	-1.00	17	99	0.14
14	8	1.35	1767	-0.33	49	98	0.16
12	9	1.2	2100	-0.67	45	112	0.13
16	10	1.35	2100	-1.00	27	143	0.13
10	11	1.2	1767	0.00	69	84	0.15
3	12	0.9	1933	-0.33	22	164	0.14
5	13	1.05	1600	-0.67	1	130	0.17
9	14	1.2	1600	-0.33	19	120	0.17
15	15	1.35	1933	-0.67	11	135	0.14
8	16	1.05	2100	-0.33	33	147	0.13

7.2.1 Development of Mathematical Models for Residual Stresses

The measurement procedure explained in paragraph 4.5.3 in the previous chapter was used to evaluate the residual stress resulting from the welding process in order to control and optimize the selected laser welding parameters. The strain gauge was bonded to the surface of the specimen (aluminium side) in the HAZ where the present of the critical (serious) residual stresses in the joined component. A blind hole of incremental depth of 1.016 mm was drilled at (1 to 2) mm from the centre welded line in the middle of the specimen as presented in Fig.4.14 (a).

Residual stress was calculated and evaluated through the depth of the welded joint at gradual levels to get a clear indication of the effect of welding parameters on the distribution of the residual stress through the depth of HAZ. The depth levels at HAZ in aluminum plat at which the micro-strains were measured are presented in Table 6.3 in the previous chapter. The calculated stresses (σ_i) at each level, expressed in Table 7.13, were considered as the responses and analyzed separately to predict the effect of

the welding parameters through the specimen depth. The result analysis using Design Expert shows that the residual stress models developed at the first and the second levels are insignificant while the residual stress models developed for the other three levels are significant. However the result presented in Table 7.13 indicates that the residual stress created due to laser welding are not serious and may not affect the joints. The maximum residual stress value achieved at σ_1 was 69 MPa and was recorded at experiment run number 10. Comparing to the base materials yield and ultimate stress, the measured residual stresses values were not serious affecting the joints. The achieved results were indicating that further analysis and investigations will not necessary.

Table 7.13: Shows the experimental calculated for Al 6082 residual stresses in MPa.

Std	σ_1	σ_2	σ_3	σ_4	σ_5
1	20	3	13	7	6
2	2	8	14	10	7
3	22	9	9	7	7
4	19	13	9	1	0
5	1	15	18	19	16
6	6	1	2	7	7
7	2	6	6	6	5
8	33	0	2	3	1
9	19	35	23	11	11
10	69	57	42	19	12
11	17	3	11	6	5
12	45	29	15	9	8
13	4	11	18	13	10
14	49	44	43	27	20
15	11	2	17	12	9
16	27	32	22	14	11

7.2.2 Development of a Mathematical Model for Tensile Strength

Samples for tensile shear testing were cut as shown in Fig 4.16 (a, b) and prepared from the tensile shear testing following the explained procedure in chapter 4 in the paragraph 4.6.2. The achieved results, presented in Table 7.12, were performed in random order to avoid any systematic error and they were tested at room temperature

(20 ºC). It was noted that during the test the fracture occurred within the welding pool regardless of the input welding parameters. The rupture of the joint was brittle-like fracture, implying that the welding process caused the ductility of the alloy to deteriorate at the WZ.

7.2.2.1 Analysis of the result

The raw data, the average tensile shear strength test results are shown in Table 7.12. To analyze the effects of the welding parameters in detail, ANOVA was conducted; these results are shown in Table 7.14. The ANOVA results are presented in Table 7.14; the F_v is used to test the significance of a factor by comparing model variance with residual (error) variance, which is calculated by dividing the model mean square by the residual mean square. As mentioned in the previous chapter the high F_v value for a parameter means that the effect of the parameter on the characteristics is large. The average tensile shear tests appear to be mainly affected by the laser power and focus position as shown in Table 7.14. The result in Table 7.14 shows that the highest F_v value in the process was obtained for laser power 'P' equal to 29.20. The F_v value for the focus position 'F' was equal to 1.0, which indicates that the 'F' has a relatively small effect on the process. The F_v value for the welding speed 'S' was not available in the ANOVA analysis, which indicates that the speed has an insignificant effect on the process. Adequate Precision compares the range of the predicted values at the design points to the average prediction error. For this model it was equal to 10.595, as shown in Table 7.14. Other adequacy measures R^2 and Adjusted R^2 are presented in the same table. All the adequacy measures indicate that an adequate model has been obtained. The final mathematical model for predicting the tensile strength of a dissimilar joint in terms of coded factors and actual factors as determined by Design Expert software are shown below in Eqs 7.9 and 7.10.

Table 7.14: ANOVA for tensile strength response

Source	Sum of Squares	df	Mean Square	F_v Value	p-value Prob. > F	
Model	16250.2	3	5416.74	16.3743	0.0002	Significant
P	9660.44	1	9660.44	29.2026	0.0002	
F	331.202	1	331.202	1.00119	0.3368	
PF	6258.58	1	6258.58	18.9191	0.0009	
Residual	3969.69	12	330.807			
Cor. Total	20219.9	15				
R-Squared = 0.8037			Adeq. Precision = 15.079			
Adj. R-Squared = 0.7546						

Final Equation in Terms of Coded Factors:

Tensile Strength = 128.65 -32.97*P -6.10*F -35.60*P* F

…(7.9)

Final Equation in Terms of Actual Factors:

Tensile Strength = 465.375 -304.741*P +343.792*F -316.445*P*F

…(7.10)

7.2.2.2 Validation of the model

Fig. 7.15 shows the actual response versus the predicted response for tensile shear testing result. From this Fig., it can be seen that the model adequately describes the response within the limits of the factors being investigated herein, as the data points are close to the diagonal line. Furthermore, three extra confirmation experiments were carried out using different test conditions, which are presented in Table 7.15 along with the resulting percentage error. It can be noticed that the average percentage error is almost 11%. The obtained tensile shear stress after laser welding is greater than the base metals value certainly comparing to the aluminum side.

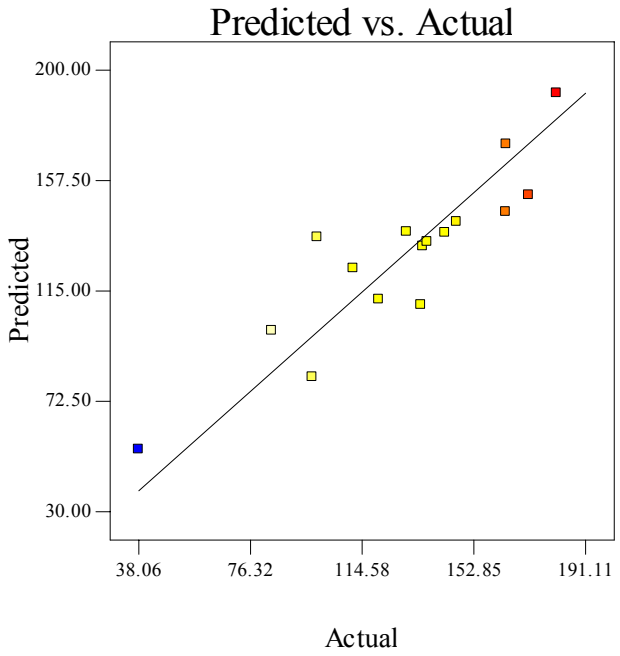

Fig. 7.15: Predicted Vs Actual for developed tensile shear strength model.

7.2.2.3 Effect of process parameters on the response:

1) Laser Power: It is evident from the results that the laser power is the most significant factor associated with the response, as shown in a contour graph in Fig. 6.23. The highest tensile strength value was 181 MPa, observed to be at a laser power of 0.9 kW as presented in Table 7.12.

2) Focus point position: The results indicate that the focus point position has also has a significant effect on the tensile strength of the laser-welded joint, as shown in Table 7.12. The model developed indicates that there is an interaction between the two welding parameters (the welding speed and the focus position) as exhibited in Fig. 7.17.

3) Welding speed**:** From the ANOVA analysis it can be seen that the welding speed has no obvious effect on the response within the parameter range domain applied. By changing the welding speed the response will not be affected. The relationship between the welding speed and laser power is exhibited in 3D graph Fig. 7.18 at focus position F=0.0 mm.

Table 7.15: Confirmation experiments of the tensile shear strength compared with model results.

Exp. No	P, kW	S, mm/ min	F, mm	Tensile strength, MPa		$\|E\%\|$
				Actual	predicted	
1	1.00	1600	0.00	139	160	13.1
2	1.10	1800	-1.00	157	134	17.2
3	0.90	2100	0.0	186	191	2.6

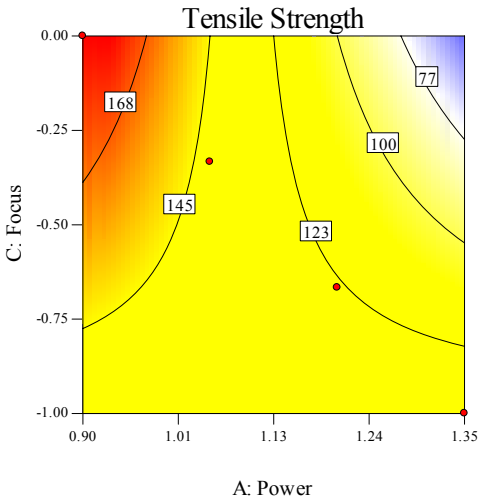

Fig. 7.16: Contour graph shows the effect Welding parameters At S = 2100 mm/min.

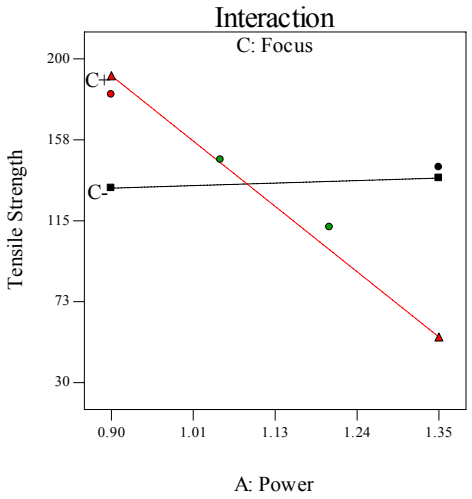

Fig 7.17: Interaction between the laser power and focus at S = 2100 mm/min.

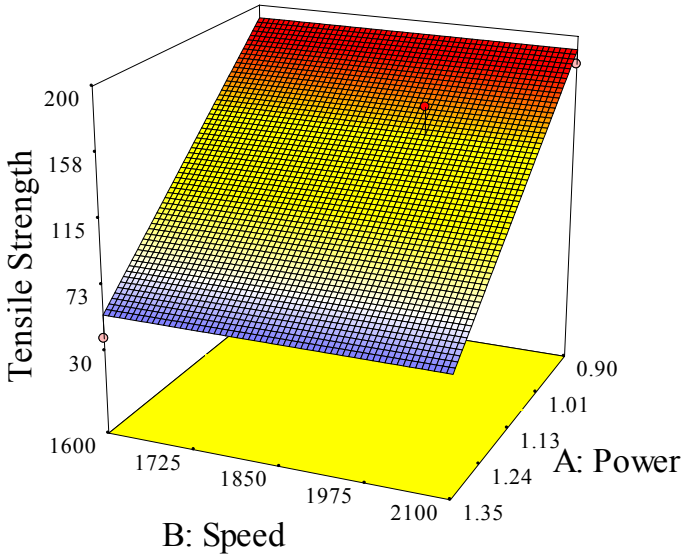

Fig. 7.18: 3D graph shows the effect of Power and Speed at F = 0.0 mm.

7.2.3 Operating Cost Modeling

The operating costs for joining the titanium / aluminum 5251H22 dissimilar materials were calculated using Eq. 4.13. The mathematical model was developed to minimize the operating cost. The same procedure was followed to check the model adequacy. The analysis results are shown in Table 7.16 for the reduced quadratic model which is suggested by the software for the received result of the welding operating cost. The same table shows the other adequacy measures R^2, Adjusted R^2 and Predicted R^2. All the adequacy measures indicate an adequate quadratic model. The adequate precision of 913 indicates adequate model discrimination. The developed quadratic mathematical model in terms of coded factors and actual values are exhibited in Eqs 7.11 and 7.12.

Table 7.16: ANOVA for operating welding cost

Source	Sum of Squares	df	Mean Square	F_v Value	p-value Prob. > F_v	
Model	0.00369	4	0.00092	110622	< 0.0001	Significant
P	9.5E-05	1	9.5E-05	11455	< 0.0001	
S	0.00357	1	0.00357	428117	< 0.0001	
PS	9.8E-07	1	9.8E-07	117.744	< 0.0001	
S^2	2.3E-05	1	2.3E-05	2800.17	< 0.0001	
Residual	9.2E-08	11	8.3E-09			
Cor. Total	0.00369	15				
R-Squared = 1			Adeq. Precision = 913.6			
Adj. R-Squared = 1						

Final Equation in Terms of Coded Factors:

Cost = 0.15 +3.28E-003*P -0.02*S -4.46E-004*P*S +2.72E-003*S^2

…(7.11)

Final Equation in Terms of Actual Factors:

Cost = 0.410 +0.0292*P -2.32E-004*S -7.92E-006* P* S +4.3E-008* S

…(7.12)

7.2.4 Microharness and Microstructure Studies

7.2.4.1 Microstructure of dissimilar jointed materials

The same preparation procedure used for Al 6082 / Ti G2 as mentioned before, the same etchant solutions were used to prepare the samples for microhardness and microstructure studies. Different grain textures can be clearly observed in Figs. 7.19 (a-d) between the upper weld and the lower weld due to the diversity of heat transfer direction. When welding started but before penetration, heat transfer occurred along cross-direction and depth direction, consequently generated the columnar grains whose orientation was perpendicular to the boundary between the fusion zone and the HAZ in titanium plate as it exhibited in Fig. 7.19 (a). No obvious second phase was observed in the WZ at upper part of welding pool and just the solidification crystals were apparent. Optical microscopy micrograph shows that the HAZ in the vicinity of molten boundary of titanium consists of mainly ά martensite exhibited in Fig. 7.19 (a). The circular ά in the HAZ was attributed to rapid cooling of the weld metal. The base metal of aluminum 5251 H22 is exhibited in Fig. 7.19(b). The laser

titanium–aluminium dissimilar joining resulted in a complex and heterogeneous microstructures composed of columnar grains and “white solute bands” in the base of welding pool. The welding zones in aluminium are partially melted zones due to the presence of low fusion point elements (magnesium) at the grain boundaries. The Al5251 WZ, HAZ and BM are exhibited in Fig. 7.19(c, d). It is well established that the microstructure of the joints affect the tensile strength critically. The influence of the heat inputs on the microstructure can be observed on the grain size variation with different heat inputs in Figs. 7.19(a-d). The higher the heat inputs and greater dwelling time at liquid temperature could accelerate the growing of the grain size and deteriorate the tensile strength of the weldment.

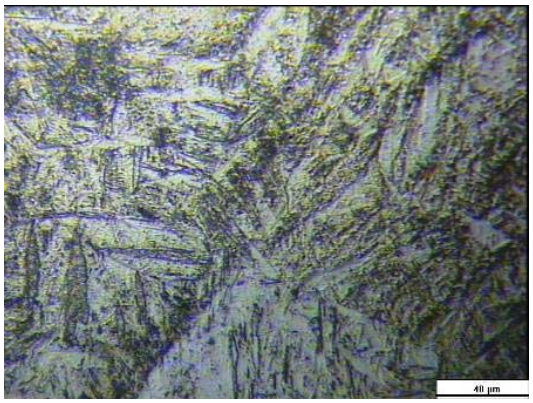

Fig. 7.19 (a) TiG2 WZ and HAZ

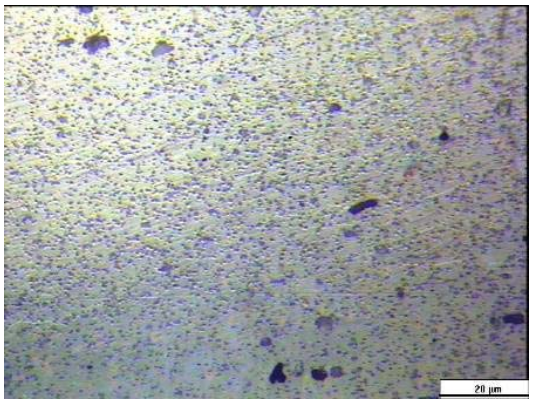

Fig. 7.19(b) Al5251 BM

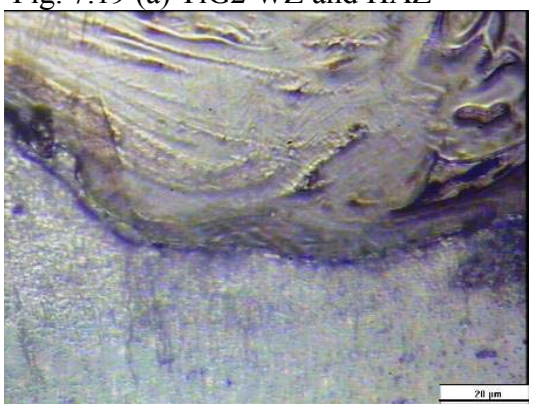

Fig. 7.19 (c) Al5251 BM, HAZ and WZ

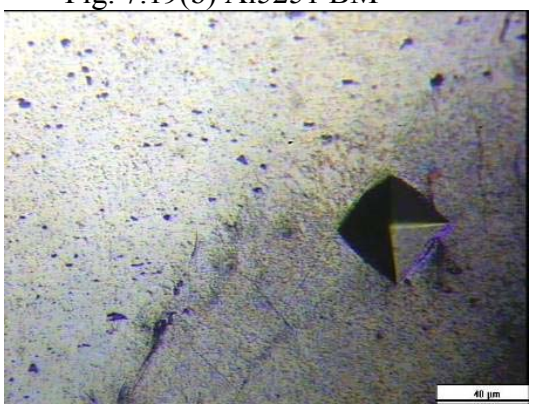

Fig. 7.19 (d) Al5251 BM, HAZ

Figs. 7.19 (a, b, c and d): The microstructure of lap weld Al5251 to Ti G2 joint.

07.2.4.2 Microhardness of dissimilar jointed materials

The specimens selected for microhardness studies were based on heat input calculation. Vickers microhardness measurements with a 50 g loading force test were applied to the selected specimens shown in Fig 7.19. For each specimen three different positions were subjected to the study (BM, HAZ, and WZ) for each plate of the dissimilar joint as presented in Table 7.17 and exhibited in microhardness profile of the dissimilar joint Fig. 7.20. The data on the liquid titanium to liquid aluminium interaction during high solidification rate key-hole laser welding is very limited. In the HAZ of the titanium side, the microhardness increase (232 – 287 HV) and further increase in WZ up to (280- 349 HV), as presented in Table 7.17, this could be related to the to the quenching effect resulting in a martensitic ά microstructure.

Table 7.17: Microhardness test result of dissimilar nonferrous to nonferrous materials

Sp No.	**Al 5251 H22**			**Ti G2**		
	BM	**HAZ**	**WZ**	**WZ**	**HAZ**	**BM**
3	95.45	104.2	379.61	347.98	232.7	226.69
8	96.34	103.1	210.2	348.65	263.45	242.75
15	99.7	94.72	149.11	280.71	261.58	245.9
16	98.81	83.85	194.29	327.44	286.99	262.41

Compared to the hardening effect evident in the weld–aluminium interfaces by intermetallic compound generation, the titanium–weld interfaces were not expected to be the weakest point of the assemblies. The fracture was mostly occurring at the aluminum WZ and referring to the microstructure transformation during the welding process which is evident from the microhardness result measured and presented in Table 7.9 and Fig 7.20 microhardness profile. The fracture could be interpreted by losing the ductility of aluminium and due to the brittle components formed during the solidification stage in WZ at aluminium side.

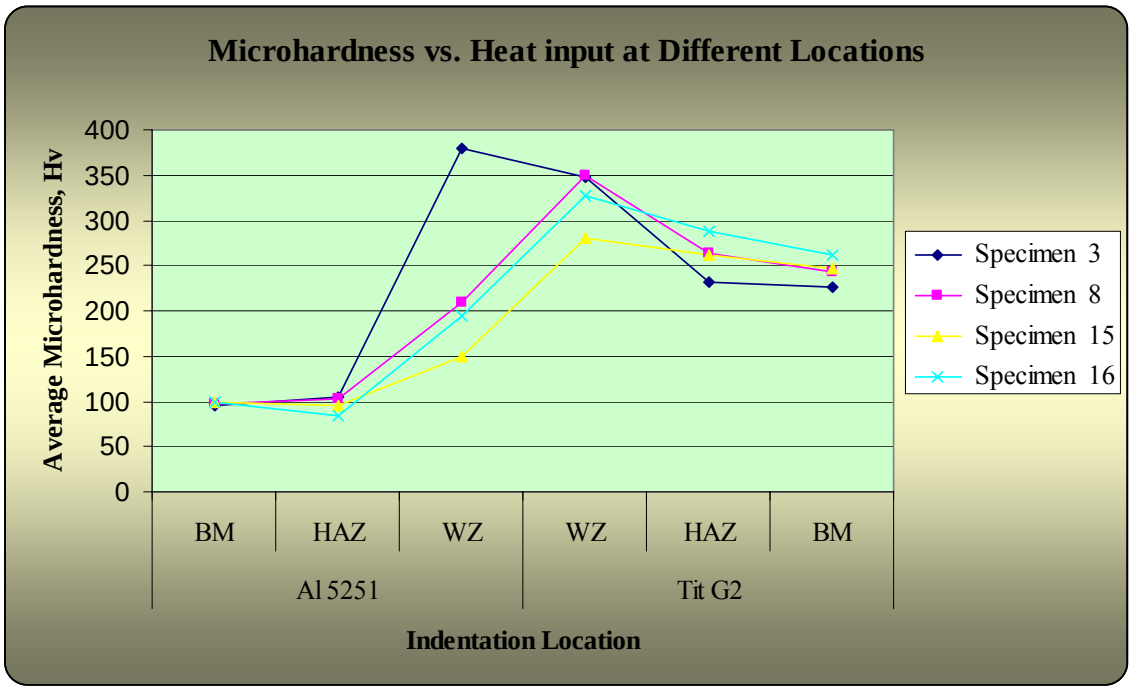

Fig. 7.20: The Microhardness profile of the dissimilar joint (Al 5251 / Ti G2).

7.2.5 Models (multiple –response) Optimization

7.2.5.1 Numerical optimization

The optimization criteria were selected for the above studied dissimilar material and are presented in Table 7.18. In the optimization criteria all the parameters received the same importance (+++) and same weight (1) as per the Design Expert software default. The optimisation result presented in the Table 7.18 is chosen from one of more than ten different optimum results calculated by the software.

The optimisation result of all the studied responses is shown in Table 7.18. For example by applying the optimisation criteria the tensile strength (resistance) value was reached up to 191 N/mm. If the target is only to maximize the tensile strength regardless of the other parameters then the response value will be greater than the received values and this is true for each response individually optimized. The residual stress at the level 1 is optimized and it was significantly reduced. The welding cost was considerably reduced to 13 cent/m in the decided criteria compared to the values presented in Table 7.12 which were more than 23 % greater than this

value. Also, the welding speed is maximum (2100 mm/min), in the optimisation criteria which leads to increased production rate and the laser power was kept to a minimum value of 0.9 kW.

7.2.5.2 Graphical optimisation

The graphical optimisation displays the area of feasible response values in the factor space. From the overlay plot in Fig. 7.21 it is obvious that the graphical optimisation allows visual selection of the optimum welding conditions according to certain criterion. The result of the graphical optimisation are the overlay plots, these type of plots are extremely practical for quick technical use in the workshop to choose the values of the welding parameters that would achieve certain response value for this type of dissimilar materials. The yellow /shaded area on the overlay plot in Fig. 7.21 is the region that meets the proposed criteria. The flag in the upper left corner of the Fig. 7.21 indicates the optimum response values and the input welding parameters (P, S) at F = -0.02 mm.

Table 7.18: The optimization criteria with the optimization results using numerical multiple-response

Welding Parameters	Power		Speed		Focus		Residual Stresses		Tensile Strength		Cost € / m		D*.
Goal	Min		Max.		In range		Min.		Max.		Min.		
Criteria	Wt.	Imp.	Wt.	Imp.	Wt.	Imp.	Wt.	Imp.	Wt.	Imp.	Wt.	Imp.	
First Criteria	1	+++	1	+++	-	-	1	+++	1	+++	1	+++	
Result	0.90		2100		0.00		22		191		0.13		0.82

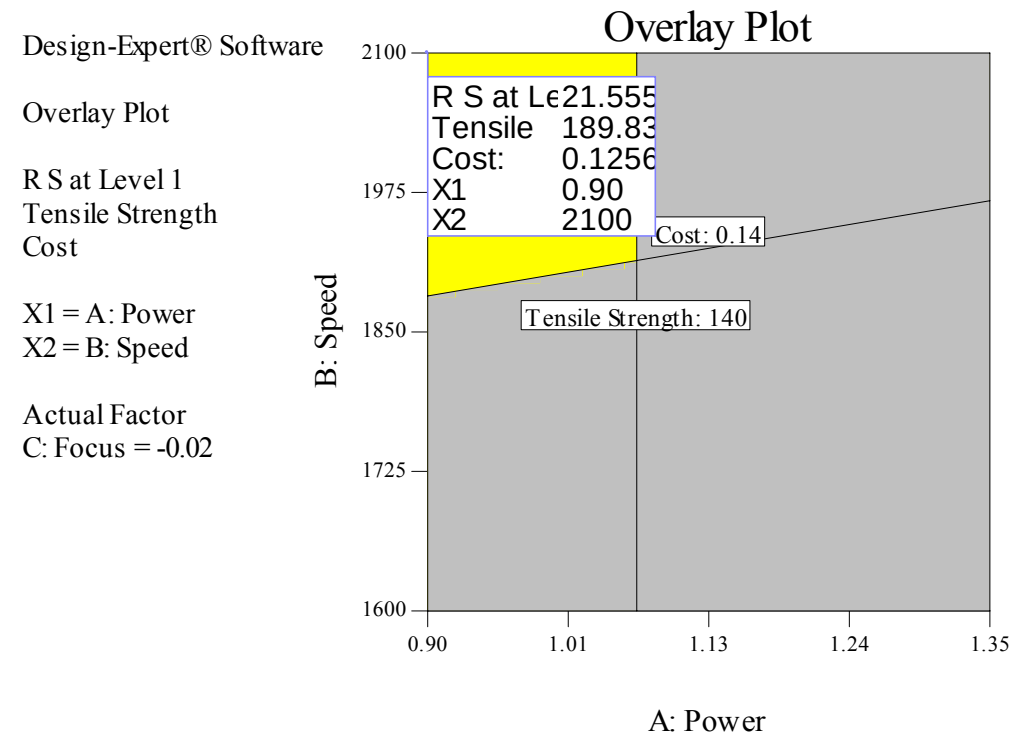

Fig.7.21: The feasible solution in yellow shaded area for optimisation criteria.

7.3 Chapter Summary

In this chapter two different aluminum alloys (Al-5251 H22 and Al-6082) with titanium G2 have been heterogeneous welded successfully using overlap assembly components by CO_2 laser welding. The achieved welded components were subjected to mechanical testing and microhardness testing to study the joints quality.

By completing a ‘‘Design of Experiment’’ inspired by ‘‘Taguchi approaches’’, it was possible to find the best operating welding parameters. Under the optimal conditions, the mechanical performances of the titanium/aluminum assemblies was reached, fracture strengths superior to 395 N/mm for Al6082 joints and 191 N/mm for Al 15251H22 joints which are greater than the strength of base metal (Al) in both joints, were achieved. Residual stress distribution in aluminum plate at HAZ of the lap-welded joint was measured by means of the hole-drilling method. The results show that compared to the base materials; yield and ultimate stress achieved were 58 % and 37 % respectively, which were not seriously affecting the joints. A study of

microstructures and microhardness was conducted and used to interpret the change in the mechanical properties due to the welding operation. Numerical optimization and graphical optimization were applied in this study and greater mechanical properties results compared to base metals were achieved after the welding. Operating welding cost per meter also was optimized through controlling welding parameters.

Taguchi optimization approach could be used to optimize any mechanical property individually or combine mechanical properties together to produce components for different engineering applications of dissimilar welding joints.

A similar welding process model for materials of any other nonferrous/nonferrous dissimilar materials, could be developed through the same approach as proposed here with same experimental procedure.

CHAPTER 8

8. CONCLUSION AND SCOPE FOR FUTURE WORK

Based on the experimental results and discussions, conclusions were drawn as follows:

8.1 General Conclusion

Laser welding of ferrous and nonferrous dissimilar material has been studied experimentally and analyzed statistically and the following points are generally concluded:

i) Laser welding is a very successful process for joining dissimilar materials such as ferrous/ferrous, nonferrous/ferrous and nonferrous/non ferrous.

ii) The models developed can adequately predict the responses within the factors domain.

iii) By means of a Design of Experiment inspired by the Taguchi approach, it is possible to achieve the best operating parameter window and then develop models to control the welding parameters.

iv) From the received results, S/N analysis and ANOVA analysis, it is noted that the change in the thickness of jointed dissimilar materials results in changing the effect of the welding parameters.

8.2 Conclusion for Joining Dissimilar Ferrous Materials

Ferrite/Austenite joints are a popular dissimilar metal combination in many applications. Therefore, exploitation of new processes for producing them is of interest to several industrial sectors. The following points can be concluded from this study:

- Successful welding can be achieved on butt stainless steel – low carbon steel joints using CO_2 laser welding. Using Laser welding improves the mechanical properties and produce a narrow HAZ.
- All the models developed for the considered stainless steel – low carbon steel joints can adequately predict the response within the factors domain.

- Welding speed has the strongest effect on the tensile strength and on the fusion area size among the selected parameters; it is inversely proportional to the responses.
- Laser power has a strong effect on fusion area. By changing the P value the response will be changed dramatically, so the P value should be carefully selected. The focusing position parameter has an insignificant effect on the total weld pool dimensions.
- Focus position and the gap between the jointed plates have a strong effect on impact strength while laser power has an insignificant effect on the impact strength.
- The presence of gap parameter influences the effect of the laser power parameter. The gap width parameter combined with the focus parameter eliminates the direct effect of the laser power on the process.
- The laser welded joint of F/A is stronger than both base metals.

8.3 Conclusion for Joining Dissimilar Ferrous to Nonferrous Materials

- Sound welding can be achieved on overlap Al–steel joints using CO_2 laser welding with steel-on-aluminium. Welds are composed of a solid solution of aluminium in iron and richer aluminium "white solute bands" assumed to be an Fe_xAl_y intermetallic phases. The welding – aluminium interfaces are composed of Fe_2Al_5 and/or $FeAl_3$ phases with thicknesses ranging between 0 μm and 30μm.
- All the models developed for the considered of Al–steel joints can adequately predict the response within the factors domain except the model developed for the Al6082 / Steel at level 2 (σ_2) which is proved by ANOVA to be an insignificant model.
- The obtained tensile shear strength values in the optimisation step increased up to 317 N/mm when joining Al 6082 / Steel 10131 and 107 N/mm when joining Al 1050 H24 / steel 10131. In both cases the achieved tensile shear strengths were greater than the Al base metal values. The mechanical strength values

obtained by this method of optimisation are compatible with the specifications relative to these assemblies in the automotive industry.

- The achieved result indicates that fusion (key-hole laser) welding is not a successful process for titanium / steel dissimilar welding. Titanium carbides formed in the welding pool during the welding process are very brittle components. Solid state welding processes are recommended rather than fusion welding processes for titanium dissimilar welding.

8.4 Conclusion for Joining Dissimilar Nonferrous to Nonferrous Materials

- The dissimilar joint between aluminum alloys (Al6082 and Al 5251 H22) and titanium G2 alloys were successfully welded by CO_2 laser welding with a single pass and without filler material using the overlap joint design.
- The tensile shear tests indicate that fracture mostly occurs at the aluminum WZ or HAZ. A high-quality joint with high tensile strength was achieved by applying the Taguchi optimisation technique.
- The weld metal was mainly composed of martensite alpha prime. In two different metals in the two different joints HAZ, grain growth was detected. The microhardness of the joint distribution also has shown microhardness increasing in the HAZ of two base metals and a varying microhardness in fusion zone.
- CO_2 laser welding which is characterized by low heat input for joint dissimilar components which have different thermal conductivity and different thermal expansion introduces low residual stresses in the laser welded plates. The present study shows that the evaluated residual stress in the HAZ of dissimilar (Al 5251 / Ti G2) are very low and may not affect the welding quality.

8.5 Thesis Contributions

- Mathematical models for the mechanical properties and cost per meter welded were developed using DOE with Taguchi optimization to predict or optimize each response separately or more than one response simultaneously (numerically or graphically). Developed models could be used for mass production for computerized welding process by programming them into a CNC laser welding machine.
- The effect of each welding parameter on each response and the interactions between the parameters were studied. It was found that the residual stresses could be controlled through the welding process in design stage which is the most effective and inexpensive way to control the stresses.
- CO_2 laser welding was used instead of solid-state welding processes which are usually used for joining dissimilar materials including titanium.

8.6 Scope for Future Work

1. Using the Taguchi Optimisation technique for more different dissimilar materials which are important for many economic and industrial applications.
2. This optimisation technique could be utilized for different welding techniques.
3. The study could to be extended to include more mechanical properties (e.g. bending, fatigue strength, etc..,) to give full picture about dissimilar jointed materials.
4. Joining the dissimilar materials may cause galvanic corrosion between the two different joined materials. This phenomenon should be subjected to a detailed study between each dissimilar jointed material.
5. The microstructures in the fusion zone of dissimilar materials call for further research using TEM.
6. The data on the subject of the liquid steel to liquid aluminium interaction during high solidification rate key-hole welding and the complex microstructure obtained after Al–steel key-hole induced mixture is very limited. More studies are necessary in order to better

understand the cracking in the lower part of the joint on the weld-intermetallic interface. Also, the data regarding the liquid titanium / liquid aluminium interaction at a high solidification rate is also limited and further studies of this subject are necessary in order to better understand the resultant phases and their affect on the mechanical properties of the welded dissimilar joint.

7. Detailed studies regarding the fractures behaviour and welding defects of dissimilar jointed materials are necessary.

REFERENCES

[1]H. B. Cary, Modern Welding Technology, Prentice-Hill, ISBN 0-13-599290-7, 1979.

[2]J. F. Lancaster, Metallurgy of Welding, Prentice-Hill, fourth edition, 1987.

[3]Hobart Institute of Welding Technology, accessed on 11.2006 http://www.welding.com/history_of_welding3.shtml.

[4]ASM Committee of laser beam welding, Material Hand Book, ninth edition, volume 6,Welding, Brazing, and Soldering, ISBN 0-87170-007 (V.1), 1983.

[5]A.Althouse, C.Turnquist, W.Bowditch and K.Bowditch, Modern Welding, The Goodheart-Willcox co., inc. ISBN 0-87006-433-9, 1984.

[6]T. Zacharia, S.A. David, J.M. Vitek and T. Debroy, Metall. Trans. 20 A (1989) 1125.

[7]Z. Sun and R. Karppi, The application of electron beam welding for the joining of dissimilar metals**,** Journal of Materials Processing Technology 59 (1996) pp. 257 - 267.

[8]L. K. Pana, C. C. Wangb, Y. C. Hsiaoc, K. Chyn Hod, Optimization of Nd:YAG laser welding onto magnesium alloy via Taguchi analysis, Jornal of Optics & Laser Technology 37 (2004) pp. 33 – 42.

[9]http://www.geocities.com/muldoon432/Laser_Types_and_Classifications.htm, accessed in 11/2006.

[10]Boraiko, Allen A, A Splendid Light: Lasers, National Geographic 165, March 1984, pp. 335.

[11]Ohanian, Hans, Physics, 2nd Ed Expanded, Norton, 1989.

[12]Barcodes inc. http://www.barcodesinc.com/cats/barcode-scanners/, accessed in 11 / 2006.

[13]http://www.uslasercorp.com/envoy/heattreating.html, accessed in 11/2006.

[14]C. Rüffler and K. Gürs, Cutting and welding using a CO_2 laser, Optics & Laser Technology, Volume 4, Issue 6, December 1972, pp. 265-269.

[15]TWI, http://www.twi.co.uk/j32k/unprotected/band_1/laser_cutting.html, accessed in 11/2006.

[16]C. Dawes, laser Welding, Mc Graw- Hill, Inc., ISBN 0-07-016123-2, 199.

[17]A. El-Batahgy, Effect of laser welding parameters on fusion zone shape and solidification structure of austenitic stainless steels, Journal of Materials Letters, Volume 32, Issues 2-3, August 1997, pp. 155-163.

[18]A. Matsunawa, S. Katayama, H. Miyazawa, S. Hiramoto, K. Oka and M. Ohmine, Basic study on laser physical vapor deposition of ceramics, Journal of Surface and Coatings Technology, Volumes 43-44, Part 1, 5 December 1990, pp.176-184.

[19]A. Ancona, T. Sibillano, L. Tricarico, R. Spina, P.M. Lugarà, G. Basile and S. Schiavone, Comparison of two different nozzles for laser beam welding of AA5083 aluminium alloy, Journal of Materials Processing Technology, Volumes 164-165, 15 May 2005, pp. 971-977.

[20]Jeng-Ywan Jeng, Tzuoh-Fei Mau and Shyeu-Ming Leu, Prediction of laser butt joint welding parameters using back propagation and learning vector quantization networks, Journal of Materials Processing Technology, Volume 99, Issues 1-3, 1 March 2000, pp. 207-218.

[21]Z. Li and G. Fontana, Autogenous laser welding of stainless steel to free-cutting steel for the manufacture of hydraulic valves, Journal of Materials Processing Technology, Volume 74, Issues 1-3, February 1998, pp. 174-182.

[22]N. Orhan, M. Aksoy and M. Eroglu, A new model for diffusion bonding and its application to duplex alloys, Journal of Materials Science and Engineering A, Volume 271, Issues 1-2, 1 November 1999, pp. 458-468.

[23]M. A. Béjar, W. Schnake and R. Urqueta, Electrocontact-discharge forge welding of steel bars, Journal of Materials Processing Technology, Volume 127, Issue 1, 20 September 2002, pp. 68-72.

[24]R. Kaçar and O. Baylan, An investigation of microstructure/property relationships in dissimilar welds between martensitic and austenitic stainless steels, Journal of Materials & Design, Volume 25, Issue 4, June 2004, pp. 317-329.

[25]V. V. Satyanarayana, G. M. Reddy and T. Mohandas, Dissimilar metal friction welding of austenitic–ferritic stainless steels, Journal of Materials Processing Technology, Volume 160, Issue 2, 20 March 2005, pp. 128-137.
[26]M. Sahin, Joining with friction welding of high-speed steel and medium-carbon steel, Journal of Materials Processing Technology, Volume 168, Issue 2, 30 September 2005, pp. 202-210.
[27]P. B. Srinivasan, V. Muthupandi, W. Dietzel and V. Sivan, An assessment of impact strength and corrosion behaviour of shielded metal arc welded dissimilar weldments between UNS 31803 and IS 2062 steels, Journal of Materials & Design, Volume 27, Issue 3, 2006, pp. 182-191.
[28]J. R. Berretta, W. de Rossi, M. D. Neves, I. de Almeida and N. D. V. Junior, Pulsed Nd:YAG laser welding of AISI 304 to AISI 420 stainless steels, Journal of Optics and Lasers in Engineering, Volume 45, Issue 9, September 2007, pp. 960-966.
[29]T. Luijendijk, Welding of dissimilar aluminium alloys, Journal of Materials Processing Technology, Volume 103, Issue 1, 1 June 2000, pp. 29-35.
[30]W.Lee, Y.Yeon and S. Jung, The joint properties of dissimilar formed Al alloys by friction stir welding according to the fixed location of materials, Journal of Scripta Materialia, Volume 49, Issue 5, September 2003, pp. 423-428.
[31]P. P. Lean, L. Gil and A. Ureña, Dissimilar welds between un-reinforced AA6082 and AA6092/SiC/25p composite by pulsed-MIG arc welding using un-reinforced filler alloys (Al–5Mg and Al–5Si), Journal of Materials Processing Technology, Volumes 143-144, 20 December 2003, pp. 846-850.
[32]H. Zhang, P. He, J. Feng and H. Wu, Interfacial microstructure and strength of the dissimilar joint Ti3Al/TC4 welded by the electron beam process, Journal of Materials Science and Engineering: A, Volume 425, Issues 1-2, 15 June 2006, pp. 255-259.
[33]A. Abdollah-Zadeh, T. Saeid and B. Sazgari, Microstructural and mechanical properties of friction stir welded aluminum/copper lap joints, Journal of Alloys and Compounds, Volume 460, Issues 1-2, 28 July 2008, pp. 535-538.

[34]E. Zumelzu and C. Cabezas ,Study on welding such dissimilar materials as AISI 304 stainless steel and DHP copper in a sea-water environment. Influence of weld metals on corrosion, Journal of Materials Processing Technology, Volume 57, Issues 3-4, 15 February 1996, pp. 249-252.

[35]A. Z. Sahin, B. S. Yiba, M. Ahmed and J. Nickel, Analysis of the friction welding process in relation to the welding of copper and steel bars, Journal of Materials Processing Technology, Volume 82, Issues 1-3, 1 October 1998, pp. 127-136.

[36]Garmire, http://hyperphysics.phy-astr.gsu.edu/Hbase/optmod/lasapp.html, accessed in 11/2006.

[37]T. A. Mai and A. C. Spowage, Characterisation of dissimilar joints in laser welding of steel–kovar, copper–steel and copper–aluminum, Journal of Materials Science and Engineering A, Volume 374, Issues 1-2, 15 June 2004, pp. 224-233.

[38]H. Uzun, C. D. Donne, A. Argagnotto, T. Ghidini and C. Gambaro, Friction stir welding of dissimilar Al 6013-T4 To X5CrNi18-10 stainless steel, Journal of Materials & Design, Volume 26, Issue 1, February 2005, pp. 41-46.

[39]T. Watanabe, H. Takayama and A.Yanagisawa, Joining of aluminum alloy to steel by friction stir welding, Journal of Materials Processing Technology, Volume 178, Issues 1-3, 14 September 2006, pp. 342-349.

[40]A. Mathieu, R. Shabadi, A. Deschamps, M. Suery, S. Matteï, and E. Cicala, Dissimilar material joining using laser (aluminum to steel using zinc-based filler wire), Optics & Laser Technology, Volume 39, Issue 3, April 2007, pp. 652-661.

[41]X. Liu, G. Yu, M. Pang, J. Fan, H. Wang and C. Zheng, Dissimilar autogenous full penetration welding of super-alloy K418 and 42CrMo steel by a high power CW Nd:YAG laser, Journal of Applied Surface Science, Volume 253, Issue 17, 30 June 2007, pp. 7281-7289.

[42]A.S. Aloraier, R.N. Ibrahim and J. Ghojel, Eliminating post-weld heat treatment in repair welding by temper bead technique: role bead sequence in metallurgical changes, Journal of Materials Processing Technology, Volumes 153-154, 10 November 2004, pp. 392-400.

[43]R. N. Ibrahim, D. Ischenko, Finite element analysis used to optimize welding patterns for marine structure, in: Proceedings of the ASME Design Engineering Technical Conference (DETC'98), ASME, Sep. 1998, pp. 13–16.
[44]R. N. Ibrahim, D. Ischenko, Investigation of welding residual stresses in structural elements of ship, Journal of Key Eng. Mater. 144–149, 1997, pp. 859–864.
[45]B.B. Kerezsi, J.W.H. Price, A. Kotousov, Features of fatigue crack growth due to repeated thermal shock, Journal of Fract. Fatigue Eng. Mater. Struct. 25 (2), 2002, pp. 215–222.
[46]B.B. Kerezsi, J.W.H. Price, R. Ibrahim, A two-stage model for predicting crack growth, due to repeated thermal shock, Eng. Fract., Mech., 70, 2003, pp.721–730.
[47]P. Don, F.W. Brust, Welding residual stresses and effects on fracture in pressure vessels and piping components: a millennium review and beyond, ASME Journal of Pressure Vessel Technology. 122, 2000, pp. 329–338.
[48]N. S. Boulton, , Lance Martin, H.E., Residual stresses in arc welded plates, Proc. Inst. Mech. Eng. 133, 1936, pp. 295–347.
[49]H. Kihara, K. Masubuchi, Studies on the Shrinkage and Residual Welding Stress of Constrained Fundamental Joint, Reports of Transportation Technical, Research Institute of Japan, No. 7 1954.
[50]M. Watanabe, K. Satoh, Effect of welding conditions on the shrinkage distortion in welded structures—shrinkage distortion is analyzed from the standpoint of welding heat and external restraint effects, Welding J. 40, 1961, pp. 377.
[51]N. R. Rao, F. R. Estuar, L. Tall, Residual stresses in welded shapes, Weld. J. 43, 1964, pp. 295.
[52]G. A. Alpsten, L. Tall, Residual stresses in heavy welded shapes, Weld. J. 49 (3), 1970, pp. 93.
[53]K. Satoh, T. Terasaki, Effect of welding conditions on residual stress distributions and welding deformation in welded structures materials. Journal of Jpn, Weld. Soc. 45, 1976, pp. 42.
[54]D.Bru, J. Devaux, J. M. Bergheau, D. Pont, Influence of material properties at high temperatures on the modeling of welding residual stress and deformation state.

In: Cerjak, H. (Ed.), Mathematical Modeling of Weld Phenomena, vol. 3, The Institute of Metals, London, 1997, pp. 456.

[55]A. Ohta, O. Watanabe, K. Matsuoka, C. Shiga, S. Nishijima, N Suzuki, T. Kubo, Fatigue strength improvement of box welded joints by using low transformation temperature welding material. Q. J. Jpn. Weld. Soc. 18, 2000, pp. 141.

[56]T. Kumose, T. Yoshida, T. Abe, H. Onoue, Prediction of angular distortion caused by one-pass fillet welding. Weld. J. 33, 1954, pp. 945.

[57]L. E. Benson, S. J. Watson, Effect of preheating on residual stresses in mild-steel weld. Br. Weld. J. 2, 1955, pp. 372.

[58]Y. I. Burak, Ya. P. Romanchuk, A. A. Kazimirov, V. P. Morgun, Selection of the optimum fields for preheating plates before welding, Autumn, Weld. 5, 1979, pp. 5.

[59]Q. Guan, D. L. Guo, R. H. Reggatt, Low stress non-distortion (LSND) welding—a new technique for thin materials, Journal of Weld. World 33, 1994, pp. 160–167.

[60]Q. Guan, C. X. Zhang, D. L. Guo, Dynamic control of welding distortion by moving spot heat Sink, Journal of Weld. World 33, 1994, pp. 308–312.

[61]S. Aoki, T. Nishimura, T. Hiroi, Y. Amano, Reduction of residual stress of welded joint using vibration, Trans. Jpn. Soc. Mech. Eng. 61C, 1995, pp. 4800.

[62]R. Fidler, The effect of time and temperature on residual stresses in austenitic welds, Trans. ASME, Journal of Pressure Vessel Technol. 104, 1982, pp. 210–214.

[63]D. J. Smith, S. J. Garwood, Influence of postweld heat treatment on the variation of residual stresses in 50mm thick welded ferritic steel plates, Int. Journal of Pressure Vessels Piping 51, 1982, pp. 241–256.

[64]Y. F. Al-Obaid, A rudimentary analysis of improving fatigue life of metals by shot peening, Trans. ASME, Journal of Appl. Mech. 1986, pp. 108, 307–312.

[65]S. Ohta, T. Ishimura, T. Tamura, Improvement of fatigue strength of fillet-welded joint by water jet treatment of weld toe region, Q. J. Jpn. Weld. Soc. 14, 1996, pp. 601–608.

[66]J. S. Porowski W. J. O'Donnell, M. L. Badlani, E. J. Hampton, Use of the mechanical stress improvement process to mitigate stress corrosion cracking in BWR piping systems, Journal of Nucl. Eng. Des. 124, 1990, pp. 91–100.
[67]M. Nayama, N. Akitomo, Residual stress relief of welded joints in pipe work using ice plugs, Journal of Weld. Int. 8, 1994, pp. 704–709.
[68]M. Watanabe, Z. Murakami, M. Nishida, Residual stress reduction in welded joint by local low-temperature cooling, Preprints of National Meeting of Japan Welding Society, vol. 33, 1983, pp. 308–309.
[69]M. Mochizuki, Control of welding residual stress for ensuring integrity against fatigue and stress–corrosion cracking, Journal of Nuclear Engineering and Design, Volume 237, Issue 2, January 2007, pp. 107-123.
[70]http://www.lanl.gov/residual/compare.shtml (accessed on August, 07).
[71]ASTM E 837, Determining Residual Stresses by the Hole-Drilling Strain-gage Method, American Society for Testing and Materials, Philadelphia, Pa, 1985.
[72]H. J.Yen, M. C. Lin, 1995, Measurement of Residual Stress in the Weld Overlay Piping Components, Exp. Mech., 35, No. 2, 1995, pp. 89–95.
[73]J. B. Roelens, F. Maltrud, J. Lu, Determination of Residual Stresses in the Submerged Arc Multi-pass Welds by Means of Numerical Simulation and Comparison with Experimental Measurements, Journal of Weld. World, 33, No. 3, 1994, pp. 152–159.
[74]C. S. Richard, G. Beranger, J. Lu, J. F. Flavenot, The Influence of Heat Treatment and Interdiffusion on the Adhesion of Plasma-Sprayed NiCrAlY Coatings, Surf. Coat. Technol., 82, 1999, pp. 99–109.
[75]Smith, J. David, N. W. Bonner, Measurement of Residual Stresses Using the Deep Hole Method, ASME, Journal of Pressure Vessels and Piping Division, Vol. 327, 1996, pp. 53–65.
[76]J. Mathar, Determination of Initial Stresses by Measuring the Deformations Around Drilled Holes, Trans. ASME, 56, 1934, pp. 249–254.

[77]Kroenke, Holloway, Mabe, Stress Calculation Update in ASTM E 837 Residual Stress Hole Drilling Standard, Journal of Advances in Computational Science and Engineering, Vol. 1, 2000, pp. 695–701.

[78]N. J. Rendler, I. Vigness, Hole Drilling Strain Gage Method of Measuring Residual Stresses, Exp. Mech., 6, No. 12, 1966, pp. 577–586.

[79]R. G. Bathgate, Measurement of Non-uniform Biaxial Residual Stresses by the Hole-Drilling Method, Strain, 4, No. 2, 1968, pp. 20–29.

[80]R. A. Kelsey, Measuring Non-uniform Residual Stresses by the Hole drilling Method, Proceedings of SESA, Vol. 14, No. 1, 1956, pp. 181–194.

[81]Measurement of Residual Stresses by the Hole-Drilling Strain Gage Method, 1993, Tech. Note 503-4, Measurements Group, Raleigh, NC.

[82]G. S. Schajer, Measurement of Non-Uniform Residual Stresses Using the Hole Drilling Method, Part I—Stress Calculation Procedures, ASME Journal of Eng. Mater. Technol., 110, No. 4, 1988, pp. 318–342.

[83]G. S. Schajer, Measurement of Non-Uniform Residual Stresses Using the Hole Drilling Method, Part II—Practical Application of the Integral Method, ASME Journal of Eng. Mater. Technol., 110, No. 4, 1988, pp. 344–349.

[84]A. Niku-Lari, J. Lu, J. F. Flavenot, Measurement of Residual Stress Distribution by the Incremental Hole-Drilling Method, Exp. Mech., 25, No. 6, 1985, pp. 175–185.

[85]M. T. Flaman, B. H. Manning, Determination of Residual Stress Variation with Depth by the Hole Drilling Method, Exp. Mech., 25, No. 6, 1985 pp. 205–207.

[86]H. Wern, Measurement of Non-uniform Residual Stresses Using the Hole-drilling Method, A New Integral Formalism, Strain, 31, No. 2, 1995, pp. 63–68.

[87]R. W. Hampton, D. V. Nelson, On the Use of the Hole-Drilling Technique for Residual Stress Measurement in Thin Plates, ASME Journal of Pressure Vessel Technol., 114, 1992, pp. 292–299.

[88]j. Aoh, and C. Wei, On the Improvement of Calibration Coefficients for Hole-Drilling Integral Method: Part I—Analysis of Calibration, Coefficients Obtained by 3-D FEM Model, Transactions of the ASME, Vol. 124, April 2002.

[89]C. Lee and K. Chang, Numerical analysis of residual stresses in welds of similar or dissimilar steel weldments under superimposed tensile loads, Journal of Computational Materials Science, Volume 40, Issue 4, October 2007, pp. 548-556.

[90]A. Kumar and T. DebRoy, Guaranteed fillet weld geometry from heat transfer model and multivariable optimization, International Journal of Heat and Mass Transfer, Volume 47, Issue 26, December 2004, pp. 5793-5806.

[91]J. Goldak, A. Chakravarti and M. Bibby, A new finite element model for welding heat sources, Journal of Metallurgical Transactions B 15B, June 1984, pp. 299–305.

[92]Y. F. Hsu and B. Rubinsky, Two-dimensional heat transfer study on the keyhole plasma arc welding process, International Journal of Heat and Mass Transfer, Volume 31, Issue 7, July 1988, pp. 1409-1421.

[93]I. J. Stares, C. Duffil, J. A. Ogilvy and C. B. Scruby , On-line weld pool monitoring and defect detection using ultrasonic, Journal of NDT International, Volume 23, Issue 4, August 1990, pp. 195-200.

[94]M. Hang and A. Okada, Computation of GMAW welding heat transfer with boundary element method, Journal of Advances in Engineering Software, Volume 16, Issue 1, 1993, pp. 1-5.

[95]R. G. Keanini and Boris Rubinsky, Three-dimensional simulation of the plasma arc welding process, International Journal of Heat and Mass Transfer, Volume 36, Issue 13, September 1993, pp. 3283-3298.

[96]S. J. Na and H. -J. Lee, A study on parameter optimization in the circumferential GTA welding of Aluminium pipes using a semi-analytical finite-element method, Journal of Materials Processing Technology, Volume 57, Issues 1-2, 1 February 1996, pp. 95-102.

[97]Y. M. Zhang, R. Kovacevic and L. Li, Characterization and real-time measurement of geometrical appearance of the weld pool, International Journal of Machine Tools and Manufacture, Volume 36, Issue 7, July 1996, pp. 799-816.

[98]J. Y. Yeh and L. N. Brush, A boundary integral equation technique for the calculation of weld pool shapes in thin plates, Journal of Computational Materials Science, Volume 6, Issue 1, July 1996, pp. 92-102.
[99]M. A. Wahab and M. J. Painter, Numerical models of gas metal arc welds using experimentally determined weld pool shapes as the representation of the welding heat source, International Journal of Pressure Vessels and Piping, Volume 73, Issue 2, September 1997, pp. 153-159.
[100]I. S. Kim and A. Basu, A mathematical model of heat transfer and fluid flow in the gas metal arc welding process, Journal of Materials Processing Technology, Volume 77, Issues 1-3, 1 May 1998, pp. 17-24.
[101]P. Petrov, C. Georgiev and G.Petrov, Experimental investigation of weld pool formation in electron beam welding, Journal of Vacuum, Volume 51, Issue 3, 1 November, 1998, pp. 339-343.
[102]A. F. Norman, V. Drazhner and P. B. Prangnell, Effect of welding parameters on the solidification microstructure of autogenous TIG welds in an Al–Cu–Mg–Mn alloy, Journal of Materials Science and Engineering A, Volume 259, Issue 1, 15 January 1999, pp. 53-64.
[103]Tarng, H. L. Tsai and S. S. Yeh, Modeling, Optimization and Classification of Weld Quality in Tungsten Inert Gas Welding, International Journal of Machine Tools and Manufacture, Volume 39, Issue 9, September 1999, pp.1427-1438
[104]J. I. Lee and K. W. Um, A prediction of welding process parameters by prediction of back-bead geometry, Journal of Materials Processing Technology, Volume 108, Issue 1, 1 December 2000, pp. 106-113.
[105]C. B. Reed, K. Natesan, Z. Xu and D. L. Smith, The effect of laser welding process parameters on the mechanical and microstructural properties of V–4Cr–4Ti structural materials, Journal of Nuclear Materials, Volumes 283-287, Part 2, December 2000, pp. 1206-1209.
[106]K. -Y. Bae, T. -H. Lee and K. -C. Ahn, An optical sensing system for seam tracking and weld pool control in gas metal arc welding of steel pipe, Journal of

Materials Processing Technology, Volume 120, Issues 1-3, 15 January 2002, pp. 458-465.
[107]G. A. Taylor, M. Hughes, N. Strusevich and K. Pericleous, Finite volume methods applied to the computational modeling of welding phenomena, Journal of Applied Mathematical Modeling, Volume 26, Issue 2, February 2002, pp. 311-322.
[108]I. S. Kim, K. J. Son, Y. S. Yang and P. K. D. V. Yaragada, Sensitivity analysis for process parameters in GMA welding processes using a factorial design method, International Journal of Machine Tools and Manufacture, Volume 43, Issue 8, June 2003, pp. 763-769.
[109]F. Lu, S. Yao, S. Lou and Y. Li, Modeling and finite element analysis on GTAW arc and weld pool, Journal of Computational Materials Science, Volume 29, Issue 3, March 2004, pp. 371-378.
[110]F. Lu, X. Tang, H. Yu and S. Yao, Numerical simulation on interaction between TIG welding arc and weld pool, Journal of Computational Materials Science, Volume 35, Issue 4, April 2006, pp. 458-465.
[111]H. Wang, Y. Shi and S. Gong, Effect of pressure gradient driven convection in the molten pool during the deep penetration laser welding, Journal of Materials Processing Technology, Volume 184, Issues 1-3, 12 April 2007, pp. 386-392.
[112]G. Tani, L. Tomesani, G. Campana and A. Fortunato, Evaluation of molten pool geometry with induced plasma plume absorption in laser-material interaction zone, International Journal of Machine Tools and Manufacture, Volume 47, Issue 6, May 2007, pp. 971 – 977.

[113]V. Gunaraj and N. Murugan, Application of response surface methodology for predicting weld bead quality in submerged arc welding of pipes, Journal of Materials Processing Technology, Volume 88, Issues 1-3, 15 April 1999, pp. 266-275.
[114]S. C. Juang and Y. S. Tarng, Process parameter selection for optimizing the weld pool geometry in the tungsten inert gas welding of stainless steel, Journal of Materials Processing Technology, Volume 122, Issue 1, 5 March 2002, pp. 33-37.

[115]A. Scotti and L. A. A. Rosa, Influence of oscillation parameters on crack formation in automatic Fe-B hardfacing, Journal of Materials Processing Technology, Volume 65, Issues 1-3, March 1997, pp. 272-280.
[116]W. Dai, Effects of high-intensity ultrasonic-wave emission on the weldability of aluminum alloy 7075-T6, Journal of Materials Letters, Volume 57, Issues 16-17, May 2003, pp. 2447-2454.
[117]J. R. Weng, J. T. Chang, K. C. Chen and J. L. He, Solid/liquid erosion behavior of gas tungsten arc welded TiNi overlay, Wear, Volume 255, Issues 1-6, August-September 2003, pp. 219-224.
[118]A. P. Costa, L. Quintino and M. Greitmann, Laser beam welding hard metals to steel, Journal of Materials Processing Technology, Volume 141, Issue 2, 20 October 2003, pp. 163-173.
[119]M. Shahin and H. E. Akata, Joining with friction welding of plastically deformed steel, Journal of Materials Processing Technology, Volume 142, Issue 1, November 2003, pp. 239-246.
[120]Z. Sterjovski, D. P. Dunne and S. Ambrose, Evaluation of cross-weld properties of quenched and tempered pressure vessel steel before and after PWHT, International Journal of Pressure Vessels and Piping, Volume 81, Issue 6, June 2004, pp. 465-470.
[121]Z. Jandric, M. Labudovic and R. Kovacevic, Effect of heat sink on microstructure of three-dimensional parts built by welding-based deposition, International Journal of Machine Tools and Manufacture, Volume 44, Issues 7-8, June 2004, pp. 785-796.
[122]F. Caiazzo, F. Curcio, G. Daurelio and F. Memola Capece Minutolo, Ti6Al4V sheets lap and butt joints carried out by CO2 laser: mechanical and morphological characterization, Journal of Materials Processing Technology, Volume 149, Issues 1-3, June 2004, pp. 546-552.
[123]R.V. Preston, H.R. Shercliff, P.J. Withers and S. Smith, Physically-based constitutive modeling of residual stress development in welding of aluminum alloy 2024, Acta Materialia, Volume 52, Issue 17, 4 October 2004, pp. 4973-4983.

[124]O. E. Canyurt, Estimation of welded joint strength using genetic algorithm approach, International Journal of Mechanical Sciences, Volume 47, Issue 8, August 2005, pp. 1249-1261.
[125]Z. Sterjovski, D. Nolan, K.R. Carpenter, D.P. Dunne and J. Norrish, Artificial neural networks for modelling the mechanical properties of steels in various applications, Journal of Materials Processing Technology, Volume 170, Issue 3, December 2005, pp. 536-544.
[126]M. Amirizad, A.H. Kokabi, M. Abbasi Gharacheh, R. Sarrafi, B. Shalchi and M. Azizieh, Evaluation of microstructure and mechanical properties in friction stir welded A356 + 15%SiCp cast composite, Journal of Materials Letters, Volume 60, Issue 4, February 2006, pp. 565-568.
[127]P. Heurtier, M.J. Jones, C. Desrayaud, J.H. Driver, F. Montheillet and D. Allehaux, Mechanical and thermal modelling of Friction Stir Welding, Journal of Materials Processing Technology, Volume 171, Issue 3, February 2006, pp. 348-357.
[128]H. Yoon, Y. Kong, S. Kim and A. Kohyama, Mechanical properties of friction welds of RAFs (JLF-1) to SUS304 steels as measured by the acoustic emission technique, Journal of Fusion Engineering and Design, Volume 81, Issues 8-14, February 2006, pp. 945-950.
[129]G. Sierra, P. Peyre, F. Deschaux-Beaume, D. Stuart and G. Fras, Steel to aluminum key-hole laser welding, Journal of Materials Science and Engineering: A, Volume 447, Issues 1-2, February 2007, pp. 197-208.
[130]B. Hu and I.M. Richardson, Microstructure and mechanical properties of AA7075(T6) hybrid laser/GMA welds, Journal of Materials Science and Engineering: A, Volume 459, Issues 1-2, 25 June 2007, pp. 94-100.
[131]Y. S. Tarng, S. C. Juang, C. H. Chang, The use of grey-based Taguchi methods to determine submerged arc welding process parameters in hardfacing, Journal of Materials Processing Technology, Volume 128, Issues 1-3, 6 October 2002, pp. 1-6.
[132]Z. L. Zhang, J. Ødegård, O. R. Myhr and H. Fjaer, From microstructure to deformation and fracture behaviour of aluminium welded joints – a holistic

modelling approach, Journal of Computational Materials Science, Volume 21, Issue 3, July 2001, pp. 429-435.
[133]W. Zhang, J. W. Elmer and T. DebRoy, Modeling and real time mapping of phases during GTA welding of 1005 steel, Journal of Materials Science and Engineering A, Volume 333, Issues 1-2, August 2002, pp. 320-335.
[134]W. Zhang, T. DebRoy, T.A. Palmer and J.W. Elmer, Modeling of ferrite formation in a duplex stainless steel weld considering non-uniform starting microstructure, Journal of Acta Materialia, Volume 53, Issue 16, September 2005, pp. 4441-4453.
[135]F. Karimzadeh, A. Ebnonnasir and A. Foroughi, Artificial neural network modeling for evaluating of epitaxial growth of Ti6Al4V weldment, Journal of Materials Science and Engineering: A, Volume 432, Issues 1-2, September 2006, pp. 184-190.
[136]N. Kamp, A. Sullivan, R. Tomasi and J.D. Robson, Modeling of heterogeneous precipitate distribution evolution during friction stir welding process, Journal of Acta Materialia, Volume 54, Issue 8, May 2006, pp. 2003-2014.
[137]N. Kamp, A. Sullivan and J.D. Robson, Modeling of friction stir welding of 7xxx aluminum alloys, Journal of Materials Science and Engineering: A, Volume 466, Issues 1-2, September 2007, pp. 246-255.
[138]J. Antony, Design of experiments for engineers and scientists, Elsevier, 2003.
[139]W. G. Cochran and G. M. Cox, Experimental Designs, 2nd Ed, John Wiley & Sons, 1957.
[140]Design-Expert software, V7, user's guide, Technical manual, Stat-Ease Inc., Minneapolis, MN, 2005.
[141]R. K. Roy, Design of Experiments Using the Taguchi Approach, John Wiley & Sons, 2001.
[142]W. Y. Fowlkes and C.M. Creveling, Engineering Methods for Robust Product Design, Addison-Wesley (1995).
[143]S. M. Phadke, Quality Engineering Using Robust Design, Prentice Hall, , 1989, Englewood Cliffs, N.J.

[144]A. Bendell, "Introduction to Taguchi Methodology", Taguchi Methods: Proceedings of the 1988 European Conference, Elsevier Applied Science, London, UK, 1988, pp. 1-14.

[145]G. Taguchi, and S. Konishi, Orthogonal Arrays and Linear Graphs, American Supplier Institute Inc., Dearborn, MI, 1987.

[146]J. L. Lin, K. S. Wang, B. H. Yan and Y. S. Tarng, Optimization of the Electrical Discharge Machining Process Based on the Taguchi Method With Fuzzy Logics, journal of Materials Processing Technology, Volume 102, Issues 1-3, May 2000, pp. 48-55.

[147]A. Kumar, J. Motwani and L. Otero, An application of Taguchi's robust experimental design technique to improve service performance, International Journal of Qualit& Reliability Management, Vol. 13 No. 4, 1996, pp. 85-98.

[148]E. M. Anawa, A. G. Olabi and M. S. J. Hashmi, Application of Taguchi Method to Optimize Dissimilar Laser Welded Components, presented at 23rd International Manufacturing Conference 30th Aug. to 1st Sep., 2006, Belfast, UK, . 241-248.

[149]http://www.pqm.cz/Engpqm/frdoe.htm, (accessed on July 2007).

[150]G. M. Clarke and D. Cooke, A Basic Course in Statistics, chapter 22, pp. 520-546, Arnold, 1998.

[151]P. R. Cohen, Empirical Methods for Artificial Intelligence, chapter 6-7, pp. 185-287, MIT Press, 1995.

[152]T. H. Wonnacott and R. J. Wonnacott, Regration: A second course in statistics, John Wiley & Sons, 1981.

[153]N. R. Draper and H. Smith, Applied Regression Analysis, 3rd Ed, John Wiley & Sons, 1998.

[154]S. Akhnazarova and V. Kafarov, Experiment optimization in chemistry and chemical engineering, 1st Ed, Mir Publishers, Moscow, 1982.

[155]M. C. Chen & D. M. Tsai, A simulated annealing approach for optimization of multi-pass turning operations, International Journal of Production Research, 34(10), 1996, pp. 2803–2825.

[156]M. C. Cakir and A. Gurarda, Optimization and graphical representation of machining conditions in multi-pass turning operations, Computer Integrated Manufacturing Systems, Volume 11, Issue 3, July 1998, pp. 157-170.
[157]Y. V. Hui, L. C. Leung & R. Linn, Optimal machining conditions with cost of quality and tool maintenance for turning. International Journal of Production Research, 39(4), 2001, pp. 647–665.
[158]I. Mukherjee and P. Kumar Ray, A review of optimization techniques in metal cutting processes, Journal of Computers & Industrial Engineering, Volume 50, Issues 1-2, May 2006, pp. 15-34.
[159]R. H. Myers and D. C. Montgomery, Response Surface Methodology- process and Product Optimization Using Designed Experiment, John Wiley & Sons, 1995.
[160]G. Derringer, and R. Suich, Simultaneous Optimization of Several Response Variables, Journal of Quality Technology, 1980.
[161]http://www.itl.nist.gov/div898/handbook/pri/section5/pri5322.htm, (accessed on July 2007).
[162]Shane Y. Hong and Y. Ding, Micro-temperature manipulation in cryogenic machining of low carbon steel, Journal of Materials Processing Technology, Volume 116, Issue 1, October 2001, pp. 22-30.
[163]Mechrtonic Technology in Motion, http://www.mechtronic.co.uk/laser-sales.html, (accessed on August 2007).
[164]Rofin Dc 015 industrial CO_2 Slab laser operating manual, serial No. 2024/2024, 2002.
[165]http://www.rofin.com/index-fe.htm?start=/english/products/macro-laser/CO_2-laser/index.php, (accessed on August 2007).
[166]W. Nickola, Practical subsurface residual stress evaluation by hole drill method, SEM Conference on Experimental Mechanics, Neew Orleans, 1986, pp. 47-57.
[167]C. P. Wu, L. W. Tsay and C. Chen, Notched tensile testing of T-200 maraging steel and its laser welds in hydrogen, Journal of Materials Science and Engineering A, Volume 346, Issues 1-2, 15 April 2003, pp. 302-309.

[168]Annual book of ASTM standards, Metals test methods and analytical procedures, ASTM international, Vol.03.01 (2003), pp. 147-163.
[169]R.a Borrisutthekul, Y. Miyashita and Y. Mutoh, Dissimilar material laser welding between magnesium alloy AZ31B and aluminum alloy A5052-O, journal of Science and Technology of Advanced Materials, Volume 6, Issue 2, March 2005, pp. 199-204.
[170]D. Havrilla and P. Antony, Laser cutting process fundamentals and troubleshooting guideline, 2ed printing Rofin, 2002, pp. 51.
[171]D. C. Montgomery, Design and analysis of Experiments, 2ed Edition, John Wiley and Sons, New York, 1984.
[172]Design-Expert software, V6, user's guide, technical manual, Stat-Ease Inc., Minneapolis, MN; 2000.
[173]E. M. Anawa and A. G. Olabi, The Application of The Hole Drilling Method to Define The Residual Stress of Dissimilar Laser Welded Components, Journal of Applied Mechanics and Materials, Vol. 7-8 ,2007. pp. 133-138.
[174] R.W. Balluffi, Grain boundary diffusion mechanism in metals, Met. Trans. A 13A (1982) pp. 2069–2095.
[175]L. Nastac, D.M. Stefanescu, An analytical model for solute redistribution during solidification of planar, columnar, or equiaxed morphology, Met. Trans. A 24A 1993, pp. 2107–2118.
[176]E. M. Anawa and A. G. Olabi, Effect of Laser Welding Conditions on Toughness of Dissimilar Welded Components, Journal of Applied Mechanics and Materials, Vol. 5-6, 2006, pp. 375-380.
[177]U.R. Kattner, Binary Alloy Phase Diagrams, ASM International, Materials Park, OH, 1990, pp. 147.
[178]A. Mathieu, R. Shabadi, A. Deschamps, M.Suery, S. Matteï, D. Grevey, E.Cicala, Dissimilar material joining using laser (aluminum to steel using zinc-based filler wire), Journal of Optics & Laser Technology, Volume 39, Issue 3, April 2007, pp. 652-661.

APPENDICES

Appendix A: Top view of the designed Shrouding system used for shrouding gas during laser welding process

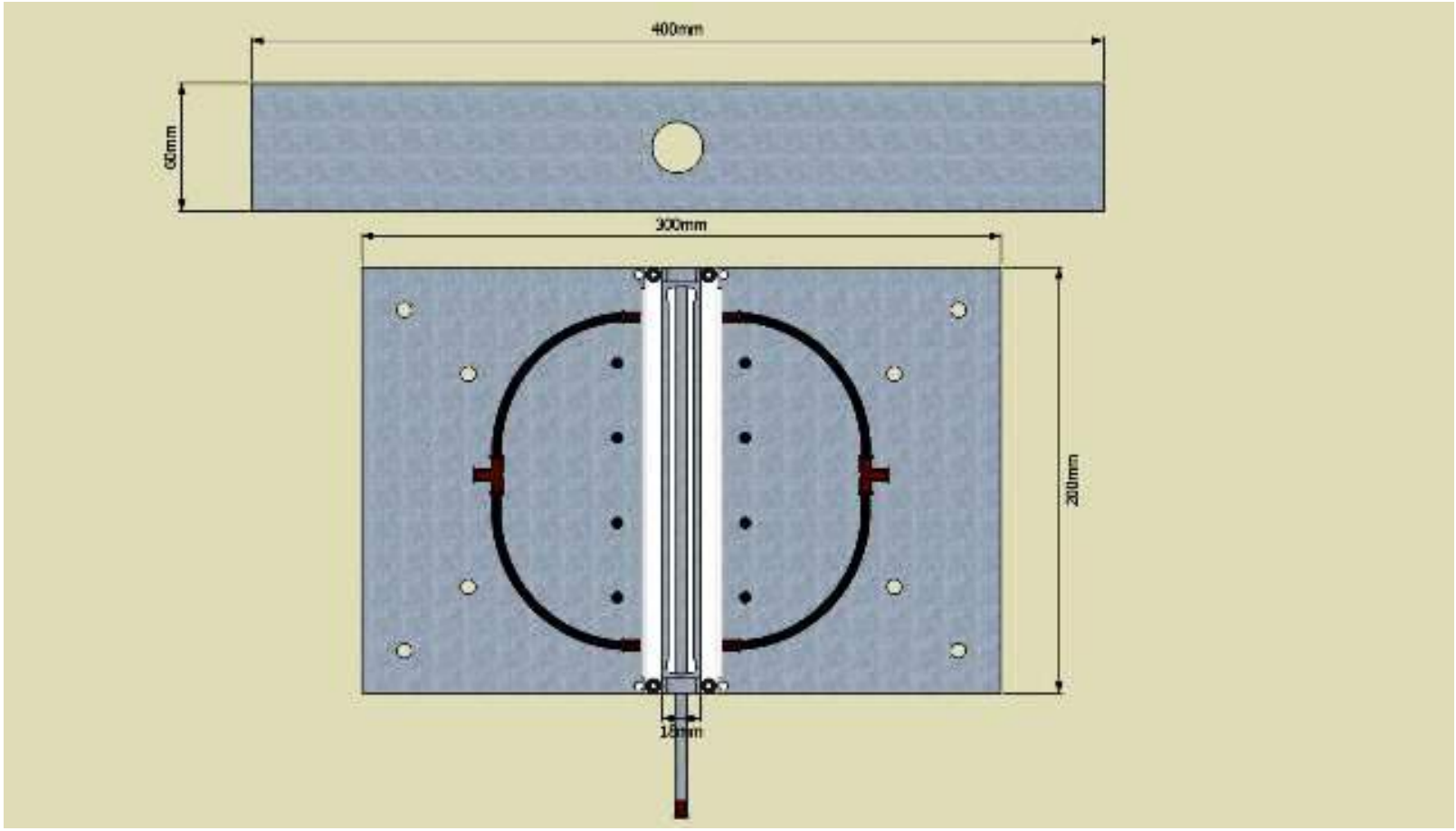

Appendix A: Side view parallel to welding direction of the Shrouding system

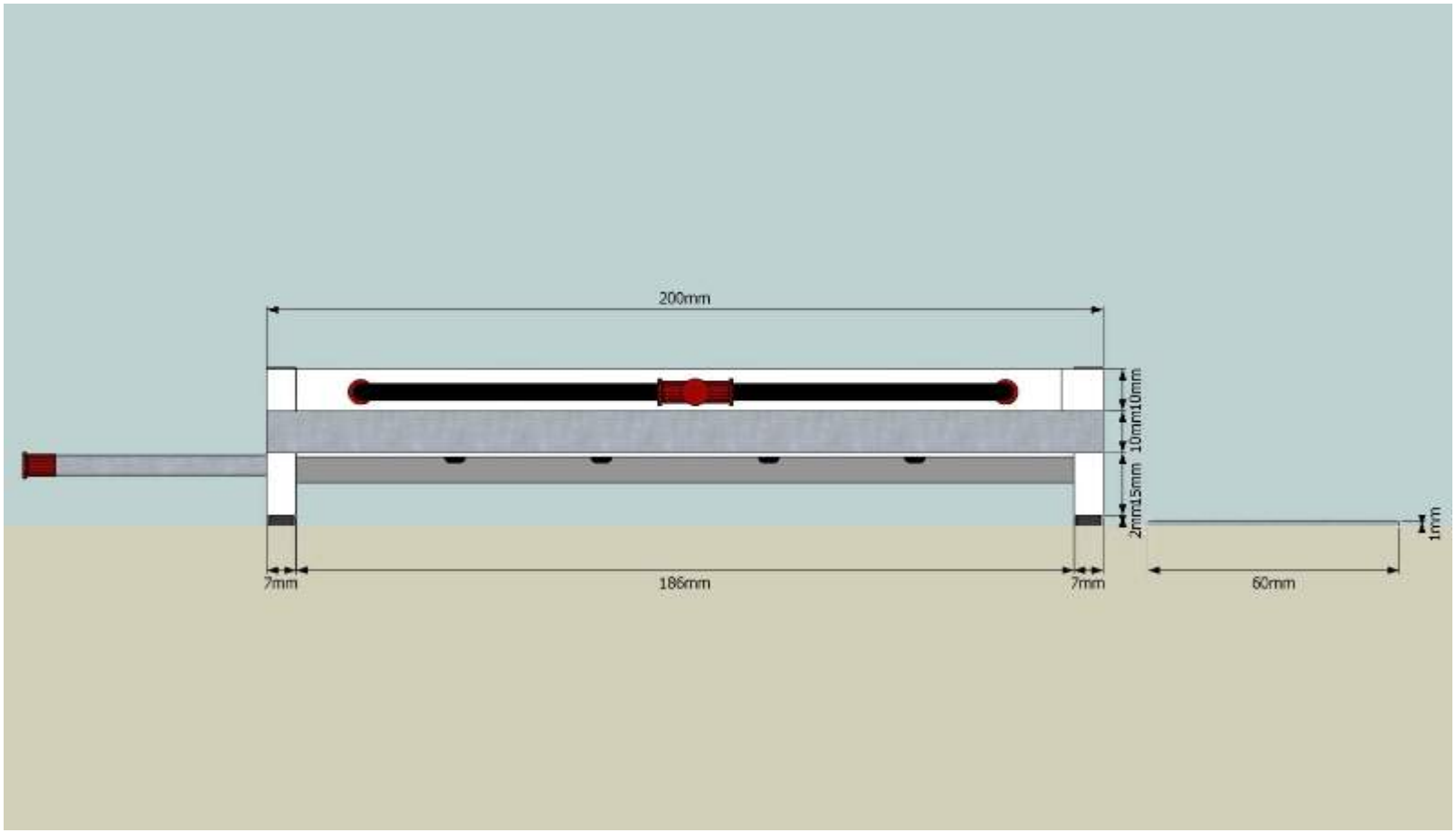

Appendix A: bottom view of the Shrouding system

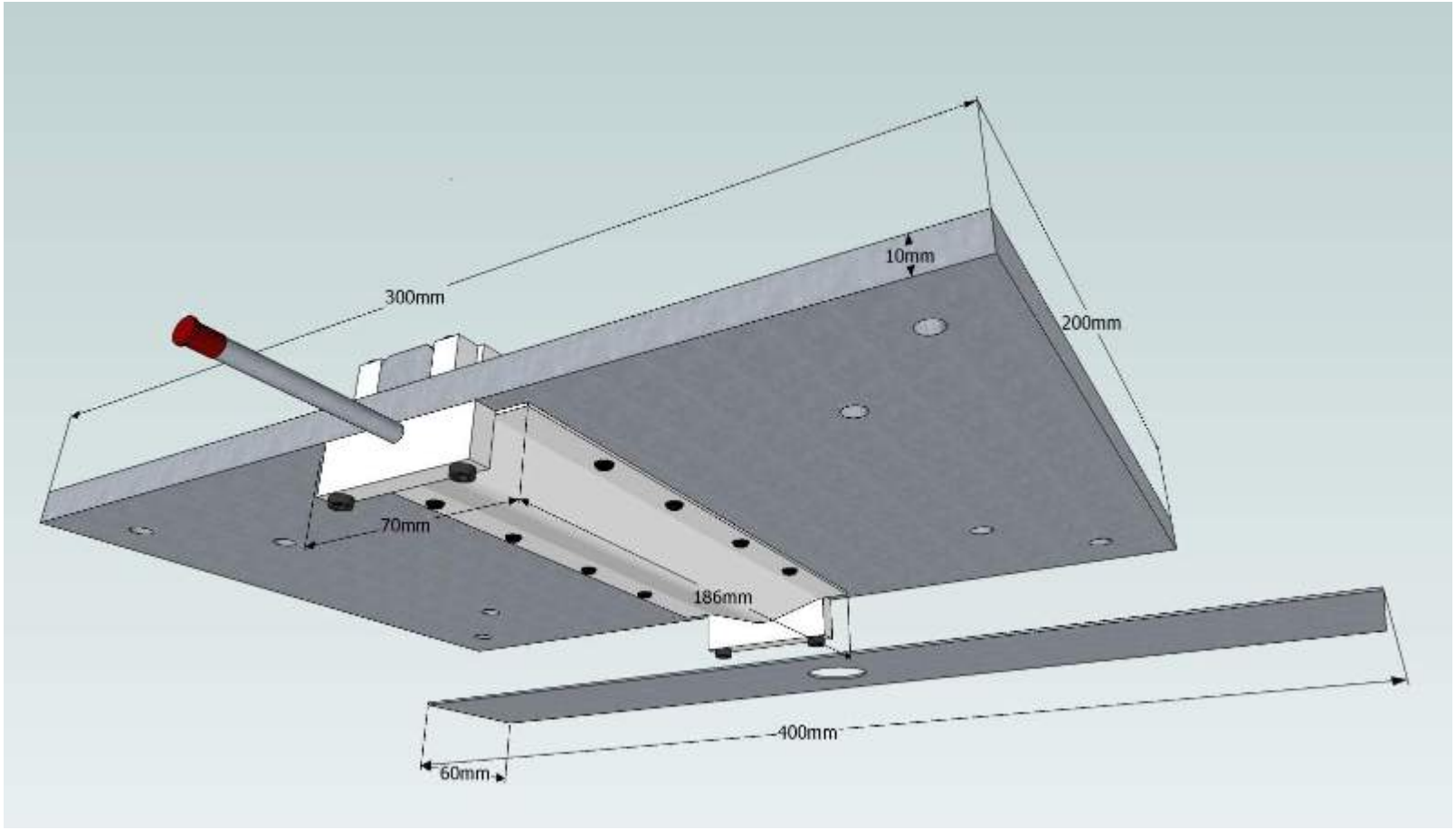

Appendix A: Side view parallel to welding direction of the designed Shrouding system

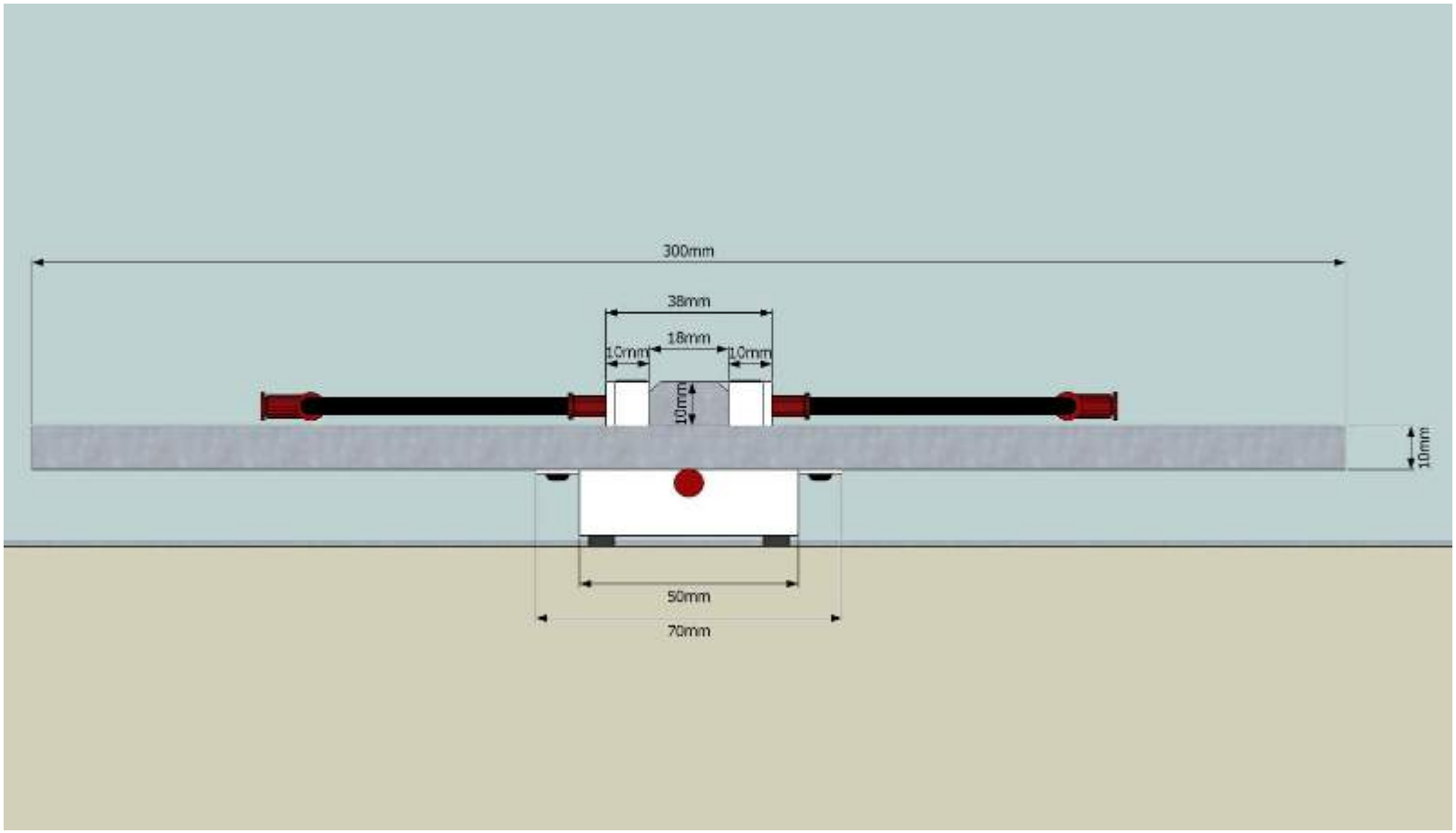

Appendix B: Raw data of the practically measured micro-strains in dissimilar welded compound of A/F in HAZ of AISI 316 side

Depth		Measured Strain micro strain	Specimen No.																									
Z mm	Z/D		1	2	3	4	5	6	7	8	9	10	11	12	13	14	15	16	17	18	19	20	21	22	23	24	25
0.127	0.025	e_1	-13	-9	-6	-4	-5	-5	-5	-6	-4	-3	-8	-7	-7	-9	-8	-14	-10	-8	-9	-3	-8	-7	-8	-6	-6
		e_2	4	4	3	5	2	3	3	4	3	2	4	3	3	2	0	6	3	4	2	2	5	5	5	4	2
		e_3	-10	-10	-5	-6	-7	-6	-10	-12	-10	-9	-9	-9	-10	-8	-7	-13	-12	-7	-7	-5	-11	-9	-9	-8	-7
0.254	0.050	e_1	-19	-8	-11	-9	-8	-10	-11	-12	-8	-9	-15	-11	-12	-11	-10	-20	-14	-10	-13	-6	-16	-14	-13	-10	-9
		e_2	4	5	5	7	3	4	5	5	4	3	5	6	5	4	2	7	4	6	4	3	6	6	6	5	3
		e_3	-15	-15	-9	-10	-8	-10	-15	-19	-12	-10	-17	-16	-15	-13	-10	-20	-18	-11	-11	-12	-19	-16	-16	-13	-10
0.508	0.099	e_1	-27	-19	-18	-15	-13	-18	-19	-22	-17	-15	-24	-22	-20	-19	-17	-29	-18	-12	-20	-13	-25	-19	-18	-15	-12
		e_2	4	8	8	11	4	6	8	8	5	5	7	7	5	5	4	7	4	9	7	6	8	9	7	7	5
		e_3	-24	-25	-16	-16	-14	-19	-22	-25	-18	-16	-24	-25	-21	-18	-15	-29	-22	-18	-17	-16	-29	-22	-20	-19	-14
0.762	0.149	e_1	-33	-26	-24	-20	-15	-27	-25	-27	-25	-22	-27	-27	-25	-24	-22	-35	-23	-17	-24	-21	-33	-23	-23	-25	-16
		e_2	3	9	9	13	3	7	10	11	6	5	8	8	7	6	6	5	5	10	9	8	12	11	9	8	6
		e_3	-30	-29	-22	-22	-19	-24	-28	-30	-24	-23	-31	-29	-28	-25	-21	-35	-25	-23	-21	-22	-35	-27	-25	-26	-21
1.016	0.198	e_1	-36	-30	-28	-23	-20	-33	-29	-28	-30	-27	-33	-31	-31	-27	-25	-37	-29	-25	-28	-23	-38	-29	-30	-29	-22
		e_2	3	10	10	14	3	7	11	12	7	6	11	8	7	7	8	6	5	11	10	9	14	12	10	9	7
		e_3	-32	-36	-27	-24	-23	-30	-32	-30	-28	-26	-33	-33	-30	-27	-22	-38	-29	-26	-23	-24	-39	-31	-31	-30	-25
1.27	0.248	e_1	-37	-27	-30	-25	-23	-36	-31	-31	-32	-30	-36	-32	-28	-28	-25	-37	-32	-30	-29	-26	-40	-34	-33	-31	-26
		e_2	4	14	11	16	3	7	12	14	7	7	11	8	7	7	9	6	5	12	11	10	15	13	11	11	7
		e_3	-33	-39	-29	-26	-25	-31	-35	-34	-31	-29	-39	-35	-28	-26	-23	-38	-35	-27	-24	-25	-39	-35	-37	-36	-27
1.524	0.297	e_1	-37	-29	-29	-25	-24	-37	-31	-29	-34	-28	-35	-31	-27	-26	-25	-35	-29	-29	-28	-27	-37	-33	-36	-30	-27
		e_2	5	15	12	17	3	8	13	14	7	6	12	9	7	6	10	6	5	13	12	12	15	14	12	12	8
		e_3	-32	-37	-29	-27	-27	-30	-35	-37	-30	-30	-37	-33	-25	-24	-22	-38	-34	-24	-22	-27	-38	-34	-35	-37	-29

Appendix B: The used Table for residual stresses calculation and Stresses directions for stainless steel 316

Sample 1														
Depth		Measured Strain micro strain		Relieved Strains			Coefficients				Direction	Equiv. Uniform stress to depth Z Mpa	
Z mm	Z/D			e3 + e1	e3 - e1	e3 +e1 - 2e2						min	max
0.127	0.025	e_1	-13	-2.30E-05	3.00E-06	-3.10E-05	a	0.01170	b	0.02808	-42.24	43.54	273.13
		e_2	4				A	-3.632E-08	B	-6.783E-08			
		e_3	-10				4A	-1.453E-07	4B	-2.713E-07			
0.254	0.050	e_1	-19	-3.40E-05	4.00E-06	-4.20E-05	a	0.02756	b	0.06552	-42.28	32.72	166.01
		e_2	4				A	-8.554E-08	B	-1.583E-07			
		e_3	-15				4A	-3.422E-07	4B	-6.330E-07			
0.508	0.099	e_1	-27	-5.10E-05	3.00E-06	-5.90E-05	a	0.05300	b	0.14040	-43.54	33.96	121.06
		e_2	4				A	-1.645E-07	B	-3.391E-07			
		e_3	-24				4A	-6.580E-07	4B	-1.357E-06			
0.762	0.149	e_1	-33	-6.30E-05	3.00E-06	-6.90E-05	a	0.09434	b	0.21645	-43.76	20.76	86.81
		e_2	3				A	-2.928E-07	B	-5.228E-07			
		e_3	-30				4A	-1.171E-06	4B	-2.091E-06			
1.016	0.198	e_1	-36	-6.80E-05	4.00E-06	-7.40E-05	a	0.10812	b	0.26910	-43.45	22.15	79.16
		e_2	3				A	-3.356E-07	B	-6.500E-07			
		e_3	-32				4A	-1.342E-06	4B	-2.600E-06			
1.27	0.248	e_1	-37	-7.00E-05	4.00E-06	-7.80E-05	a	0.12084	b	0.31239	-43.53	20.78	72.53
		e_2	4				A	-3.751E-07	B	-7.546E-07			
		e_3	-33				4A	-1.500E-06	4B	-3.018E-06			
1.524	0.297	e_1	-37	-6.90E-05	5.00E-06	-7.90E-05	a	0.12402	b	0.32865	-43.19	19.88	69.74
		e_2	5				A	-3.849E-07	B	-7.938E-07			
		e_3	-32				4A	-1.540E-06	4B	-3.175E-06			

Appendix B: Maximum principal stress calculated for AISI 316 in HAZ of A/F Joint

sample No.	Maximum principal stress at depth mm near HAZ							
	0.127	0.254	0.508	0.762	1.016	1.27	1.524	2.052
1	273.13	166.01	121.06	86.81	79.16	72.53	69.74	0.00
2	230.39	120.51	111.32	81.89	82.32	75.39	73.20	0.00
3	138.49	105.95	88.56	69.89	69.82	66.16	63.49	0.00
4	142.93	107.68	86.19	68.39	63.86	61.49	60.86	0.00
5	142.04	81.51	66.84	48.25	50.91	49.90	51.10	0.00
6	138.49	102.68	92.36	74.66	76.57	71.55	69.74	0.00
7	182.83	133.20	104.39	80.19	77.39	73.84	71.86	0.00
8	222.27	156.30	117.92	86.47	74.76	74.15	72.57	0.00
9	173.34	103.13	86.37	71.01	70.91	67.51	66.16	0.00
10	145.59	95.05	77.34	64.72	64.49	63.51	59.72	0.00
11	209.25	159.94	118.65	84.95	83.01	82.14	77.00	0.00
12	191.57	141.02	116.45	82.25	78.46	72.18	67.40	0.00
13	202.52	137.55	99.91	77.32	74.29	60.52	54.57	0.00
14	194.52	120.79	90.88	71.01	66.38	58.53	52.01	0.00
15	158.67	96.36	78.15	63.02	59.27	53.87	51.65	0.00
16	329.67	202.20	141.22	98.02	89.34	78.82	74.19	0.00
17	254.92	157.02	96.30	68.73	69.36	70.19	63.96	0.00
18	188.12	113.53	81.25	62.98	66.07	64.85	59.35	0.00
19	184.23	120.79	93.89	68.58	65.37	60.23	55.85	0.00
20	99.91	91.68	74.38	64.93	60.02	57.52	59.63	0.00
21	238.26	176.68	133.75	102.06	97.75	88.77	81.78	0.00
22	206.26	154.10	105.86	77.17	77.01	77.47	73.43	0.00
23	216.62	149.69	96.11	72.55	76.60	77.17	76.03	0.00
24	177.80	119.56	87.18	75.58	73.57	74.19	72.26	0.00
25	152.26	95.05	66.09	55.14	58.50	57.53	59.05	0.00

Appendix B: Raw data of the practically measured micro-strains in Al 6082 / LCS 10131 in HAZ of AL6082 side

Depth		Measured Strain micro strain	Specimen No.															
Z mm	Z/D		1	2	3	4	5	6	7	8	9	10	11	12	13	14	15	16
0.127	0.025	e_1	-18	-19	-10	-12	-24	-22	-8	-19	-15	-10	-10	-13	-9	-31	-23	-15
		e_2	-3	15	22	12	2	12	12	13	16	12	12	20	14	16	25	20
		e_3	-4	-15	-11	2	-9	-3	-1	-4	4	-12	-12	-4	1	13	6	-9
0.254	0.050	e_1	-20	-23	-13	-15	-25	-24	-9	-25	-16	-24	-24	-14	-10	-32	-26	-14
		e_2	-3	27	18	9	1	9	10	6	16	7	7	19	15	14	20	19
		e_3	-6	-15	-13	-1	-8	-6	-3	-9	4	-13	-13	-5	2	14	3	-10
0.508	0.099	e_1	-21	-28	-18	-15	-26	-26	-14	-24	-19	-21	-21	-19	-12	-36	-25	-18
		e_2	-7	19	12	4	-2	3	3	1	10	4	4	13	11	8	14	13
		e_3	-7	-19	-16	-3	-10	-11	-7	-8	0	-12	-12	-9	-3	9	0	-14
0.762	0.149	e_1	-18	-27	-16	-13	-26	-24	-13	-20	-18	-13	-13	-19	-14	-36	-22	-17
		e_2	-10	13	8	0	-5	-1	-2	-3	8	3	3	9	7	6	9	8
		e_3	-5	-19	-14	-4	-9	-10	-5	-5	-3	-6	-6	-8	-4	8	1	-13
1.016	0.198	e_1	-12	-20	-12	-10	-23	-19	-10	-14	-13	-5	-5	-13	-12	-32	-17	-13
		e_2	-12	9	5	-3	-7	-3	-4	-8	6	0	0	7	5	4	4	5
		e_3	-3	-13	-9	-3	-8	-7	-2	0	-1	-2	-2	-7	-3	11	3	-9
1.27	0.248	e_1	-7	-11	-8	-7	-18	-11	-5	-9	-5	-4	-4	-6	-7	-25	-10	-7
		e_2	-13	5	3	-7	-8	-4	-6	-8	5	0	0	4	4	5	-4	2
		e_3	2	-6	-4	0	-4	-3	3	5	3	-3	-3	-3	-1	16	4	-5

Appendix B: The used Table for residual stresses calculation and Stresses directions for AL 6082

Sample 1													
Depth		Measured Strain micro strain		Relieved Strains			Coefficients				Direction	Equiv. Uniform stress to depth Z MPa	
Z mm	Z/D			e3 + e1	e3 - e1	e3 +e1 - 2e2						min	max
0.127	0.025	e_1	-18	-2.20E-05	1.40E-05	-1.60E-05	a	0.01170	b	0.02808	-24.41	22.98	75.98
		e_2	-3				A	-1.112E-07	B	-2.006E-07			
		e_3	-4				4A	-4.446E-07	4B	-8.023E-07			
0.254	0.050	e_1	-20	-2.60E-05	1.40E-05	-2.00E-05	a	0.02756	b	0.06552	-27.50	11.79	37.87
		e_2	-3				A	-2.618E-07	B	-4.680E-07			
		e_3	-6				4A	-1.047E-06	4B	-1.872E-06			
0.508	0.099	e_1	-21	-2.80E-05	1.40E-05	-1.40E-05	a	0.05300	b	0.14040	-22.50	8.97	18.84
		e_2	-7				A	-5.035E-07	B	-1.003E-06			
		e_3	-7				4A	-2.014E-06	4B	-4.011E-06			
0.762	0.149	e_1	-18	-2.30E-05	1.30E-05	-3.00E-06	a	0.09434	b	0.21645	-6.50	4.26	8.57
		e_2	-10				A	-8.962E-07	B	-1.546E-06			
		e_3	-5				4A	-3.585E-06	4B	-6.184E-06			
1.016	0.198	e_1	-12	-1.50E-05	9.00E-06	9.00E-06	a	0.10812	b	0.26910	22.50	2.00	5.31
		e_2	-12				A	-1.027E-06	B	-1.922E-06			
		e_3	-3				4A	-4.109E-06	4B	-7.689E-06			
1.27	0.248	e_1	-7	-5.00E-06	9.00E-06	2.10E-05	a	0.12084	b	0.31239	33.40	-1.47	3.65
		e_2	-13				A	-1.148E-06	B	-2.231E-06			
		e_3	2				4A	-4.592E-06	4B	-8.925E-06			

Appendix B: Maximum principal stress calculated for Al 6082 in HAZ welded to LCS 10131

sample No.	Maximum principal stress at depth(mm) in HAZ					
	0.127	0.254	0.508	0.762	1.016	1.27
1	75.98	37.87	18.84	8.57	5.31	3.65
2	156.40	85.62	44.64	24.55	14.73	6.78
3	128.26	57.95	31.35	15.81	9.16	4.68
4	68.32	34.92	16.08	7.85	4.45	2.63
5	123.99	52.30	26.79	14.65	10.49	6.50
6	121.74	56.03	29.72	15.13	9.36	4.17
7	62.29	28.85	17.38	7.63	4.08	1.87
8	115.61	58.48	25.26	10.89	5.25	2.94
9	83.34	37.28	20.25	12.31	7.13	2.05
10	106.87	63.20	26.85	9.50	2.69	2.32
11	106.49	47.38	15.10	14.95	9.50	4.90
12	110.16	48.97	27.59	15.02	9.36	3.89
13	64.56	28.93	16.94	10.44	7.11	3.66
14	123.50	51.94	28.92	17.43	11.86	7.02
15	129.24	59.01	27.02	13.18	7.27	2.89
16	134.10	56.11	30.38	15.83	9.55	4.42

Appendix B: Raw data of the practically measured micro-strains in Al 1050H24 / LCS 10131 in HAZ of Al 1050 side

Depth		Measured Strain micro strain	Specimen No.															
Z mm	Z/D		1	2	3	4	5	6	7	8	9	10	11	12	13	14	15	16
0.254	0.050	e_1	2	-11	-8	-7	-18	-11	-5	-9	-25	-14	-8	-6	-17	-25	-17	-7
		e_2	-13	-13	3	-7	-8	-4	-6	-8	5	0	4	4	4	5	-4	2
		e_3	-7	-6	-4	0	-4	-3	8	5	15	-3	-4	-3	-2	16	4	-5
0.508	0.099	e_1	-12	-12	-12	-10	-17	-19	-10	-14	-13	-15	-14	-13	-12	-24	-17	-13
		e_2	-12	-12	5	-3	-7	-3	-4	-8	6	0	6	7	5	4	4	5
		e_3	-3	-3	-9	-3	-8	-7	-2	0	-1	-2	-7	-7	-3	11	3	-9
0.762	0.149	e_1	-18	-27	-16	-13	-26	-24	-13	-20	-18	-13	-18	-19	-14	-36	-22	-17
		e_2	-10	13	8	0	-5	-1	-2	-3	8	3	9	9	7	6	9	8
		e_3	-5	-19	-14	-4	-9	-10	-5	-5	-3	-6	-9	-8	-4	8	1	-13
1.016	0.198	e_1	-21	-28	-18	-15	-26	-26	-14	-24	-19	-21	-18	-19	-12	-36	-25	-18
		e_2	-7	19	12	4	-2	3	3	1	10	4	12	13	11	8	14	13
		e_3	-7	-19	-16	-3	-10	-11	-7	-8	0	-12	-9	-9	-3	9	0	-14
1.27	0.248	e_1	-20	-23	-13	-15	-25	-24	-9	-25	-16	-24	-15	-14	-10	-32	-26	-14
		e_2	-3	27	18	9	1	9	10	6	16	7	16	19	15	14	20	19
		e_3	-6	-15	-13	-1	-8	-6	-3	-9	4	-13	-5	-5	2	14	3	-10
1.524	0.297	e_1	-18	-23	-10	-12	-24	-22	-8	-19	-15	-21	-14	-13	-9	-31	-23	-15
		e_2	-3	29	22	12	2	12	12	13	16	12	17	20	14	15	25	20
		e_3	-4	-15	-11	2	-9	-3	-1	-4	4	-12	-4	-4	1	13	6	-9

Appendix B: Table for residual stresses calculation and Stresses directions for Al 1050 H24

Sample 1														
Depth		Measured Strain micro strain		Relieved Strains			Coefficients				Direction	Equiv. Uniform stress to depth Z Mpa	
Z mm	Z/D			e3 + e1	e3 - e1	e3 +e1 -2e2						min	max
0.254	0.050	e_1	2	-5.00E-06	-9.00E-06	2.10E-05	a	0.02756	b	0.06552	-33.40	-7.43	16.98
		e_2	-13				A	-2.618E-07	B	-4.680E-07			
		e_3	-7				4A	-1.047E-06	4B	-1.872E-06			
0.508	0.099	e_1	-12	-1.50E-05	9.00E-06	9.00E-06	a	0.05300	b	0.14040	22.50	4.27	10.62
		e_2	-12				A	-5.035E-07	B	-1.003E-06			
		e_3	-3				4A	-2.014E-06	4B	-4.011E-06			
0.762	0.149	e_1	-18	-2.30E-05	1.30E-05	-3.00E-06	a	0.09434	b	0.21645	-6.50	4.26	8.57
		e_2	-10				A	-8.962E-07	B	-1.546E-06			
		e_3	-5				4A	-3.585E-06	4B	-6.184E-06			
1.016	0.198	e_1	-21	-2.80E-05	1.40E-05	-1.40E-05	a	0.10812	b	0.26910	-22.50	4.24	9.39
		e_2	-7				A	-1.027E-06	B	-1.922E-06			
		e_3	-7				4A	-4.109E-06	4B	-7.689E-06			
1.27	0.248	e_1	-20	-2.60E-05	1.40E-05	-2.00E-05	a	0.12084	b	0.31239	-27.50	2.93	8.40
		e_2	-3				A	-1.148E-06	B	-2.231E-06			
		e_3	-6				4A	-4.592E-06	4B	-8.925E-06			
1.524	0.297	e_1	-18	-2.20E-05	1.40E-05	-1.60E-05	a	0.12402	b	0.32865	-24.41	2.40	6.93
		e_2	-3				A	-1.178E-06	B	-2.348E-06			
		e_3	-4				4A	-4.713E-06	4B	-9.390E-06			

Appendix B: Maximum principal stress calculated for AL 1050 H24 in HAZ welded to LCS 10131

sample No.	The Calculated maximum principal stress at depth(mm) in HAZ					
	0.254	0.508	0.762	1.016	1.27	1.524
1	16.98	10.62	8.57	9.39	8.40	6.93
2	21.73	10.62	24.55	22.56	18.62	18.32
3	21.31	18.19	15.81	15.82	12.61	11.38
4	11.97	8.92	7.85	8.11	7.60	6.04
5	29.14	15.96	14.65	13.42	11.55	11.25
6	18.71	18.72	15.13	14.93	12.28	10.90
7	7.74	8.19	7.63	8.74	6.26	5.50
8	13.67	10.48	10.89	12.68	12.86	10.34
9	33.44	14.09	12.31	10.27	8.03	7.34
10	27.05	13.78	9.50	13.49	13.90	13.15
11	22.35	18.84	14.95	13.31	10.29	9.46
12	17.82	18.54	15.02	13.96	10.60	9.75
13	34.64	14.07	10.44	8.60	6.21	5.68
14	32.73	16.63	17.43	14.67	11.21	10.75
15	23.94	14.36	13.18	13.71	12.78	11.38
16	20.07	18.96	15.83	15.35	12.19	11.94

Appendix B: Raw data of the practically measured micro-strains in Al 5251H22 / Ti G2 in HAZ of Al 5251H22 side

Depth		Measured Strain micro strain	Specimen No.															
Z mm	Z/D		1	2	3	4	5	6	7	8	9	10	11	12	13	14	15	16
0.127	0.025	e1	4	2	4	3	2	4	1	6	4	5	4	-1	0	-3	4	2
		e2	6	5	4	2	4	5	-1	11	5	4	7	-1	5	4	7	3
		e3	4	2	3	4	1	-1	3	8	3	-12	4	-7	3	-3	3	-4
0.254	0.050	e1	1	-2	4	4	0	1	3	2	-6	-7	1	-5	-2	-10	5	1
		e2	6	4	6	4	6	7	1	8	1	4	6	-3	5	1	9	5
		e3	2	2	4	6	-2	5	4	4	-8	-14	2	-9	1	-8	1	-10
0.508	0.099	e1	-5	-7	-3	6	-5	-1	-4	3	-9	-13	-4	-4	-7	-21	-5	7
		e2	4	1	4	5	5	6	-4	12	0	5	2	-2	1	-7	0	7
		e3	-3	-4	-2	8	-7	4	-3	7	-11	-19	-4	-10	-8	-20	-9	-18
0.762	0.149	e1	-3	-9	-4	0	-11	-5	-6	-1	-5	-3	-4	-2	-7	-21	-8	9
		e2	8	1	4	2	6	3	-5	9	3	16	3	1	3	-2	-1	10
		e3	-1	-5	-3	7	-12	-3	-6	3	-9	-12	-3	-9	-10	-19	-10	-18
0.889	0.173	e1	-5	-8	-4	-1	-11	-6	-6	2	-5	0	-2	-1	-4	-17	-6	11
		e2	6	3	5	1	7	2	-5	12	4	14	6	2	7	4	2	14
		e3	-1	-2	-4	6	-12	-5	-6	4	-10	-10	-2	-10	-8	-15	-8	-16

Appendix B: Table for residual stresses calculation and Stresses directions for Al 5251 H22

Sample 1															
Depth		Measured Strain micro strain		Relieved Strains			Coefficients						Direction	Equiv. Uniform stress to depth Z MPa	
Z mm	Z/D			e3 + e1	e3 - e1	e3 +e1 -2e2								min	max
0.127	0.025	e1	4	8.00E-06	0.00E+00	-4.00E-06	a	0.01170	b	0.02808			#DIV/0!	-36.11	-20.44
		e2	6				A	-7.073E-08	B	-1.276E-07					
		e3	4				4A	-2.829E-07	4B	-5.105E-07					
0.254	0.050	e1	1	3.00E-06	1.00E-06	-9.00E-06	a	0.02756	b	0.06552			-41.83	-12.10	3.10
		e2	6				A	-1.666E-07	B	-2.978E-07					
		e3	2				4A	-6.665E-07	4B	-1.191E-06					
0.508	0.099	e1	-5	-8.00E-06	2.00E-06	-1.60E-05	a	0.05300	b	0.14040			-41.44	-0.07	12.56
		e2	4				A	-3.204E-07	B	-6.382E-07					
		e3	-3				4A	-1.282E-06	4B	-2.553E-06					
0.762	0.149	e1	-3	-4.00E-06	2.00E-06	-2.00E-05	a	0.09434	b	0.21645			-42.14	-3.35	6.86
		e2	8				A	-5.703E-07	B	-9.839E-07					
		e3	-1				4A	-2.281E-06	4B	-3.935E-06					
0.889	0.173	e1	-5	-6.00E-06	4.00E-06	-1.80E-05	a	0.10812	b	0.26910			-38.74	-1.47	6.06
		e2	6				A	-6.536E-07	B	-1.223E-06					
		e3	-1				4A	-2.615E-06	4B	-4.893E-06					

Maximum principal stress calculated for AL 5251 H22 in HAZ welded to Ti G2

sample No.	Maximum principal stress at depth mm near HAZ				
	0.127	0.254	0.508	0.762	0.889
1	-20.44	3.10	12.56	6.86	6.06
2	-2.39	7.51	13.81	10.33	7.32
3	-21.97	-8.65	9.01	6.89	6.74
4	-18.55	-12.63	-9.17	-1.13	-0.36
5	-0.62	14.87	18.02	18.98	16.36
6	6.25	-1.49	1.69	7.10	7.28
7	-1.75	-6.22	6.02	5.77	5.00
8	-33.33	-0.44	-2.10	3.31	1.41
9	-18.55	34.54	23.48	11.32	10.55
10	69.15	56.55	41.59	18.73	11.86
11	-16.52	3.10	10.94	6.38	4.80
12	44.90	28.51	15.49	8.57	7.78
13	4.31	11.07	18.37	13.35	9.97
14	48.63	43.88	42.57	26.70	20.42
15	-10.89	1.62	16.63	11.99	9.06
16	26.66	31.93	22.43	14.01	10.63

Appendix C: Tensile strength testing results and the average (graph and table)

DCU Mechanical & Manufacturing Engineering 21.11.07

Test report

Specimen type :
Tester : Ezzeddin
Machine data :

Pre-load : 0.25 MPa Speed Yield point : 1 mm/min
Speed E-Modulus : 1 mm/min Test speed : 1 mm/min

Test results:

Nr	a_0 mm	b_0 mm	L_0 mm	σ_M uts 2 N	A_t Break Strain %
1	2	14	40.00	1229.94	1.5
2	2	14	40.00	988.87	1.5
⌖3	2	14	40.00	763.54	4.1
4	2	14	40.00	1066.04	1.5

Series graph:

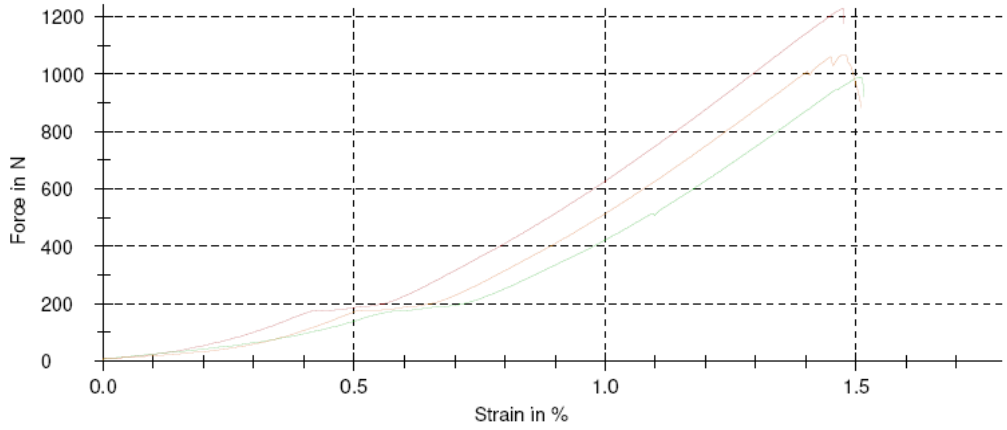

Statistics:

Series n = 3	a_0 mm	b_0 mm	L_0 mm	σ_M uts 2 N	A_t Break Strain %
x	2	14	40.00	1094.95	1.5
s	0.000	0.000	0.00	123.11	0.0
v	0.00	0.00	0.00	11.24	1.42

Appendix C: Tensile strength testing results and the average (graph and table)

DCU Mechanical & Manufacturing Engineering 21.11.07

Test report

Specimen type :
Tester : Ezzeddin
Machine data :

Pre-load : 0.25 MPa Speed Yield point : 1 mm/min
Speed E-Modulus : 1 mm/min Test speed : 1 mm/min

Test results:

Nr	a_0 mm	b_0 mm	L_0 mm	σ_M uts 2 N	A_t Break Strain %
1	2	14	40.00	1647.54	3.7
2	2	14	40.00	1709.52	4.2
3	2	14	40.00	1729.35	3.8
4	2	14	40.00	1652.40	3.8

Series graph:

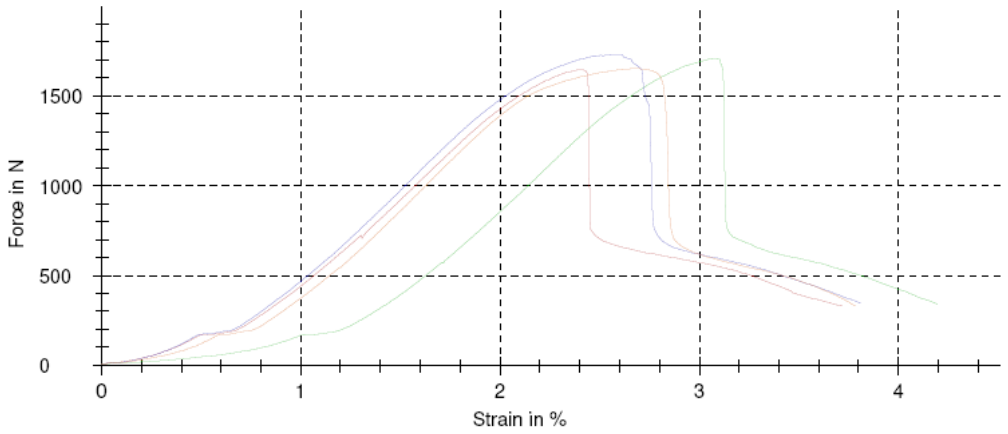

Statistics:

Series n = 4	a_0 mm	b_0 mm	L_0 mm	σ_M uts 2 N	A_t Break Strain %
$\bar{x}$	2	14	40.00	1684.70	3.9
s	0.000	0.000	0.00	40.96	0.2
v	0.00	0.00	0.00	2.43	5.58

Appendix D: Microhardness testing results and the average (graph and table)

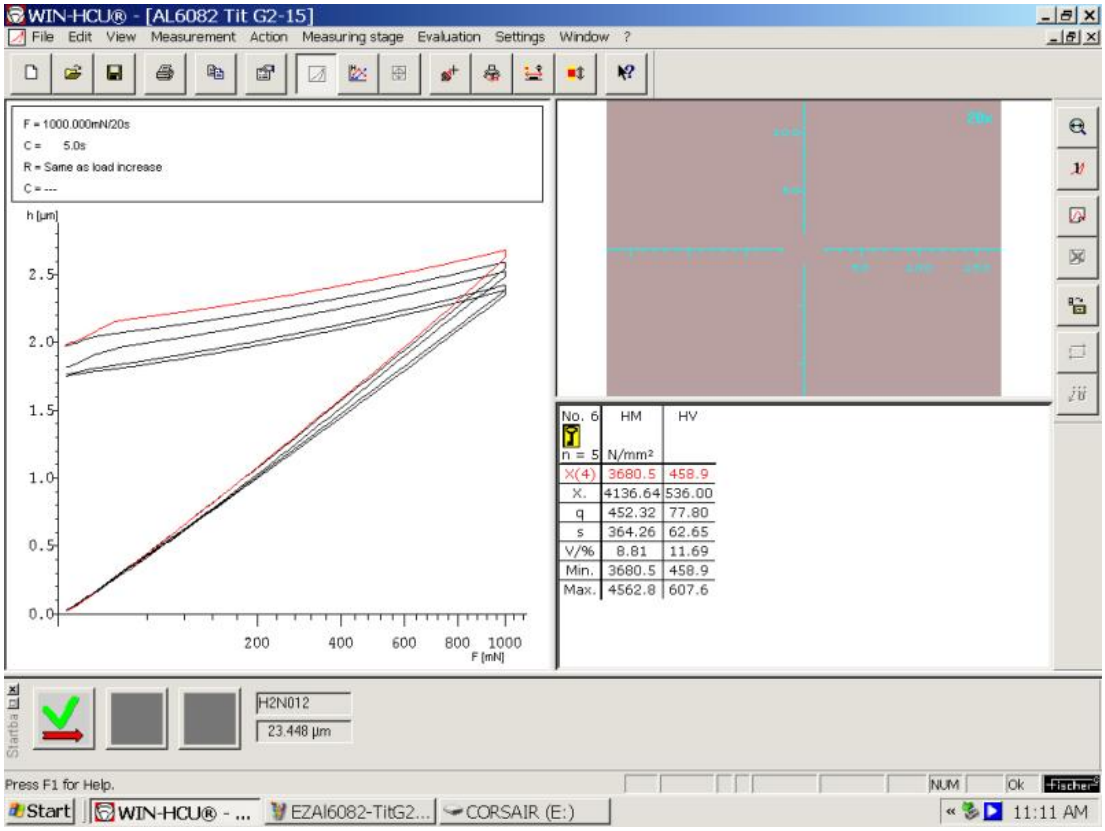

Appendix E: List of Publications

I. Peer Reviewed Journals papers:

1. E. M. Anawa and A. G. Olabi, Effect of Laser Welding Conditions on Toughness of Dissimilar Welded Components, Journal of Applied Mechanics and Materials, Vol. 5-6, 2006, pp. 375-380.
2. E. M. Anawa and A. G. Olabi, The Application of The Hole Drilling Method to Define The Residual Stress of Dissimilar Laser Welded Components, Journal of Applied Mechanics and Materials, Vol. 7-8, 2007. pp. 133-138.
3. E. M. Anawa and A. G. Olabi, Using Taguchi method to optimize welding pool of dissimilar laser-welded components, Journal of Optics & Laser Technology, Vol. 40, 2008, pp. 379–388.
4. E. M. Anawa and A. G. Olabi, Control of Welding Residual Stress for Dissimilar Laser Welded Materials, Journal of Materials Processing Technology, Volume 204, Issues 1-3, 11 August 2008, pp. 22-33.
5. E. M. Anawa and A. G. Olabi, Optimization Tensile Strength of Ferritic / Austenitic Laser Welded Component, Journal of Optics and Lasers in Engineering, Volume 46, Issue 8, August 2008, pp. 571-577.
6. E.M. Anawa, A.G. Olabi, and M.S. J. Hashmi, Application of Taguchi method to optimize dissimilar laser welded components, Int. Journal of Manufacturing Technology and Management, Vol. X, No. Y, pp. .XXX–XXX.
7. E. M. Anawa and A. G. Olabi, Toughness Evaluation of Stainless Steel 316 / low Carbon Steel Dissimilar Laser Welded Components, J of Optics & Laser Technology, under reviewing
8. E. M. Anawa and A. G. Olabi, Prediction and Optimization of Ferrous / Nonferrous Dissimilar Welding Components, under reviewing
9. E. M. Anawa and A. G. Olabi, Measuring and Optimization Fusion Zone Dimensions of Ferrous / Nonferrous of Dissimilar Welding Components, under reviewing

II. Conferences Proceedings:

1. E. M. Anawa, A. G. Olabi and M. S. J. Hashmi, Optimization of ferritic/Austenitic laser welded components, presented at AMPT2006 Inter. Conf. July 30 to 3 Aug., 2006, Las Vegas, Nevada, USA, 2006, pp.04 325.
2. E. M. Anawa and A. G. Olabi, Impact Strength of Dissimilar Laser Welded Joint, presented at 24th International Manufacturing Conference 29th and 31st August 2007, Waterford, Ireland, pp. 611 – 620.
3. E. M. Anawa and A. G. Olabi, Optimization of Tensile strength of Aluminum / Steel Dissimilar Welding Components, will be presented at 25th International Manufacturing Conference 3rd - 5th September 2008, Dublin, Ireland.